Signatures of the quantum vacuum in inhomogeneous electromagnetic fields

Dissertation

zur Erlangung des akademischen Grades
doctor rerum naturalium (Dr. rer. nat.)

seit 1558

vorgelegt dem Rat der Physikalisch-Astronomischen Fakultät
der Friedrich-Schiller-Universität Jena

von M.Sc. Nico Seegert
geboren am 23.06.1986 in Berlin

Gutachter

1. Prof. Dr.rer.nat. habil. Holger Gies,
   Theoretisch-Physikalisches Institut,
   Friedrich-Schiller-Universität Jena, Deutschland

2. PD Dr.rer.nat. habil. Antonino Di Piazza,
   Max-Planck-Institut für Kernphysik,
   Heidelberg, Deutschland

3. Prof. Dr.rer.nat. habil. Tom Heinzl
   Faculty of Science and Engineering
   Plymouth University, United Kingdom

Datum der Disputation: 08.02.2017

Zusammenfassung

Die Theorie der Quantenelektrodynamik beschreibt das Vakuum als durchsetzt von virtuellen kurzlebigen Elektron-Positron-Paaren, welche als Folge quantenmechanischer Nullpunktsfluktuationen auftreten. Diese ermöglichen (klassisch verbotene) nichtlineare Wechselwirkungen zwischen starken elektromagnetischen Feldern in Vakuum, welche zum ersten Mal 1936 von Heisenberg und Euler theoretisch beschrieben wurden. Da diese Wechselwirkungen erst bei extrem hohen Feldstärken sichtbar werden, gibt es bis heute keine experimentelle Bestätigung rein optischer Signaturen der Nichtlinearität des Quantenvakuums.

In dieser Arbeit werden einige Signaturen des Quantenvakuums in inhomogenen elektromagnetischen Feldern mit analytischen Methoden untersucht. Die Betrachtung von inhomogenen Felder wird durch die rasante Entwicklung von Hochintensitätslasern, welche in ihrem Fokus große Feldstärken erreichen können, motiviert. Diese Eigenschaft macht moderne Laser zu idealen Kandidaten um die nichtlinearen Eigenschaften des Quantenvakuums in zukünftigen Experimenten nachzuweisen.

Der erste Teil dieser Arbeit befasst sich mit "Quantenreflexion" als eine neue Signatur des Quantenvakuums, welche nur in manifest inhomogenen Feldern auftritt. Unser Formalismus erweitert den bekannten Ausdruck des Polarisationstensors in konstanten Feldern auf bestimmte Klassen inhomogener Felder. Dies ermöglicht eine tiefgehende Untersuchung verschiedener Konfigurationen und Inhomogeneitäten im experimentell relevanten Limes schwacher Felder und gewährt sogar Einblicke in das Phänomen der Quantenreflexion im Limes starker Hintergrundfelder. Für typische Parameter von modernen Hochintensitätslasern berechnen wir Schätzwerte für die zu erwartende Anzahl von quantenreflektierten Photonen.

Der zweite Teil der Arbeit beschäftigt sich mit Photonen-Splitting und -Merging (Spaltung und Vereinigung) in inhomogenen Hintergrundfeldern. Zu diesem Zweck berechnen wir erstmals eine Darstellung des "Drei-Photonen-Polarisationstensors" für langsam veränderliche aber ansonsten beliebige Hintergundfelder im Niedrigenergie-Limes. Neben einer Analyse der Auswahlregeln für diese beiden Prozesse untersuchen wir ausführlich einige mögliche experimentelle Anordnungen mit Hochintensitätslasern zum Zwecke des Nachweises von Photonen-Merging im Vakuum. Die Emission des Signals in den feldfreien Raum kombiniert mit der einhergehenden Frequenzkonversion sowie induziertem Polarisationswechsel machen Photonen-Merging zu einem vielversprechenden Kandidaten zum experimentellen Nachweis und zur Untersuchung der nichtlinearen Eigenschaften des Quantenvakuums.

Abstract

According to the theory of quantum electrodynamics, zero-point fluctuations of the vacuum manifest themselves through the ubiquitous creation and annihilation of virtual electron-positron pairs. These give rise to classically forbidden nonlinear interactions between strong electromagnetic fields in vacuum, first described by Heisenberg and Euler in 1936. As these interactions only become sizable for large strengths of the involved fields, an experimental verification of purely optical signatures of the quantum vacuum nonlinearity is yet to be achieved.

This thesis deals with various signatures of the quantum vacuum nonlinearity in the presence of inhomogeneous electromagnetic fields, putting emphasis on analytical methods. The proper treatment of inhomogeneities is motivated by the rapid development of high-intensity lasers capable of generating enormous field strengths in their focal spot, making them promising tools for upcoming discovery experiments.

In the first part of this work we introduce "quantum reflection" as a new signature of the quantum vacuum nonlinearity, requiring manifestly inhomogeneous pump fields. To this end we start with an analytical expression of the "two-photon" polarization tensor (photon two-point function) in constant pump fields, and develop a formalism to generalize it to inhomogeneous pump fields. In the experimentally relevant weak-field limit our formalism permits a detailed study of various types of inhomogeneities and configurations. Additionally, we also gain insight into the nonperturbative strong-field limit. The investigation of quantum reflection is concluded by giving estimates for the attainable number of quantum reflected photons in experiments consisting of state-of-the-art high-intensity lasers.

We then turn to the investigation of photon splitting and merging in inhomogeneous pump fields. For the first time, we compute the "three-photon" polarization tensor for slowly-varying but otherwise arbitrary pump field inhomogeneities in the low-energy limit. With its help we discuss in detail the polarization properties and selection rules governing these two processes. For photon merging we perform an elaborate study of possible experimental set-ups employing parameters of present-day state-of-the-art high-intensity lasers. The combination of polarization shifts, frequency conversion and the emission of the signal into background-free areas establishes photon merging as an ideal candidate to experimentally verify the nonlinear nature of the quantum vacuum in upcoming experiments.

Contents

1. Introduction

The theoretical concept and the nature of the vacuum has mystified philosophers and scientists alike for many centuries. Originating from Latin the word vacuum means "empty" space, and commonly denotes a finite region devoid of any material substance. Already the ancient philosophers of Greece including Aristotle and Plato, and later such great minds of the Renaissance as Descartes debated the existence of the vacuum [1, 2]. Towards the end of the nineteenth century it was established that light can be described as an electromagnetic wave, and it was therefore believed that a medium, similar to water or air, must be the carrier of its propagation. However, the famous interferometry experiments by Michelson and Morley [3] could not confirm the existence of such a "luminiferous aether", a fact which eventually contributed to the development of the special theory of relativity by Einstein in 1905 [4]. The theory of relativity proposes the complete equivalence of inertial frames of references and hence discards the notion of a void-filling aether of material substance.

The advent of quantum mechanics in the 1920s expanded the view on the vacuum. In his relativistic theory of the electron, Dirac interpreted the vacuum as an infinite sea of occupied negative energy states, which remains stable due to the Pauli exclusion principle [5]. Removing an electron from these states leaves behind a "hole" which was eventually associated with the positively-charged counterpart (antiparticle) of an electron, the positron, in 1933 [6]. Despite its success the concept of the Dirac sea was soon after superseded by the development of quantum electrodynamics (QED). QED is a relativistic quantum field theory (QFT) and constitutes at the moment the most fundamental and accurate theory for the interaction between light and matter. Although the QED vacuum (or quantum vacuum) is defined as a state with zero particle number, it possesses rather complicated properties. Energy fluctuations, which are a consequence of the uncertainty principle, lead to the ubiquitous creation and annihilation of virtual electron-positron pairs. These short-lived zero-point fluctuations can induce effective nonlinear couplings between electromagnetic fields [7]. A first quantitative description of the nonlinear dynamics of slowly-varying electromagnetic fields in vacuum was already given in 1936 (before the advent of QED), when Heisenberg and

his student Euler introduced a generalization of the Maxwell Lagrangian which takes into account couplings of the fields to a single electron-positron loop to all orders in the field strength [8]; cf. also Ref. [9]. Their work shows that the quantum vacuum acquires medium-like properties, which can significantly modify the propagation of light through vacuum if it is exhibited to strong fields. In 1951, employing proper-time methods and effective-action approaches, Schwinger rederived the Heisenberg-Euler result in the formalism of QED, putting it on firm theoretical grounds [10].

Despite ongoing efforts, quantum vacuum nonlinearities in macroscopic electromagnetic fields have not been directly verified so far.[1] This is mainly due to the fact that nonlinear interactions among laboratory electromagnetic fields are suppressed by powers of the field strength ratio $\mathcal{E}/\mathcal{E}_{\mathrm{cr}}$, where $\mathcal{E}$ denotes the electric/magnetic field amplitude and $\mathcal{E}_{\mathrm{cr}} = m^2/e \approx 1.3 \cdot 10^{18}\mathrm{V/m} \approx 4 \cdot 10^9\mathrm{T}$ the critical field strength.[2,3] On a laboratory scale, the highest field strengths can be generated in the focal spots of pulsed high-intensity lasers. Their rapid development during the preceding decades with intensities now in excess of $10^{22}\mathrm{W/cm^2}$ makes them promising candidates to verify the nonlinear nature of the pure QED vacuum for the first time. Many proposals to verify quantum vacuum nonlinearities rely on a pump-probe scheme, where one laser ("probe") traverses a region of space-time subject to strong electromagnetic fields generated in the focal spot of another laser ("pump").

Prominent optical signatures of the quantum vacuum include direct light-by-light scattering [20, 21], vacuum magnetic birefringence [22–24], photon splitting [25] and merging [26], and the spontaneous decay in terms of Schwinger pair-production in electric fields [10, 27]; for recent reviews see Refs. [28–33]. Gaining an understanding of these signatures in inhomogeneous pump fields is of great importance, as laser pulses feature an intrinsic spatio-temporal structure which might strongly influence the emission characteristics of signal photons induced by the nonlinear interactions. Furthermore, space-time inhomogeneities allow for a richer variety of quantum vacuum signatures that remains invisible in the idealized theoretical limit of constant pump fields, see, e.g., Refs. [34–42].

After briefly introducing in Chap. 2 the theoretical prerequisites required for the investigation of nonlinear vacuum effects, this work focuses on signatures of the quantum vacuum nonlinearity in inhomogeneous pump fields. Our aim is two-fold: On the one

[1] Experimental verifications have been limited to high-energy experiments probing quantum vacuum nonlinearities in the vicinity of highly charged ions [11,12] (Delbrück scattering [13,14] and photon splitting [15,16]), as well as high-precision measurements of the Casimir effect [17–19].

[2] In this work we employ units with $\hbar = c = 1$, cf. the appendix A.

[3] The critical intensity corresponding to these field strengths is $I_{\mathrm{cr}} \approx 5 \times 10^{29}\mathrm{W/cm^2}$.

hand we strive to gain insight into and expand on theoretical techniques to investigate nonlinear photon-photon interactions in inhomogeneous pump fields by means of analytical methods. In Chap. 3, this leads to the introduction of a new signature coined "quantum reflection", which emphasizes the viewpoint that the quantum vacuum in the presence of strong electromagnetic fields acts as an effective potential for traversing probe photons [43, 44]. Even though this potential is purely attractive, photons can experience above-the-barrier scattering (quantum reflection). In contrast to the signatures mentioned above, quantum reflection manifestly requires spatially inhomogeneous pump fields. The formalism devised in this part of the work relies heavily on analytical insights into the two-photon polarization tensor (photon two-point function) in constant pump fields. The inhomogeneous profile is then incorporated *a posteriori* by means of a locally-constant field approximation. We investigate in detail the various types of inhomogeneities and field configurations accessible within our framework, including a study of the strong-field limit.

The second objective of this thesis is to use these results to identify experimental settings which enable the detection of optical signatures of the quantum vacuum nonlinearity for the first time. To this end, in the context of quantum reflection we give experimental estimates for the prospective number of reflected photons attainable with present-day high-intensity laser facilities.

Chapter 4 deals with photon splitting and merging in inhomogeneous pump fields. We employ a recently developed formalism to derive an analytical expression of the photon three-point function to one-loop order in the limit of low energies and momenta and for slowly-varying, but otherwise arbitrary electromagnetic field inhomogeneities [45]. This expression takes into account the coupling of the pump field to the electron-positron loop to all orders. It allows a straightforward analysis of the polarization properties and various selection rules governing splitting and merging. For a pump field profile approximately resembling the focal spot of a pulsed high-intensity laser, we perform a detailed analysis of the attainable number of merged photons again employing parameters of state-of-the-art high-intensity laser facilities. Special emphasis is placed on configurations aimed to increase the signal-to-background ratio, which eventually might permit the use of sensitive single-photon detection mechanisms.

Finally, this work concludes with a short summary and outlook in Chap. 5.

2. Fundamentals of quantum electrodynamics

In the first chapter we give a brief overview of the fundamentals of quantum electrodynamics as they are needed for the description of the purely optical quantum vacuum effects considered in this work, such as quantum reflection and photon merging and splitting. Using the effective-action approach we derive the one-loop effective action, which gives corrections to photon propagation in external electromagnetic "pump" fields and describes higher-order photon-photon interactions. In our formalism the effective multi-photon couplings are mediated by the so-called "photon polarization tensors", which carry the complete physical information for a given interaction process. Analytical expressions for the polarization tensors in various pump field inhomogeneities obtained by suitable approximations will play a major role in the upcoming chapters.

Quantum electrodynamics is a relativistic theory governing the interactions between charged fermionic particle fields, i.e. electrons and positrons, mediated by electromagnetic fields, i.e. photons. Detailed introductions can be found in various textbooks such as [46–48]. The defining "bare" action integral of QED reads[1]

$$\mathcal{S}[\psi,\bar{\psi},\mathcal{A}] = \int_x \mathcal{L}_{\mathrm{QED}} = \int_x \left(i\bar{\psi}\not{D}\psi - m\bar{\psi}\psi - \frac{1}{4}F_{\mu\nu}F^{\mu\nu} \right), \tag{2.1}$$

where $\not{D} = \gamma_\mu D^\mu = \gamma_\mu(\partial^\mu - ie\mathcal{A}^\mu)$ denotes the contracted gauge covariant derivative and $F_{\mu\nu} = \frac{i}{e}[D_\mu, D_\nu]$ the field strength tensor. The four-component Dirac spinors ψ and $\bar{\psi} = \psi^+\gamma^0$ represent fermionic particles and antiparticles respectively, while the covariant four-potential $\mathcal{A}^\mu$ represents the degrees of freedom of the electromagnetic field.[2] The electric charge e of the electron gives the strength of the coupling between the fermionic particles and the electromagnetic field.

[1] The shorthand notation for position and momentum integrals, $\int_x$ and $\int_k$, employed in this work is explained in the appendix A.

[2] In this work we suppress the spinor indices associated with ψ, $\bar{\psi}$ and the γ-matrices.

In this work, we employ the functional integral formulation of QFT and closely follow Ref. [49] to derive the one-loop effective action. For the derivation, we switch to the Euclidean formulation of QFT by rotating the time variable $t \to t_\mathrm{E}/i$ via an analytic continuation. Furthermore, as a shorthand notation we introduce the collective field $\chi = (\psi, \bar{\psi}, \mathcal{A})$. The central object of the functional integral formulation of QFT is the generating functional $Z[J]$,

$$Z[J] = \mathrm{e}^{\mathcal{W}[J]} = \int_\Lambda \mathscr{D}\chi \, \mathrm{e}^{-\mathcal{S}[\chi]+\int_x J\chi} = \langle 0|0\rangle_J \,, \tag{2.2}$$

which is the vacuum-to-vacuum persistence amplitude in the presence of an external "source" field $J(x)$.[3] A UV cut-off $\Lambda > 0$ has been introduced, as the integral diverges and has to be properly renormalized. The Schwinger functional $\mathcal{W}[J]$, introduced in Eq. (2.2), provides a more efficient way of storing relevant information, as one can generate from it *connected* correlation functions $\langle \chi(x_1) \dots \chi(x_n)\rangle$, also called n-point functions, by multiple functional differentiation of $\mathcal{W}[J]$,

$$\langle \chi(x_1) \cdots \chi(x_n)\rangle = \frac{\int_\Lambda \mathscr{D}\chi \; \chi(x_1) \dots \chi(x_n) e^{-\mathcal{S}[\chi]}}{\int_\Lambda \mathscr{D}\chi \; e^{-S[\chi]}} = \frac{\delta}{\delta J(x_1)} \cdots \frac{\delta}{\delta J(x_n)} \mathcal{W}[J]\bigg|_{J=0} \,. \tag{2.3}$$

The vacuum expectation value of the quantum field χ in the presence of a source term J is called the "classical" field $\phi(x)$, and given by

$$\phi(x) := \frac{\delta \mathcal{W}[J]}{\delta J(x)} = \langle \chi(x)\rangle_J \,. \tag{2.4}$$

The "effective" action $\Gamma[\phi]$ is then obtained by the following Legendre transformation

$$\Gamma[\phi] := \sup_J \left(-\mathcal{W}[J] + \int_x J\phi \right) \,. \tag{2.5}$$

In analogy to Eq. (2.3), $\Gamma[\phi]$ is the generating functional for the one-particle irreducible correlation functions. It governs the dynamics of the field expectation value in the presence of an external source by means of the "quantum equation of motion",

$$\frac{\delta \Gamma[\phi]}{\delta \phi(x)} = J(x) \,. \tag{2.6}$$

In principle, the dynamics of the system including its quantum effects can therefore

[3] In line with the shorthand notation employed here, J likewise denotes a collective current. The product $J\chi$ in Eq. (2.2) is then understood as a sum over all possible field components of χ.

be computed if one knows $\Gamma[\phi]$ explicitly. To make headway towards such an explicit representation of $\Gamma[\phi]$, we perform a variable shift $\chi \to \chi + \phi$ to obtain the following expression from Eq. (2.2):

$$\mathrm{e}^{-\Gamma[\phi]} = \int_\Lambda \mathscr{D}\chi \, \mathrm{e}^{-\mathcal{S}[\phi+\chi]+\int_x \frac{\delta\Gamma[\phi]}{\delta\phi}\chi} \,. \tag{2.7}$$

Equation (2.7) is a first-order differential equation involving functionals to determine $\Gamma[\phi]$. Only for a few special cases there have been found analytical solutions [50]. For our purposes it is sufficient to perform an expansion in the number of loops, or equivalently the fine structure constant $\alpha = e^2/4\pi$. To this end we temporarily reinstate the Planck constant $\hbar$ and substitute $\chi \to \sqrt{\hbar}\chi$. Expanding the exponent of the right-hand side of Eq. (2.7) in terms of $\hbar$ yields

$$-\mathcal{S}[\phi] - \int_x \left(\frac{\delta\mathcal{S}[\phi]}{\delta\phi(x)} - \frac{\delta\Gamma[\phi]}{\delta\phi(x)}\right)\sqrt{\hbar}\chi(x) - \frac{1}{2}\int_x\int_{x'} \chi(x)\frac{\delta^2\mathcal{S}[\phi]}{\delta\phi(x)\delta\phi(x')}\hbar\chi(x') + O\left(\hbar^{3/2}\right) \,. \tag{2.8}$$

In a perturbative expansion of the exponent in $\hbar$ the order of $\hbar$ counts the number of loops in a graph [51].[4] The first-order term in χ in Eq. (2.8) is then at least of order $\hbar^{3/2}$, since the term in brackets denotes the difference between the classical and the quantum action and is therefore at least of order $\hbar$. Therefore, up to order $\hbar$ the one-loop effective action reads

$$\Gamma[\phi] = \mathcal{S}[\phi] + \Gamma^{(1)}[\phi] = \mathcal{S}[\phi] + \frac{1}{2}\mathrm{Tr}\ln\left(\frac{\delta^2\mathcal{S}[\phi]}{\delta\phi^2}\right) \,. \tag{2.9}$$

Here, the trace denotes integration in momentum or position space as well as summation over the Dirac indices. We can now evaluate Eq. (2.9) for the QED action (2.1). In this work we are interested in purely optical effects of the quantum vacuum, i.e. those where the ingoing and outgoing states consist only of photon fields. To this end we need to evaluate the effective action for vanishing expectation values of the fermion fields, i.e. $\langle\psi\rangle_J = \langle\bar{\psi}\rangle_J = 0$. In this limit the mixed derivatives of $\mathcal{S}$ which appear in Eq. (2.9) vanish. We switch back from Euclidean to Minkowski space, which generates

[4] The argument goes as follows: $\hbar$ only enters Eq. (2.7) as a factor $1/\hbar$ in front of $\mathcal{S}$ and Γ. The propagator corresponding to an internal line I in a graph is the inverse of the differential operator of the interaction-free Lagrangian, and therefore proportional to $\hbar$. Furthermore, each vertex V introduces an additional factor of $1/\hbar$, such that the power P of $\hbar$ for a certain graph is given by $P = I - V$. From the known relation $L = I - V + 1$, where L denotes the number of loops in a graph, we find $P = L - 1$. Together with the overall factor of $1/\hbar$ in Eq. (2.8), the power of $\hbar$ indeed corresponds to the number of loops.

an extra factor of i in front of the one loop term, and obtain

$$\Gamma[\mathcal{A}] = \mathcal{S}[\mathcal{A}] - i\mathrm{Tr}\ln(i\not{D} - m)\,. \tag{2.10}$$

The minus sign follows from the fermionic Grassmann integration over the Gaussian integral in Eq. (2.1). Furthermore, for brevity we have denoted the "classical" gauge field simply by $\mathcal{A}(x) \equiv \langle \mathcal{A}(x) \rangle_J$. From now on it is implicitly understood that all photon fields referred to in this work are actually the corresponding "classical" fields, or vacuum expectation values, as defined by Eq. (2.4).

Equation (2.10) constitutes the starting point for the investigation of purely optical quantum vacuum effects induced by electron-positron fluctuations to one-loop order. For constant or at most "slowly"-varying electromagnetic fields, i.e. for photons in the low-energy regime $\omega \ll m$, the functional determinant in the effective action (2.10) can be computed analytically. The result is the famous Heisenberg-Euler effective action, which for the first time offered a quantitative description of fluctuation-induced interactions of electromagnetic fields in vacuum [8]. Its explicit representation is reproduced in the appendix F, together with a short derivation motivating the result. The Heisenberg-Euler effective action will play a major role in Chap. 4 for the derivation of the two- and three-photon polarization tensors in the low-energy limit.

Another expression for the effective action not restricted to the low-energy regime can be obtained the following way: Let us split the vector potential of the gauge field according to $\mathcal{A}^\mu(x) = A^\mu(x) + a^\mu(x)$, where the potential $A^\mu(x)$ denotes an external "pump" photon field and $a^\mu(x)$ a "probe" photon field. We rewrite the effective action $\Gamma^{(1)}$ according to

$$\Gamma^{(1)}[a, A] = -i\mathrm{Tr}\ln\left[1 + (i\not{\partial} + e\not{A} - m)^{-1}(e\not{a})\right]\,, \tag{2.11}$$

where the normalization has been chosen in such a way that $\Gamma^{(1)} \to 0$ for $a^\mu \to 0$. The aim is now to expand the effective action in terms of the probe photon fields, while keeping the pump field to all orders. The external pump field is then treated as a classical solution of Maxwell's vacuum equations. As a consequence we are limited to processes where the pump field remains practically unaffected by the nonlinear interactions with the probe field. Due to the tiny cross sections pertaining to purely optical quantum vacuum effects, this the case for practically all all-optical set-ups which can be experimentally realized at the moment and in near future. Note, however, that the validity range of some theoretical investigations regarding the strong-field limit is restricted by treating $A^\mu(x)$ classically.

Using the expansion of the logarithm $\ln(1+x) = x - (1/2)x^2 + (1/3)x^3 + \mathcal{O}(x^4)$, we obtain for the one-loop contribution to the effective action

$$\begin{aligned}\Gamma^{(1)}[a,A] = &-i\mathrm{Tr}\left[\frac{1}{i\partial\!\!\!/ + eA\!\!\!/ - m}(e\phi\!\!\!/)\right] + \frac{i}{2}\mathrm{Tr}\left[\frac{1}{i\partial\!\!\!/ + eA\!\!\!/ - m}(e\phi\!\!\!/)\frac{1}{i\partial\!\!\!/ + eA\!\!\!/ - m}(e\phi\!\!\!/)\right] \\ &- \frac{i}{3}\mathrm{Tr}\left[\frac{1}{i\partial\!\!\!/ + eA\!\!\!/ - m}(e\phi\!\!\!/)\frac{1}{i\partial\!\!\!/ + eA\!\!\!/ - m}(e\phi\!\!\!/)\frac{1}{i\partial\!\!\!/ + eA\!\!\!/ - m}(e\phi\!\!\!/)\right] \\ &+ \mathcal{O}\left(\left[\frac{1}{i\partial\!\!\!/ + eA\!\!\!/ - m}(-e\phi\!\!\!/)\right]^4\right) .\end{aligned} \tag{2.12}$$

Diagrammatically, this can be represented as

$\Gamma^{(1)}[a,A] =$ 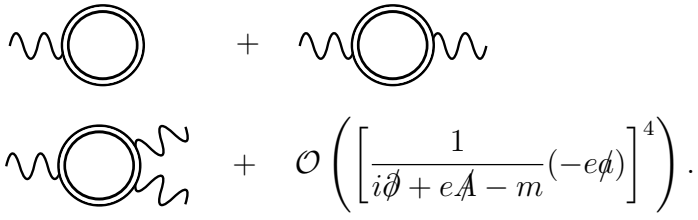 (2.13)

Doubled ("dressed") fermion lines denote the coupling of the external pump field $A^\mu(x)$ to the fermion loop to all orders in the pump field strength. Note that charge conjugation symmetry of QED implies that only an even total number of pump and probe photons may couple to a closed fermion loop, which is know as Furry's theorem [52].

The individual expansion terms in Eq. (2.12) lend themselves to straightforward physical interpretations. The term to first order in $\phi\!\!\!/$ has a tadpole-like structure: It corresponds to the stimulated emission or absorption of probe photons by the external pump field [53]. For probe photons with finite energy/momentum and homogeneous pump fields, the requirement of energy and momentum conservation at the vertex leads to the vanishing of this first-order term. Emission processes in the low-energy limit have recently been theoretically studied in the context of Laser-based experiments [54].

The second-order term in the expansion (2.12) encodes one-loop corrections to photon propagation in an external electromagnetic pump field. The most prominent signature related to photon propagation is vacuum birefringence [22, 23, 55]: A probe photon propagating through the quantum vacuum will feel different indices of refraction depending on its polarization with respect to an applied external pump field. At the moment several experiments aim to detect vacuum birefringence by combining high-finesse cavities and dipole magnets with high-sensitivity polarimetry [56–62]; see Ref. [63] for a recent proposal. Additionally, in Ref. [64] an analogous scheme to be re-

alized with the aid of high-intensity lasers has been proposed, see also Refs. [29,65–68]. Alternative concepts suggest the use of time-varying fields and high-precision interferometry [69–71]. A complementary signature related to photon propagation will be introduced in Chap. 3: "Optical quantum reflection". This effect relies on the ability of pump fields to exchange energy and momentum with probe photons. Accordingly, in contrast to magnetic birefringence and many other signatures of the quantum vacuum, quantum reflection manifestly requires *inhomogeneous* pump fields. Lastly, by virtue of the optical theorem the imaginary part of the second-order diagram corresponds to mode-specific photon losses due to electron-positron pair production [10].

Finally, third-order processes encompass photon splitting and merging under the influence of an external pump field. As depicted in Eq. (2.13), splitting describes the conversion of a single incoming photon into two outgoing photons, while merging denotes the inverse process. These two processes will be studied in detail in Chap. 4 for inhomogeneous pump fields in the low-energy limit.

Let us formally define the position space representation of the dressed electron propagator,

$$G_+(x,x'|A) \;=\; \frac{1}{i}\,\langle x|\frac{1}{i\partial\!\!\!/ + eA\!\!\!/ - m}|x'\rangle \;=\; x \;\; \text{═══} \;\; x'\,, \tag{2.14}$$

which is the solution of the Green's function equation of a Dirac particle in the pump field $A^\mu(x)$,

$$\left[\gamma^\mu\left(\frac{1}{i}\partial'_\mu - e\;A_\mu(x')\right) + m\right] G_+(x',x''|A) = \delta(x'-x'')\,. \tag{2.15}$$

The effective action, encoding processes up to third order in the number of probe photons coupling to the loop, can be compactly written as

$$\begin{aligned}\Gamma[a,A] = -\frac{1}{4}\int_x F_{\mu\nu}F^{\mu\nu}\Big|_{a+A} - \int_x j^\mu(x|A)a_\mu(x) - \frac{1}{2}\int_x\int_{x'} a_\mu(x)\Pi^{\mu\nu}(x,x'|A)a_\nu(x') \\ - \frac{1}{3}\int_x\int_{x'}\int_{x''}\Pi^{\mu\nu\rho}(x,x',x''|A)a_\mu(x)a_\nu(x')a_\rho(x'')\,.\end{aligned} \tag{2.16}$$

Here, for the interaction term linear in the probe photon field a^μ, we have introduced the current

$$j^\mu(x) = ie\,\mathrm{tr}_\gamma\left[\gamma^\mu\,G_+(x,x|A)\right], \tag{2.17}$$

which is the vacuum expectation value in position space of the current operator $j^\mu = \frac{e}{2}\left[\bar\psi,\gamma^\mu\psi\right]$ in the presence of the pump field A^μ [10]. Furthermore, we have defined

the "two-photon" and "three-photon polarization tensor" in an electromagnetic pump field at one-loop order in position space via

$$\Pi^{\mu\nu}(x,x'|A) = ie^2\mathrm{tr}_\gamma\left[\gamma^\mu G_+(x,x'|A)\gamma^\nu G_+(x',x|A)\right] \qquad \text{and} \tag{2.18}$$

$$\Pi^{\mu\nu\rho}(x,x',x''|A) = e^3\mathrm{tr}_\gamma\left[\gamma^\mu G_+(x,x'|A)\gamma^\nu G_+(x',x''|A)\gamma^\rho G_+(x'',x|A)\right] . \tag{2.19}$$

In this work the polarization tensors will form the basis to investigate quantum reflection as well as splitting and merging in external fields in the upcoming chapters.

The two-photon polarization tensor without external fields $\Pi^{\mu\nu}(k)$ is also known as the photon self energy, as it stores the complete information about the modified photon structure which arises due to the interactions with the vacuum fluctuations [28]. A derivation to one-loop order at zero pump field can be found in textbooks, e.g., Ref. [46]. Computing analytical expressions in the presence of external pump fields is much more complicated, and exact results are only available for a few special pump field configurations. For constant electric and magnetic fields of arbitrary orientations the two-photon polarization tensor has been calculated in 1971 by Batalin and Shabad [72], cf. also Refs. [28, 73, 74]. Traditionally, special focus has been laid in the past on the investigation of the polarization tensor in a constant purely magnetic field; cf., e.g., Refs. [23, 75, 76] and particularly the works of Tsai and Erber [77–79]. Likewise, crossed fields constitute another well-examined set of constant-field configurations [80, 81]. The second large class of pump field configurations which allows an exact analytical calculation of the two-photon polarization tensor are generic, elliptically polarized monochromatic plane-wave fields, see Refs. [82–84]. In Chap. 3 we will employ some of these analytical expressions of the two-photon polarization tensor and go beyond the constant-field limit by incorporating inhomogeneous pump fields by means of a locally-constant field approximation. To this end, explicit representations as well as weak-field expansions of the polarization tensor in constant fields are collected in the appendix B.

The three-photon polarization tensor mediates fluctuation-induced interactions between three photons in the presence of an external pump field.[5] Owing to its even more complicated structure, analytical expressions have only been derived for a constant purely magnetic pump field [85] as well as crossed-field configurations [86, 87].[6] A

[5] Note that without the assistance of an external field, three-photon processes such as the specific merging and splitting processes depicted in Eq. (2.13) are prohibited as a consequence of Furry's theorem.

[6] However, splitting and merging *amplitudes* for a wider variety of pump field configurations have been computed, as will be briefly discussed in Chap. 4.

more detailed overview of the various analytical solutions will be given at the beginning of Chap. 4.

3. Quantum reflection

This chapter is dedicated to the phenomenon of quantum reflection. In the first section we briefly discuss the concept of quantum reflection in atomic physics, which we label "atomic quantum reflection". In the following section we carry over this concept to a purely optical set-up, introducing "optical quantum reflection" (or in short quantum reflection) as a new signature of the quantum vacuum nonlinearities. We lay out the framework which we employ to investigate this effect, and calculate reflection coefficients and scattering rates for various pump field inhomogeneities. Finally, we obtain prospective numbers of quantum reflected photons attainable with present-day and near-future high-intensity laser facilities.

3.1. Atomic quantum reflection

Particles traveling in a potential $V(x)$ experience classical reflection at those points where the magnitude of the potential becomes larger than the kinetic energy E_{kin} of the particles. The simplest scenario is reflection at a potential step, where the potential suddenly changes from $V_0 < E_{\text{kin}}$ to $V_1 > E_{\text{kin}}$. However, taking the wave nature of the particles into account it is well known that partial reflection may occur at potential steps which are actually lower than the kinetic energy of the particle, i.e. $V_0, V_1 < E_{\text{kin}}$. The latter effect is based purely on the quantum mechanical properties of particles, as classically particles are not expected to experience any reflection at such a potential step. Furthermore, the ratio of the number of reflected to transmitted particles is unaffected by whether the change in the potential at the step is positive or negative, i.e. $V_0 \lessgtr V_1$. In the limit of smooth potentials, this leads to the classically counterintuitive phenomenon that particles may get reflected off an *attractive* potential, i.e. their motion is reverted "against the classical force" acting on them.[1] With respect to matter waves, this effect is known as "quantum reflection" [88–90]. In recent years

[1] Cf. the homepage of the *Institute for Theoretical Atomic, Molecular and Optical Physics* workshop on quantum reflection, which took place in Cambridge, Massachusetts, USA on October 22-24th, 2007: "https://www.cfa.harvard.edu/itamp/QuantumReflection.html" (accessed May 6th, 2016)

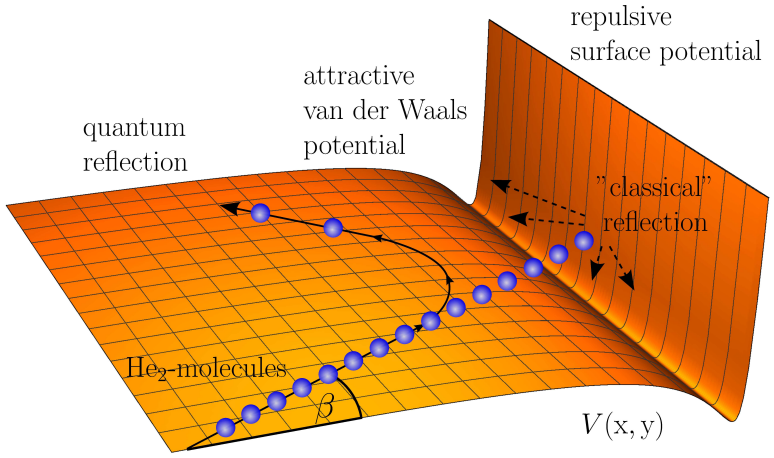

Figure 3.1.: Schematic depiction of atomic quantum reflection in the spirit of Ref. [92]. A beam of neutral atoms or molecules, usually Helium or Neon, hits the surface of a solid under an angle β with respect to the normal of the surface. A fraction of atoms experiences quantum reflection (solid arrow) at the He_2-attractive van der Waals potential of the solid well before hitting the repulsive potential at the surface, where the remainder gets reflected classically (dashed arrows).

quantum reflection has generated great interest in the field of surface science, as it offers the possibility to study long-range surface forces such as the London-Van der Waals and the Casimir-Polder force [91]. Moreover, due to recent technological advances in the cooling and trapping of atoms quantum reflection has been made experimentally accessible.

The basic scenario is depicted in Fig. 3.1. A beam of ultracold neutral atoms or molecules, usually Helium or Neon, is directed onto the surface of a condensed matter specimen, under an angle β to the normal of the specimen's surface. The atoms can be associated with a fluctuating dipole, which polarizes the charges in the wall of the specimen. This leads to an attractive interaction between the atoms and the wall, with associated long-range forces acting upon the atoms. Far away from the surface they feel the Casimir-Polder force [93], which for atoms in the ground state has the potential $V_{\mathrm{CP}}(\mathrm{x}) \sim -1/\mathrm{x}^4$, where x denotes the distance to the surface of the specimen. Approaching the surface, retardation effects can be neglected and the potential becomes the London-Van der Waals potential $V_{\mathrm{VdW}}(\mathrm{x}) \sim -1/\mathrm{x}^3$ [94]. The crossover happens roughly at a distance $\mathrm{x} \sim \lambda/2\pi$, where λ denotes the atomic transition wavelength which contributes to the polarizability of the atoms [95]. Classically, the motion of the atoms is therefore directed further towards the surface. Once the atoms are close to the surface of the solid, however, they feel the repulsive potential stemming from

the atoms in the solid and they get either reflected or adsorbed. Due to the discrete character of the solid, this "classical" reflection is rather diffuse.

Additionally, in the above scenario a fraction of atoms may experience quantum reflection in the region of attractive potential, i.e. even before hitting the surface of the solid. This effect becomes more pronounced as the energy of the incoming particles, or more precisely their velocity component v_n normal to the surface, is decreased. In the limit of vanishing normal velocity the (quantum) reflection coefficient approaches unity [96, 97]. Thus, experiments to investigate quantum reflection employ a set-up where the atomic beam hits the surface at a "grazing" angle of incidence, i.e. $\beta \to \pi/2$. As the long-range attractive potential is rather homogeneous along the surface compared to the repulsive surface potential itself, it induces a specularly reflected signal beam whose magnitude is very sensitive upon the normal velocity v_n, and hence the angle of incidence β. In fact, the quantum mechanical reflection coefficient R_{Qref} typically features an exponential suppression in the normal velocity component of the beam and the decay length w of the attractive potential (see, e.g., Ref. [90]),

$$R_{\text{Qref}} \sim \exp(-A\, w\, v_n)\,, \tag{3.1}$$

with constant $A > 0$. This specular reflection according to Eq. (3.1) provides a means to distinguish the quantum reflected contributions, constituting the signal, from the classically reflected contributions making up the background.

Quantum reflection is nowadays an established technique employed in the field of surface science [98]. Possible applications include its utilization in atomic microscopes, or "nanoscopes", where rigded mirrors working on the basis of quantum reflection might offer a way to focus atomic beams which are then used to probe nanometer-scale samples [99].

3.2. Optical quantum reflection

In this section[2] we carry over the concept of atomic quantum reflection, as described in the last section, to a purely optical scenario. First, we substitute the beam of atoms hitting the surface of the specimen by an incoming probe photon beam $a^{\text{in}}_{\mu}(x)$, which is provided by a high-intensity laser. This photon beam then propagates through a region of the quantum vacuum which is subjected to a strong electromagnetic pump field. As will be shown below, such a pump field modifies the vacuum to act as an

[2]This section follows closely and expands on the results published in Refs. [43, 44].

effective attractive potential for traversing probe photons. If this effective potential features spatial inhomogeneities, similar to atomic quantum reflection, momentum can be transferred from the inhomogeneous pump field onto a fraction of the probe photons, altering their propagation direction and leading to the phenomenon of quantum reflection (albeit this time for photons instead of atoms). In the optical scenario the modified quantum vacuum hence adopts the role of the attractive potential created by the Van-der-Waals and Casimir-Polder forces in the scenario of atomic quantum reflection. Unlike there, however, the optical scenario introduced here features no repulsive surface potential (in fact, there simply exists no purely optical analogue of a repulsive potential). This means that those probe photons which have not interacted with the modified quantum vacuum remain unaffected and continue to propagate on their original path, constituting a background beam with the same properties as the original probe beam. Optical quantum reflection could therefore provide in principle for a clear separation between signal and background photons, that might eventually enable the use of sensitive single-photon detection schemes.

3.2.1. The equations of motion

The starting point for the theoretical investigation of optical quantum reflection is the one-loop effective action (2.16). We discard terms which are of first, third or higher order in the probe photon fields, and retain only contributions to the effective action which encode dynamics of photon propagation, leading to

$$\Gamma[a] = -\frac{1}{4}\int_x F_{\mu\nu}F^{\mu\nu}\bigg|_a - \frac{1}{2}\int_x\int_{x'} a_\mu(x)\Pi^{\mu\nu}(x,x'|A)a_\nu(x')\,. \tag{3.2}$$

From the effective action we can straightforwardly infer the equations of motion by employing the principle of least action. Switching to momentum space,[3] the result is given by

$$\left(k^2 g^{\mu\nu} - k^\mu k^\nu\right) a_\nu(k) = -\int_{k'} \tilde{\Pi}^{\mu\nu}(k,-k'|A)a_\nu(k')\,. \tag{3.3}$$

Here, we have introduced the symmetrized photon polarization tensor $\tilde{\Pi}^{\mu\nu}(k,k'|A) := [\Pi^{\mu\nu}(k,k'|A) + \Pi^{\nu\mu}(k',k|A)]/2$, which mediates between two distinct photon four-momenta k^μ and k'^μ and encodes the entire interaction of the probe photon field a^μ with

[3] The conventions for the Fourier transformation used in this work are given in the appendix A. Note, that for functions $f(x,x')$ with translational invariance a Fourier transformation according to these conventions results in $\int_x\int_{x'} \mathrm{e}^{-ikx} f(x-x')\mathrm{e}^{-ik'x'} \sim \delta^{(4)}(k+k')$, such that on the level of these functions four-momentum conservation is in fact encoded by delta functions $\delta^{(4)}(k+k')$.

the pump field A^μ.

As has been mentioned in the last chapter, analytical expressions of the photon polarization tensor are limited to just two classes of pump fields: (1) Homogeneous electric and magnetic fields of arbitrary field strength, and (2) generic plane-wave fields. To the present date, no exact analytical expressions are known for the photon polarization tensor in a generic pump field configuration. To nonetheless be able to theoretically investigate quantum reflection, which manifestly requires inhomogeneous pump fields, we start with the analytical expression for the photon polarization tensor in a homogeneous electromagnetic field, and incorporate the inhomogeneity by means of the following scheme:

$$\begin{aligned}\tilde{\Pi}^{\mu\nu}(k'|A)\,(2\pi)^4\,\delta^{(4)}(k+k') \;&\xrightarrow{\text{F.T.}}\; \tilde{\Pi}^{\mu\nu}(x-x'|A)\\ &\xrightarrow{\mathbf{E},\mathbf{B}\to\mathbf{E}(x),\mathbf{B}(x)}\; \tilde{\Pi}^{\mu\nu}(x,x'|A) \;\xrightarrow{\text{F.T.}^{-1}}\; \tilde{\Pi}^{\mu\nu}(k,k'|A)\,. \quad (3.4)\end{aligned}$$

The photon polarization tensor in a homogeneous electromagnetic field conserves four-momentum of the probe photons, as indicated by the delta function $\delta^{(4)}(k+k')$. Therefore, a Fourier transformation (F.T) to position space yields a polarization tensor exhibiting translational invariance, as it depends only on $x-x'$. We now substitute the constant electric and magnetic field amplitudes $\mathbf{E}$ and $\mathbf{B}$ by temporally and spatially varying amplitudes, $\mathbf{E}(x)$ and $\mathbf{B}(x)$, which explicitly breaks the translational invariance by construction. Note that by employing the symmetrized polarization tensor the substitution with $\mathbf{E}(x')$ and $\mathbf{B}(x')$ gives the same end result. Finally, a Fourier transformation back to momentum space yields a photon polarization tensor mediating between two distinct photon momenta k^μ and k'^μ.

The strategy (3.4) restricts the types of inhomogeneous field configurations which may be implemented to those which can locally be approximated by a constant. To be more precise, we note that virtual electron-positron fluctuations probe typical distances of $\mathcal{O}(\lambda_c)$ and exist for typical time scales of $\mathcal{O}(\tau_c)$, where $\lambda_c = \frac{1}{m} \approx 3.9\cdot 10^{-13}\text{m}$ and $\tau_c = \frac{1}{m} \approx 1.3\cdot 10^{-21}\text{s}$ denote the electron's Compton wavelength and Compton time. Hence, for inhomogeneities which vary on spatial and temporal scales, w and τ, much larger than the Compton wavelength and time, i.e. $w \gg \lambda_c$ and $\tau \gg \tau_c$, the locally-constant field approximation is well justified. In momentum space this amounts to a restriction to pump fields consisting of low-energy photons, i.e. pump photons whose frequency Ω fulfills $\frac{\Omega}{m} \ll 1$. As a matter of fact, practically all current and proposed all-optical probes of QED vacuum nonlinearities in macroscopic fields fall into this category. Furthermore, it should be noted that the restriction to slowly-varying

fields applies only to the pump field. The probe photon field $a^\mu(k)$, on the other hand, is not affected by the procedure (3.4) and may thus be employed to describe e.g. photon beams in the X-ray regime and beyond.

Let us now perform procedure (3.4) explicitly. We employ the perturbative expansion of the photon polarization tensor in terms of the field strength amplitude $e\mathcal{E}$,

$$\Pi^{\mu\nu}(k'|A)\,(2\pi)^4\,\delta^{(4)}(k+k') = (2\pi)^4\,\delta^{(4)}(k+k')\sum_{\ell=0}^{\infty}\Pi^{\mu\nu}_{(2\ell)}(k)\left[e\mathcal{E}\right]^{2\ell}, \tag{3.5}$$

which corresponds to an expansion in the couplings of the pump field to the electron-positron loop. As a consequence of Furry's theorem the expansion is in even powers of the pump field only. The expansion coefficients $\Pi^{\mu\nu}_{(2\ell)}(k)$ can be inferred from a Taylor expansion of the polarization tensor for constant pump fields about $e\mathcal{E} = 0$. For the special pump field configurations to be considered in this work, namely purely magnetic pump fields characterized by $\mathbf{E} = 0$ and $|\mathbf{B}| =: \mathcal{B}$, and constant-crossed fields characterized by $\mathbf{E}\cdot\mathbf{B} = 0$ and $|\mathbf{E}| = |\mathbf{B}| =: \mathcal{E}$, the lowest-order expansion coefficients (up to $\ell = 1$) are given in Sections B.2 and B.3 of appendix B. A Fourier transformation to position space, and a subsequent substitution of $\mathcal{E} \to \mathcal{E}(x)$ results in

$$\Pi^{\mu\nu}(x,x'|A) = \sum_{\ell=0}^{\infty}\left[e\mathcal{E}(x)\right]^{2\ell}\int_k \mathrm{e}^{ik(x-x')}\,\Pi^{\mu\nu}_{(2\ell)}(k)\,. \tag{3.6}$$

Clearly, the translational invariance is broken by the substitution of an inhomogeneous pump field. As a final step we perform the inverse Fourier transformation and symmetrize to obtain the desired result for the photon polarization tensor,

$$\tilde{\Pi}^{\mu\nu}(k,k'|A) = \sum_{\ell=0}^{\infty}\pi^{\mu\nu}_{(2\ell)}(-k,-k')\int_{x'}\mathrm{e}^{-i(k+k')x'}\left[e\mathcal{E}(x')\right]^{2\ell}, \tag{3.7}$$

mediating between the two distinct momenta k and k'. Here, we have introduced the tensorial quantity

$$\pi^{\mu\nu}_{(2\ell)}(k,k') = \frac{1}{2}\left[\Pi^{\mu\nu}_{(2\ell)}(k) + \Pi^{\mu\nu}_{(2\ell)}(k')\right], \tag{3.8}$$

which is completely independent of the pump field amplitude. For the most part, in our analysis to follow we will only retain the lowest nontrivial order in the pump field strength (i.e. $\ell = 1$). Such a weak-field approximation is justified for pump fields whose amplitude is much smaller than the critical field strength $\mathcal{E}_{\mathrm{cr}} = m^2/e \approx 1.3\cdot10^{18}\mathrm{V/m} \approx 4\cdot10^{9}\mathrm{T}$, since the expansion (3.5) actually amounts to an expansion in the critical field strength ratio $\mathcal{E}/\mathcal{E}_{\mathrm{cr}}$. The electromagnetic fields generated in the focal spots of current

state-of-the-art as well as near-future high-intensity lasers fulfill $\mathcal{E}/\mathcal{E}_{\rm cr} \ll 1$, and therefore discarding of higher-order terms ($\ell > 1$) constitutes an excellent approximation enabling us to analytically investigate a plethora of field configurations. As we can see, implementing an arbitrary field strength profile $\mathcal{E}(x)$ amounts to nothing more than performing a four-dimensional Fourier transformation of powers $[e\mathcal{E}(x)]^{2\ell}$ of the pump field profile.

Alternatively, procedure (3.4) may also be carried out for the full nonperturbative expressions of the polarization tensors, given by Eqs. (B.10) and (B.19). For a small class of pump field profiles the ensuing Fourier transformation can be performed analytically, such that the resulting polarization tensors can eventually be written in terms of a double parameter integral of similar complexity as for the case $\mathcal{E} = \text{const.}$, allowing insights into the strong-field limit. In Sect. 3.2.5 we will deal with the nonperturbative strong-field case in more detail.

At first glance, procedure (3.4) seems to be well suited to incorporate arbitrary pump field profiles $\mathcal{E}(x)$ into the polarization tensor. However, limitations are imposed by the requirement that the equations of motion (3.3) be gauge invariant: Any gauge transformation $a^\mu(k) \to a^\mu(k) + k^\mu f(k)$ of the photon field, where $f(k)$ denotes an arbitrary function of the photon momentum k^μ, should leave the equations of motion invariant. As a necessary condition on the photon polarization tensor we obtain the so-called "Ward identity", reading $k_\mu \Pi^{\mu\nu}(k,k') = 0 = \Pi^{\mu\nu}(k,k')k'_\nu$. We see that the polarization tensor (3.7) constructed along the scheme (3.4) generically violates the Ward identity. This becomes more obvious in position space, where the Ward identity is given by $\partial_\mu \Pi^{\mu\nu}(x,x'|\mathcal{E}) = 0 = \partial'_\nu \Pi^{\mu\nu}(x,x'|\mathcal{E})$, which has to hold for arbitrary pump fields $\mathcal{E}$. Starting from the expression $\Pi^{\mu\nu}(x,x'|\mathcal{E})$ for constant pump fields, and naively inserting an inhomogeneous field $\mathcal{E}(x)$ will now generically break the Ward identity, as the position space derivatives will also hit the position space dependence of the pump field $\mathcal{E}(x)$.

The violation of the Ward identity and the emergence of equations of motion which are not gauge invariant challenges the validity of the entire approach employed thus far. To deal with this issue, in a first step we make use of the fact that the tensorial quantity on the left-hand side of Eq. (3.3) can be represented as follows,

$$\left(k^2 g^{\mu\nu} - k^\mu k^\nu\right) = k^2 \sum_{p=1}^{3} (P'_p)^{\mu\nu} \,. \tag{3.9}$$

Here, the $(P'_p)^{\mu\nu}$ correspond to a set of projectors fulfilling the usual projector identities

$(P'_pP'_q)^{\mu\nu} = \delta_{p,q}(P'_p)^{\mu\nu}$, $(P'_p)^{\mu}{}_{\mu} = 1$. They represent projections onto photon polarization modes p, which will be specified later. Likewise, on the right-hand side the polarization tensor generically can be decomposed according to

$$\tilde{\Pi}^{\mu\nu}(k,-k'|A) = \sum_p \tilde{\Pi}_p(k,-k'|A)\,(P_p)^{\mu\nu} + Q^{\mu\nu}, \tag{3.10}$$

with scalar coefficients $\tilde{\Pi}_p$. Similar to above, the projectors $(P_p)^{\mu\nu}$ fulfill the identities $(P_pP_q)^{\mu\nu} = \delta_{p,q}(P_p)^{\mu\nu}$, $(P_p)^{\mu}{}_{\mu} = 1$. Note, however, that $(P'_p)^{\mu\nu}$ and $(P_p)^{\mu\nu}$ correspond to two – *a priori* unrelated – sets of projectors. Additionally, Eq. (3.10) features a residual contribution $Q^{\mu\nu}$ which cannot be expressed in terms of the projectors $(P_p)^{\mu\nu}$, and which furthermore does not necessarily fulfill $(P_pQ)^{\mu\nu} = 0$ for all p. The structure given in Eq. (3.10), including the residual component $Q^{\mu\nu}$, can be observed in the expression for the polarization tensor in generic constant pump fields, Eq. (B.6). To keep notation simple, we have omitted any explicit reference to the momentum and pump field dependencies for both sets of projectors and the residual contribution $Q^{\mu\nu}$.

In a second step, we have to identify at least one *global* projector $(\tilde{P}_p)^{\mu\nu}$ fulfilling $(\tilde{P}_p)^{\mu\nu} \equiv (P_p)^{\mu\nu} \equiv (P'_p)^{\mu\nu}$ and $(\tilde{P}_pQ)^{\mu\nu} \equiv 0$. We can then contract the equations of motion (3.3) with this particular projector to arrive at the scalar equation of motion

$$k^2\, a_p(k) = -\int_{k'} \tilde{\Pi}_p(k,-k'|A)\, a_p(k')\,. \tag{3.11}$$

Here, we have introduced photons $a_p^{\mu} = \tilde{P}_p^{\mu\nu}a_\nu$ polarized in mode p. Projecting onto a single polarization mode p has caused the equations of motion to loose any nontrivial Lorentz index structure, and therefore we have dropped the trivial Lorentz indices of the photon field, i.e. $a_{p,\mu}(k) \to a_p(k)$.

The second step outlined above amounts in fact to a projection onto a subset of photon polarization modes p for which the Ward identity remains unbroken. To clarify this we note that the photon polarization tensor (3.7) is composed, through the tensorial quantity (3.8), of the weak-field expansion coefficients $\Pi^{\mu\nu}_{(2\ell)}(k)$ and $\Pi^{\mu\nu}_{(2\ell)}(k')$ of the polarization tensor in a constant field. These coefficients can be expressed in terms of projectors $(P_p)^{\mu\nu}(k)$ and $(P_p)^{\mu\nu}(k')$ respectively, as is shown in appendix B.[4] Likewise, we can decompose the left-hand side of the equations of motion, Eq. (3.9), in terms of the projectors $(P'_p)^{\mu\nu}(k) = (P_p)^{\mu\nu}(k)$. It now becomes apparent that a global projector fulfilling $(\tilde{P}_p)^{\mu\nu} \equiv (P_p)^{\mu\nu}(k) = (P_p)^{\mu\nu}(k')$ projects out precisely these photon polariza-

[4] Cf. Eq. (B.10) and its respective projectors for a purely magnetic pump field configuration, and Eq. (B.19) along with the respective projectors for a constant-crossed pump field configuration.

tion modes for which the Ward identity remains intact, as $k_\mu(\tilde{P}_p)^{\mu\nu} = (\tilde{P}_p)^{\mu\nu}k'_\nu = 0$ holds exactly. Hence, the existence of such a global projector is absolutely paramount to our formalism. For the two pump field configurations to be discussed in detail below, namely purely magnetic and crossed pump fields, we can indeed identify large classes of inhomogeneities compatible with the existence of a global projector.

Having arrived at the scalar equation (3.11) by means of the global projector cuts both ways: On the one hand we have managed to reduce the rather involved tensor structure of the original equations of motion (3.3), enabling us to find solutions by employing standard Green's function methods. On the other hand, the scope of the analysis is now limited to scenarios where the polarization mode p of the incoming photons and the signal photons remains invariant, i.e. no scattering events between different polarization mode channels can be investigated.

In order to solve the scalar equation of motion (3.11), we perform a Fourier transformation to position space,

$$\Box a_p(x) = \int_{x'} \tilde{\Pi}_p(x, x'|A)\, a_p(x') \equiv j_p(x)\,. \tag{3.12}$$

The induced current on the right-hand side is nonzero only in spacetime regions where the pump field deviates from zero, and falls off rapidly to zero outside. In our subsequent analysis we aim at investigating pump fields which are localized in a finite region of space. Equation (3.12) features a structure known from quantum mechanical scattering problems, enabling us to employ similar methods to construct a solution. To incorporate the proper boundary conditions, we cast Eq. (3.12) into an integral equation given in terms of the desired solution for the photon field $a_p^{\text{out}}(x)$, the incoming photon field $a_p^{\text{in}}(x)$ and the retarded Green's function $G^{\text{R}}(x, x')$ for the d'Alembert operator $\Box = \partial_\mu\partial^\mu$,

$$a_p^{\text{out}}(x) = a_p^{\text{in}}(x) + \int_{x'} G^{\text{R}}(x, x') \int_{x''} \tilde{\Pi}_p(x', x'')a_p^{\text{out}}(x'')\,. \tag{3.13}$$

Equation (3.13) is the nonrelativistic Lippmann-Schwinger equation with a nonlocal, nonseparable potential $\tilde{\Pi}(x', x'')$.[5] The right-hand side still depends on the resulting photon field $a_p^{\text{out}}(x'')$. A solution can be constructed by successively inserting the

[5]For completeness let us remark that the Lippmann-Schwinger equation (3.13) can as well be cast into the usual quantum mechanical operator language, by defining the operators $\hat{G}^{\text{R}}$ and $\hat{\Pi}_p(A)$ via their position space representation, $\langle x|\hat{G}^{\text{R}}|x'\rangle = G^{\text{R}}(x, x')$ and $\langle x|\hat{\Pi}_p(A)|x'\rangle = \tilde{\Pi}_p(x, x'|A)$. The solution of the Lippmann-Schwinger equation $|a_p^{\text{out}}\rangle = |a_p^{\text{in}}\rangle + \hat{G}^{\text{R}}\hat{\Pi}_p(A)|a_p^{\text{out}}\rangle$ is then formally given by the resolvent of the operator $\hat{G}^{\text{R}}\hat{\Pi}_p(A)$, i.e. $|a_p^{\text{out}}\rangle = [\hat{1} - \hat{G}^{\text{R}}\hat{\Pi}_p(A)]^{-1}|a_p^{\text{in}}\rangle$.

left-hand side of Eq. (3.13), $a_p^{\rm out}(x)$, into the right-hand side, leading to the von Neumann-series

$$a_p^{\rm out}(x) = a_p^{\rm in}(x) + \int_{x'} G^{\rm R}(x,x') \int_{x''} \tilde{\Pi}(x',x'') a_p^{\rm in}(x'') + \int_{x'} G^{\rm R}(x,x') \int_{x''} \tilde{\Pi}_p(x',x'') \int_{x'''} G^{\rm R}(x'',x''') \int_{x^{IV}} \tilde{\Pi}_p(x''',x^{IV}) a_p^{\rm in}(x^{IV}) + \dots \,. \quad (3.14)$$

Such an expansion in fact corresponds to an expansion in the fine structure constant α, or equivalently in the number of successive electron-positron loops taken into account. Higher-order terms quickly become rather complicated, as multiple integrals of the photon polarization tensor have to be computed. Furthermore, the effective action (3.2) has been calculated to one-loop order only, such that for reasons of consistency we should only retain terms up to $\mathcal{O}(\alpha)$, i.e. the first line of Eq. (3.14). Hence, discarding higher-order terms results in

$$a_p^{\rm out}(x) \;=\; a_p^{\rm in}(x) \,+\, \int_{x'} G^{\rm R}(x,x') \int_{x''} \tilde{\Pi}(x',x'') a_p^{\rm in}(x'') \;\equiv\; a_p^{\rm in}(x) \,+\, a_p^{\rm ind}(x)\,, \quad (3.15)$$

which is also known as the Born approximation to the von Neumann-series. This approximation is only justified if the amplitude of the induced photon field $a_p^{\rm ind}(x)$ for each point in spacetime is much smaller than the amplitude of the incoming photon field $a_p^{\rm in}(x)$, yielding the necessary condition

$$\left| \int_{x'} G^{\rm R}(x,x') \int_{x''} \tilde{\Pi}(x',x'') a_p^{\rm in}(x'') \right| \ll \left| a_p^{\rm in}(x) \right| \,. \quad (3.16)$$

In the following analysis we will limit ourselves to incident photon fields to be described by a positive-energy plane wave, $a_p^{\rm in}(x) = a(\omega_{\rm in}) {\rm e}^{ik_{\rm in}x}$, of energy $\omega_{\rm in} > 0$ and amplitude $a(\omega_{\rm in})$. The plane wave is considered to be made up of on-shell photons, i.e. $k_{\rm in}^2 = 0$, with wave vector $k_{\rm in}^\mu = \omega_{\rm in}(1, \cos\beta, \sin\beta, 0)$, propagating w.l.o.g. in the x-y plane. Their propagation direction in this plane is controlled by the choice of the angle $\beta \in (-\pi, \pi]$.

Specializing to positive energy photons requires us to only retain the positive energy branch $G_+^{\rm R}$ of the retarded Green's function $G^{\rm R} = G_+^{\rm R} + G_-^{\rm R}$ in Eq. (3.15).[6] In momentum space, the defining equation for the retarded Green's function of the d'Alembert

[6] This is in line with the Fock space representation of the photon field in position space $|a_p(x)\rangle = \int_{\mathbf{k}} \frac{1}{\sqrt{2k^0}} {\rm e}^{ikx} a_{\mathbf{k},p}^\dagger |0\rangle$, with $k^0 = \sqrt{\mathbf{k}^2}$, where only positive-energy waves amount to propagating real photons.

operator $\Box = \partial_\mu \partial^\mu$ reads[7]

$$-\left[\mathbf{k}^2 - (\omega + i0^+)^2\right] G^{\mathrm{R}}(k, k') = (2\pi)^4\, \delta^{(4)}(k + k')\,. \tag{3.17}$$

After a Fourier transformation to position space we obtain a useful integral representation of the Green's function,

$$G^{\mathrm{R}}(x, x') = \Theta(t - t') \int \frac{\mathrm{d}^3 k}{(2\pi)^3}\, \frac{1}{2i\sqrt{\mathbf{k}^2}} \left(\mathrm{e}^{ik_+(x-x')} - \mathrm{e}^{ik_-(x-x')}\right), \tag{3.18}$$

with $k_\pm^\mu \equiv (\pm\sqrt{\mathbf{k}^2}, \mathbf{k})$ and $k_\pm^2 = 0$. The Heaviside function $\Theta(t - t')$ ensures causality, as it leads the Green's function to vanish for $t - t' < 0$. Furthermore, it provides a time direction enabling us to distinguish between the positive and negative-energy contributions which are present in Eq. (3.18), such that we find

$$G_\pm^{\mathrm{R}}(x, x') = \pm\Theta(t - t') \int \frac{\mathrm{d}^3 k}{(2\pi)^3}\, \frac{1}{2i\sqrt{\mathbf{k}^2}}\, \mathrm{e}^{ik_\pm(x-x')}\,. \tag{3.19}$$

Plugging the plane-wave representation of the incoming photon field and the positive-energy branch of the Green's function (3.19) into Eq. (3.15) yields for the induced photon field

$$a_p^{\mathrm{ind}}(x) = a(\omega_{\mathrm{in}}) \int \frac{\mathrm{d}^3 k}{(2\pi)^3}\, \frac{\mathrm{e}^{ik_+ x}}{2i\sqrt{\mathbf{k}^2}} \int_{x'} \int_{x''} \Theta(t - t')\, \mathrm{e}^{-ik_+ x'}\, \tilde{\Pi}(x', x'')\mathrm{e}^{ik_{\mathrm{in}} x''}\,. \tag{3.20}$$

We are interested in asymptotic solutions for the induced photon field, with the detection of photons taking place far outside the interaction region where the pump field inhomogeneity is nonvanishing, and at times $t \to \infty$ much later than the time of interaction. For temporally localized pump field inhomogeneities the integrand of Eq. (3.20) vanishes at these asymptotic detection times, implying the assumption that $t - t' > 0$ is always fulfilled. This renders the Heaviside function $\Theta(t - t') = 1$, effectively extending the upper boundary of the t' integration to $+\infty$. While this is clearly justified for temporally *localized* pump field inhomogeneities, we argue that we may also extend the boundary for inhomogeneities which are *infinitely extended* in time. For the latter case, the situation is similar to stationary scattering problems in ordinary quantum mechanics. We have assumed a continuous inflow of plane-wave probe photons, and therefore expect the induced photon field to be time-independent except for a trivial time dependence in the exponential. In particular, other explicit references to time

[7] Here, 0^+ denotes an infinitesimal quantity approaching zero from above.

scales in intermediate steps of the calculation should drop out, with the resulting scattering rates being independent of time. Let us remark that a given incident photon only interacts with the spatially localized inhomogeneity for a finite amount of time, namely as long as it traverses the region where the pump field inhomogeneity is non-vanishing. The induced photon originating from this particular interaction is part of the continuous stream of induced photons making up the steady state. Its individual detection, however, takes place long after the actual interaction has occurred, and can therefore be assumed to happen at asymptotic times.

By extending the upper boundary of the t' integration to $+\infty$, the position space integrals in Eq. (3.20) can be computed straight away by recognizing that they are simply the Fourier transform of the photon polarization tensor from position to momentum space. Hence, we finally obtain

$$a_p^{\mathrm{ind}}(x) = a(\omega_{\mathrm{in}}) \int \frac{\mathrm{d}^3 k}{(2\pi)^3}\, \mathrm{e}^{ik_+ x}\, \frac{\tilde{\Pi}_p(k_+, -k_{\mathrm{in}}|A)}{2i\sqrt{\mathbf{k}^2}}\,. \tag{3.21}$$

The induced photon field can therefore be written in terms of a Fourier integral of the photon polarization tensor evaluated on the light cone, as both the momenta of the incoming and the outgoing photons fulfill $k_+^2 = k_{\mathrm{in}}^2 = 0$. In this case, as will be seen below, the expansion coefficients (3.8) take on very simple expressions. In fact, zero-field contributions ($\ell = 0$) to the polarization tensor vanish completely on the light cone; cf. Eq. (B.16). Correspondingly, the polarization tensor, after contraction with the global projector $\tilde{P}_p^{\mu\nu}$, and when adapted to the particular kinematics of Eq. (3.21), reads

$$\tilde{\Pi}_p(k_+, -k_{\mathrm{in}}|A) = \sum_{\ell=1}^{\infty} \pi_{p,(2\ell)}(-k_+, k_{\mathrm{in}}) \int_{x'} \mathrm{e}^{i(k_{\mathrm{in}} - k_+)x'}\, [e\mathcal{E}(x')]^{2\ell}\,. \tag{3.22}$$

Lower-dimensional pump field inhomogeneities, i.e. fields which only vary along a subset of spacetime coordinates, will yield one or several delta functions in Eq. (3.22). These delta functions enforce conservation of those four-momentum components of the probe photons which point along the direction of constant pump field, and they can be used to reduce the dimension of the momentum integral in Eq. (3.21).

As an example, let us take a pump field profile $\mathcal{E}(x) = \mathcal{E}(\mathrm{x})$ which depends only on the x coordinate. Integrations along directions orthogonal to $\hat{\mathbf{e}}_{\mathrm{x}}$ in Eq. (3.22) yield delta functions $\delta(k_{\mathrm{y}} - \omega_{\mathrm{in}} \sin\beta)\, \delta(k_{\mathrm{z}})\, \delta(\sqrt{\mathbf{k}^2} - \omega_{\mathrm{in}})$. The delta function implementing energy conservation can be rewritten as $\delta(\sqrt{\mathbf{k}^2} - \omega_{\mathrm{in}}) \to \frac{1}{|\cos\beta|} \sum_{l=\pm 1} \delta(k_{\mathrm{x}} - l\omega_{\mathrm{in}} \cos\beta)$, when taking the delta functions for the y and z components into account. Thus, the inhomogeneity induces signal photons in both forward direction, $k_{\mathrm{x}} > 0$, and backward

direction, $k_\mathrm{x} < 0$, corresponding to the two values of $l = \pm 1$. The induced photon field $a_p^{\mathrm{ind}}(x)$ therefore decomposes into these two distinct contributions, and for an incoming photon field $a_p^{\mathrm{in}}(x) = a(\omega_\mathrm{in})\mathrm{e}^{i\omega_\mathrm{in}(\cos\beta\,\mathrm{x}+\sin\beta\,\mathrm{y})}$ we obtain

$$a_p^{\mathrm{ind}}(x) = a_p^{\mathrm{in}}(x)\Bigg\{\frac{\tilde{\Pi}_p^{\mathrm{1dim}}(\omega_\mathrm{in}\cos\beta, -\omega_\mathrm{in}\cos\beta|A)}{2i\omega_\mathrm{in}|\cos\beta|} + \mathrm{e}^{-i2\omega_\mathrm{in}\mathrm{x}\cos\beta}\,\frac{\tilde{\Pi}_p^{\mathrm{1dim}}(-\omega_\mathrm{in}\cos\beta, -\omega_\mathrm{in}\cos\beta|A)}{2i\omega_\mathrm{in}|\cos\beta|}\Bigg\}. \quad (3.23)$$

Here, we have defined the lower-dimensional version of the contracted photon polarization tensor (3.22),

$$\tilde{\Pi}_p^{\mathrm{1dim}}(k_\mathrm{x}, -\omega_\mathrm{in}\cos\beta|A) = \sum_{\ell=1}^{\infty}\pi_{p,(2\ell)}(-k_+, k_\mathrm{in})\big|_{(k_\mathrm{y}=\omega_\mathrm{in}\sin\beta, k_\mathrm{z}=0)}\int \mathrm{dx}'\,\mathrm{e}^{i(\omega_\mathrm{in}\cos\beta - k_\mathrm{x})\mathrm{x}'}\,[e\mathcal{E}(\mathrm{x}')]^{2\ell}\,, \quad (3.24)$$

which accounts only for the remaining one-dimensional inhomogeneity. The arguments of $\tilde{\Pi}_p^{\mathrm{1dim}}(k_\mathrm{x}, -\omega_\mathrm{in}\cos\beta|A)$ refer to those momentum components of the probe photons which are not conserved in the scattering process.

The first term in the curly brackets of Eq. (3.23) denotes induced photons which are transmitted in forward direction. They have the same four-momentum k_in^μ as the incoming photons. The second term in the curly brackets describes induced photons whose k_x momentum is reversed: The electromagnetic field inhomogeneity transferred a momentum $-2\omega_\mathrm{in}|\cos\beta|$ onto the incident probe photons. These photons have therefore undergone *reflection* at the inhomogeneous electric field, and their resulting propagation direction differs from the incoming probe photon beam (cf. Fig. 3.2 in the upcoming Sect. 3.2.2). We can define the associated reflection coefficient R_p as the modulus squared of the ratio of reflected photons and incoming photons,

$$R_p = \left|\frac{\tilde{\Pi}_p^{\mathrm{1dim}}(-\omega_\mathrm{in}\cos\beta, -\omega_\mathrm{in}\cos\beta|A)}{2\omega_\mathrm{in}\cos\beta}\right|^2. \quad (3.25)$$

The reflection coefficient (3.25) can be employed for arbitrary one-dimensional pump field configurations compatible with the existence of a global projector. Furthermore, it is not limited to weak pump fields, $\mathcal{E}/\mathcal{E}_\mathrm{cr} \ll 1$, if the corresponding expression Π_p^{1dim} for arbitrary field strengths is known, cf. the upcoming Sect. 3.2.5.

3.2.2. Purely magnetic pump fields

First, we will discuss quantum reflection for configurations featuring a purely magnetic pump field $\mathbf{B}(x)$ with amplitude $|\mathbf{B}(x)| = \mathcal{B}(x)$, whose orientation $\hat{\mathbf{e}}_B := \mathbf{B}(x)/\mathcal{B}(x)$ is fixed in space and time. In this case, $\hat{\mathbf{e}}_B$ provides a global spatial reference direction, and we can decompose vectors and tensors with regard to this global reference direction into parallel and perpendicular components, i.e.

$$k^\mu = k^\mu_\parallel + k^\mu_\perp\,, \quad k^\mu_\parallel = (\omega, \mathbf{k}_\parallel)\,, \quad k^\mu_\perp = (0, \mathbf{k}_\perp)\,, \tag{3.26}$$

with $\mathbf{k}_\parallel = (\mathbf{k}\cdot\hat{\mathbf{e}}_B)\hat{\mathbf{e}}_B$ and $\mathbf{k}_\perp = \mathbf{k} - \mathbf{k}_\parallel$. The polarization tensor for a constant, purely magnetic pump field reads

$$\Pi^{\mu\nu}(k|\mathbf{B}) = P_0^{\mu\nu}\Pi_0(k|\mathbf{B}) + P_\parallel^{\mu\nu}\Pi_\parallel(k|\mathbf{B}) + P_\perp^{\mu\nu}\Pi_\perp(k|\mathbf{B})\,, \tag{3.27}$$

and its coefficients $\Pi_p(k|\mathbf{B})$ are collected in the appendix B.2. Note that the off-diagonal term "$Q^{\mu\nu}$" featured in Eq. (3.10) vanishes, and the polarization tensor (3.27) is solely spanned by projectors $P_p^{\mu\nu}(k)$, including

$$P_\parallel^{\mu\nu}(k) = g_\parallel^{\mu\nu} - \frac{k_\parallel^\mu k_\parallel^\nu}{k_\parallel^2}\,, \quad P_\perp^{\mu\nu}(k) = g_\perp^{\mu\nu} - \frac{k_\perp^\mu k_\perp^\nu}{k_\perp^2}\,. \tag{3.28}$$

The parallel photon polarization mode $p = \parallel$, associated with $P_\parallel^{\mu\nu}$, denotes polarization in the plane spanned by the photon momentum $\mathbf{k}$ and the magnetic field $\mathbf{B}$. Likewise, the perpendicular polarization mode $p = \perp$, associated with $P_\perp^{\mu\nu}$, corresponds to polarization perpendicular to this plane. A third projector $P_0^{\mu\nu}(k) = g^{\mu\nu} - \frac{k^\mu k^\nu}{k^2} - P_\parallel^{\mu\nu}(k) - P_\perp^{\mu\nu}(k)$ spans the remaining transverse subspace.

Equation (3.21) requires the evaluation of the polarization tensor on the light cone. As has been remarked earlier the lowest-order expansion coefficient $\Pi^{\mu\nu}_{(0)}(k^2 = 0|\mathbf{B})$ then vanishes and an expansion in the magnetic field strength starts with terms $\mathcal{O}\big[(e\mathcal{B})^2\big]$. In the analysis to follow, we will limit ourselves to the perturbative regime of small field strengths $\frac{\mathcal{B}}{\mathcal{B}_{\rm cr}} \ll 1$. Therefore, we retain only the lowest-order nonvanishing expansion coefficient of the photon polarization tensor, $\Pi^{\mu\nu}_{(2)}$, which is given by Eq. (B.18). On the light cone the remaining parameter integral in Eq. (B.18) can be performed analytically, yielding

$$\Pi^{\mu\nu}_{(2)}(k) = \frac{1}{45}\frac{\alpha}{\pi}\Big(7\,k_\parallel^2\,P_\parallel^{\mu\nu}(k) - 4\,k_\perp^2\,P_\perp^{\mu\nu}(k)\Big)\frac{1}{m^4}\,, \tag{3.29}$$

where we have made use of the relation $k_\parallel^2 = -k_\perp^2$. The particular expansion em-

ployed here is furthermore limited to moderate photon energies fulfilling $\frac{\mathcal{B}}{\mathcal{B}_{\rm cr}}\frac{k_\perp^2}{m^2} \ll 1$, as detailed in Ref. [100]. As a consequence, the expansion coefficient (3.29) is entirely real.

Note that there exists no contribution for the longitudinal polarization mode $p = 0$, associated with the projector $P_0^{\mu\nu}(k)$, as the coefficient belonging to this mode vanishes for on-the-light-cone dynamics. This is compatible with the fact that this particular mode vanishes in the limit of vanishing magnetic field, since only the modes $p = \parallel, \perp$ can be continuously related to the two transversal free-field propagation modes of a photon [28].[8] Correspondingly, the tensorial quantity $\pi_{(2)}^{\mu\nu}(k,k')$ as defined by Eq. (3.8) reads

$$\pi_{(2)}^{\mu\nu}(k,k') = \frac{1}{90}\frac{\alpha}{\pi}\left[7\Big(k_\parallel^2\, P_\parallel^{\mu\nu}(k) + k_\parallel'^2\, P_\parallel^{\mu\nu}(k')\Big) - 4\Big(k_\perp^2\, P_\perp^{\mu\nu}(k) + k_\perp'^2\, P_\perp^{\mu\nu}(k')\Big)\right]\frac{1}{m^4}\,. \tag{3.30}$$

In order to proceed we have to identify inhomogeneous pump field configurations which are compatible with the existence of a globally invariant projector $\tilde{P}_p^{\mu\nu}$. Note that this projector has to remain invariant both on and off the light cone, even though the polarization tensor in Eq. (3.21) has to be finally evaluated only on the light cone: The equations of motion (3.3) encompass an integration over arbitrary four-momenta, which formally requires the evaluation of the projectors off the light cone.

The structure of the projectors (3.28) determines the restrictions on the type of inhomogeneities which allow for the existence of a global projector: For the parallel projector to be globally invariant, i.e. $P_\parallel^{\mu\nu}(k) = P_\parallel^{\mu\nu}(k') \equiv \tilde{P}_\parallel^{\mu\nu}$, the inhomogeneity has to leave unaffected the four-momentum components associated with $k_\parallel^\mu$, namely the energy ω and the momentum $\mathbf{k}_\parallel$. Analogously, for the perpendicular projector to be globally invariant, i.e. $P_\perp^{\mu\nu}(k) = P_\perp^{\mu\nu}(k') \equiv \tilde{P}_\perp^{\mu\nu}$, the inhomogeneity may not alter the momentum $\mathbf{k}_\perp$.

An inhomogeneous pump field profile $\mathcal{B}(x)$ can only affect those four-momentum components of the probe photons which correspond to the spacetime directions along which the pump field profile varies. As an example take a temporally changing field profile $\mathcal{B}(\mathrm{x}, t)$, varying along the direction $\hat{\mathbf{e}}_\mathrm{x}$. This particular profile can only affect the energy ω as well as the momentum k_x of the probe photons, but leaves the momenta k_y and k_z unaltered. For a magnetic field pointing along $\hat{\mathbf{e}}_\mathrm{x}$ the unaltered momentum components make up the perpendicular momentum $\mathbf{k}_\perp = k_\mathrm{y}\hat{\mathbf{e}}_\mathrm{y} + k_\mathrm{z}\hat{\mathbf{e}}_\mathrm{z} = \mathbf{k}'_\perp$, and hence the perpendicular projector $\tilde{P}_\perp^{\mu\nu}$ constitutes a global projector. More generally, for the

[8] Note that this is strictly true only for $\mathbf{k} \nparallel \mathbf{B}$. For the special setting $\mathbf{k} \parallel \mathbf{B}$ the two modes 0 and $\perp$ prevail in the limit $\mathcal{B} \to 0$ [101].

purely magnetic field case our formalism allows us to study (i) inhomogeneities which vary in time and along, at most, one spatial direction, or (ii) static inhomogeneities which vary along two spatial directions. For the latter scenario, the projector $\tilde{P}_{\parallel}^{\mu\nu}$ may constitute a global projector, if the orientation of the magnetic field is perpendicular to the directions of the variation of the inhomogeneity. For an inhomogeneity which w.l.o.g. depends on the coordinates x and y, i.e. $\mathcal{B}(\mathrm{x},\mathrm{y})$, this implies $\hat{\mathbf{e}}_B = \hat{\mathbf{e}}_\mathrm{z}$.

We see that the existence of a global projector requires special alignments of the direction of the inhomogeneity $\nabla\mathcal{B}(x)$ with respect to the orientation of the magnetic field $\hat{\mathbf{e}}_B$, permitting only these two scenarios which have been discussed in the last paragraph and are gathered here:

$$\begin{aligned}
(i): \quad & k_{\parallel}^{\mu}\partial_\mu\mathcal{E}(x) = 0 \quad \rightarrow \quad P_{\parallel}^{\mu\nu}(k) = P_{\parallel}^{\mu\nu}(k') \equiv \tilde{P}_{\parallel}^{\mu\nu} \quad \text{and} \quad k_{\parallel}^2 = k_{\parallel}'^2\,, \\
(ii): \quad & k_{\perp}^{\mu}\partial_\mu\mathcal{E}(x) = 0 \quad \rightarrow \quad P_{\perp}^{\mu\nu}(k) = P_{\perp}^{\mu\nu}(k') \equiv \tilde{P}_{\perp}^{\mu\nu} \quad \text{and} \quad k_{\perp}^2 = k_{\perp}'^2\,.
\end{aligned} \tag{3.31}$$

The lowest-order coefficients $\pi_{p,(2)}$ of the contracted polarization tensor (3.22) corresponding to the two alignments (i) and (ii) read

$$(i): \quad \pi_{\parallel,(2)} = \frac{7}{45}\frac{\alpha}{\pi}\,k_{\parallel}^2\,\frac{1}{m^4}\,, \quad \text{and} \quad (ii): \quad \pi_{\perp,(2)} = -\frac{4}{45}\frac{\alpha}{\pi}\,k_{\perp}^2\,\frac{1}{m^4}\,, \tag{3.32}$$

where we have made use of the fact that $k_{\parallel}^2 = k_{\parallel}'^2$ and $k_{\perp}^2 = k_{\perp}'^2$ for the respective cases. Only case (ii), as there the conserved momentum $\mathbf{k}_\perp$ is independent of the energy ω, is compatible with the assumption of a temporally varying inhomogeneity. As a drawback such an inhomogeneity may only vary in at most one additional spatial direction. The existence of a global projector then additionally requires $\nabla\mathcal{B}(x) \sim \hat{\mathbf{e}}_B$, i.e. only a *single* alignment of the direction of the inhomogeneity and orientation of the magnetic field is permitted for a 1+1 dimensional inhomogeneity. Case (i), on the other hand, only permits static inhomogeneities which may vary along at most two spatial directions. Here, the existence of a global projector requires the special alignment $\nabla\mathcal{B}(x) \perp \hat{\mathbf{e}}_B$. Purely magnetic fields therefore allow for the investigation of only a few special configurations, which will be looked at in the following sections.

Static one-dimensional inhomogeneity

We start with the investigation of a static pump field inhomogeneity which varies only along $\hat{\mathbf{e}}_\mathrm{x}$, and is infinitely extended along the other directions, cf. Fig. 3.2. We consider a probe photon beam propagating in the x-y plane, hitting the inhomogeneity under an angle β with respect to the x axis.

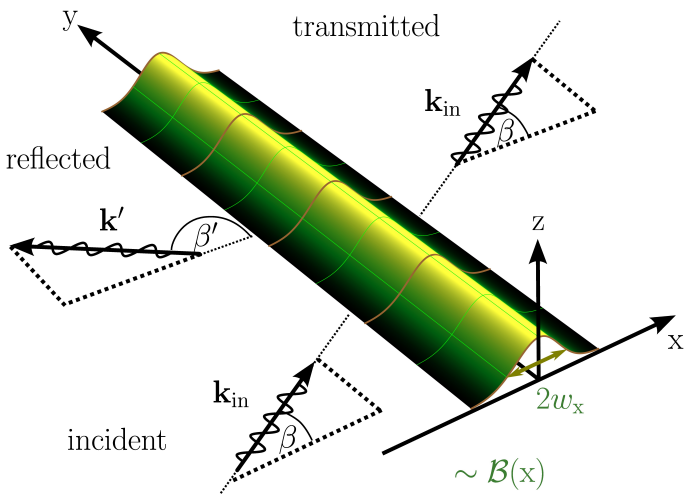

Figure 3.2.: Schematic depiction of quantum reflection for a static one-dimensional field inhomogeneity, from Ref. [44]. The incident probe photons with four wave vector $k^\mu_{\rm in} = \omega_{\rm in}(1, \cos\beta, \sin\beta, 0)$ propagate towards the inhomogeneity of amplitude profile $\mathcal{B}(\mathrm{x})$ which asymptotically falls off to zero for large values of $|\mathrm{x}|$. The inhomogeneity is infinitely extended in the transversal directions.

A low-dimensional inhomogeneity $\mathcal{B}(\mathrm{x})$ allows the identification of global projectors for both cases (i) or (ii) given in Eqs. (3.31). This is the case if the direction $\hat{\mathbf{e}}_B$ of the magnetic field strength vector and the probe photon momentum $\mathbf{k}$ fulfill the relations

$$\begin{aligned} (i): \quad & \hat{\mathbf{e}}_{\rm x}\cdot\mathbf{k}_\parallel = (\hat{\mathbf{e}}_B\cdot\hat{\mathbf{e}}_{\rm x})(\mathbf{k}\cdot\hat{\mathbf{e}}_B) && = 0\,, \qquad \text{and} \\ (ii): \quad & \hat{\mathbf{e}}_{\rm x}\cdot\mathbf{k}_\perp = \hat{\mathbf{e}}_{\rm x}\cdot\mathbf{k} - (\hat{\mathbf{e}}_B\cdot\hat{\mathbf{e}}_{\rm x})(\mathbf{k}\cdot\hat{\mathbf{e}}_B) && = 0\,. \end{aligned} \tag{3.33}$$

The induced photon field for these two scenarios is then given by (cf. Eq. (3.23))

$$\begin{aligned} a_p^{\rm ind}(x) = i a_p^{\rm in}(x)\,\frac{\alpha}{\pi}\,\frac{c_p}{90}\,\frac{\sin^2\sphericalangle(\mathbf{k}_{\rm in},\mathbf{B})}{|\cos\beta|}\,\omega_{\rm in}\left\{\int \mathrm{dx}'\left(\frac{e\mathcal{B}(\mathrm{x}')}{m^2}\right)^2\right. \\ \left. + \mathrm{e}^{-i(2\omega_{\rm in}\cos\beta)\mathrm{x}}\int \mathrm{dx}'\,\mathrm{e}^{i(2\omega_{\rm in}\cos\beta)\mathrm{x}'}\left(\frac{e\mathcal{B}(\mathrm{x}')}{m^2}\right)^2\right\} + \mathcal{O}\left(\left(\tfrac{e\mathcal{B}}{m^2}\right)^4\right)\,, \end{aligned} \tag{3.34}$$

where we have defined the numerical coefficients $c_\parallel = 7$, $c_\perp = 4$. Likewise, the reflection coefficient reads

$$R_p = \left|\frac{\alpha}{\pi}\,\frac{c_p}{90}\,\frac{\sin^2\sphericalangle(\mathbf{k}_{\rm in},\mathbf{B})}{\cos\beta}\,\omega_{\rm in}\int \mathrm{dx}'\,\mathrm{e}^{i(2\omega_{\rm in}\cos\beta')\mathrm{x}'}\left(\frac{e\mathcal{B}(\mathrm{x}')}{m^2}\right)^2\right|^2 + \mathcal{O}\left(\left(\tfrac{e\mathcal{B}}{m^2}\right)^6\right)\,. \tag{3.35}$$

As can be seen in Eq. (3.34), the reflected contributions (second line) to the induced

photon field are generically suppressed compared to the forward induced contributions (first line): The Fourier transformation of a generic localized field profile $\mathcal{B}(\mathrm{x}')^2$ will yield exponential terms, whose arguments are some function of the Fourier parameter. This usually leads to an exponential suppression in the transferred momentum $2\omega_{\mathrm{in}}|\cos\beta|$ from the inhomogeneity onto the reflected probe photons, cf. also Eq. (3.1).

Similar to strategies employed in atomic quantum reflection, we can increase the magnitude of the reflected photons by increasing the incoming angle β. In the limit of grazing incidence, i.e. for $\beta \to \pm\frac{\pi}{2}$, the reflection coefficient diverges. This unphysical behavior can be attributed to an infinitely long interaction of the probe photons with the inhomogeneity. Obviously, in this case the Born approximation employed in the derivation of Eq. (3.35) breaks down. We will take a look at the validity range of the Born approximation later when dealing with the strong-field limit in Sect. 3.2.5.

1+1 dimensional spatio-temporal inhomogeneity

In this section we go a step further and consider inhomogeneities varying in time and along the x direction, i.e. $\mathcal{B}(\mathrm{x},t)$. As has been mentioned earlier, only for the perpendicular polarization mode $p = \perp$ there exists a global projector $\tilde{P}_\perp^{\mu\nu}$. This is the case if and only if $\mathbf{B}(\mathrm{x},t) \sim \hat{\mathbf{e}}_\mathrm{x}$, immediately implying $\sin^2 \sphericalangle(\mathbf{k}_{\mathrm{in}}, \mathbf{B}) \to \sin^2\beta$. For such a pump field, Eqs. (3.21) and (3.22) result in

$$a_\perp^{\mathrm{ind}}(x) = ia(\omega_{\mathrm{in}})\mathrm{e}^{i\omega_{\mathrm{in}}\sin\beta\,\mathrm{y}}\frac{2}{45}\frac{\alpha}{\pi}\omega_{\mathrm{in}}^2\sin^2\beta\int\frac{\mathrm{d}k_\mathrm{x}}{2\pi}\frac{1}{\omega(k_\mathrm{x})}\mathrm{e}^{i(k_\mathrm{x}\mathrm{x}-\omega(k_\mathrm{x})t)} \times\int\mathrm{dx}'\int\mathrm{d}t'\,\mathrm{e}^{i[(\omega_{\mathrm{in}}\cos\beta-k_\mathrm{x})\mathrm{x}'-(\omega_{\mathrm{in}}-\omega(k_\mathrm{x}))t']}\left(\frac{e\mathcal{B}(\mathrm{x}',t')}{m^2}\right)^2+\mathcal{O}\left(\left(\tfrac{e\mathcal{B}}{m^2}\right)^4\right), \quad (3.36)$$

with $\omega(k_\mathrm{x}) = \sqrt{k_\mathrm{x}^2+\omega_{\mathrm{in}}^2\sin^2\beta}$. We can employ Eq. (3.36) to calculate the induced photon field for inhomogeneities with arbitrary field profiles $\mathbf{B}(\mathrm{x},t) \sim \hat{\mathbf{e}}_\mathrm{x}$. For simplicity, however, we will limit ourselves to inhomogeneities of the type $\mathcal{B}(\mathrm{x},t) = \mathcal{B}(\mathrm{x})\cos(\Omega t)$, with frequency $\Omega > 0$. The scenario resembles the one depicted in Fig. 3.2, with the inhomogeneity additionally featuring a harmonic time dependence $\sim\cos(\Omega t)$. Performing the Fourier integral over time results in

$$\int\mathrm{d}t'\,\mathrm{e}^{-i(\omega_{\mathrm{in}}-\omega(k_\mathrm{x}))t'}\cos^2(\Omega t') = \frac{\pi}{2}\sum_{n=-1}^{+1}(1+\delta_{n0})\,\Theta\big(\omega_{\mathrm{in}}(1-|\sin\beta|)-2n\Omega\big) \times\frac{\omega(k_\mathrm{x})}{|k_{\mathrm{x},2n}|}\Big[\delta\big(k_\mathrm{x}-|k_{\mathrm{x},2n}|\big)+\delta\big(k_\mathrm{x}+|k_{\mathrm{x},2n}|\big)\Big], \quad (3.37)$$

where $\delta_{nn'}$ denotes the Kronecker delta. As in the previous section, we have rewritten the delta function for the energy in terms of delta functions for the x momentum of the probe photons k_x. Furthermore, we have defined $k_{\mathrm{x},2n}^2 \equiv (\omega_\mathrm{in} - 2n\Omega)^2 - \omega_\mathrm{in}^2 \sin^2\beta$. Upon insertion of Eq. (3.37) into Eq. (3.36), we obtain

$$\begin{aligned} a_\perp^\mathrm{ind}(x) = ia(\omega_\mathrm{in}) \mathrm{e}^{i\omega_\mathrm{in} \mathrm{y} \sin\beta} \frac{1}{90}\frac{\alpha}{\pi}\omega_\mathrm{in}^2 \sin^2\beta \sum_{n=-1}^{+1} (1+\delta_{n0})\, \Theta\big(\omega_\mathrm{in}(1-|\sin\beta|) - 2n\Omega\big) \\ \times \frac{1}{|k_{\mathrm{x},2n}|}\, \mathrm{e}^{i|k_{\mathrm{x},2n}|\mathrm{x} - i(\omega_\mathrm{in}-2n\Omega)t} \Bigg\{ \int \mathrm{dx}'\, \mathrm{e}^{i(\omega_\mathrm{in}\cos\beta - |k_{\mathrm{x},2n}|)\mathrm{x}'} \left(\frac{e\mathcal{B}(\mathrm{x}')}{m^2}\right)^2 \\ + \mathrm{e}^{-2i|k_{\mathrm{x},2n}|\mathrm{x}} \int \mathrm{dx}'\, \mathrm{e}^{i(\omega_\mathrm{in}\cos\beta + |k_{\mathrm{x},2n}|)\mathrm{x}'} \left(\frac{e\mathcal{B}(\mathrm{x}')}{m^2}\right)^2 \Bigg\} + \mathcal{O}\left(\left(\tfrac{e\mathcal{B}}{m^2}\right)^4\right), \end{aligned} \tag{3.38}$$

which is still applicable for arbitrarily shaped pump field profiles $\mathcal{B}(\mathrm{x})$ compatible with the locally-constant field approximation.

As has been the case for a static one-dimensional inhomogeneity discussed in the last section, the induced photon field features contributions scattered in forward and in backward direction. The situation is illustrated in Fig. 3.3. Backward scattered (or reflected) contributions to the induced photon field are those which fulfill $\mathrm{sign}(k'_\mathrm{x} k_{\mathrm{in},x}) = \mathrm{sign}(k'_\mathrm{x}\cos\beta) < 0$, i.e. the sign of the x momentum component of the incoming photon beam $k_\mathrm{in,x}$ has to differ from the sign of the x momentum component of the induced beam, $k'_\mathrm{x} = \pm|k_{\mathrm{x},2n}|$. For an incoming photon beam with $k_\mathrm{in,x} > 0$, as depicted in Fig. 3.3, reflected contributions are therefore scattered into the left half-space (–). Likewise, forward scattered photons are those with $\mathrm{sign}(k'_\mathrm{x} k_{\mathrm{in},x}) = \mathrm{sign}(k'_\mathrm{x}\cos\beta) > 0$. With regard to the situation in Fig. 3.3, they are scattered into the right half-space (+).

The backward and forward scattered contributions to the induced photon field are each made up of several wave components, cf. Fig. 3.3. This is a consequence of the pump field's temporal harmonic oscillation, as the pump field can now absorb or provide energy to the probe photons. For a harmonic oscillation $\sim \cos(\Omega t)$, the integrand in Equation (3.36) features a term $\cos^2(\Omega t') = \frac{1}{2} + \frac{1}{4}\left(\mathrm{e}^{2i\Omega t'} + \mathrm{e}^{-2i\Omega t'}\right)$. Correspondingly, the induced photon field is a superposition of plane waves with different positive frequencies, $\omega'_\mathrm{in} = \omega_\mathrm{in} - 2n\Omega$, and different propagation directions $\mathbf{k}'_{\pm,2n} = (\pm|k_{\mathrm{x},2n}|, \omega_\mathrm{in}\sin\beta, 0)$, where $n \in \{0, \pm 1\}$. As these waves propagate on the light cone and the momentum component along $\hat{\mathbf{e}}_\mathrm{x}$ is conserved, a change in frequency inevitably alters the x component of their wave vector and thus their propagation direction. The component with $n = 0$ corresponds to an elastic interaction of the probe photons with the pump field: One quantum of energy Ω is each absorbed and

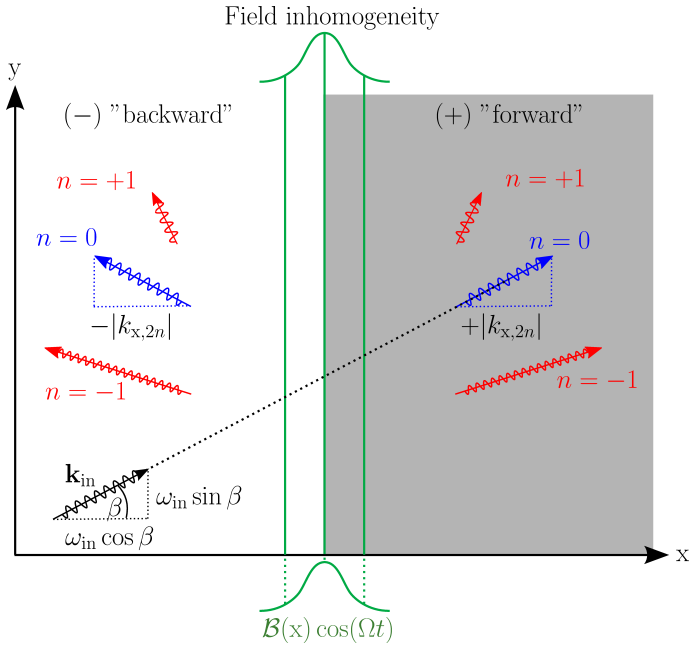

Figure 3.3.: Depiction of quantum reflection for a $1+1$ dimensional field inhomogeneity featuring a harmonic time dependence $\sim \cos(\Omega t)$, taken from Ref. [44]. The basic scenario is the same as depicted in Fig. 3.2 and the inhomogeneity is infinitely extended in the transversal directions. However, due to the harmonic oscillation with Ω, apart from the elastic contributions ($n = 0$), also inelastic contributions ($n = \pm 1$) with frequencies $\omega'_{2n} = \omega_{in} - 2n\Omega$ and propagation directions $\mathbf{k}'_{\pm,2n} = (\pm|k_{x,2n}|, \omega_{in} \sin\beta, 0)$ are induced (cf. main text). We label induced photon waves propagating into the half-space right of the inhomogeneity with $(+)$ and those propagating into the left half-space with $(-)$. For convenience we will also speak of "backward" (white) and "forward" (gray-shaded) directions: If the x momentum component of a given induced contribution has the opposite (same) sign as the x momentum component of the incident probe photon, it is induced in backward (forward) direction.

emitted by the inhomogeneity, yielding no net energy transfer. Correspondingly, the components with $n = +1$ ($n = -1$) have emitted (absorbed) two quanta of energy Ω onto (from) the inhomogeneity. In the limit $\Omega \to 0$, the three components merge and we recover Eq. (3.34) from the last section, with $p = \perp$ and the substitution $\sin^2 \sphericalangle(\mathbf{k}_{in}, \mathbf{B}) \to \sin^2\beta$. The nonlinearity of the quantum vacuum is therefore nicely exemplified by the occurrence of typical optical phenomena as they occur in nonlinear crystals, here sum and difference-frequency generation, see Fig. 3.4.

In close analogy to the last section, for a given induced photon wave of frequency ω'_{2n}, we can define scattering coefficients $R^{(\pm)}_{2n}$ as the modulus squared of the respective

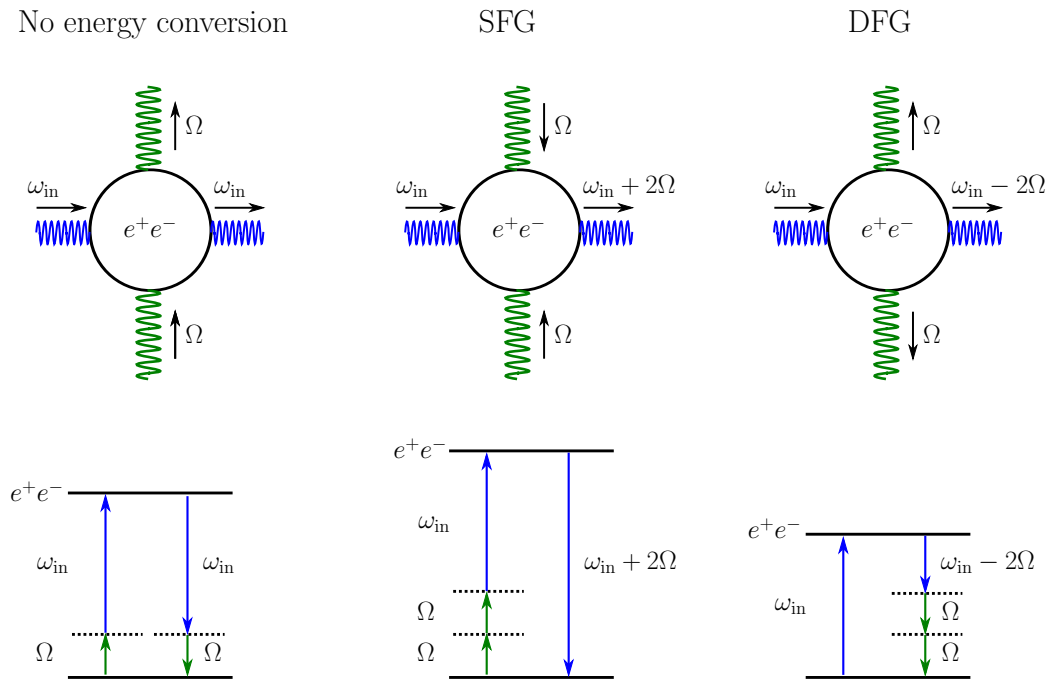

Figure 3.4.: Depiction of the various nonlinear effects occurring in a temporal inhomogeneity with harmonic time dependence $\sim \cos(\Omega t)$, in terms of Feynman-like diagrams and the corresponding term diagrams. The virtual electron-positron loop can be interpreted as an excited state of the nonlinear medium. The excited states are generated by different combinations of the probe and pump photons, which can combine via virtual levels, depicted by the dotted lines. The left-most diagram shows the elastic case, i.e. the probe photon field interacts with the pump field without net energy conversion. The middle diagram depicts sum-frequency generation (SFG), and the right-most diagram illustrates difference-frequency generation (DFG).

induced photon field normalized by $a(\omega_{\text{in}})$. For Eq. (3.38), this results in

$$R^{(\pm)}_{\perp,2n} = \Theta\big(\omega_{\text{in}}(1-|\sin\beta|) - 2n\Omega\big) \times \left| \frac{\alpha}{\pi} \frac{1+\delta_{n0}}{90} \frac{\omega_{\text{in}}^2 \sin^2\beta}{k_{\text{x},2n}} \int \mathrm{dx}'\, \mathrm{e}^{i(\omega_{\text{in}}\cos\beta \mp |k_{\text{x},2n}|)\mathrm{x}'} \left(\frac{e\mathcal{B}(\mathrm{x}')}{m^2}\right)^2 \right|^2 + \mathcal{O}\left(\left(\tfrac{e\mathcal{B}}{m^2}\right)^6\right) . \quad (3.39)$$

The Heaviside function only allows for contributions satisfying $\omega'_{2n} \geq \omega_{\text{in}}|\sin\beta|$, which is trivially fulfilled for the components with $n \in \{-1, 0\}$. However, for $n = +1$ this condition becomes nontrivial: It encodes the fact that incident photons with energy ω_{in} can induce photons with $n = 1$ only if the photon energy after the emission of two quanta of energy is still large enough to support induced outgoing photons propagating

on the light cone while simultaneously ensuring momentum conservation along k_y.

Let us shortly discuss pump fields featuring more complicated temporal profiles than the harmonic time dependence considered here. For the scenario discussed so far the frequencies ω' of the signal photons, and hence their propagation directions, are sharply localized peaks resembling delta function peaks at $\cos\beta' = \pm|k_{\mathrm{x},2n}|/\omega'_{2n}$. However, adding a finite envelope function, for example a Gaussian function $\sim \exp(-t^2/\tau^2)$, will cause these frequencies, and hence the propagation directions, to "smear out" as the temporal scale τ of the inhomogeneity is decreased. Therefore, photons will be scattered not just along these sharply localized directions, but every direction β' will feature a nonvanishing amount of induced photons. For an inhomogeneity infinitely extended along the y direction, this poses a problem: When trying to estimate the fraction of photons hitting a detector in the y-z plane, the result (3.36) will necessarily diverge due to the contribution of signal photons with directions close to $\beta' = \pm\pi/2$. In this limit the perturbative treatment breaks down, as the photons propagate in the region of nonvanishing magnetic pump field for an infinite amount of time. Consequentially, the unphysical assumption of an infinitely extended inhomogeneity in the y direction prevents a naive quantitative investigation of more general time dependencies, and requires additional measures such as, e.g., the introduction of a cut-off parameter $\beta'_c < |\pi/2|$ to the integration bounds in Eq. (3.36) after casting the k_x-integral into an integral over the angle β'.

Static two-dimensional inhomogeneity

Case (i) also allows for the treatment of a localized static two-dimensional amplitude profile $\mathcal{B}(\mathrm{x},\mathrm{y})$, which is depicted in Fig. 3.5. As has been discussed at the beginning of Sect. 3.2.2, only the setting $\mathbf{B} \sim \hat{\mathbf{e}}_\mathrm{z}$ permits the global projector $\tilde{P}_\parallel^{\mu\nu}$. We now insert the profile $\mathcal{B}(\mathrm{x},\mathrm{y})$ into Eqs. (3.21) and (3.22), and perform the k_x and k_y integrations. This yields the following compact expression for the induced photon field

$$a_\parallel^\mathrm{ind}(x) = ia(\omega_\mathrm{in})\,\mathrm{e}^{-i\omega_\mathrm{in}t}\frac{7}{90}\frac{\alpha}{\pi}\omega_\mathrm{in}^2 \times \int \mathrm{d}^2\mathbf{x}'\,\mathrm{e}^{i\omega_\mathrm{in}[\cos\beta\,\mathrm{x}'+\sin\beta\,\mathrm{y}']}\,J_0(\omega_\mathrm{in}|\mathbf{x}-\mathbf{x}'|)\left(\frac{e\mathcal{B}(\mathrm{x}',\mathrm{y}')}{m^2}\right)^2 + \mathcal{O}\left(\left(\tfrac{e\mathcal{B}}{m^2}\right)^4\right), \quad (3.40)$$

with $\mathbf{x} = (\mathrm{x},\mathrm{y},0)$, $\mathbf{x}' = (\mathrm{x}',\mathrm{y}',0)$ and $\int \mathrm{d}^2\mathbf{x}' = \int \mathrm{d}\mathrm{x}'\mathrm{d}\mathrm{y}'$. Furthermore, we have introduced the Bessel function $J_n(\chi)$ of the first kind of order $n \in \mathbb{N}_0$.

For a localized inhomogeneity as depicted in Fig. 3.5, the integral in Eq. (3.40) receives contributions only from a limited range of $\mathbf{x}'$, namely those regions where

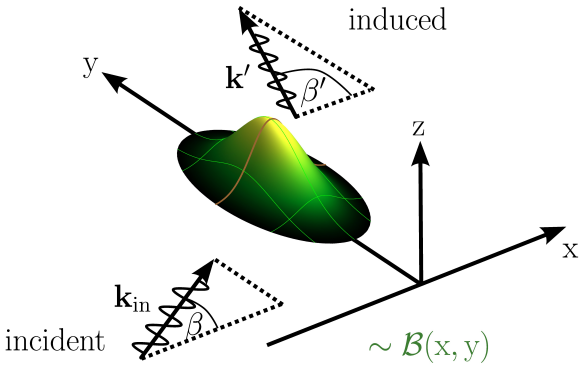

Figure 3.5.: Quantum reflection at a localized static two-dimensional pump field inhomogeneity (image taken from Ref. [44]). Upon interaction with the inhomogeneity, the incident probe photons with wave vector $\mathbf{k}_{\mathrm{in}} = \omega_{\mathrm{in}}(\cos\beta, \sin\beta, 0)$ induce outgoing circular photon waves with wave vector $\mathbf{k}' = \omega_{\mathrm{in}}(\cos\beta', \sin\beta', 0)$. As the pump field inhomogeneity is independent of time, the energy of the photons is conserved, i.e. $|\mathbf{k}_{\mathrm{in}}| = |\mathbf{k}'|$.

the inhomogeneity is nonvanishing. The detection of the induced photon signal takes place in the far field, i.e., far outside the region where the integral over $\mathbf{x}'$ receives any substantial contributions. We can therefore define the momentum of the induced photon, $\mathbf{k}' = \omega_{\mathrm{in}}\frac{\mathbf{x}}{|\mathbf{x}|} = \omega_{\mathrm{in}}(\cos\beta', \sin\beta', 0)$, and expand the argument of the Bessel function as follows,

$$\omega_{\mathrm{in}}|\mathbf{x} - \mathbf{x}'| = \omega_{\mathrm{in}}|\mathbf{x}| - \mathbf{k}' \cdot \mathbf{x}' + \mathcal{O}(\varepsilon^2)\,, \tag{3.41}$$

with $\varepsilon \equiv |\mathbf{x}'|/|\mathbf{x}| \ll 1$. The Bessel function for large real arguments behaves like (cf. formula 8.451.1 of Ref. [102])

$$J_n(\chi) = \frac{1}{i^{n+1}}\sqrt{\frac{i}{2\pi\chi}}\,\mathrm{e}^{i\chi}\left[1 + i\,(-1)^n\,\mathrm{e}^{-2i\chi}\right] + \mathcal{O}\big(\chi^{-3/2}\big)\,. \tag{3.42}$$

We employ this asymptotic expansion in Eq. (3.40) the following way: In the exponentials the argument (3.41) is accounted for up to and including $\mathcal{O}(\varepsilon)$, while the argument in the prefactor only includes the lowest-order term $\omega_{\mathrm{in}}|\mathbf{x}|$. Focussing on the contribution describing an outgoing circular wave only, we obtain for the induced photon field

$$a_{\parallel}^{\mathrm{ind}}(x) \approx a(\omega_{\mathrm{in}})\,\frac{\mathrm{e}^{i\omega_{\mathrm{in}}(|\mathbf{x}|-t)}}{\sqrt{|\mathbf{x}|}}\,f_{\parallel}(\mathbf{k}', \mathbf{k}_{\mathrm{in}})\,, \tag{3.43}$$

with the scattering amplitude

$$f_{\parallel}(\mathbf{k}', \mathbf{k}_{\mathrm{in}}) = \sqrt{\frac{i}{2\pi\omega_{\mathrm{in}}}}\,\frac{7}{90}\,\frac{\alpha}{\pi}\,\omega_{\mathrm{in}}^2 \int \mathrm{d}^2\mathbf{x}'\;\mathrm{e}^{i(\mathbf{k}_{\mathrm{in}}-\mathbf{k}')\cdot\mathbf{x}'}\left(\frac{e\mathcal{B}(\mathrm{x}', \mathrm{y}')}{m^2}\right)^2 + \mathcal{O}\left(\left(\tfrac{e\mathcal{B}}{m^2}\right)^4\right)\,. \tag{3.44}$$

We find that for large far-field distances $|\mathbf{x}|$ about the scattering center, the modulus squared of the induced photon field amplitude through a polar angle interval $\mathrm{d}\beta'$ is independent of $|\mathbf{x}|$, i.e., $|a^{\mathrm{ind}}(x)|^2|\mathbf{x}|\mathrm{d}\beta' = |a^{\mathrm{in}}(x)|^2|f(\mathbf{k}', \mathbf{k}_{\mathrm{in}})|^2\mathrm{d}\beta'$. Hence, in analogy to the last two sections we can define a differential scattering cross section for induced outgoing photons propagating along the direction $\mathbf{k}'$,

$$\frac{\mathrm{d}\sigma}{\mathrm{d}\beta'}(\mathbf{k}', \mathbf{k}_{\mathrm{in}}) \equiv \frac{|a^{\mathrm{ind}}(x)|^2|\mathbf{x}|}{|a^{\mathrm{in}}(x)|^2} = |f(\mathbf{k}', \mathbf{k}_{\mathrm{in}})|^2 \,. \tag{3.45}$$

The cross section for photons hitting a detector located at β' and spanning an opening angle $\delta\beta'(\beta')$ about a given value of β' is obtained straightforwardly by integration, $\sigma[\beta, \delta\beta'(\beta')] = \int_{\delta\beta'} \mathrm{d}\beta' \, (\frac{\mathrm{d}\sigma}{\mathrm{d}\beta'})$. Additionally, the differential number $\mathrm{d}\mathcal{N}^{\mathrm{ind}}$ of induced outgoing photons can be estimated by $\frac{\mathrm{d}\mathcal{N}^{\mathrm{ind}}}{\mathrm{d}\beta'} \approx \frac{\mathcal{N}^{\mathrm{probe}}}{w_{\mathrm{eff}}} \frac{\mathrm{d}\sigma}{\mathrm{d}\beta'}$, where $w_{\mathrm{eff}} = \max\{w_{\mathrm{probe}}, w_{\mathrm{pump}}\}$ is the *effective* transverse interaction length between the probe and pump beam to be used in the calculation of the two-dimensional current density $\mathcal{N}^{\mathrm{probe}}/w_{\mathrm{eff}}$ associated with the incoming probe photons.[9] Likewise, the number of induced outgoing photons corresponding to a cross section $\sigma[\beta, \delta\beta'(\beta')]$ is given by

$$\mathcal{N}^{\mathrm{ind}}[\beta, \delta\beta'(\beta')] \approx \frac{\mathcal{N}^{\mathrm{probe}}}{w_{\mathrm{eff}}} \sigma[\beta, \delta\beta'(\beta')] \,. \tag{3.46}$$

These formulae allow us to easily calculate the number of induced photons for all angles $-\pi < \beta' \leq \pi$, and for variable detector sizes $\delta\beta'$.

The procedure employed and the results obtained in this section, Eqs. (3.43) and (3.44), resemble a quantum mechanical calculation in the Born approximation. In the standard language of quantum mechanical scattering theory, the angle β' is related to the scattering angle θ by $\theta = \beta' - \beta$, where θ denotes the angle between $\mathbf{k}_{\mathrm{in}}$ and $\mathbf{k}'$. As the process is elastic, $|\mathbf{k}'| = |\mathbf{k}_{\mathrm{in}}|$, the scattering amplitude is in fact only a function of ω_{in}, θ and the parameters of the inhomogeneity (for inhomogeneities not exhibiting rotational symmetry, this includes the angle β of the incoming photons).

[9] We work with incident plane waves which do not feature a transverse profile, while the inhomogeneity is localized in the transverse direction. If the probe beam diameter w_{probe} is smaller than the extent of the inhomogeneity, the probe photon current has to be chosen in such a way that an integration over the extension of the pump field inhomogeneity w_{pump} results in $\mathcal{N}_{\mathrm{probe}}$ interacting probe photons. If on the other hand the probe beam diameter is larger than the extent of the inhomogeneity, only a fraction of probe beam photons interacts with the inhomogeneity, and additionally the current has to be multiplied by a factor $w_{\mathrm{pump}}/w_{\mathrm{probe}}$. This can be combined into the *effective* interaction length w_{eff}.

3.2.3. Relation to Schrödinger equation

In this section we aim to rewrite the equation of motion for optical quantum reflection in terms of a Schrödinger equation in order to highlight the analogy between atomic and optical quantum reflection in the weak-field limit. For simplicity we focus on the scenario discussed in the previous section: A purely magnetic, two-dimensional static inhomogeneity $\mathcal{B}(\mathrm{x},\mathrm{y})$ with the probe beam traveling in the x-y plane. The direction of the magnetic field vector is orthogonal to the propagation direction of the probe photons.

The stationary Schrödinger equation of ordinary quantum mechanics usually features a local potential $V(\mathbf{x})$. To match the formalism of Sect. 3.2.1 to a local potential, we adopt a slightly different strategy to incorporate the inhomogeneity into the equations of motion. We start with the equation of motion (3.11) for the polarization mode $p = \parallel$, which resulted from the contraction of Eq. (3.3) with the global projector $\tilde{P}_{\parallel}^{\mu\nu}$. This time right away we insert the polarization tensor for a constant magnetic pump field, $\tilde{\Pi}_{\parallel}(k,k'|A) = \Pi_{\parallel}(k'|A)\,(2\pi)^4\,\delta^{(4)}(k+k')$, yielding the equation of motion for photons in constant pump fields

$$\Big(k^2 + \Pi_{\parallel}(k|A)\Big)a_{\parallel}(k) = 0\,. \tag{3.47}$$

As we have seen in Sect. 3.2.1, the final expression for the induced photon field (3.21) only takes contributions from the photon polarization tensor evaluated on the light cone. Furthermore, working with the weak-field expansion of the polarization tensor (B.15) we only retain terms of the lowest nontrivial order, i.e. $\sim (e\mathcal{B})^2$. In this limit, the dispersion relation for the probe photons reads $k^2 = 0 + \mathcal{O}\big((e\mathcal{B})^2\big)$, such that off-the-light-cone contributions are of higher order in the pump field strength, and can therefore be neglected in the expansion of the photon polarization tensor. Correspondingly, in the equation of motion (3.47) we employ the second-order expansion coefficient of the polarization tensor in a constant magnetic field (B.18) for the parallel polarization mode $p = \parallel$ evaluated on the light cone $k^2 = 0$. As the probe photons travel in the x-y plane, we find $k_{\parallel}^2 = -\omega^2$. The equation of motion therefore becomes

$$\left[k_{\mathrm{x}}^2 + k_{\mathrm{y}}^2 - \omega^2\left(1 + \frac{7}{45}\frac{\alpha}{\pi}\left(\frac{\mathcal{B}}{\mathcal{B}_{\mathrm{cr}}}\right)^2\right)\right]a_{\parallel}(k) = 0\,. \tag{3.48}$$

To transform Eq. (3.48) into a Schrödinger equation and be able to incorporate the inhomogeneous pump field, we perform a Fourier transformation acting on the spatial

momentum components k_x and k_y. Next, we substitute $\mathcal{B} \to \mathcal{B}(\mathrm{x},\mathrm{y})$ to arrive at

$$\left[-\frac{\partial^2}{\partial \mathrm{x}^2} - \frac{\partial^2}{\partial \mathrm{y}^2} - \omega^2 \frac{7}{45}\frac{\alpha}{\pi}\left(\frac{e\mathcal{B}(\mathrm{x},\mathrm{y})}{m^2}\right)^2\right] a_\parallel(\omega,\mathrm{x},\mathrm{y}) = \omega^2\, a_\parallel(\omega,\mathrm{x},\mathrm{y})\,. \tag{3.49}$$

Equation (3.49) resembles a stationary Schrödinger equation for particles with wave function $a_\parallel(\omega,\mathrm{x},\mathrm{y})$ traveling in a localized effective potential

$$V(\mathrm{x},\mathrm{y}) = -\omega^2 \frac{7}{45}\frac{\alpha}{\pi}\left(\frac{e\mathcal{B}(\mathrm{x},\mathrm{y})}{m^2}\right)^2, \tag{3.50}$$

with the corresponding energy eigenvalue ω^2, cf. Fig. 3.6. As $V(\mathrm{x},\mathrm{y}) \leq 0$, it acts as an *attractive* effective potential for the probe photons regardless of the profile of the pump field inhomogeneity $\mathcal{B}(\mathrm{x},\mathrm{y})$. A fraction of probe photons encountering this potential may then experience above-the-barrier scattering, while the remaining photons continue to propagate undisturbed on their original path. This should be contrasted to the scenario of atomic quantum reflection as shown in Figure 3.1, where the additional repulsive part of the potential gives rise to a large background stemming from classical reflection. As there exists no optical analogue of a repulsive potential, the classical background is missing for optical quantum reflection. Hence, optical quantum reflection might provide an increased signal-background separation which could make it well suited to probe the nonlinearities of the quantum vacuum.

To conclude this section, let us remark that for a pump field inhomogeneity which

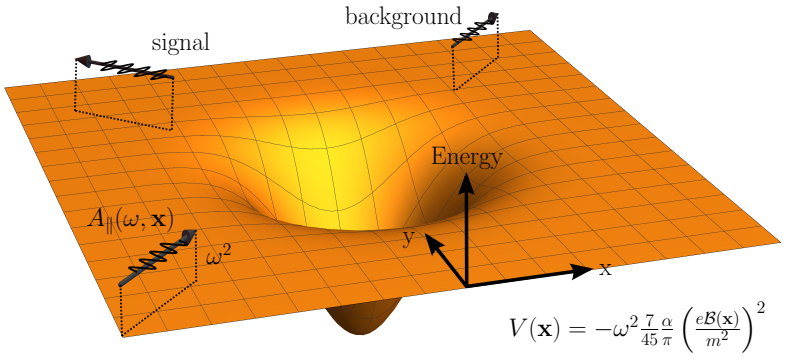

Figure 3.6.: Quantum reflection of photons at a stationary and localized effective potential $V(\mathrm{x},\mathrm{y})$. The photons, resembling particles with wave function $a_\parallel(\omega,\mathrm{x},\mathrm{y})$ and effective energy eigenvalue ω^2, can experience above-the-barrier scattering, as the potential is purely attractive. These induced photons, which constitute the signal, partially propagate in different directions than the photons unaffected by the inhomogeneity, which constitute the background.

is homogeneous along y, the Schrödinger equation (3.49) can be cast into a one-dimensional equation

$$\left[-\frac{\partial^2}{\partial \mathrm{x}^2} - \omega^2 \frac{7}{45}\frac{\alpha}{\pi}\left(\frac{e\mathcal{B}(\mathrm{x})}{m^2}\right)^2\right] a_\parallel(\omega, \mathrm{x}, \beta) = \omega^2 \cos^2\beta\, a_\parallel(\omega, \mathrm{x}, \beta)\,, \tag{3.51}$$

for photons propagating at an angle $\beta = \sphericalangle(\mathbf{k}, \hat{\mathbf{e}}_\mathrm{x})$ with respect to the x axis (cf. Fig. 3.2). The quantum mechanical scattering problem as posed in Eq. (3.51) can then be conveniently solved in the transfer matrix formalism. The strategy is to first substitute the smooth potential $V(\mathrm{x})$ by a piecewise continuous potential $V_n = V(n\Delta\mathrm{x})$ for $\mathrm{x} \in [n\Delta\mathrm{x}, (n+1)\Delta\mathrm{x})$, with $n \in \mathbb{Z}$. We then compute the transfer matrix for the infinitesimal step $\Delta\mathrm{x}$ from x_n to x_{n+1}, keeping only terms up to $\mathcal{O}(\Delta\mathrm{x})$. This is done the usual way by assuming a plane wave consisting of left and right-moving contributions $t_n \mathrm{e}^{ik_n\mathrm{x}} + r_n \mathrm{e}^{-ik_n\mathrm{x}}$ for the infinitesimal section n as well as for the subsequent section $n+1$, and matching the amplitudes and first derivatives of the waves at the potential step $V_n \to V_{n+1}$. The dispersion relation of the photons for each infinitesimal section reads $k_n = \sqrt{\omega^2\cos^2\beta - V_n}$. We can then multiply the transfer matrices for subsequent steps, again keeping only terms up to $\mathcal{O}(\Delta\mathrm{x})$. Reverting to the continuum limit we assume the ratio $\frac{\Delta k}{\Delta \mathrm{x}}$ to be finite, necessitating smooth potentials $V(\mathrm{x})$. The components of the transfer matrix for macroscopic distances can then be written in terms of integrals. Choosing the boundary conditions such that at $\mathrm{x} \to -\infty$ we have both left and right-moving contributions, and only right moving contributions at $\mathrm{x} \to \infty$, we can derive the quantum mechanical reflection coefficient

$$R_\parallel = \left|\frac{\int_{-\infty}^{\infty} \mathrm{dx}\, \mathrm{e}^{2ik\mathrm{x}} \frac{k'}{2k}}{1 + \int_{-\infty}^{\infty} \mathrm{dx}\left(\frac{k'}{2k} + i\mathrm{x}k'\right)}\right|^2 , \tag{3.52}$$

with $k(\mathrm{x}) = \sqrt{\omega^2\cos^2\beta - V(\mathrm{x})}$ and $k'(\mathrm{x}) = \frac{\mathrm{d}}{\mathrm{dx}}k(\mathrm{x})$. Expanding the reflection coefficient in terms of the magnetic pump field $e\mathcal{B}$ retrieves the result (3.35) from Sect. 3.2.2 for the parallel polarization mode,

$$R_\parallel = \left|\frac{\alpha}{\pi}\frac{7}{90}\frac{\omega}{\cos\beta}\int \mathrm{dx}'\, \mathrm{e}^{i(2\omega\cos\beta)\mathrm{x}'}\left(\frac{e\mathcal{B}(\mathrm{x}')}{m^2}\right)^2\right|^2 + \mathcal{O}\left(\left(\tfrac{e\mathcal{B}}{m^2}\right)^6\right) . \tag{3.53}$$

The requirement of a smooth potential is necessarily fulfilled, as our approach of incorporating the inhomogeneity into the expression of the polarization tensor for constant pump fields is restricted to inhomogeneities varying on scales much larger than

the Compton wavelength. Retrieving the result (3.35) illustrates the equivalence between the quantum mechanical scattering formalism in the Born approximation and the formalism employed in Sect. 3.2.1 to solve the equations of motion (3.11). For completeness, the explicit derivation of the reflection coefficient in the transfer matrix formalism is given in Appendix C.

3.2.4. Crossed pump fields

Whereas in the last section we have dealt with electromagnetic field inhomogeneities featuring only a magnetic field component, in this section we focus on fields featuring both magnetic and electric components. We limit the analysis to what is called the crossed-field scenario: The unit vectors of the electric and magnetic field, $\hat{\mathbf{e}}_E$ and $\hat{\mathbf{e}}_B$, are orthogonal to each other, i.e. $\hat{\mathbf{e}}_B \perp \hat{\mathbf{e}}_E$, and the electric and magnetic fields have identical amplitude profiles, such that we can write $|\mathbf{E}(x)| = |\mathbf{B}(x)| =: \mathcal{E}(x)$. This particular pump field configuration can be employed to describe the electromagnetic fields delivered by high-intensity lasers.

It will be useful to introduce the normalized Poynting four-vector $\hat{s}^\mu := (1, \hat{\mathbf{e}}_E \times \hat{\mathbf{e}}_B) = (1, \hat{\mathbf{s}})$. For a fixed direction of $\hat{\mathbf{s}}$, the orientation of the trihedron formed by $\hat{\mathbf{e}}_E, \hat{\mathbf{e}}_B$ and $\hat{\mathbf{s}}$ will be parametrized by the angle $\varphi \in [0, 2\pi)$.

We repeat the analysis performed at the beginning of Sect. 3.2.2, this time employing the polarization tensor in constant crossed fields,

$$\Pi^{\mu\nu}(k|\mathbf{E} \perp \mathbf{B}) = P_0^{\mu\nu}\Pi_0(k) + P_1^{\mu\nu}\Pi_1(k) + P_2^{\mu\nu}\Pi_2(k)\,. \tag{3.54}$$

In a weak-field expansion, the expansion coefficient of the polarization tensor (3.54) belonging to the lowest nontrivial order ($\ell = 1$) in the field strength is given in the appendix B.3, Eq. (B.26). As detailed there, an expansion in the field strength ratio $\frac{e\mathcal{E}}{m^2} \ll 1$ actually amounts to an expansion in $\left(\frac{e\mathcal{E}}{m^2}\right)^2 \frac{(\hat{s}k)^2}{m^2} \ll 1$. On the light-cone $k^2 = 0$, the remaining parameter integral can be performed analytically, yielding

$$\Pi^{\mu\nu}_{(2)}(k) = -\frac{1}{45}\frac{\alpha}{\pi}(\hat{s}k)^2\Big(7\,P_1^{\mu\nu}(k) + 4\,P_2^{\mu\nu}(k)\Big)\frac{1}{m^4}\,. \tag{3.55}$$

Correspondingly, for the tensorial quantity (3.8) of order $\ell = 1$ we find

$$\begin{aligned}\pi^{\mu\nu}_{(2)}(k,k') = {}& \frac{1}{90}\frac{\alpha}{\pi}\frac{1}{m^4} \\ & \times \left[7\Big((\hat{s}k)^2\,P_1^{\mu\nu}(k) + (\hat{s}k')^2\,P_1^{\mu\nu}(k')\Big) + 4\Big((\hat{s}k)^2\,P_2^{\mu\nu}(k) + (\hat{s}k')^2\,P_2^{\mu\nu}(k')\Big)\right].\end{aligned} \tag{3.56}$$

The crossed-field polarization tensor evaluated on the light cone is spanned by the two projectors $P_1^{\mu\nu}(k)$ and $P_2^{\mu\nu}(k)$, projecting onto photon polarization modes.[10] We can again identify two cases which render one of the projectors globally invariant: (i) The projector $P_1^{\mu\nu}(k)$ remains invariant under the transformation $\mathbf{k} \to \mathbf{k} + f(k)\hat{\mathbf{e}}_E$, where $f(k)$ is an arbitrary function of the components of the probe photon's four-momentum k^μ. Hence, for pump fields with inhomogeneities along $\nabla\mathcal{E} \sim \hat{\mathbf{e}}_E$ we observe that $P_1^{\mu\nu}(k)$ constitutes a global projector. (ii) Likewise, $P_2^{\mu\nu}(k)$ is invariant under $\mathbf{k} \to \mathbf{k} + f(k)\hat{\mathbf{e}}_B$, and therefore constitutes a global projector for $\nabla\mathcal{E} \sim \hat{\mathbf{e}}_B$.

At first glance it seems that crossed pump fields only allow for the analysis of static inhomogeneities varying at most along one spatial direction. However, it turns out that also more general inhomogeneities may be considered for certain specific configurations. To this end let us analyze the projectors $P_1^{\mu\nu}(k) = u_1^\mu u_1^\nu$ and $P_2^{\mu\nu}(k) = u_2^\mu u_2^\nu$ in more detail: Without loss of generality we set $\hat{\mathbf{s}} = \hat{\mathbf{e}}_y$, such that the directions of the electric and magnetic field read $\hat{\mathbf{e}}_E = (-\sin\varphi, 0, \cos\varphi)$ and $\hat{\mathbf{e}}_B = (\cos\varphi, 0, \sin\varphi)$, respectively. The polarization four-vectors u_1^μ and u_2^μ span the projectors and are given by Eqs. (B.22), reading

$$
\begin{aligned}
u_1^\mu &= \left(\frac{k_\mathrm{z}\sin\varphi + k_\mathrm{x}\cos\varphi}{(\hat{s}k)}, -\cos\varphi, \frac{k_\mathrm{z}\sin\varphi + k_\mathrm{x}\cos\varphi}{(\hat{s}k)}, -\sin\varphi \right) , \\
u_2^\mu &= \left(\frac{k_\mathrm{z}\cos\varphi - k_\mathrm{x}\sin\varphi}{(\hat{s}k)}, \sin\varphi, \frac{k_\mathrm{z}\cos\varphi - k_\mathrm{x}\sin\varphi}{(\hat{s}k)}, -\cos\varphi \right) .
\end{aligned}
\tag{3.57}
$$

From the explicit representation (3.57) we can easily read off the invariance of the projectors under the transformations given in the last paragraph for the cases (i) and (ii). However, restricting photon propagation to the x-y plane, i.e. setting $k_\mathrm{z} = 0$, there exist two cases for which either u_1^μ or u_2^μ take on a particularly simple form: For $\varphi = \pi/2$ we find $u_1^\mu = (0, -\hat{\mathbf{e}}_\mathrm{z})$. Likewise, for $\varphi = 0$, we find $u_2^\mu = (0, -\hat{\mathbf{e}}_\mathrm{z})$. Consequentially, for these two special configurations the projectors $P_1^{\mu\nu}$ and $P_2^{\mu\nu}$, respectively, are independent of the momentum coordinates $k_\mathrm{x}, k_\mathrm{y}$ and the energy ω, and therefore constitute global projectors for general kinematics restricted to the x-y plane. Hence, crossed pump fields allow for the investigation of a larger class of inhomogeneity profiles compared to purely magnetic pump fields.

For the cases outlined above, a contraction of the tensorial quantity (3.56) with the

[10] As the explicit expressions for these projectors are less intuitive than in the magnetic field case, they have been relegated to the appendix B.3, where all necessary details for the polarization tensor in constant crossed fields are recollected.

corresponding global projector $\tilde{P}_p^{\mu\nu}$, with $p \in \{1,2\}$, results in

$$\pi_{1,(2)}(k,k') = -\frac{7}{45}\frac{\alpha}{\pi}\frac{(\hat{s}k)^2+(\hat{s}k')^2}{2}\frac{1}{m^4}\,, \quad \text{and} \tag{3.58}$$

$$\pi_{2,(2)}(k,k') = -\frac{4}{45}\frac{\alpha}{\pi}\frac{(\hat{s}k)^2+(\hat{s}k')^2}{2}\frac{1}{m^4}\,. \tag{3.59}$$

Static one-dimensional pump field

Let us briefly discuss quantum reflection for a one-dimensional purely spatial field inhomogeneity $\mathcal{E}(\mathrm{x})$. If the electric field component of the pump field points along $\hat{\mathbf{e}}_\mathrm{x}$, the projector $P_1^{\mu\nu}$ constitutes a global projector. Likewise, if the magnetic field component points along $\hat{\mathbf{e}}_\mathrm{x}$, the projector $P_2^{\mu\nu}$ constitutes a global projector. The former scenario had been labeled as case (i), and the latter as (ii). For these two cases the calculation of the reflection coefficient essentially resembles Sect. 3.2.2. The result can be inferred straightforwardly from Eq. (3.35) by substituting $\sin^2\sphericalangle(\mathbf{k}_\mathrm{in},\mathbf{B}) \to (1-\hat{\mathbf{s}}\cdot\hat{\mathbf{e}}_\mathrm{y}\sin\beta)^2$, reading

$$R_p = \left|\frac{\alpha}{\pi}\frac{c_p}{90}\frac{(1-\hat{\mathbf{s}}\cdot\hat{\mathbf{e}}_\mathrm{y}\sin\beta)^2}{\cos\beta}\,\omega_\mathrm{in}\int \mathrm{dx}'\,\mathrm{e}^{i(2\omega_\mathrm{in}\cos\beta')\mathrm{x}'}\left(\frac{e\mathcal{E}(\mathrm{x}')}{m^2}\right)^2\right|^2 + \mathcal{O}\left(\left(\tfrac{e\mathcal{E}}{m^2}\right)^6\right)\,, \tag{3.60}$$

with $c_1 = 7$ and $c_2 = 4$.

Similar to the result of Sect. 3.2.2, the reflection coefficient generically diverges for $|\beta| \to \pi/2$. However, the special case of $\hat{\mathbf{s}} = \hat{\mathbf{e}}_\mathrm{y}$ yields only one divergent direction, while the reflection coefficient vanishes for $\beta \to \pi/2$. This behavior is due to the fact that the propagation of light in weak crossed pump fields remains unaffected if $(\hat{\mathbf{e}}_k, \hat{\mathbf{e}}_E, \hat{\mathbf{e}}_B)$ form the basis of an orthonormal coordinate system [28]; cf. Sect. B.3. The existence of this invariant direction is a special property of crossed pump fields, and has to be taken into consideration when performing reflection experiments involving laser-generated pump fields.

2+1 dimensional spatio-temporal inhomogeneity

We skip the discussion of the 1+1 dimensional inhomogeneity for crossed fields, as it would essentially follow the lines of Sect. 3.2.2. Instead, we jump right into the discussion of a 2+1 dimensional spatio-temporal inhomogeneity $\mathcal{E}(\mathrm{x},\mathrm{y},t)$, which includes the 1+1 dimensional inhomogeneity as a limiting case. Limiting propagation to the x-y plane and referring to the beginning of Sect. 3.2.4, the two settings for which the

projectors become momentum independent, are

$$\{p=1\,,\ \hat{\mathbf{E}}=-\hat{\mathbf{e}}_{\mathrm{x}}\,,\ \hat{\mathbf{B}}=+\hat{\mathbf{e}}_{\mathrm{z}}\}\quad\text{and}\quad\{p=2\,,\ \hat{\mathbf{E}}=+\hat{\mathbf{e}}_{\mathrm{z}}\,,\ \hat{\mathbf{B}}=+\hat{\mathbf{e}}_{\mathrm{x}}\}\,. \tag{3.61}$$

For brevity, these two settings will also be labeled with $p\in\{1,2\}$. The induced electromagnetic field follows from Eqs. (3.21) and (3.22), and reads

$$\begin{aligned}a_p^{\mathrm{ind}}(x)=ia(\omega_{\mathrm{in}})\frac{c_p}{90}\frac{\alpha}{\pi}\int\frac{\mathrm{d}k_{\mathrm{x}}}{2\pi}\int\frac{\mathrm{d}k_{\mathrm{y}}}{2\pi}\\ \times\,\mathrm{e}^{i\left[k_{\mathrm{x}}\mathrm{x}+k_{\mathrm{y}}\mathrm{y}-\sqrt{k_{\mathrm{x}}^2+k_{\mathrm{y}}^2}t\right]}\frac{1}{2\sqrt{k_{\mathrm{x}}^2+k_{\mathrm{y}}^2}}\left[\omega_{\mathrm{in}}^2(1-\sin\beta)^2+\left(\sqrt{k_{\mathrm{x}}^2+k_{\mathrm{y}}^2}-k_{\mathrm{y}}\right)^2\right]\\ \times\int\mathrm{d}t'\int\mathrm{d}\mathrm{x}'\int\mathrm{d}\mathrm{y}'\,\mathrm{e}^{i\left[(\omega_{\mathrm{in}}\cos\beta-k_{\mathrm{x}})\mathrm{x}'+(\omega_{\mathrm{in}}\sin\beta-k_{\mathrm{y}})\mathrm{y}'-(\omega_{\mathrm{in}}-\sqrt{k_{\mathrm{x}}^2+k_{\mathrm{y}}^2})t'\right]}\left(\frac{e\mathcal{E}(\mathrm{x}',\mathrm{y}',t')}{m^2}\right)^2\\ +\mathcal{O}\left(\left(\tfrac{e\mathcal{E}}{m^2}\right)^4\right)\,,\end{aligned} \tag{3.62}$$

where $c_1=7$, $c_2=4$ are the numerical coefficients associated with the two cases in Eq. (3.61).

As a special example which allows us to examine wave mixing effects more lucidly, we evaluate Eq. (3.62) for a pump field inhomogeneity $\mathcal{E}(\mathrm{x},\mathrm{y},t)=\mathcal{E}(\mathrm{x})\cos\big(\Omega(\mathrm{y}-t)\big)$, which factorizes into a *longitudinal* "plane-wave" profile $\sim\cos\big(\Omega(\mathrm{y}-t)\big)$ and a transversal profile $\mathcal{E}(\mathrm{x})$. Such a profile is depicted in Fig. 3.7. This profile is very advantageous from a computational point of view: The five integrals occurring in Eq. (3.62) can be reduced to a single remaining integral, as the y' and t' integrations yield delta functions, which can in turn be employed to compute the k_{x} and k_{y} integrals. Furthermore, this profile roughly resembles the electromagnetic field generated by a high-intensity laser in the vicinity of its beam waist, if one ignores the longitudinal envelope profile or beam divergence. It can therefore serve as a starting point to obtain first insights into basic phenomena related to quantum reflection in a laser-generated pump field. Performing the integrations over y' and t' in Eq. (3.62), we obtain the following identity,

$$\begin{aligned}\int\mathrm{d}t'\int\mathrm{d}\mathrm{y}'\,\mathrm{e}^{i\left[(\omega_{\mathrm{in}}\sin\beta-k_{\mathrm{y}})\mathrm{y}'-(\omega_{\mathrm{in}}-\sqrt{k_{\mathrm{x}}^2+k_{\mathrm{y}}^2})t'\right]}\cos^2\big(\Omega(\mathrm{y}'-t')\big)\\ =\pi^2\sum_{n=-1}^{+1}(1+\delta_{n0})\,\Theta\big(k_{\mathrm{x},2n}^2\big)\,\frac{\sqrt{k_{\mathrm{x}}^2+k_{\mathrm{y}}^2}}{|k_{\mathrm{x},2n}|}\\ \times\,\delta\big(k_{\mathrm{y}}-\omega_{\mathrm{in}}\sin\beta+2n\Omega\big)\left[\delta\big(k_{\mathrm{x}}-|k_{\mathrm{x},2n}|\big)+\delta\big(k_{\mathrm{x}}+|k_{\mathrm{x},2n}|\big)\right],\end{aligned} \tag{3.63}$$

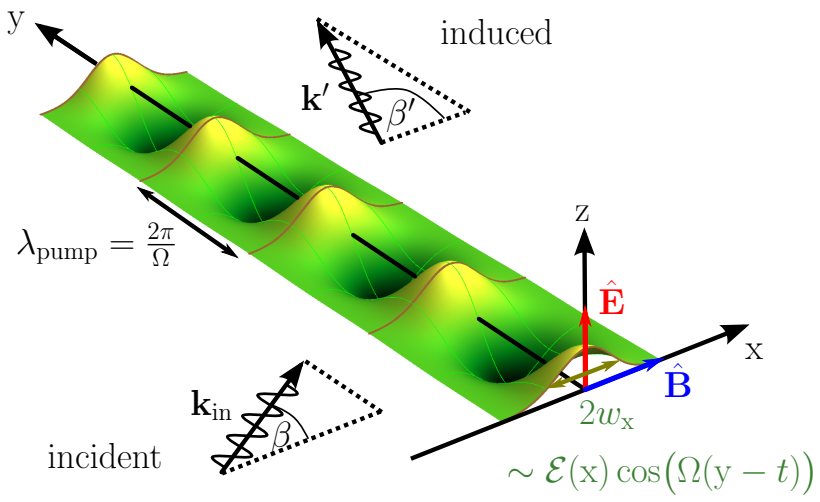

Figure 3.7.: Schematic depiction of quantum reflection for a $2+1$ dimensional field inhomogeneity $\mathcal{E}(\text{x},\text{y},t) = \mathcal{E}(\text{x})\cos\big(\Omega(\text{y}-t)\big)$ for $p = 2$ (taken from Ref. [44]). This inhomogeneity incorporates the basic features of quantum reflection in a high-intensity laser set-up. Incident probe photons of four-momentum k^μ_{in} travel in the x-y plane and induce outgoing photons of four-momentum k'^μ. The spacetime dependence of the field inhomogeneity allows for both energy and momentum exchange between the probe and pump fields, such that the energy and momentum of the induced photons in general differ from that of the incident probe photons.

where we have now defined $k^2_{\text{x},2n} \equiv (\omega_{\text{in}} - 2n\Omega)^2 - (\omega_{\text{in}}\sin\beta - 2n\Omega)^2$, in analogy to Eq. (3.37). The first delta function contains the various wave mixing contributions, while the second delta function separates forward and backward scattered contributions. Inserting Eq. (3.63) into (3.62), the induced photon field is given by

$$
\begin{aligned}
a_p^{\text{ind}}(x) = ia(\omega_{\text{in}})\frac{c_p}{360}\frac{\alpha}{\pi}\omega_{\text{in}}^2(1-\sin\beta)^2\sum_{n=-1}^{+1}(1+\delta_{n0})\,\Theta\big(k^2_{\text{x},2n}\big)\frac{1}{|k_{\text{x},2n}|} \\
\times \text{e}^{i[|k_{\text{x},2n}|\text{x}+(\omega_{\text{in}}\sin\beta-2n\Omega)\text{y}-(\omega_{\text{in}}-2n\Omega)t]}\Bigg\{\int \text{dx}'\text{e}^{i(\omega_{\text{in}}\cos\beta-|k_{\text{x},2n}|)\text{x}'}\left(\frac{e\mathcal{E}(\text{x}')}{m^2}\right)^2 \\
+\,\text{e}^{-2i|k_{\text{x},2n}|\text{x}}\int \text{dx}'\text{e}^{i(\omega_{\text{in}}\cos\beta+|k_{\text{x},2n}|)\text{x}'}\left(\frac{e\mathcal{E}(\text{x}')}{m^2}\right)^2\Bigg\} + \mathcal{O}\left(\left(\tfrac{e\mathcal{E}}{m^2}\right)^4\right). \qquad (3.64)
\end{aligned}
$$

The induced photon field is made up of photon waves of positive frequencies $\omega'_{2n} = \omega_{\text{in}} - 2n\Omega$ and wave vectors $\mathbf{k}'_{\pm,2n} = (\pm|k_{\text{x},2n}|, \omega_{\text{in}}\sin\beta - 2n\Omega, 0)$, with $n \in \{0, \pm 1\}$. The basic scenario is similar to Fig. 3.4 from Sect. 3.2.2. In analogy to this section we

can write down the scattering coefficients, reading

$$R_{p,2n}^{(\pm)} = \Theta\big(k_{\mathrm{x},2n}^2\big)\left|\frac{\alpha}{\pi}\frac{c_p(1+\delta_{n0})}{360}\,\frac{\omega_{\mathrm{in}}^2(1-\sin\beta)^2}{k_{\mathrm{x},2n}}\right.$$
$$\left.\times\int \mathrm{dx}'\mathrm{e}^{i(\omega_{\mathrm{in}}\cos\beta\mp|k_{\mathrm{x},2n}|)\mathrm{x}'}\left(\frac{e\mathcal{E}(\mathrm{x}')}{m^2}\right)^2\right|^2 + \mathcal{O}\left(\left(\tfrac{e\mathcal{E}}{m^2}\right)^6\right). \quad (3.65)$$

Similar to Sect. 3.2.2, the Heaviside function ensures that the photons induced by the interaction of the probe field with the pump field are *real* photons. The restriction $k_{\mathrm{x},2n}^2 > 0$ can be rewritten as $\frac{2n\Omega}{\omega_{\mathrm{in}}} \leq \frac{1+\sin\beta}{2}$ (taking into account that $\omega_{\mathrm{in}} > 0$ and $\Omega \geq 0$). For $n \in \{-1, 0\}$ this condition is trivially fulfilled, as then $\frac{2n\Omega}{\omega_{\mathrm{in}}} \leq 0$, while $0 < \frac{1+\sin\beta}{2} < 1$. Conversely, for $n = 1$ the left-hand side of the above condition becomes positive, $\frac{2\Omega}{\omega_{\mathrm{in}}} > 0$, which implies that we have to ensure that $\frac{2\Omega}{\omega_{\mathrm{in}}} \leq \frac{1+\sin\beta}{2}$. If the energy of the photons making up the pump beam is too large compared with the probe photon energy, such that $\frac{2\Omega}{\omega_{\mathrm{in}}} \geq 1$, the inequality can never be fulfilled and no photons with energies corresponding to $n = 1$ will be induced irrespective of the angle of incidence β. This is due to the fact that in this case the energy of the probe photons is too small to facilitate an energy transfer of 2Ω to the background field. Likewise, for $\frac{2\Omega}{\omega_{\mathrm{in}}} < 1$ the inequality is only fulfilled for large enough incidence angles β. This encodes the physical requirement that the probe photons possess a large enough momentum component along the y direction, k_{y}, in order to allow for a momentum transfer 2Ω onto the pump field: Due to the $\mathrm{y} - t$ dependence of the inhomogeneity under consideration the energy transfer between the pump and probe field corresponds entirely to a transfer of momentum along the y direction.

A different way to arrive at the scattering coefficients (3.65) is to start with the expression of the polarization tensor in a linearly polarized plane-wave field, which is a special case of the polarization tensor in a generic, elliptically polarized monochromatic plane-wave field, first obtained by Becker and Mitter in 1975 [83], and independently by Baier, Milstein and Strakhovenko [82]. Using this polarization tensor the procedure employed in this chapter, namely incorporating the inhomogeneous pump fields *a posteriori*, can then be applied. The important difference is that the polarization tensor already accounts for the longitudinal field profile $\cos\big(\Omega(\mathrm{y} - t)\big)$. Hence, only the transversal profile $\mathcal{E}(\mathrm{x})$ has to be built in along the lines of Sect. 3.2.1. In the limit of weak pump field strengths, the scattering coefficients then agree with (3.65). An explicit derivation of the induced photon field in this formalism is given in the appendix D.

Let us conclude this section by providing an expression for the differential cross section of quantum reflection in a pump field inhomogeneity $\mathcal{E}(\mathrm{x},\mathrm{y},t)$, not restricted to the purely harmonic time dependence considered in the two preceding paragraphs. As a first step we rewrite Eq. (3.62) in terms of polar coordinates, $(k_\mathrm{x},k_\mathrm{y})\to(\omega',\beta')$, with $\omega'=\sqrt{k_\mathrm{x}^2+k_\mathrm{y}^2}$. The resulting β'-integral can then be solved in terms of the Bessel function J_0, analogous to Sect. 3.2.2. Furthermore, employing the same far-field expansion as in Sect. 3.2.2 we finally arrive at

$$a_p^{\mathrm{ind}}(x)=a(\omega_\mathrm{in})\int_0^\infty\frac{\mathrm{d}\omega'}{2\pi}\frac{\mathrm{e}^{i\omega'(|\mathbf{x}|-t)}}{\sqrt{|\mathbf{x}|}}f_p(k',k_\mathrm{in})\,. \tag{3.66}$$

Here we have defined, in analogy to Sect. 3.2.2, the scattering amplitude

$$\begin{aligned}f_p(k',k_\mathrm{in})=&\sqrt{\frac{i}{2\pi\omega'}}\frac{c_p}{90}\frac{\alpha}{\pi}\frac{\omega_\mathrm{in}^2(1-\sin\beta)^2+\omega'^2(1-\sin\beta')^2}{2}\\&\times\int\mathrm{dx}'\,\mathrm{dy}'\,\mathrm{d}t'\;\mathrm{e}^{i[(\omega'-\omega_\mathrm{in})t'-(\mathbf{k}'-\mathbf{k}_\mathrm{in})\cdot\mathbf{x}']}\left[\frac{e\mathcal{E}(\mathrm{x}',\mathrm{y}',t')}{m^2}\right]^2+\mathcal{O}\left(\left(\tfrac{e\mathcal{E}}{m^2}\right)^4\right)\,,\end{aligned} \tag{3.67}$$

where the propagation dynamics are restricted to the x-y plane such that $\mathbf{x}'=(\mathrm{x}',\mathrm{y}',0)$. Likewise, the ingoing and outgoing momentum vectors of the photons read $\mathbf{k}_\mathrm{in}=\omega_\mathrm{in}(\cos\beta,\sin\beta,0)$ and $\mathbf{k}'=\omega'(\cos\beta',\sin\beta',0)=\omega'\frac{\mathbf{x}}{|\mathbf{x}|}$.

The standard definition of the differential cross section applies to scattering scenarios with stationary scattering potentials. For the scenario of a nonstationary inhomogeneity as considered here we calculate the differential cross section by employing time integrated fluxes of incoming and induced photons. A natural choice of the integration interval is the time $T=\min\{\tau_\mathrm{pump},\tau_\mathrm{probe}\}$ of interaction between the probe beam and the field inhomogeneity, leading to the following time-independent differential cross section for inducing photons in the direction $\mathbf{k}'\sim(\cos\beta',\sin\beta',0)$,

$$\frac{\mathrm{d}\sigma}{\mathrm{d}\beta'}\equiv\frac{\int_{-T/2}^{T/2}\mathrm{d}t\,|a_p^{\mathrm{ind}}(x)|^2|\mathbf{x}|}{T|a_p^{\mathrm{in}}(x)|^2}\,. \tag{3.68}$$

Here we used the fact that the incoming probe photon beam is modeled as a plane wave. For stationary inhomogeneities the well-known expression for the differential cross section $\frac{\mathrm{d}\sigma}{\mathrm{d}\beta'}\equiv\frac{|a_p^{\mathrm{ind}}(x)|^2|\mathbf{x}|}{|a_p^{\mathrm{in}}(x)|^2}$ is recovered, cf. Eq. (3.45). In analogy to Sect. 3.2.2, the differential number of induced outgoing photons to be registered by a detector in the far-field region can then be determined from $\frac{\mathrm{d}\mathcal{N}_p^{\mathrm{ind}}}{\mathrm{d}\beta'}=f_\mathrm{int}\frac{\mathcal{N}_p^{\mathrm{probe}}}{w_\mathrm{eff}}\frac{\mathrm{d}\sigma}{\mathrm{d}\beta'}$. As we take the finite duration of the pump beam into account, we have introduced a factor

$f_{\text{int}} \equiv \min\{1, \tau_{\text{pump}}/\tau_{\text{probe}}\}$ providing a rough estimate of the fraction of probe photons interacting with the inhomogeneity. If we consider inhomogeneities localized in time we can extend the integration limits of the remaining integral in Eq. (3.68) to $\pm\infty$, resulting in

$$\frac{\mathrm{d}\mathcal{N}_p^{\text{ind}}}{\mathrm{d}\beta'} = \frac{\mathcal{N}_p^{\text{probe}}}{T_{\text{eff}} w_{\text{eff}}} \int_0^\infty \frac{\mathrm{d}\omega'}{2\pi} |f_p(k', k_{\text{in}})|^2 \,, \tag{3.69}$$

with $w_{\text{eff}} = \max\{w_{\text{probe}}, w_{\text{pump}}\}$ (cf. Sect. 3.2.2), and $T_{\text{eff}} \equiv \max\{\tau_{\text{pump}}, \tau_{\text{probe}}\}$.[11]

We have mentioned before that for weak and *constant* crossed pump fields the Poynting vector $\hat{\mathbf{s}}$ constitutes an "invariant" direction such that no nonlinear effects are induced for probe photons propagating along this direction, cf. Sections 3.2.4 and B.3. This behavior carries over to inhomogeneous pump fields insofar as the scattering amplitude $f_p(k', k_{\text{in}})$, Eq. (3.67), vanishes for $\beta = \beta' = \pi/2$, and therefore an incident photon beam propagating along $\hat{\mathbf{s}} = \hat{\mathbf{e}}_{\text{y}}$ does not induce outgoing photons along this very direction. However, we also see that $f_p(k', k_{\text{in}})$ is generically nonvanishing for outgoing directions β' other than $\beta' = \pi/2$. Hence, aligning the inhomogeneous pump beam with the probe beam such that $\mathbf{k}_{\text{in}} \parallel \hat{\mathbf{s}}$ still modifies the propagation of probe photons, a property which is in remarkable contrast to the propagation in constant crossed pump fields.

Finally, let us briefly discuss the limit of stationary pump fields $\mathcal{E}(\text{x}, \text{y})$. In this limit, the scattering amplitude (3.67) will be proportional to a delta function stemming from the temporal integration, $f_p(k', k_{\text{in}}) \sim \delta(\omega' - \omega_{\text{in}})$, implementing energy conservation. Plugging the scattering amplitude into Eq. (3.69) and using one delta function to eliminate the ω' integral yields a formally diverging expression $\delta(0)$. This energy delta function can be identified with the interaction time T (which, of course, also diverges in the limit of stationary inhomogeneities), such that they cancel out in Eq. (3.69). The resulting expressions for the induced photon field, the number of merged photons and the scattering amplitude then resemble the corresponding results from Sect. 3.2.2,

[11] The introduction of the effective interaction length T_{eff} is a necessary consequence of the extension of the integration boundaries in Eq. (3.68): For $\tau_{\text{probe}} < \tau_{\text{pump}}$, the actual probe photon beam interacts with the pump field inhomogeneity only for a certain fraction $\tau_{\text{probe}}/\tau_{\text{pump}}$ of the duration of the inhomogeneity, which is expressed by the finite integration bounds $\pm T/2$ in Eq. (3.68). Simply extending these bounds to $\pm\infty$ will lead to an overestimation of the number of induced photons, because the probe beam is modeled as a plane wave of infinite duration which therefore formally interacts with the inhomogeneity over its entire duration τ_{pump}, i.e. even at times where the probe beam should have vanished due to its finite duration τ_{probe}. We can, however, account for this fact roughly by multiplication of the integral in Eq. (3.68) with a factor $\tau_{\text{probe}}/\tau_{\text{pump}} < 1$. On the other hand, no such subtleties arise for $\tau_{\text{probe}} > \tau_{\text{pump}}$ and the integration boundaries can be extended straightforwardly without the introduction of any additional factor. The effect of the expressions T, f_{int} and the potential additional factor $\tau_{\text{probe}}/\tau_{\text{pump}}$ can all be combined in Eq. (3.69) in the effective interaction length T_{eff}.

differing only by a factor $\frac{(1-\sin\beta)^2+(1-\sin\beta')^2}{2}$ as a consequence of the different field configuration considered in this section. Of course, the same result can as well be obtained by limiting to a static two-dimensional inhomogeneity from the outset as has been done in Sect. 3.2.2.

3.2.5. The strong-field limit

In the last section we have derived reflection and scattering coefficients as well as cross sections for photons undergoing quantum reflection, limited to weak pump fields $\mathcal{E}/\mathcal{E}_{\rm cr} \ll 1$. This justified to only retain the lowest nontrivial order terms of a perturbative expansion in the pump field strength. For large classes of pump field profiles we are thus able to give analytical formulae pertaining to the phenomenon of quantum reflection.

Although achievable maximum field strengths in the laboratory are well below $\mathcal{E}_{\rm cr}$, an analysis of the strong-field limit is nonetheless interesting from an academic point of view. Naively, we would already expect the strong-field limit to exhibit a different scaling in terms of the pump field strength: Photons traversing an inhomogeneous localized profile will probe both a weak-field region at the edges as well as a strong-field region around the center of the inhomogeneity. In general it will therefore not suffice to first employ the strong-field limit of the polarization tensor in a constant pump field, and then implement the inhomogeneity by means of the scheme (3.4), as this approach discards information about the weak-field behavior of the polarization tensor. Instead, we will have to deal with the full nonperturbative expression of the polarization tensor. Remarkably, for a small class of pump field profiles the procedure (3.4) to incorporate the inhomogeneity of the pump field into the nonperturbative expression of the polarization tensor can be performed explicitly. Specializing to one such pump field profile, in this section we will derive the nonperturbative polarization tensor for both crossed and purely magnetic pump field configurations. For the latter, we will perform a detailed analysis of the strong-field regime.

Crossed pump fields

We start with the nonperturbative polarization tensor for constant crossed fields, given by Eq. (3.54) with the mode coefficients $\Pi_p(k|\mathbf{E}\perp\mathbf{B})$ listed in the appendix B.3, Eq. (B.20). Substituting $s \to s/\mathcal{E}$, the coefficients can be cast into the form

$$\Pi_p(k|\mathbf{E}\perp\mathbf{B}) = \frac{\alpha}{2\pi}\int_0^\infty \frac{ds}{s}\int_{-1}^1 \frac{d\nu}{2}(1-\nu^2)\left(e^{-i\frac{s\phi_1}{\mathcal{E}}}\tilde{N}_p(k) - k^2 e^{-i\frac{sm^2}{\mathcal{E}}}\right), \tag{3.70}$$

with

$$\tilde{N}_0(k) \equiv k^2, \quad \tilde{N}_1(k) \equiv k^2 + \frac{(es)^2}{6}(3-\nu^2)\tilde{z}_k \quad \text{and} \quad \tilde{N}_2(k) \equiv k^2 + \frac{(es)^2}{12}(3+\nu^2)\tilde{z}_k\,, \tag{3.71}$$

as well as

$$\phi_1(k) = m^2 + \frac{k^2}{4}(1-\nu^2) + \frac{(es)^2}{48}\tilde{z}_k(1-\nu^2)^2 \quad \text{and} \quad \tilde{z}_k \equiv z_k/\mathcal{E}^2 = -(kF)^\mu(kF)_\mu/\mathcal{E}^2\,. \tag{3.72}$$

Following the scheme (3.4), we perform a Fourier transformation to position space, substitute $\mathcal{E} \to \mathcal{E}(x)$ and transform back to momentum space to arrive at

$$\begin{aligned}\Pi_p(k,k'|\mathbf{E}\perp\mathbf{B}) = \frac{\alpha}{2\pi}\int_0^\infty \frac{\mathrm{d}s}{s}\int_{-1}^1 \frac{\mathrm{d}\nu}{2}(1-\nu^2) \\ \times\left[\left(\int_x \mathrm{e}^{-i(k+k')x} e^{-i\frac{s\phi_1(k')}{\mathcal{E}(x)}}\tilde{N}_p(k')\right) - k'^2\left(\int_x \mathrm{e}^{-i(k+k')x} e^{-i\frac{sm^2}{\mathcal{E}(x)}}\right)\right].\end{aligned} \tag{3.73}$$

The only dependence upon the field strength profile occurs in the phase of the polarization tensor (3.70). Correspondingly, for certain classes of localized pump field profiles $\mathcal{E}(x)$ (which, of course, also have to be compatible with the existence of a global projector) the Fourier transformation can be performed analytically. Most notably, this is the case for Lorentz-like profiles, as the resulting integral will be of Gaussian type. A rather general example of such a profile is

$$\mathcal{E}(\mathrm{x},\mathrm{y},t) = \frac{\mathcal{E}}{1+\left(\frac{2\mathrm{x}}{w_\mathrm{x}}\right)^2+\left(\frac{2\mathrm{y}}{w_\mathrm{y}}\right)^2+\left(\frac{2(\mathrm{y}-t)}{\tau}\right)^2}\,, \tag{3.74}$$

with transverse width w_x, longitudinal width w_y and pulse length τ. With the exception of a harmonic variation, this profile incorporates the basic features of a localized, propagating laser pulse. However, to keep expressions as compact as possible, in this section we restrict ourselves to a stationary one-dimensional Lorentz pump field profile,

$$\mathcal{E}(\mathrm{x}) = \frac{\mathcal{E}}{1+\left(\frac{2\mathrm{x}}{w_\mathrm{x}}\right)^2}\,. \tag{3.75}$$

The polarization tensor in the presence of such an inhomogeneous pump field then reads

$$\Pi_p(k,k'|\mathbf{E}\perp\mathbf{B}) = 2\pi\delta(k_\mathrm{y}+k'_\mathrm{y})2\pi\delta(k_\mathrm{z}+k'_\mathrm{z})2\pi\delta(\omega+\omega')\Pi_p^{1\mathrm{dim}}(k_\mathrm{x},k'_\mathrm{x}|\mathbf{E}\perp\mathbf{B})\,, \tag{3.76}$$

with

$$\Pi_p^{\text{1dim}}(k_\text{x}, k'_\text{x}|\mathbf{E}\perp\mathbf{B}) = \frac{\sqrt{\pi}w_\text{x}}{2}\mathrm{e}^{-i\frac{\pi}{4}}\sqrt{\mathcal{E}}\frac{\alpha}{2\pi}\int_0^\infty\frac{\mathrm{d}s}{s}\int_{-1}^1\frac{\mathrm{d}\nu}{2}(1-\nu^2) \\ \times\left[\frac{\mathrm{e}^{-i\frac{\phi_1(k')}{\mathcal{E}}s}}{\sqrt{\phi_1(k')s}}\mathrm{e}^{i\frac{w_\text{x}^2(k_\text{x}+k'_\text{x})^2\mathcal{E}}{16\phi_1(k')s}}\tilde{N}_p(k') - k'^2\frac{\mathrm{e}^{-i\frac{m^2}{\mathcal{E}}s}}{\sqrt{m^2 s}}\mathrm{e}^{i\frac{w_\text{x}^2(k_\text{x}+k'_\text{x})^2\mathcal{E}}{16m^2 s}}\right]. \quad (3.77)$$

Recall that convergence of the propertime integral in Eq. (3.77) is ensured by the implicit prescription $s \to s(1-i0^+)$. The polarization tensor in the limit of constant pump fields can be obtained from Eq. (3.77) by $w_\text{x} \to \infty$.

We evaluate Eq. (3.77) for the asymptotic kinematics considered in Sect. 3.2.2, namely a probe beam comprised of real photons with energy ω_in propagating in the x-y plane under an angle β with respect to the x axis. This causes the contact term and the $p = 0$ contribution in Eq. (3.77) to vanish (as both are proportional to k'^2). Furthermore, on the light cone the polarization tensor is already symmetric with respect to k and k'. For the polarization tensor encoding reflection kinematics we obtain

$$\tilde{\Pi}_p^{\text{1dim}}(-\omega_\text{in}\cos\beta, -\omega_\text{in}\cos\beta|\mathbf{E}\perp\mathbf{B}) = \frac{\sqrt{\pi}w_\text{x}\omega_\text{in}^2(1-\hat{\mathbf{s}}\cdot\hat{\mathbf{e}}_\text{y}\sin\beta)^2}{24}\mathrm{e}^{-i\frac{\pi}{4}}\left(\frac{\mathcal{E}}{\mathcal{E}_\text{cr}}\right)^2 \\ \times\frac{\alpha}{2\pi}\int_0^\infty\mathrm{d}z\,z\int_{-1}^1\frac{\mathrm{d}\nu}{2}(1-\nu^2)\begin{Bmatrix}0\\2(3-\nu^2)\\(3+\nu^2)\end{Bmatrix}\frac{\mathrm{e}^{-i\phi_1 z}}{\sqrt{\phi_1 z}}\mathrm{e}^{i\frac{\kappa^2}{\phi_1 z}}, \quad (3.78)$$

where

$$\phi_1 = 1 + \frac{z^2}{48}\bar{\delta}\,(1-\nu^2)^2\,. \quad (3.79)$$

Additionally we have defined the two dimensionless parameters

$$\bar{\delta} := \left(\frac{\mathcal{E}}{\mathcal{E}_\text{cr}}\right)^2\frac{\omega_\text{in}^2}{m^2}(1-\hat{\mathbf{s}}\cdot\hat{\mathbf{e}}_\text{y}\sin\beta)^2\,, \qquad \text{and} \qquad \kappa := \frac{1}{2}\omega_\text{in}w_\text{x}\cos\beta\,. \quad (3.80)$$

The polarization tensor $\tilde{\Pi}_p^{\text{1dim}}(+\omega_\text{in}\cos\beta, -\omega_\text{in}\cos\beta|\mathbf{E}\perp\mathbf{B})$, encoding scattering in forward direction, corresponds to Eq. (3.78) evaluated for $\kappa = 0$. The analytical expression obtained here for the polarization tensor in an inhomogeneous pump field is given in terms of a double parameter integral which is of similar complexity as the corresponding expression in the limit of homogeneous pump fields, cf. Eq. (B.19).

The integral in Eq. (3.78) depends only on the two parameters $\bar{\delta}$ and κ. The parameter $\bar{\delta}$ encodes the dependence upon the pump field strength, which is in fact always

coupled to the ratio ω_{in}^2/m^2. Therefore, a weak-field expansion of the crossed-field polarization tensor inherently corresponds to an expansion in $\left(\frac{\mathcal{E}}{\mathcal{E}_{\text{cr}}}\right)^2 \left(\frac{\omega_{\text{in}}}{m}\right)^2$. This is a consequence of the fact that the polarization tensor (3.70) in constant crossed pump fields, which has been used as a starting point to derive Eq. (3.78), depends only on the two scalar invariants k^2 and z_k, of which only the latter persists in an evaluation of the polarization tensor on the light cone.[12]

The parameter κ depends on the spatial extension w_{x} of the inhomogeneity, but not on the pump field strength, and is proportional to the momentum transfer of the pump field onto the probe photons. It vanishes in the limit of grazing incidence $|\beta| \to \pi/2$. For typical parameters derived from state-of-the-art optical high-intensity lasers ($\mathcal{E}/\mathcal{E}_{\text{cr}} \lesssim 10^{-3}$, $\omega_{\text{in}}/m \simeq 10^{-5}$, $w_{\text{x}}\omega_{\text{in}} \simeq 10$), and moderate angles of incidence $|\beta| < \pi/2$, we find both $\bar{\delta} \lesssim 10^{-16} \ll 1$ and $\kappa \simeq 1$. Consequently, a perturbative expansion of the polarization tensor in the pump field strength as has been performed in the preceding sections is fully justified for the investigation of quantum reflection in laser-induced pump fields. Even employing hard X-ray probe beams ($\omega_{\text{in}}/m \simeq 10^{-1}$, $w_{\text{x}}\omega_{\text{in}} \simeq 10^5$) as generated, e.g., by a Free-Electron-Laser will yield $\bar{\delta} \simeq 10^{-8}$ and $\kappa \simeq 10^4$. The perturbative treatment of laser-induced quantum reflection only breaks down once pump field strengths approach the critical field strength *and* high-energy probe photons are employed, such that $\bar{\delta} \simeq 1$.

A Taylor expansion of the polarization tensor in the parameter $\bar{\delta} \ll 1$ reads

$$\tilde{\Pi}_p^{\text{1dim}}(-\omega_{\text{in}}\cos\beta, -\omega_{\text{in}}\cos\beta|\mathbf{E}\perp\mathbf{B}) = -\frac{\alpha w_{\text{x}} m^2}{96}\mathrm{e}^{-2|\kappa|}\sum_{n=0}^{\infty} I_{p,n}\bar{\delta}^{n+1}\,, \tag{3.81}$$

with $p \in \{1,2\}$. The lowest-order expansion coefficients are polynomials in the transferred momentum κ, and read

$$\begin{aligned}
I_{p,0} &= \frac{1}{2}\big(1+2|\kappa|\big)\left\{\begin{matrix}\frac{112}{15}\\ \frac{64}{15}\end{matrix}\right\},\\
I_{p,1} &= \frac{1}{3}\big(15+30|\kappa|+24|\kappa|^2+8|\kappa|^3\big)\left\{\begin{matrix}\frac{52}{315}\\ \frac{4}{45}\end{matrix}\right\},\\
I_{p,2} &= \frac{1}{12}\big(945+1890|\kappa|+1680|\kappa|^2+840|\kappa|^3+240|\kappa|^4+32|\kappa|^5\big)\left\{\begin{matrix}\frac{19}{1287}\\ \frac{10}{1287}\end{matrix}\right\}.
\end{aligned} \tag{3.82}$$

The reflection coefficient can now be inferred from Eq. (3.25) together with Eq. (3.78)

[12] For crossed pump fields, any additional linearly independent scalar or pseudoscalar invariant which can be constructed from combinations of $F^{\mu\nu}$, ${}^\star F^{\mu\nu} = \frac{1}{2}\varepsilon^{\mu\nu\alpha\beta}F_{\alpha\beta}$ and k^μ vanishes.

for the nonperturbative limit, or alternatively Eq. (3.81) for the perturbative limit of small field strengths. As has been previously observed quantum reflection features an exponential suppression in the transferred momentum, manifesting itself in the global factor $\mathrm{e}^{-4|\kappa|}$. This suppression prevails to all orders in the pump field strength.

Purely magnetic pump fields

Purely magnetic pump fields exhibit different dynamics. We start from the polarization tensor in a constant magnetic field (3.27), with the nonperturbative mode coefficients $\Pi_p(k|\mathbf{B})$ listed in the appendix B.2. After implementing the one-dimensional Lorentzian pump field profile (3.75) according to the preceding section, we obtain for the lower-dimensional version of the contracted polarization tensor

$$\Pi_p^{\mathrm{1dim}}(k_\mathrm{x},k'_\mathrm{x}|\mathbf{B}) = \frac{\sqrt{\pi}w_\mathrm{x}}{2}\mathrm{e}^{-i\frac{\pi}{4}}\sqrt{e\mathcal{B}}\frac{\alpha}{2\pi}\int_0^\infty\frac{dz}{z}\int_{-1}^1\frac{d\nu}{2} \times\left[\frac{z}{\sin z}\frac{\mathrm{e}^{-i\frac{\phi_0(k')}{e\mathcal{B}}z}\mathrm{e}^{i\frac{w_\mathrm{x}^2(k_\mathrm{x}+k'_\mathrm{x})^2e\mathcal{B}}{16\phi_0(k')z}}}{\sqrt{\phi_0(k')z}}\begin{Bmatrix}k^2 & N_0\\ N_0k_\perp^2+N_1k_\parallel^2\\ N_2k_\perp^2+N_0k_\parallel^2\end{Bmatrix}-k'^2(1-\nu^2)\frac{\mathrm{e}^{-i\frac{\mathcal{B}_\mathrm{cr}}{\mathcal{B}}z}\mathrm{e}^{i\frac{w_\mathrm{x}^2(k_\mathrm{x}+k'_\mathrm{x})^2}{16z}\frac{\mathcal{B}}{\mathcal{B}_\mathrm{cr}}}}{\sqrt{m^2z}}\right]. \tag{3.83}$$

Here, $p\in\{0,\parallel,\perp\}$, and the coefficients N_0, N_1 and N_2 are given by (B.12). Again, the parameter κ denotes the momentum transfer and has been defined in Eq. (3.80). Implementing the kinematics for the reflection process from Sect. 3.2.2, the contact term and Π_0^{1dim} vanish. Furthermore, on the light cone the relation $k_\perp^2 = -k_\parallel^2 = \omega^2\sin^2\sphericalangle(\mathbf{k},\mathbf{B})$ holds, such that we find

$$\tilde{\Pi}_p^{\mathrm{1dim}}(-\omega_\mathrm{in}\cos\beta,-\omega_\mathrm{in}\cos\beta|\mathbf{B}) = \frac{\sqrt{\pi}\omega_\mathrm{in}^2w_\mathrm{x}\sin^2\sphericalangle(\mathbf{k},\mathbf{B})}{2}\mathrm{e}^{-i\frac{\pi}{4}}\sqrt{\frac{\mathcal{B}}{\mathcal{B}_\mathrm{cr}}} \times\frac{\alpha}{2\pi}\int_0^\infty\frac{dz}{z}\int_{-1}^1\frac{d\nu}{2}\frac{\mathrm{e}^{-i\tilde{\phi}_0z\frac{\mathcal{B}_\mathrm{cr}}{\mathcal{B}}}}{\sqrt{\tilde{\phi}_0z}}\mathrm{e}^{i\frac{\kappa^2}{\tilde{\phi}_0z}\frac{\mathcal{B}}{\mathcal{B}_\mathrm{cr}}}\tilde{N}_p(\nu,z)\,, \tag{3.84}$$

with

$$\begin{aligned}\tilde{N}_\parallel(\nu,z) &\equiv \frac{z\cos\nu z}{\sin z}-z\cot z\left(1-\nu^2+\nu\frac{\sin\nu z}{\sin z}\right),\\ \tilde{N}_\perp(\nu,z) &\equiv 2z\frac{\cos\nu z-\cos z}{\sin^3 z}-\frac{z\cos\nu z}{\sin z}+\frac{\nu z\sin\nu z\cos z}{\sin^2 z}\,,\end{aligned} \tag{3.85}$$

as well as

$$\tilde{\phi}_0(\nu, z) \equiv 1 + \tilde{\delta}\left[\frac{1}{2}\frac{\cos\nu z - \cos z}{z\sin z} - \frac{1-\nu^2}{4}\right], \qquad \text{and} \qquad \tilde{\delta} \equiv \sin^2\sphericalangle(\mathbf{k},\mathbf{B})\frac{\omega_{\text{in}}^2}{m^2}. \tag{3.86}$$

Again, by setting $\kappa = 0$ we recover the polarization tensor encoding forward scattering, $\tilde{\Pi}_p^{1\text{dim}}(+\omega_{\text{in}}\cos\beta, -\omega_{\text{in}}\cos\beta|\mathbf{B})$. In analogy to the crossed field case we have introduced $\tilde{\delta}$ as a measure of the momentum scale governing the probe beam (cf. the parameter $\bar{\delta}$ in Eq. (3.80)). However, for purely magnetic pump fields the momentum scale is not inherently coupled to the field strength ratio $\mathcal{B}/\mathcal{B}_{\text{cr}}$. Consequently, quantum reflection for purely magnetic pump fields is governed by three parameters $\kappa, \tilde{\delta}$ and $\mathcal{B}/\mathcal{B}_{\text{cr}}$, in contrast to the two parameters κ and δ for crossed pump fields. For probe beams in the optical regime the parameter $\tilde{\delta} \simeq 10^{-10}$, while it can approach values of $\tilde{\delta} \simeq 1$ and higher for beams in the hard X-ray and Gamma regime.

An expansion of the polarization tensor (3.84) in powers of the pump field strength ratio $\mathcal{B}/\mathcal{B}_{\text{cr}}$ reads[13]

$$\tilde{\Pi}_p^{1\text{dim}}(-\omega_{\text{in}}\cos\beta, -\omega_{\text{in}}\cos\beta|\mathbf{B}) = -\frac{\alpha\omega_{\text{in}}^2 w_{\text{x}}\sin^2\sphericalangle(\mathbf{k},\mathbf{B})}{8}\mathrm{e}^{-2|\kappa|}\sum_{n=0}^{\infty} I_{p,n}\left(\frac{\mathcal{B}}{\mathcal{B}_{\text{cr}}}\right)^{2n+2}, \tag{3.87}$$

where the lowest-order expansion coefficients are given by

$$\begin{aligned}
I_{p,0} &= \frac{1}{45}(1+2|\kappa|)\begin{Bmatrix}14\\8\end{Bmatrix},\\
I_{p,1} &= \frac{1}{5670}(15+30|\kappa|+24|\kappa|^2+8|\kappa|^3)\begin{Bmatrix}-39+26\,\tilde{\delta}\\-72+14\,\tilde{\delta}\end{Bmatrix},\\
I_{p,2} &= \frac{1}{32432400}(945+1890|\kappa|+1680|\kappa|^2+840|\kappa|^3+240|\kappa|^4+32|\kappa|^5)\\
&\quad\times\begin{Bmatrix}6292-10166\,\tilde{\delta}+3325\,\tilde{\delta}^2\\20592-12090\,\tilde{\delta}+1750\,\tilde{\delta}^2\end{Bmatrix}.
\end{aligned} \tag{3.88}$$

As in the crossed-field case, reflection kinematics feature a global suppression in the transferred momentum $|\kappa|$. Furthermore, the maximum power of $\tilde{\delta}$ in a given expansion coefficient $I_{p,n}$ is $\tilde{\delta}^n$, which is a consequence of the evaluation of the polarization tensor on the light cone (for more information cf. the appendix F.2). The reflection coefficient,

[13] As has been the case in Sect. 3.2.2 with the weak-field expansion (3.29) of the polarization tensor in a constant magnetic field, the particular expansion employed here requires moderate probe photon energies $(\mathcal{B}/\mathcal{B}_{\text{cr}})\tilde{\delta} \ll 1$. As a consequence, the expansion coefficients $I_{p,n}$ are entirely real (cf. also the appendix B.2).

Eq. (3.25), which can be obtained from the expression (3.87), agrees with the result from Ref. [43] to the lowest order in the field strength. Furthermore, in the limit $w_\mathrm{x} \to \infty$ we obtain the well-known weak-field expansion of the polarization tensor in a constant magnetic pump field, cf. Ref. [28].

The nonperturbative expression (3.84) allows insights into a wider range of parameter regimes. To this end we follow the strategy employed in Refs. [77,78], and perform a rotation of the integration contour onto the negative imaginary axis, $z \to -is$, which is permissible for $\tilde{\delta} < 4$. Due to the implicit integration prescription $z \to z(1 - i0^+)$, this procedure is not inhibited by the poles of the integrand at $z = n\pi$.[14] Consequentially, the polarization tensor can be cast into

$$\tilde{\Pi}_p^{\mathrm{1dim}}(-\omega_\mathrm{in}\cos\beta, -\omega_\mathrm{in}\cos\beta|\mathbf{B}) = \frac{\alpha\omega_\mathrm{in}^2 w_\mathrm{x}\sin^2\sphericalangle(\mathbf{k},\mathbf{B})}{8\sqrt{\pi}}\sqrt{\frac{\mathcal{B}}{\mathcal{B}_\mathrm{cr}}} \times \int_0^\infty \frac{\mathrm{d}s}{s}\int_{-1}^1 \mathrm{d}\nu \frac{\mathrm{e}^{-\tilde{\phi}_0 s\frac{\mathcal{B}_\mathrm{cr}}{\mathcal{B}}}}{\sqrt{\tilde{\phi}_0 s}} \mathrm{e}^{-\frac{\kappa^2}{\tilde{\phi}_0 s}\frac{\mathcal{B}}{\mathcal{B}_\mathrm{cr}}} \tilde{N}_p(\nu,s)\,, \tag{3.89}$$

with

$$\begin{aligned}
\tilde{N}_\parallel(\nu,s) &\to \frac{s\cosh\nu s}{\sinh s} - s\coth s\left(1-\nu^2+\nu\frac{\sinh\nu s}{\sinh s}\right),\\
\tilde{N}_\perp(\nu,s) &\to -2s\frac{\cosh\nu s-\cosh s}{\sinh^3 s} - \frac{s\cosh\nu s}{\sinh s} + \frac{\nu s\sinh\nu s\cosh s}{\sinh^2 s},\\
\tilde{\phi}_0(\nu,s) &\to 1-\tilde{\delta}\left[\frac{1}{2}\frac{\cosh\nu s-\cosh s}{s\sinh s}+\frac{1-\nu^2}{4}\right].
\end{aligned} \tag{3.90}$$

Expression (3.89) facilitates a straightforward numerical evaluation, as the integrand is real (for $\tilde{\delta} < 4$) and well-behaved. It is valid for both weak ($\mathcal{B} \ll \mathcal{B}_\mathrm{cr}$) and strong ($\mathcal{B} \gg \mathcal{B}_\mathrm{cr}$) pump fields, but restricted to photon energies $\omega_\mathrm{in} < 2m$.

The analytical analysis can be driven further for low-energy probe photons obeying $\tilde{\delta} \ll 1$, as we may then approximate $\tilde{\phi}_0 \to 1$ in the integrand of Eq. (3.89). The only ν dependence is then found in the coefficient functions $N_p(\nu,s)$, which become

$$\begin{aligned}
\tilde{N}_\parallel(s) &\equiv \int_{-1}^1 \mathrm{d}\nu\,\tilde{N}_\parallel(\nu,s) = 2\left[1+\left(\frac{1}{s}-\frac{2s}{3}\right)\coth s-\coth^2 s\right],\\
\tilde{N}_\perp(s) &\equiv \int_{-1}^1 \mathrm{d}\nu\,\tilde{N}_\perp(\nu,s) = -2\left[\frac{\coth s}{s}+\frac{1-2s\coth s}{\sinh^2 s}\right].
\end{aligned} \tag{3.91}$$

[14] Larger values than $\tilde{\delta} = 4$ signal the onset of electron-positron pair production, as indicated by the poles on the real axes.

Remarkably, as forward scattering implies $\kappa = 0$ it permits an explicit analytical evaluation of the remaining s integration. Note, however, that integrating over individual sum terms of Eq. (3.91) leads to divergent expressions, necessitating the introduction of a convergence enforcing exponent $\epsilon > 0$; the calculations resemble those detailed in Ref. [28] for the polarization tensor in constant magnetic fields. Employing partial integrations, all s integrals can finally be expressed in terms of the tabulated integral $\int_0^\infty \frac{\mathrm{d}s}{s} s^\mu \mathrm{e}^{-\beta s} \coth(s) = \left[2^{1-\mu}\zeta\left(\mu, \frac{\beta}{2}\right) - \beta^{-\mu}\right]\Gamma(\mu)$, cf. Formula 3.551.3 of Ref. [102]. Employing the abbreviation $\mathfrak{h} \equiv \mathcal{B}/\mathcal{B}_{\mathrm{cr}}$ for the magnetic field strength ratio, we obtain the following expression for the polarization tensor encoding forward scattering in the Lorentzian pump field profile (3.75) in the limit of low energies $\omega_{\mathrm{in}} \ll 1$:

$$\tilde{\Pi}_p^{1\mathrm{dim}}(+\omega_{\mathrm{in}}\cos\beta, -\omega_{\mathrm{in}}\cos\beta|\mathbf{B}) = \frac{\alpha\omega_{\mathrm{in}}^2 w_{\mathrm{x}} \sin^2\sphericalangle(\mathbf{k},\mathbf{B})}{8\sqrt{\pi}} I_p(\mathfrak{h})\,, \tag{3.92}$$

with

$$\begin{aligned} I_\parallel(\mathfrak{h}) = \sqrt{\mathfrak{h}}\frac{2}{3}\sqrt{2\pi}\Bigg[&20\zeta\left(-\frac{3}{2},\frac{1}{2\mathfrak{h}}\right) + 20\zeta\left(-\frac{3}{2},\frac{1+2\mathfrak{h}}{2\mathfrak{h}}\right) - \frac{6}{\mathfrak{h}}\zeta\left(-\frac{1}{2},\frac{1}{2\mathfrak{h}}\right) \\ &- \frac{6}{\mathfrak{h}}\zeta\left(-\frac{1}{2},\frac{1+2\mathfrak{h}}{2\mathfrak{h}}\right) - \zeta\left(\frac{1}{2},\frac{1}{2\mathfrak{h}}\right) - \zeta\left(\frac{1}{2},\frac{1+2\mathfrak{h}}{2\mathfrak{h}}\right)\Bigg], \\ I_\perp(\mathfrak{h}) = \sqrt{\mathfrak{h}}\frac{1}{3}\sqrt{2\pi}\Bigg[&20\zeta\left(-\frac{3}{2},\frac{1}{2\mathfrak{h}}\right) + 20\zeta\left(-\frac{3}{2},\frac{1+2\mathfrak{h}}{2\mathfrak{h}}\right) - \frac{24}{\mathfrak{h}}\zeta\left(-\frac{1}{2},\frac{1}{2\mathfrak{h}}\right) \\ &- \frac{24}{\mathfrak{h}}\zeta\left(-\frac{1}{2},\frac{1+2\mathfrak{h}}{2\mathfrak{h}}\right) + \frac{3}{\mathfrak{h}^2}\zeta\left(\frac{1}{2},\frac{1}{2\mathfrak{h}}\right) + \frac{3}{\mathfrak{h}^2}\zeta\left(\frac{1}{2},\frac{1+2\mathfrak{h}}{2\mathfrak{h}}\right)\Bigg]. \end{aligned} \tag{3.93}$$

This representation employs the Hurwitz zeta function $\zeta(s,\chi)$, which is a generalization of the Riemann zeta function $\zeta(\chi) \equiv \zeta(1,\chi)$ (see, e.g., Ref. [102]). We can expand the result for small field strengths,

$$\begin{aligned} I_\parallel(\mathfrak{h}) &= -\frac{14}{45}\sqrt{\pi}\,\mathfrak{h}^2 + \frac{13}{126}\sqrt{\pi}\,\mathfrak{h}^4 - \frac{11}{60}\sqrt{\pi}\,\mathfrak{h}^6 + \mathcal{O}\left(\mathfrak{h}^8\right), \\ I_\perp(\mathfrak{h}) &= -\frac{8}{45}\sqrt{\pi}\,\mathfrak{h}^2 + \frac{4}{21}\sqrt{\pi}\,\mathfrak{h}^4 - \frac{3}{5}\sqrt{\pi}\,\mathfrak{h}^6 + \mathcal{O}\left(\mathfrak{h}^8\right), \end{aligned} \tag{3.94}$$

thereby recovering the weak-field expansion of the polarization tensor (3.87) for $\kappa = \tilde{\delta} = 0$.

Additionally, Eq. (3.92) gives us access to the strong-field limit of the polarization

tensor in a Lorentz pump field profile. Expanding Eq. (3.93) in terms of $1/\mathfrak{h}$ yields

$$\begin{aligned} I_\parallel(\mathfrak{h}) &= -\frac{4}{3}\sqrt{\pi}\,\mathfrak{h} + \frac{4}{3}\sqrt{2\pi}\left[20\zeta\left(-\frac{3}{2}\right) - \zeta\left(\frac{1}{2}\right)\right]\sqrt{\mathfrak{h}} + \mathcal{O}\left(\mathfrak{h}^{-\frac{1}{2}}\right), \\ I_\perp(\mathfrak{h}) &= \frac{40}{3}\sqrt{2\pi}\zeta\left(-\frac{3}{2}\right)\sqrt{\mathfrak{h}} + \mathcal{O}\left(\mathfrak{h}^{-\frac{1}{2}}\right). \end{aligned} \tag{3.95}$$

For large magnetic fields the parallel mode increases linearly with the field strength ratio $\mathfrak{h}$, while the perpendicular mode goes with the square root of $\mathfrak{h}$.

Turning to reflection dynamics ($\kappa \neq 0$), we can extract the strong-field limit for $\tilde{\delta} \ll 1$ starting from the coefficients (3.91). We substitute $s \to \mathfrak{h}s$, and employ the asymptotic expressions $\tilde{N}_\parallel(s) \sim 2/\mathfrak{h}s - 4\mathfrak{h}s/3$ and $\tilde{N}_\perp(s) \sim -2/\mathfrak{h}s$, valid for $s > 0$ and $\mathfrak{h} \to \infty$. The assumption is that for $\kappa^2 > 0$ the exponential term $\exp[-\kappa^2/s]$ in the integral will sufficiently dampen the divergent contributions for small s. Hence, this assumption is increasingly well justified for large κ^2, while the limit $\kappa^2 \to 0$ has to be handled with care. Performing the s integration results in the polarization tensor

$$\tilde{\Pi}_p^{\text{1dim}}(-\omega_{\text{in}}\cos\beta, -\omega_{\text{in}}\cos\beta|\mathbf{B}) = \frac{\alpha\omega_{\text{in}}^2 w_{\text{x}}\sin^2\sphericalangle(\mathbf{k},\mathbf{B})}{8\sqrt{\pi}} I_p(\mathfrak{h},\kappa), \tag{3.96}$$

with

$$\begin{aligned} I_\parallel(\mathfrak{h},\kappa) &= -\sqrt{\pi}\frac{4}{3}\mathrm{e}^{-2|\kappa|}\,\mathfrak{h} + \mathcal{O}\left(\frac{1}{\mathfrak{h}}\right), \\ I_\perp(\mathfrak{h},\kappa) &= -\sqrt{\pi}\frac{1+2|\kappa|}{|\kappa|^3}\mathrm{e}^{-2|\kappa|}\,\frac{1}{\mathfrak{h}}. \end{aligned} \tag{3.97}$$

Equation (3.97) confirms our previous statement that the exponential suppression in the transferred momentum $|\kappa|$ also prevails in the limit of strong pump fields. As has been already observed for forward scattering, the parallel mode grows linearly with $\mathfrak{h}$. Setting $|\kappa| \to 0$ even retrieves the result (3.95) to the lowest order in $1/\mathfrak{h}$. By contrast, the polarization tensor (3.96) for the perpendicular mode cannot be continuously related to the result (3.95) in the limit $|\kappa| \to 0$. To leading order it scales as $1/\mathfrak{h}$, differing markedly from forward scattering dynamics ($\sim\sqrt{\mathfrak{h}}$).

The constant-field limit for the parallel mode can be obtained by sending $w_{\text{x}} \to \infty$, and it coincides with the corresponding expression in Ref. [28] to leading order in $\mathfrak{h}$.[15] In fact, for the parallel mode we could have obtained the leading-order behavior (3.97) by simply taking the leading-order term of the strong-field expansion of the polarization

[15] Cf. also appendix F, where the strong-field limit for constant fields in the low-energy regime has been obtained starting from the Heisenberg-Euler effective action (F.7).

tensor in a constant magnetic field (e.g. from Ref. [28]), and then implementing the inhomogeneity by means of the procedure (3.4). By contrast, for the perpendicular mode the strong-field limits (3.95) and (3.97) differ greatly from the leading-order behavior for constant fields. In fact, for this mode the leading-order term of the polarization tensor in constant fields is independent of $\mathfrak{h}$, cf. Ref. [28]. Therefore, it cannot be employed to implement the inhomogeneous pump field via the scheme (3.4). This confirms that in order to obtain the correct leading-order strong-field behavior it is essential to first implement the inhomogeneity profile into the nonperturbative polarization tensor before performing the strong-field limit, as has been remarked at the beginning of this section.[16]

Figure 3.8 shows plots of the nonperturbative reflection coefficients R_p, obtained from Eq. (3.25) together with Eq. (3.89), as well as the coefficients $T_p \equiv R_p(\kappa = 0)$ for forward scattering, as a function of the field strength ratio $\mathcal{B}/\mathcal{B}_{\mathrm{cr}}$. For the $\parallel$-setting the magnetic field is chosen to point along $\hat{\mathbf{e}}_{\mathrm{z}}$, yielding $\sin^2 \sphericalangle(\mathbf{k}, \mathbf{B}) \to 1$. For the $\perp$-setting we choose $\hat{\mathbf{e}}_B = \hat{\mathbf{e}}_{\mathrm{x}}$, implying $\sin^2 \sphericalangle(\mathbf{k}, \mathbf{B}) \to \sin^2 \beta$. The remaining parameters are fixed according to $\beta = \pi/4$, $\omega_{\mathrm{in}} = 1\mathrm{eV}$ and $\omega_{\mathrm{in}} w_{\mathrm{x}} = 1$. Note that for both the parallel and perpendicular configuration forward scattering always dominates over reflection, as the latter features an exponential suppression in κ. For weak pump field strengths, both the reflection and forward scattering coefficients increase according to $\sim (\mathcal{B}/\mathcal{B}_{\mathrm{cr}})^4$, cf. the weak-field expansion (3.87). In contrast to that, for large field strengths we observe the strong-field behavior examined above, cf. Eqs. (3.95) and (3.97). The transition region between these two regimes is displayed in the inset. For our choice of parameters the reflection coefficient for the perpendicular mode reaches a maximum $R_{\perp,\mathrm{max}} \approx 2.8 \cdot 10^{-8}$ at $\mathcal{B} \approx 13.7\,\mathcal{B}_{\mathrm{cr}}$, while the remaining scattering coefficients are unbounded.

At first sight it appears counterintuitive that increasing the field strength ratio $\mathfrak{h}$ eventually leads to decreasing reflection for the perpendicular mode. However, recall that reflection is a process which depends on the sensitivity of the probe beam to *variations* in the field strength profile. For constant fields and in the strong-field limit $\mathfrak{h} \to \infty$ (see above) the dynamics of the perpendicular mode actually become independent of the field strength [28,78], suggesting that in this limit spatial variations of the field strength should have no effect on the probe photons and therefore no

[16] This also becomes apparent by the fact that for $w_{\mathrm{x}} \to \infty$ only the *leading-order* term for the $\parallel$-mode (3.97) agrees with the strong-field expansion of the polarization tensor in constant fields [28]. Note furthermore that in contrast to the strong-field limit, the weak-field behavior does not induce any subtleties for either mode, as a weak-field expansion of the constant-field polarization tensor still retains complete information about the relevant field strength regime.

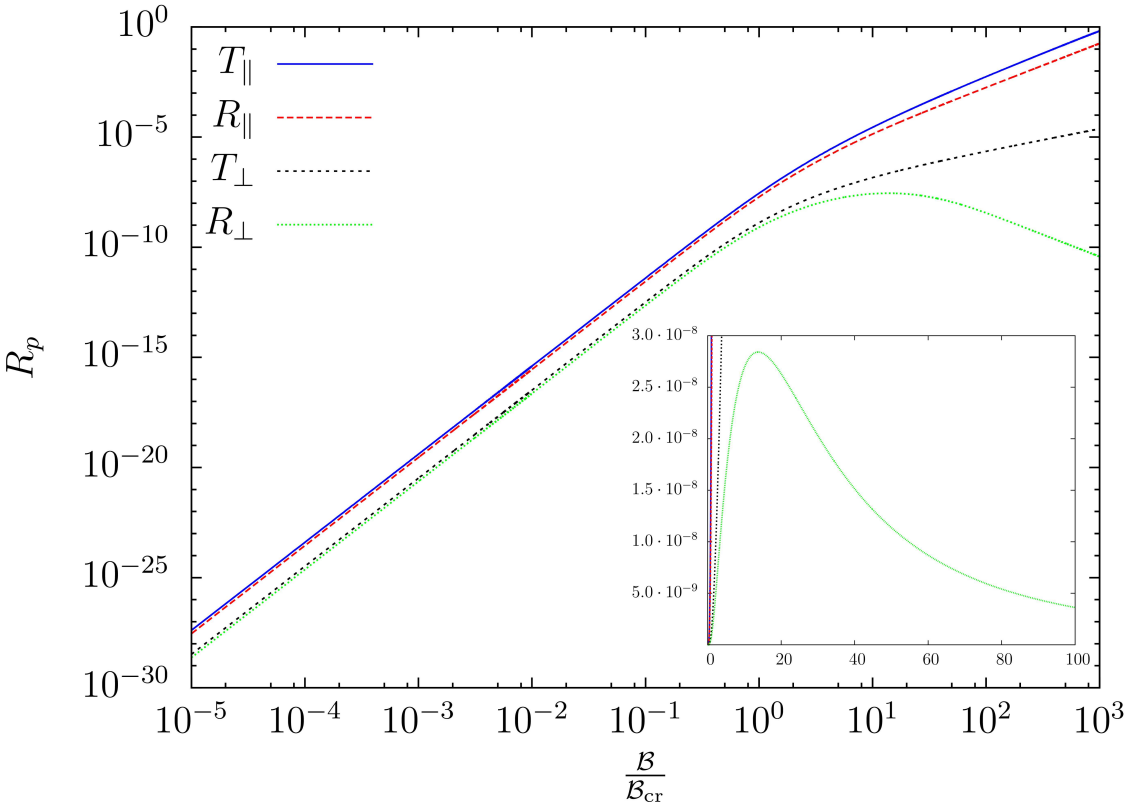

Figure 3.8.: Double logarithmic plot of the nonperturbative scattering coefficients R_p (reflection) and T_p (forward scattering) as a function of the field strength ratio $\mathcal{B}/\mathcal{B}_{\rm cr}$, for a purely magnetic pump field profile $\mathcal{B}(\mathrm{x}) = \mathcal{B}/[1 + (2\mathrm{x}/w_{\mathrm{x}})^2]$. The direction of the magnetic field vector for the parallel (perpendicular) setting was set to $\hat{\mathbf{e}}_B = \hat{\mathbf{e}}_{\mathrm{z}}$ ($\hat{\mathbf{e}}_B = \hat{\mathbf{e}}_{\mathrm{x}}$). The remaining parameters were chosen as $\omega_{\rm in} = 1\mathrm{eV}$ and $w_{\mathrm{x}} = 1\mathrm{eV}^{-1}$. The inlet shows a linear plot of the transition region from weak to strong-field dynamics. Most notably, the reflection coefficient for the perpendicular setting in the limit of strong fields decreases like $\sim (\mathcal{B}_{\rm cr}/\mathcal{B})^2$.

reflected contributions are induced.[17]

Figure 3.9 shows the reflection coefficient as a function of the incoming angle β, for varying values of the pump field strength. Both for the parallel and perpendicular mode the reflection coefficient increases monotonically for growing β until it diverges at $\beta \to \pi/2$. However, for $\beta \to 0°$ the reflection coefficient for the parallel mode approaches a finite value, while it goes to zero for the perpendicular mode, which is a

[17] It should be noted that for finite peak field strength $\mathcal{B} \gg \mathcal{B}_{\rm cr}$ and a localized inhomogeneity as considered in this section, there always exists a region at the edge of the inhomogeneity where $\mathcal{B}(\mathrm{x}) \lesssim \mathcal{B}_{\rm cr}$, and where in principle reflection might still be induced. However, the specific inhomogeneity profile considered in this section is a Lorentz curve, whose slope in the relevant region at the edges defined by $\mathcal{B}(\mathrm{x}) \lesssim \mathcal{B}_{\rm cr}$ flattens out as the peak field strength is increased. Hence, the field strength profile in this region becomes more and more homogeneous in the limit $\mathcal{B} \to \infty$, and eventually does not induce any reflected contributions either.

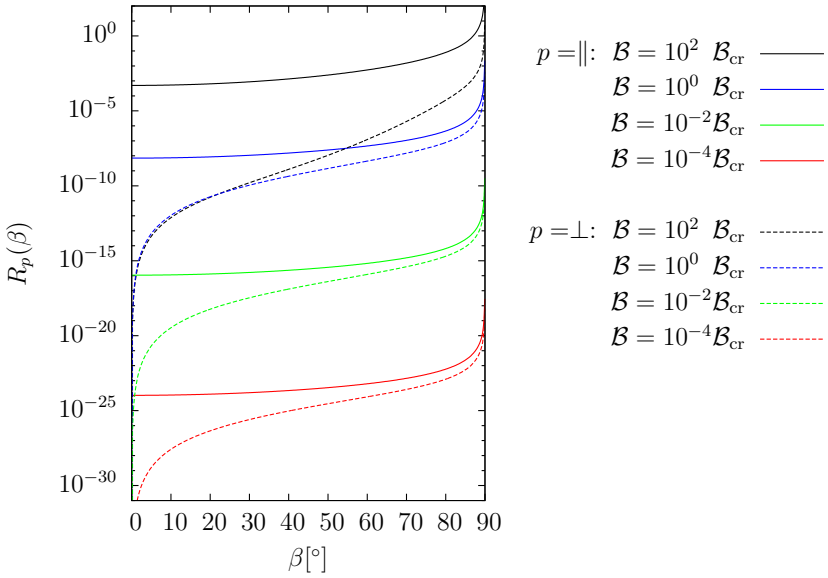

Figure 3.9.: Plot of the nonperturbative coefficient $R_p(\beta)$ as a function of the incoming angle β, for a purely magnetic pump field profile $\mathcal{B}(\mathrm{x}) = \mathcal{B}/[1 + (2\mathrm{x}/w_{\mathrm{x}})^2]$. The solid (dashed) lines show the parallel (perpendicular) setting, with the choice $\hat{\mathbf{e}}_B = \hat{\mathbf{e}}_{\mathrm{z}}$ ($\hat{\mathbf{e}}_B = \hat{\mathbf{e}}_{\mathrm{x}}$). The remaining parameters were chosen as $\omega_{\mathrm{in}} = 1\mathrm{eV}$ and $w_{\mathrm{x}} = 1\mathrm{eV}^{-1}$.

consequence of the different directions of the magnetic field vector $\hat{\mathbf{e}}_B$ chosen for the parallel and the perpendicular configuration.

Validity of the Born approximation

The derivation of the reflection coefficients assumes that the induced photon signal is small compared to the incoming photon beam, cf. Eq. (3.16). This is the case if the condition

$$\left| \int \frac{\mathrm{d}^3 k}{(2\pi)^3}\, \mathrm{e}^{ik_+ x}\, \frac{\tilde{\Pi}_p(k_+, -k_{\mathrm{in}}|A)}{2\sqrt{\mathbf{k}^2}} \right| \ll 1 \tag{3.98}$$

holds for all values of x.

Naturally, we expect the Born approximation to break down for increasing field strengths and/or interaction lengths L_{int}. To this end we evaluate Eq. (3.98) for the one-dimensional purely magnetic Lorentz profile (3.75) employed in this section. For illustration we choose $p = \parallel$ and set $\sin^2 \sphericalangle(\mathbf{k}, \mathbf{B}) = 1$, and concentrate on the forward scattered contribution to the induced photon signal. The interaction length can be estimated as $L_{\mathrm{int}} = w_{\mathrm{x}}/|\cos\beta|$. Condition (3.98) in the limit of weak pump fields

$\mathcal{B}/\mathcal{B}_{\rm cr} \ll 1$ then reads

$$\left| \frac{\alpha}{45} \omega_{\rm in} L_{\rm int} \left(\frac{\mathcal{B}}{\mathcal{B}_{\rm cr}} \right)^2 \right| \ll 1 \,. \tag{3.99}$$

This condition is fulfilled for practically all set-ups involving focussed state-of-the-art optical and X-ray high-intensity lasers, as the maximum pump field strength is weak compared to the critical field strength. For strong pump fields, the condition (3.98) becomes

$$\left| \frac{\alpha}{12} \omega_{\rm in} L_{\rm int} \frac{\mathcal{B}}{\mathcal{B}_{\rm cr}} \right| \ll 1 \,. \tag{3.100}$$

For the parameters employed in Figure 3.8, we find that the analysis is valid for pump field strengths $\mathcal{B} \lesssim 10^2 \mathcal{B}_{\rm cr}$. Going beyond these field strengths requires the departure from the Born approximation by consistently taking into account terms which are of higher-order in the fine-structure constant α, i.e. both in the polarization tensor and the von Neumann-series (3.14).

3.2.6. Towards experimental estimates

In this section we aim to quantitatively discuss the results from Sect. 3.2.4. To this end we consider an experimental pump-probe type scenario consisting of two high-intensity lasers. The electromagnetic field inhomogeneity is generated in the focal spot of the *pump* laser, which is then being probed by a second *probe* laser. The scenario resembles the one displayed in Fig. 3.7, where the probe laser intersects the pump beam at its waist under an angle β. The aim is to measure the induced photons by a suitably placed detector in the background-free field region, requiring a clear geometric signal-to-background separation.

The inhomogeneity profile of a focussed electromagnetic field pulse as generated by a high-intensity laser is usually well approximated as a Gaussian beam. A freely propagating Gaussian beam is characterized by crossed fields with plane-wave like longitudinal modulations. Therefore, the derivations of Sect. 3.2.4, in particular Eq. (3.69), are of most relevance with regard to an actual experimental realization. Furthermore, a linearly polarized laser beam features magnetic and electric fields of fixed orientation $\hat{\mathbf{e}}_E$ and $\hat{\mathbf{e}}_B$. To generate inhomogeneities with only a magnetic field component requires additional experimental efforts, such as the superposition of two counterpropagating lasers mutually canceling their electric field components at the beam waist.

In the upcoming discussion, we will consider pump fields with an inhomogeneity

profile

$$\mathcal{E}(\mathrm{x},\mathrm{y},t) = \mathcal{E}\, e^{-\left(\frac{2\mathrm{x}}{w_\mathrm{x}}\right)^2} e^{-\left(\frac{2\mathrm{y}}{w_\mathrm{y}}\right)^2} e^{-\left(\frac{2(\mathrm{y}-t)}{\tau}\right)^2} \cos\big(\Omega(\mathrm{y}-t)\big)\,, \tag{3.101}$$

with peak field strength $\mathcal{E}$, resembling the main features of a laser pulse propagating in the x-y plane, but not accounting for any explicit z dependence. Equation (3.101) mimics a laser pulse of frequency Ω and pulse duration τ, which propagates in y direction and is focussed around $\mathrm{y} = 0$. The transversal profile is a Gaussian curve with 1/e-width w_x, resembling the transversal profile of a Gaussian laser beam. Moreover, $w_\mathrm{y}/2$ mimics the Rayleigh length, which is a measure of the focus extent in longitudinal direction. The longitudinal profile of a Gaussian beam is the square root of a Lorentzian ($\propto 1/\sqrt{1+(2\mathrm{y}/w_\mathrm{y})^2}$) rather than a Gaussian, as has been chosen here. Our substitution, however, allows for a simple analytic evaluation of the integral (3.67), while retaining the basic properties induced by the longitudinal envelope. Note furthermore, that the field profile (3.101) neglects diffraction spreading about its beam waist. We expect this to be a viable approximation as the considered effects only become sizable within the Rayleigh length z_R of the pump laser, which in the diffraction limit is given by $z_R = \pi\lambda_\mathrm{pump}$ [103].

The differential number of induced photons $\mathrm{d}\mathcal{N}^\mathrm{ind}$ with energy $[\omega', \omega' + \mathrm{d}\omega']$ to be detected in the polar angle interval $[\beta', \beta' + \mathrm{d}\beta']$, which can be inferred from the profile (3.101), reads

$$\begin{aligned}\mathrm{d}^2\mathcal{N}_p^\mathrm{ind}(\beta',\omega') = &\left(\frac{e\mathcal{E}}{m^2}\right)^4 \frac{\mathcal{N}_\mathrm{probe}}{T_\mathrm{eff} w_\mathrm{eff}} \frac{c_p^2\alpha^2 w_\mathrm{x}^2 w_\mathrm{y}^2 \tau^2}{2\pi\cdot 23040^2\omega'}\,\mathrm{d}\omega'\,\mathrm{d}\beta' \\ \times &\left(\omega_\mathrm{in}^2(1-\sin\beta)^2 + \omega'^2(1-\sin\beta')^2\right)^2 \mathrm{e}^{-\frac{w_\mathrm{x}^2}{16}(\omega'\cos\beta' - \omega_\mathrm{in}\cos\beta)^2} \mathrm{e}^{-\frac{w_\mathrm{y}^2}{16}[\omega_\mathrm{in}(1-\sin\beta)-\omega'(1-\sin\beta')]^2} \\ &\times \left[2\mathrm{e}^{-\frac{\tau^2}{32}(\omega'-\omega_\mathrm{in})^2} + \mathrm{e}^{-\frac{\tau^2}{32}(\omega'-\omega_\mathrm{in}-2\Omega)^2} + \mathrm{e}^{-\frac{\tau^2}{32}(\omega'-\omega_\mathrm{in}+2\Omega)^2}\right]^2, \end{aligned} \tag{3.102}$$

with $p \in \{1,2\}$, $n \in \{0, \pm 1\}$, $c_1 = 7$ and $c_2 = 4$.

Additionally, we will consider the pump field profile (3.101) in the limit of infinite pulse duration $\tau \to \infty$ and Rayleigh length $w_\mathrm{y}/2 \to \infty$, corresponding exactly to the scenario shown in Fig. 3.7. Neglecting the finite pulse length and longitudinal focussing is only a good approximation for pump beams with sufficiently long pulse durations and large Rayleigh lengths. The advantage of such a profile is, however, that

the resulting scattering coefficients (3.60) are given analytically, reading

$$R_{p,2n}^{(\pm)} = \Theta\big(\tfrac{1+\sin\beta}{2} - \tfrac{2n\Omega}{\omega_{\rm in}}\big)\,(1+\delta_{n0})^2\,\left(\frac{e\mathcal{E}}{m^2}\right)^4\,\frac{\alpha^2 c_p^2 \omega_{\rm in}^2 w_{\rm x}^2}{2\pi\cdot 720^2} \\ \times \frac{(1-\sin\beta)^4}{(1-\frac{2n\Omega}{\omega_{\rm in}})^2-(\sin\beta-\frac{2n\Omega}{\omega_{\rm in}})^2}\mathrm{e}^{-\frac{w_{\rm x}^2}{16}\omega_{\rm in}^2\left(\cos\beta\mp\sqrt{(1-\frac{2n\Omega}{\omega_{\rm in}})^2-(\sin\beta-\frac{2n\Omega}{\omega_{\rm in}})^2}\right)^2} + \mathcal{O}\left(\left(\tfrac{e\mathcal{E}}{m^2}\right)^6\right)\,, \tag{3.103}$$

with $n \in \{0, \pm 1\}$.

To attain a large number of signal photons requires large peak field strengths $\mathcal{E}$. We therefore assume the probe and the inhomogeneous pump fields to be generated by high-intensity laser beams focussed down to the diffraction limit, with the transversal extensions then given by twice their respective laser wavelengths λ multiplied with the so-called f-number. The latter is defined as the ratio of the focal length and the diameter of the focussing aperture. Experimentally, f-numbers as small as $f^{\#} = 1$ can be realized [103].[18] Hence we choose $w_{\rm x} = 2\lambda_{\rm pump}$ and $w_{\rm eff} = \max\{2\lambda_{\rm probe}, 2\lambda_{\rm pump}\}$. Likewise, the interaction time between pump and probe laser (modeled as a plane wave) is given by $T = \min\{\tau_{\rm pump}, \tau_{\rm probe}\}$, where τ denotes the laser pulse duration. Furthermore, we identify $w_{\rm y}$ with twice the Rayleigh length of a Gaussian beam, i.e. $w_{\rm y} = 2{\rm z}_R = 2\pi\lambda_{\rm pump}$. The frequency scale Ω governing the submodulation in Eq. (3.101) is to be identified with $\Omega = 2\pi/\lambda_{\rm pump}$. Assuming that the effective focal area contains 86% of the laser energy W ($\frac{1}{e^2}$-criterion), we estimate the peak field strength as

$$\mathcal{E}^2 = 2\langle I\rangle \approx 2\frac{0.86\,W}{\tau\,\sigma}\,, \tag{3.104}$$

with focal area $\sigma \approx \pi\lambda^2$ and cycle-averaged intensity $\langle I\rangle$. We will employ Eq. (3.104) to determine the field strengths of the pump laser. Furthermore, the number of available probe photons of frequency $\omega_{\rm in} = 2\pi/\lambda_{\rm probe}$ can be estimated from the pulse energy $W_{\rm probe}$ of the probe laser, $\mathcal{N}_{\rm probe} \approx W_{\rm probe}/\omega_{\rm probe}$. Referring to Eq. (3.103), the number of induced photons per laser shot with reflection or transmission kinematics can then be estimated as $\mathcal{N}^{\rm ind} = R_{p,2n}^{(\pm)} f_{\rm int} \mathcal{N}_{\rm probe}$. The factor $f_{\rm int} \equiv \min\{1, \tau_{\rm pump}/\tau_{\rm probe}\}$ provides a first estimate of the fraction of the number of incident probe photons interacting with

[18] It has been theoretically shown that the tightest possible focussing of monochromatic light can be achieved with converging dipole radiation, going even below the diffraction limit [104]. A proposed experimental set-up is given in Ref. [105], which employs a large parabolic mirror to focus down a certain radially polarized laser beam (so-called 4π focussing). The geometry of this set-up, however, implies a rather large number of pump photons distributed over the full solid angle, thereby impeding a proper signal-background separation. In this work we focus on more "conventional" set-ups.

Set-up	$W_{\text{pump}}/W_{\text{probe}}$[J]	$\lambda_{\text{pump}}/\lambda_{\text{probe}}$[nm]	$\tau_{\text{pump}}/\tau_{\text{probe}}$[fs]
(1) POLARIS+JETI	150/4	1030/800	150/20
(2) POLARIS+JETI(SHG)	150/2	1030/400	150/20
(3) Vulcan 1PW	250/250	1053/1053	500/500
(4) ELI-NP 2×1PW	25/25	800/800	25/25

Table 3.1.: Design parameters for the four pump-probe set-ups considered in this section. For more details see the appendix E.

the inhomogeneity.

In this work we investigate quantum reflection for a small variety of set-ups employing parameters of various existing state-of-the-art or near-future optical high-intensity lasers, see the appendix E. The four set-ups under consideration are listed in Table (3.1). Set-up (1) combines the two high-intensity lasers to be available in Jena [106–108]: Employing the 1PW POLARIS laser as pump and the 200TW JETI200 laser as probe yields a configuration with a rather large difference in pulse length and energy between pump and probe laser. Set-up (2) resembles Set-up (1) with the utilization of the second harmonic of the probe beam; we assumed a conversion loss of $Q = 0.5$ yielding a probe beam energy of $W_{\text{probe}} = 2\text{J}$. Set-up (3) employs the Vulcan laser located at the Central Laser Facility in the United Kingdom [109]: Splitting its 1PW beam yields two 500TW beams, one of which is used as pump and the other as probe. In contrast to Set-ups (1) and (2), this yields a configuration with pump and probe beams of comparable energy and pulse duration. Finally, Set-up (4) employs conservative estimates of the high-intensity laser facility ELI-NP currently under construction in Romania [110], where we assume identical pump and probe beams with a peak power of 1PW each. The main difference between Set-ups (3) and (4) is that the former employs beams with a comparatively high energy and long pulse duration compared to the latter.

Let us start the discussion by first considering the simplified model for which the scattering coefficients (3.103) have been derived. As has been discussed in Sect. 3.2.4, additional requirements have to be met in order to allow for nonvanishing contributions for the $n = 1$ channel, namely $\frac{2\Omega}{\omega_{\text{in}}} < 1$ and $\beta \geq \arcsin\left(\frac{4\Omega}{\omega_{\text{in}}} - 1\right)$. For the parameters of the Set-ups (1),(3) and (4) given in Table 3.1, these conditions cannot be fulfilled and correspondingly their $n = 1$ contributions vanish, i.e. $R_{p,2}^{(\pm)} = 0$. Only the probe photons of Set-up (2) possess enough energy to provide $2\Omega_{\text{pump}}$ to the pump beam. Figure 3.10 depicts the emission directions $\beta' \in (-180°...180°]$ of the induced photons as a function of the incidence angle $\beta' \in (-180°...180°]$ for Set-up (2). Channels

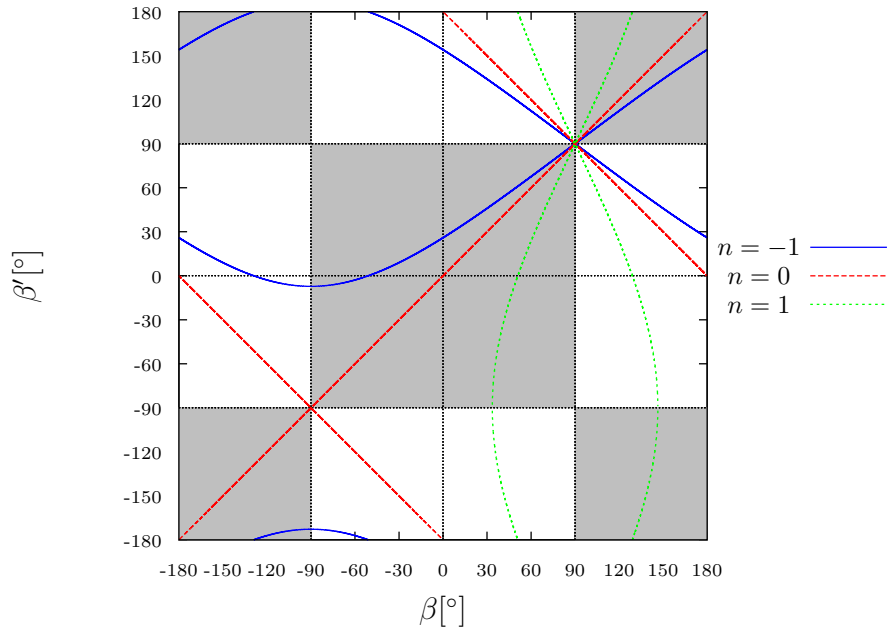

Figure 3.10.: Plot of the outgoing angle $\beta' = \sphericalangle(\mathbf{k}', \hat{\mathbf{e}}_x)$ of the induced photons as a function of the incidence angle $\beta = \sphericalangle(\mathbf{k}, \hat{\mathbf{e}}_x)$, adopting the design parameters of Set-up (2). Depicted are the various emission channels $n \in \{-1, 0, 1\}$. While the two channels with $n \in \{-1, 0\}$ sustain a quantum reflection signal for arbitrary incoming angles β, the channel $n = 1$ only has a nonvanishing signal for a subset of incoming angles β. Quantum reflection gives rise to contributions with transmission (gray-shaded area) and reflection kinematics (white area).

$n \in \{-1, 0\}$ give rise to a quantum reflection signal for arbitrary incidence angles β, while the channel $n = 1$ has nonzero contributions only for a subset of incidence angles which comply with momentum conservation. The elastic channel $n = 0$ (straight lines) features no net exchange of energy between the pump and probe beam, such that the outgoing directions are fully determined by the probe photon kinematics. Conversely, the emission directions for the inelastic channels (curved lines) additionally depend on the energy Ω of the pump field photons.

Figures 3.11 and 3.12 show plots of the numbers of induced photons as functions of the incidence angle β, for the various set-ups of Table 3.1. The corresponding outgoing angles can be read off from Fig. 3.10. For all set-ups the highest numbers of induced photons are given for the elastic channel $n = 0$, while the other channels are significantly suppressed. The unphysical assumption of an infinite extension of the inhomogeneity along y leads to the number of induced photons diverging for certain channels. This happens for precisely those incidence directions which induce photons propagating along the y-axis, leading to an infinitely long interaction between the

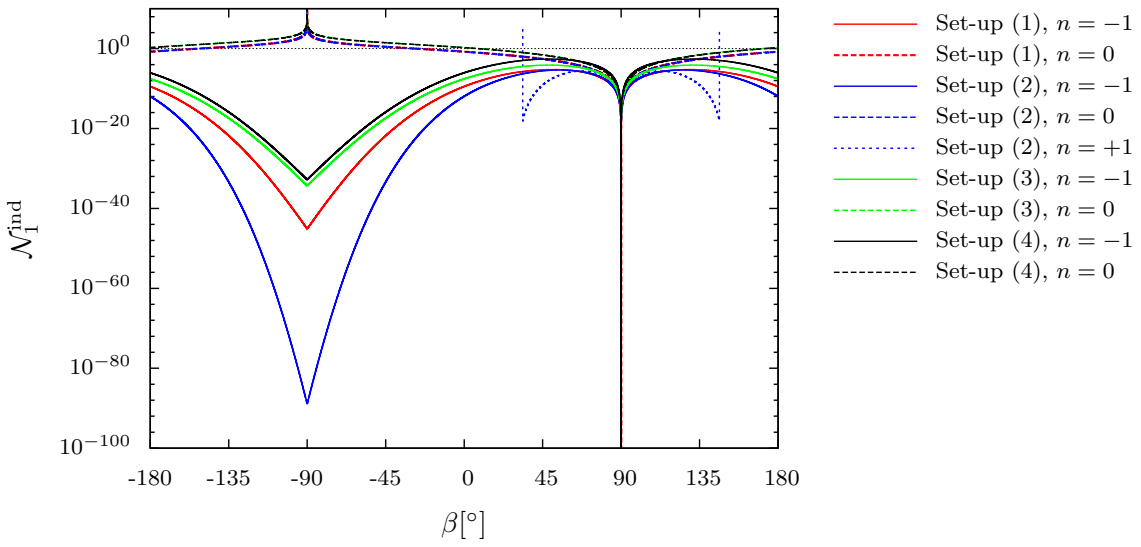

Figure 3.11.: Logarithmic plot of the number of induced photons in forward direction for the pump field inhomogeneity (3.104) in the limit of $w_{\mathrm{y}}, \tau \to \infty$ as a function of the incidence angle β, with polarization $p = 1$ and for the different channels $n \in \{-1, 0, 1\}$. The differently colored graphs refer to the Set-ups (1)-(4), detailed in Table 3.1. Only Set-up (2) allows for a contribution with $n = 1$, restricted to a subset of incidence angles β (cf. the main text). For $\beta = 90°$, all contributions vanish. Conversely, for $\beta = -90°$ the number of induced photons with $n = 0$ diverges, while the contributions with $n = -1$ are finite. The results for $p = 2$ follow by a multiplication with a factor $(c_2/c_1)^2 \approx 0.33$.

induced photons and the inhomogeneity. Correspondingly, for the elastic channel we find a divergence at $\beta = -90°$, while the channel with $n = +1$ diverges for $\beta \to \frac{\pi}{2} \pm \left[\frac{\pi}{2} - \arcsin\left(\frac{4\Omega}{\omega_{\mathrm{in}}} - 1\right)\right]$. The inelastic channel $n = -1$ does not exhibit any divergence, as for this channel the induced photons are scattered away from the y-axis, cf. Fig. 3.10. For $\beta = 90°$, the number of induced photons vanishes for all channels, owing to the fact that the quantity $(\hat{s}k)|_{k^2=0} = \mathbf{k} \cdot (\hat{\mathbf{E}} \times \hat{\mathbf{B}}) - \omega$ vanishes for this particular choice of β (cf. Sect. 3.2.4).

Set-ups (3)-(4) induce the largest number of photons and exhibit very similar behavior. This is to be expected as so far we have only considered the idealized limit of $\tau \to \infty$. Furthermore, we find that the numbers of induced photons for Set-up (2) are significantly suppressed with respect to Set-up (1) (an exception is given by the induced photons in forward direction for the elastic channel $n = 0$, where the curves for Set-ups (1) and (2) are identical). This is a consequence of the exponential suppression of quantum reflection in the momentum transfer, which is more pronounced for large probe photon frequencies, cf. Eq. (3.103).

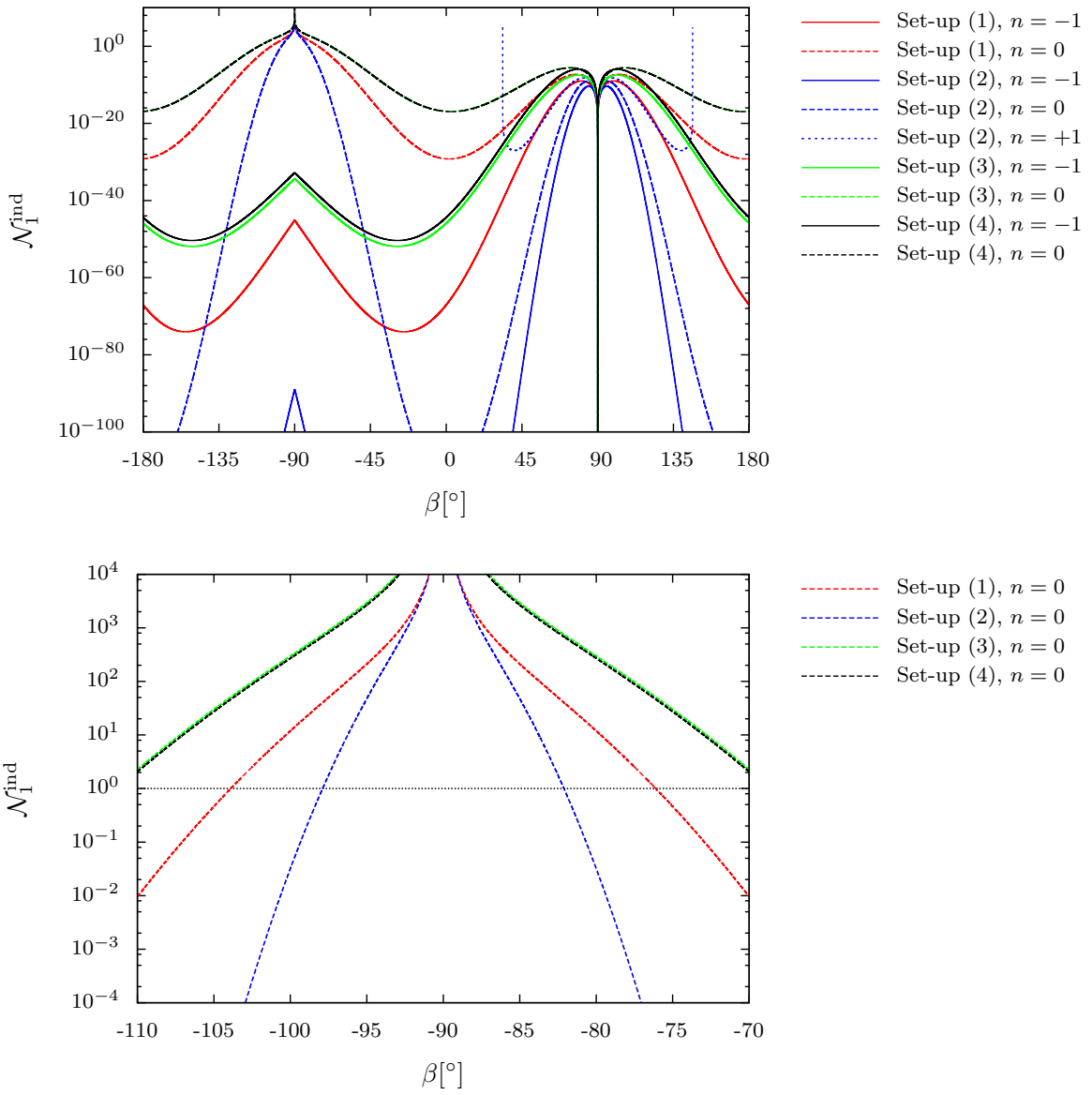

Figure 3.12.: Logarithmic plot of the number of induced photons in backward direction for the pump field inhomogeneity (3.104) in the limit of $w_{\rm y}, \tau \to \infty$ as a function of the incidence angle β, with polarization $p = 1$ and for the different channels $n \in \{-1, 0, 1\}$. Comparing with the results in Fig. 3.11, the numbers of induced photons with reflection kinematics are generically lower than those with transmission kinematics. **Bottom:** Close up of the upper plot in the angular range where $\mathcal{N}_1^{\rm ind} \gtrsim 1$.

The bottom plot of Fig. 3.12 shows a close-up of the region, where the induced signal in backward direction is greater than one, i.e. $\mathcal{N}_1^{\rm ind} \gtrsim 1$. For the various set-ups under consideration, this is the case for angles $-110° \lesssim \beta \lesssim -70°$, which means that both the incident and outgoing photons are within $\approx \pm 20°$ about $-\hat{\mathbf{e}}_{\rm y}$. Comparing this with the angular beam divergence of a Gaussian beam focussed down to the diffraction limit, $\theta \approx 1/\pi \approx 18°$, we find that a non-negligible fraction of photons is practically only induced into regions where the photons originating from the pump beam constitute a large background.

The divergences appearing in Figs. 3.11 and 3.12 are expected to be regularized as soon as a finite extension of the inhomogeneity along y is taken into account. To this end, in Fig. 3.13 we have plotted the induced photon signal (3.102) stemming from the localized pump field inhomogeneity (3.101), for finite $w_{\rm y}$ and τ. The top-left graph shows the total number of induced photons as a function of the incidence angle $\beta = [-\pi, \pi)$, obtained by integrating Eq. (3.102) over $\beta' = -\pi ... \pi$ and $\omega' = 0 ... \infty$. As has been observed in Figs. 3.11 and 3.12, the maximum number of induced photons is obtained if the probe beam counterpropagates with the pump beam, i.e. for $\beta = -90°$. As expected, the maximum number of induced photons is now finite. Correspondingly, the minimum number of induced photons is given for $\beta = 90°$. In contrast to Figs. 3.11 and 3.12, incident photons traveling along $\hat{\mathbf{e}}_{\rm y}$ may now be scattered away from this very axis, giving rise to a *nonzero* number of induced photons for parallelly propagating beams. The top-right and middle-left plots show the total number of induced photons for the elastic and inelastic contributions only. As has been observed earlier, the elastic contribution generically dominates over the inelastic ones. Note that the inelastic contributions have a minimum for $\beta = -90°$, whereas the elastic one has a maximum there. The curves in these two plots resemble the corresponding curves in Fig. 3.11, implying that the induced photons are mainly emitted into the forward direction.

In the last three plots of Fig. 3.13 we have specialized to counterpropagating beams, $\beta = -90°$, maximizing the number of induced photons. The middle-right plot shows the angular emission characteristics for this setting, obtained by integrating Eq. (3.102) over $\omega' = 0 ... \infty$. The largest number of photons is induced along $\beta' = -90°$, corresponding to the elastic contribution. Further maxima are visible at $\beta' \approx -8° ... 22°$, and $\beta' \approx 158° ... -172°$, which are strongly suppressed and correspond to the inelastic contribution $n = -1$. The positions of the maxima can as well be inferred from Fig. 3.10. The graph on the bottom-left is a close-up of the angular emission characteristics around $\beta' = -90°$. As can be observed, Set-up (3) yields the highest number of induced photons. Its dominance over Set-up (4), which nominally has a higher peak

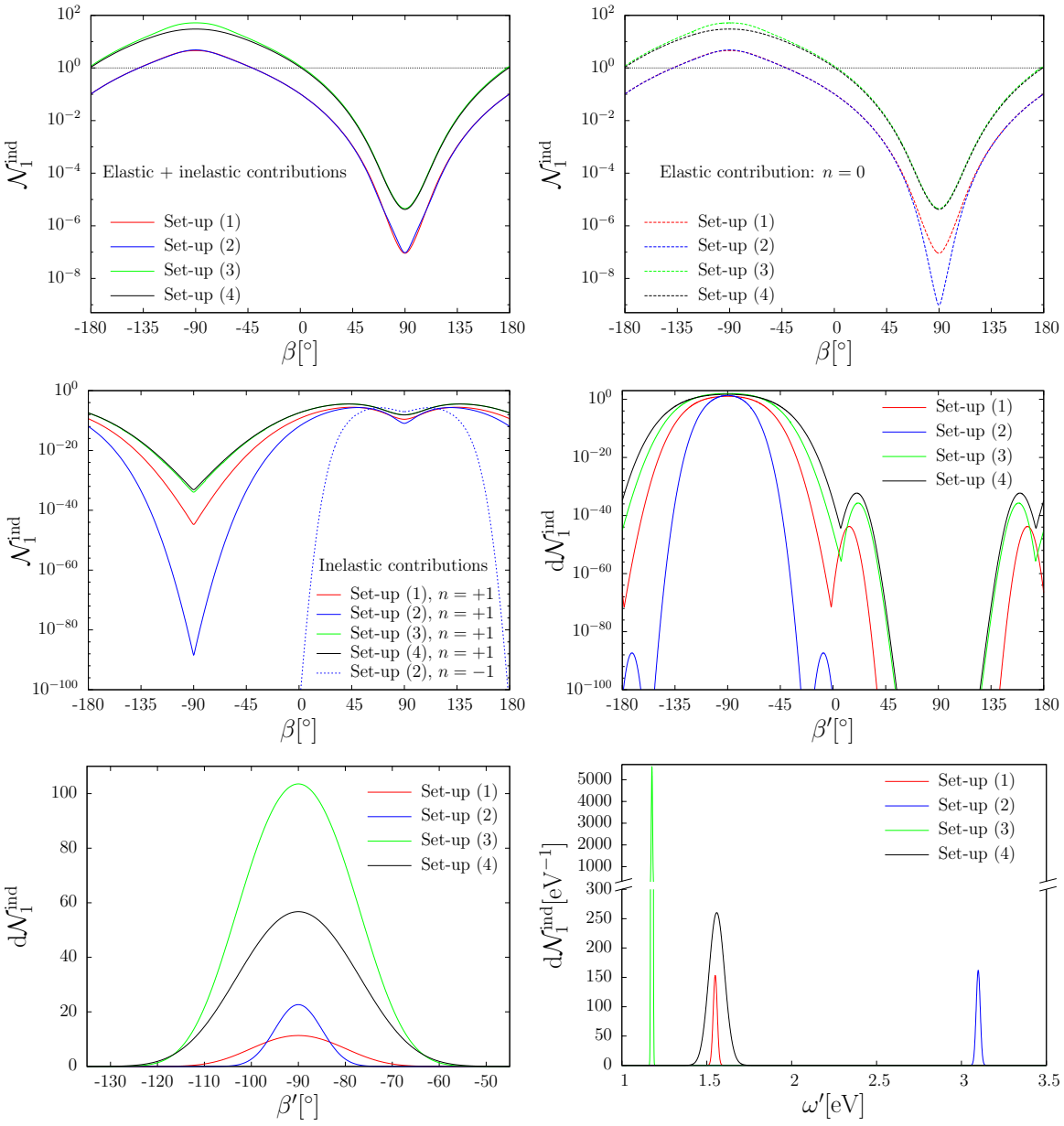

Figure 3.13.: Numbers of induced photons for the pump field inhomogeneity (3.101). **Top left:** Total number of induced photons $\mathcal{N}_1^{\rm ind}$, obtained by integrating Eq. (3.102) over $\beta' = -\pi...\pi$ and $\omega' = 0...\infty$, as a function of the incidence angle β. **Top right:** Total number of induced photons stemming from the elastic contribution $n = 0$. **Middle left:** Total number of induced photons stemming from the inelastic contributions $n = -1, +1$. **Middle right:** Differential number of induced photons $\mathrm{d}\mathcal{N}_1^{\rm ind}(\beta')$, obtained by integrating Eq. (3.102) over $\omega' = 0...\infty$. The incidence angle was chosen as $\beta = -90°$, maximizing the total number of induced photons (cf. top left graph). **Bottom left:** Close-up of the middle right plot around the region of maximum induced photons. **Bottom right:** Energy spectrum of the induced photons, obtained by integrating Eq. (3.102) from $\beta' = -\pi...\pi$, again for $\beta = -90°$.

Set-up	$\mathcal{N}^{\mathrm{ind}}_{1,\mathrm{max}}$	Θ' $(1/\mathrm{e}^2)$ [°]	$\Delta\omega'$ $(1/\mathrm{e}^2)$ [eV]	$\sqrt{128}/\tau_{\mathrm{pump}}$ [eV]
(1)	4.6	18.1	0.048	0.050
(2)	4.8	9.7	0.048	0.050
(3)	51.9	22.2	0.015	0.015
(4)	30.1	23.8	0.185	0.30

Table 3.2.: Maximum total number $\mathcal{N}^{\mathrm{ind}}_{1,\mathrm{max}}$, $1/\mathrm{e}^2$-angular divergence Θ' and $1/\mathrm{e}^2$-energy spread $\Delta\omega'$ of induced photons per shot, for Set-ups (1)-(4) listed in Table 3.2. The corresponding curves for the middle and right columns can be found in Fig. 3.13, bottom-left and bottom-right plot respectively. The last column gives theoretical predictions for the energy spread for large pump durations τ_{pump}.

power, can be attributed to the larger pulse energy of the Vulcan laser and thus the larger number of photons to probe the inhomogeneity with than is provided by the ELI laser from Set-up (4). The angular divergence Θ', defined as half the $1/\mathrm{e}^2$-width, of the induced photons in the elastic channel can be read off from the bottom-left plot of Fig. 3.13 and is listed in Table 3.2. It is mainly determined by the probe photon frequency ω_{probe} and the spatial extension of the pump beam. As these parameters are comparable for Set-ups (1), (3) and (4), the divergence of the induced photons is rather similar. Set-up (2) features frequency-doubled probe photons, and consequentially induces photons with roughly half the divergence of the other set-ups. Lastly, the bottom-right plot shows the energy spectrum of the induced photons in the elastic channel $n = 0$, obtained by integrating Eq. (3.103) from $\beta' = -\pi...\pi$. The corresponding $1/\mathrm{e}^2$-widths are listed in Table 3.2. From Eq. (3.102) we infer that for large $\tau \gg \sqrt{w_{\mathrm{x}}^2 + 2w_{\mathrm{y}}^2}$ the width is mainly influenced by the pulse length of the pump laser, and in this regime can be well approximated by $\Delta\omega' \approx \sqrt{128}/\tau_{\mathrm{pump}}$, cf. Table 3.2. Going towards shorter pulse durations the maximum width of the energy spectrum is finally limited by the requirement of momentum conservation, which can still only be fulfilled for induced photon energies ω' sufficiently close to $\omega_{\mathrm{in}} \pm 2\Omega$. This is exemplified by the energy spectrum for Set-up (4).

The distinguishing feature of quantum reflection is the alteration of a probe photon's momentum, and thus the theoretically attainable physical separation between the signal and the background. Analogous to the case of atomic quantum reflection, the signal strength is exponentially suppressed by the momentum transfer. For atomic quantum reflection, this suppression is overcome by shining the probe beam at "grazing" incidence onto the *macroscopic* sample. For optical quantum reflection, the need to generate large electromagnetic fields necessitates the employment of high-intensity lasers with comparatively very small focussing volumes. Consequently, resorting to

grazing incidence will not yield an enhancement comparable to atomic quantum reflection, as the effective interaction length between the probe beam and the region of the quantum vacuum modified by the pump laser remains small, $L_{\text{eff}} \sim w$.

We therefore conclude that an experimental verification of pure quantum reflection as discussed in this section will prove to be very challenging: First of all, the total number of induced photons per laser shot is of $\mathcal{O}(1-10)$ and thus very small compared to the number of incoming photons, which is of $\mathcal{O}(10^{20})$. For the special alignment of pump and probe laser yielding a maximum number of induced photons, $\beta = -90°$, the bulk of the signal photons is emitted into the region dominated by the background noise. Secondly, these signal photons belong mainly to the elastic channel, thereby hampering the employment of frequency filtering techniques. Inelastic channels inducing photon energies $\omega' \approx \omega_{\text{in}} - 2n\Omega$ are strongly suppressed. Lastly, for the configurations accessible with our formalism, the polarization of the signal photons is always identical to the probe photons' polarization. An experimental verification of pure quantum reflection may therefore require special pulse designs and high time resolution for the probe photon detection.

4. Photon merging and splitting

In the last chapter we have investigated nonlinear quantum vacuum effects pertaining solely to quantum reflection, i.e. the exchange of energy and momentum between probe and pump beam photons. However, we have found that the requirement of employing high-intensity optical lasers generically only yields large numbers of induced photons in those regions where the background noise dominates, cf. Sect. 3.2.6. Regarding an experimental verification of nonlinear quantum vacuum effects, it is desirable to have as many means as possible to discriminate the induced signal from the background. Ideally, the signal consists of a sizable amount of photons (*i*) whose energy differs from both the pump and probe beam photons' energy, (*ii*) whose polarization differs from the photons constituting the background noise, and (*iii*) which are emitted into the region where the background field vanishes or is at least suppressed inasmuch that, after polarization and frequency filtering, single-photon detection schemes may be employed. Property (*ii*), in fact, constitutes a necessary ingredient for some proposed experimental set-ups. A prominent example is the fundamental physics program within the HIBEF project [111], aiming to detect vacuum magnetic birefringence by employing a petawatt optical laser as pump and the European XFEL as probe, looking for induced photons in forward direction [64, 112]. While important progress has been made on the detection side in the form of high-purity X-ray polarimetry [113, 114], a recent study [115] highlighted the importance of accounting for the scattering of photons outside of the noise cone and into regions of low background intensity due to the inhomogeneous field profile of the pump laser.

In this chapter we will examine two signatures potentially exhibiting all of the aforementioned properties $(i) - (iii)$: the splitting and merging of probe photons. Photon splitting describes processes where a single photon splits into two or more outgoing photons under the influence of an external electromagnetic field [15, 24, 86, 116–118]. Photon merging can be viewed as the inverse process: two or more photons merge under the influence of the external field, yielding a single outgoing photon [26, 119, 120]. The first comprehensive investigation of photon splitting has been performed by Adler in 1971 [25], who considered this process in a constant, purely magnetic pump field.

The formalism of Chapter 3 made use of the two-photon polarization tensor and *a priori* restricted only the external pump field to vary on scales much larger than the Compton wavelength, while in principle allowing for probe photon beams of arbitrary frequency[1]. Correspondingly, we were limited to certain classes of inhomogeneities compatible with the existence of *invariant* polarization modes. However, for all-optical set-ups involving high-intensity lasers the electromagnetic fields generated by both the pump *and* the probe lasers usually vary on scales much larger than the Compton wavelength. Making use of this fact, recently a more general representation of the photon polarization tensor $\Pi^{\mu\nu}(k,k')$ in the limit of low probe photon energies and momenta and for slowly-varying but otherwise arbitrary electromagnetic field inhomogeneities has been derived [121]. The formalism developed therein will form the basis of this chapter.

We adopt the strategy devised in Refs. [115, 121] to investigate photon splitting and merging in the strong, inhomogeneous electromagnetic fields as attained with high-intensity laser experiments. To this end we derive the three-photon polarization tensor $\Pi^{\mu\nu\rho}(k,k',k'')$ to one-loop order in the limit of low energies and momenta, and for generic slowly-varying electromagnetic field inhomogeneities. This quantity describes the effective interaction between three photon fields facilitated by vacuum fluctuations in the presence of external electromagnetic fields, and accounts for the coupling to the external pump field to all orders. With its help we compute merging and splitting amplitudes, and similar to the previous section provide estimates for the number of merged photons for experimental set-ups involving current state-of-the-art or near-future high-intensity laser facilities[2].

[1] In fact, the permissible energy range of the probe photons depends on the specific approximation of the two-photon polarization tensor that has been employed to incorporate the pump field inhomogeneity. Compare, e.g., the weak-field expansions employed in Sects. 3.2.2 and 3.2.4 with the more general representation of the polarization tensor obtained in a Lorentz pump profile in Sect. 3.2.5.

[2] This chapter closely follows and expands on the results published in Ref. [45]. For completeness, in Sect. 4.1 we also reproduce the expressions for the two-photon polarization tensor obtained in Ref. [121]. Section 4.4 offers a more in-depth study of the experimental scenarios published in Ref. [45].

4.1. The three-photon polarization tensor

The physical information about photon splitting and merging in the presence of an external electromagnetic pump field inhomogeneity $F^{\mu\nu}(x)$ is contained in the three-photon polarization tensor $\Pi^{\mu\nu\rho}(k, k', k''|F)$. It quantifies the effective coupling of three photon fields with momenta k^μ, k'^μ and k''^μ mediated by an electron-positron loop, cf. Fig. 4.1. At present, no exact analytical expressions for the three-photon

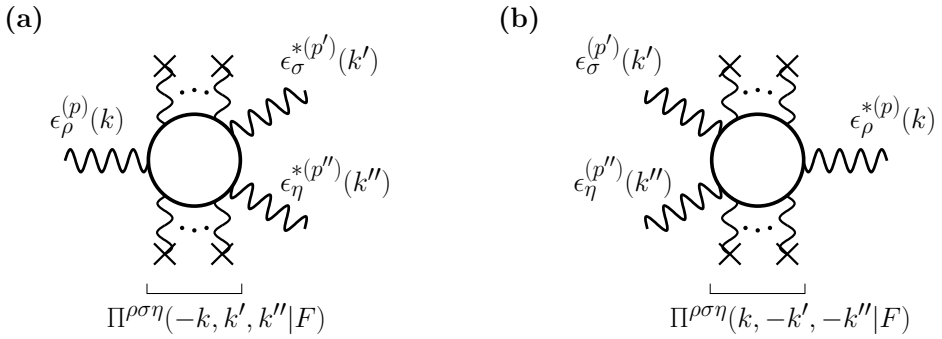

Figure 4.1.: Feynman diagrams of the three-photon interactions considered in this work, taken from Ref. [45]. (a) Photon Splitting: An incoming photon with momentum four-vector k^μ and polarization four-vector $\epsilon_\rho^{(p)}(k)$ splits, under the assistance of the external field inhomogeneity $F^{\mu\nu}(x)$, into two photons with $\{k'^\mu, \epsilon_\sigma^{*(p')}(k')\}$ and $\{k''^\mu, \epsilon_\eta^{*(p'')}(k'')\}$. (b) Photon Merging: Two incoming photons with $\{k'^\mu, \epsilon_\sigma^{(p')}(k')\}$ and $\{k''^\mu, \epsilon_\eta^{(p'')}(k'')\}$ merge to yield a single outgoing photon with $\{k^\mu, \epsilon_\rho^{*(p)}(k)\}$. The coupling of the probe photons and the external field inhomogeneity $F^{\mu\nu}(x)$ to the electron-positron loop is encoded in the three-photon polarization tensor $\Pi^{\rho\sigma\eta}$.

polarization tensor for arbitrary momentum transfers and pump field inhomogeneities are known. Exact analytical results are limited to one-loop order, and for generic momentum transfers they comprise two classes of pump field inhomogeneities. The first class are uniform electromagnetic fields. In 1971, Papanyan and Ritus derived a parameter integral representation of the polarization tensor for constant-crossed pump fields [86, 87]. The calculation is eased by the fact that for the constant-crossed configuration the field invariants $\mathcal{F} = \frac{1}{4}F_{\mu\nu}F^{\mu\nu} = \frac{1}{2}(\mathbf{B}^2 - \mathbf{E}^2)$ and $\mathcal{G} = \frac{1}{4}F_{\mu\nu}{}^\star F^{\mu\nu} = -\mathbf{E}\cdot\mathbf{B}$ vanish; ${}^\star F^{\mu\nu} = \frac{1}{2}\varepsilon^{\mu\nu\alpha\beta}F_{\alpha\beta}$ denotes the dual field strength tensor. In 1979, Stoneham obtained the corresponding result for a constant, purely magnetic pump field [85]. Later, splitting amplitudes have been derived for generically oriented pump field configurations [116]. Recall that these amplitudes basically amount to on-shell matrix elements of the photon polarization tensor. In constant fields, energy-momentum conservation requires that all three photons propagate collinearly, and therefore an expansion in the

pump field strength starts with terms $\propto \left(\frac{\mathcal{E}}{\mathcal{E}_{\rm cr}}\right)^3$, corresponding to *hexagon diagrams*. This is also known as the "Adler theorem".

The second class of configurations are plane-wave pump fields with vector potential $A_\mu(\kappa x)$, where $\kappa^\mu = (|\boldsymbol{\kappa}|, \boldsymbol{\kappa})$ denotes the four-momentum of the plane wave. For this class, splitting amplitudes for arbitrary photon energies have been derived in Ref. [118]. As photons can exchange energy and momentum with the plane-wave pump field, an expansion in the pump field strength generically starts with terms $\propto \left(\frac{\mathcal{E}}{\mathcal{E}_{\rm cr}}\right)$, corresponding to *box diagrams*. For completeness let us remark that for small angles between the photon momenta splitting amplitudes have also been calculated in Coulomb fields [16].

Similar to the previous chapter we could employ these analytical expressions and implement the inhomogeneous pump fields along the lines of scheme (3.4). Correspondingly, the need to preserve gauge invariance again limits the dimensionality of the inhomogeneities to those permitting invariant modes of polarization. The ensuing analysis would then follow the lines of the last chapter. Here, however, we aim to obtain insights into the splitting and merging of photons in slowly-varying, but otherwise *arbitrary* pump field inhomogeneities. To this end we derive the polarization tensor starting from the effective Heisenberg-Euler Lagrangian $\mathcal{L}(F)$ and implement the locally-constant field approximation (LCFA) on the level of the Lagrangian, therefore obtaining a local function of spacetime $\mathcal{L}(x|F)$. In contrast to the last chapter, the resulting representation of the polarization tensor is then additionally restricted to small four-momentum transfers, i.e. also the probe photon fields have to be slowly-varying. However, this procedure manifestly preserves gauge invariance and thereby obviates the need to specialize to invariant polarization modes. This allows us to consider configurations with probe photons of arbitrary polarization.

We start with the one-loop effective action $\mathcal{S}_{\rm int}(F, f) = \int_x \mathcal{L}(x|F + f)$, mediating effective interactions between probe photon fields $a_\mu(x)$ with field strength tensor $f^{\mu\nu}(x)$ in a pump field inhomogeneity with field strength tensor $F^{\mu\nu}(x)$. It can be obtained from the Heisenberg-Euler effective Lagrangian, Eq. (F.7), by substituting $F^{\mu\nu} \to F^{\mu\nu}(x) + f^{\mu\nu}(x)$.[3] The various effective interactions between the photons can

[3] A short derivation of the Heisenberg-Euler effective Lagrangian in magnetic fields is given in the appendix F.

be extracted by expanding the action in terms of the probe photons,

$$\mathcal{S}_{\text{int}} = \mathcal{S}^{(1)}_{\text{int}} + \mathcal{S}^{(2)}_{\text{int}} + \mathcal{S}^{(3)}_{\text{int}} + \ldots = \int_x \frac{\partial \mathcal{L}}{\partial F^{\mu\nu}} f^{\mu\nu} + \frac{1}{2!}\int_x \frac{\partial^2 \mathcal{L}}{\partial F^{\mu\nu}\partial F^{\alpha\beta}} f^{\mu\nu} f^{\alpha\beta} + \frac{1}{3!}\int_x \frac{\partial^3 \mathcal{L}}{\partial F^{\mu\nu}\partial F^{\alpha\beta}\partial F^{\gamma\delta}} f^{\mu\nu} f^{\alpha\beta} f^{\gamma\delta} + \ldots , \quad (4.1)$$

where $S^{(l)}_{\text{int}}$ contains the effective interaction between l probe photons. Here and in future we omit the spacetime arguments of the fields. As opposed to the unknown exact effective Lagrangian, the Lagrangian derived from the LCFA inherently neglects derivatives of the field strength tensors. In momentum space derivatives of the fields translate to multiplications of the fields with their typical momentum scale v. The action is a dimensionless scalar quantity, and therefore the LCFA neglects contributions of $\mathcal{O}\big(\frac{v^2}{m^2}\big)$.[4]

The lowest-order interaction term $\mathcal{S}^{(1)}_{\text{int}}$ of the expansion (4.1) entails stimulated vacuum emission processes [54]. The second-order term $\mathcal{S}^{(2)}_{\text{int}}$ describes photon propagation processes, while the third-order term $\mathcal{S}^{(3)}_{\text{int}}$ entails photon splitting and merging. Substituting $f^{\mu\nu}(x) = i\int_k \mathrm{e}^{ikx}\big[k^\mu g^{\nu\sigma} - k^\nu g^{\mu\sigma}\big]a_\sigma(k)$ into $\mathcal{S}^{(2)}_{\text{int}}$ and $\mathcal{S}^{(3)}_{\text{int}}$, we obtain

$$\begin{aligned} \mathcal{S}^{(2)}_{\text{int}} &= -\frac{1}{2!}\int_k\int_{k'} a_\rho(k)a_\sigma(k')\Pi^{\rho\sigma}(k,k'|F)\,, \\ \mathcal{S}^{(3)}_{\text{int}} &= -\frac{1}{3!}\int_k\int_{k'}\int_{k''} a_\rho(k)a_\sigma(k')a_\eta(k'')\Pi^{\rho\sigma\eta}(k,k',k''|F)\,. \end{aligned} \quad (4.2)$$

The two-photon and three-photon polarization tensors in momentum space are then given by

$$\begin{aligned} \Pi^{\rho\sigma}(k,k'|F) &= -(k^\mu g^{\nu\rho} - k^\nu g^{\mu\rho})(k'^\alpha g^{\beta\sigma} - k'^\beta g^{\alpha\sigma})\int_x \mathrm{e}^{i(k+k')x}\frac{\partial^2\mathcal{L}}{\partial F^{\mu\nu}\partial F^{\alpha\beta}}(x)\,, \\ \Pi^{\rho\sigma\eta}(k,k',k''|F) &= -i(k^\mu g^{\nu\rho} - k^\nu g^{\mu\rho})(k'^\alpha g^{\beta\sigma} - k'^\beta g^{\alpha\sigma})(k''^\gamma g^{\delta\eta} - k''^\delta g^{\gamma\eta}) \\ &\quad\times\int_x \mathrm{e}^{i(k+k'+k'')x}\frac{\partial^3\mathcal{L}}{\partial F^{\mu\nu}\partial F^{\alpha\beta}\partial F^{\gamma\delta}}(x)\,. \end{aligned} \quad (4.3)$$

The expressions (4.3) fulfill the Ward identity (and hence gauge invariance) by virtue of their tensorial structures: We find $k_\rho\Pi^{\rho\sigma}(k,k') = k'_\sigma\Pi^{\rho\sigma}(k,k') = 0$ as well as $k_\rho\Pi^{\rho\sigma\eta}(k,k',k'') = k'_\sigma\Pi^{\rho\sigma\eta}(k,k',k'') = k''_\eta\Pi^{\rho\sigma\eta}(k,k',k'') = 0$. The two-photon polarization tensor neglects contributions of $v^2\mathcal{O}\big(\frac{v^2}{m^2}\big)$, while the three-photon polarization

[4] A more extensive elaboration on the scaling w.r.t. the momentum is given in the appendix F.2.

tensor neglects contributions of $v^3\mathcal{O}\big(\frac{v^2}{m^2}\big)$. We now rewrite the derivatives of the Lagrangian with respect to $F^{\mu\nu}$ in terms of the field invariants $\mathcal{F}$ and $\mathcal{G}$. The second derivative is then spanned by six independent tensor structures, corresponding to the full set of basis elements of a fully symmetric rank-2 tensor. Employing the shorthand notation $(kF)^\rho := k_\nu F^{\nu\rho}$, the resulting two-photon polarization tensor then reads [121]

$$\begin{aligned}\Pi^{\rho\sigma}(k,k'|F) = -\int_x \mathrm{e}^{i(k+k')x}\Bigg\{&\left(kk'g^{\rho\sigma} - k'^\rho k^\sigma\right)\frac{\partial\mathcal{L}}{\partial\mathcal{F}} + k_\alpha k'_\beta\varepsilon^{\alpha\beta\rho\sigma}\frac{\partial\mathcal{L}}{\partial\mathcal{G}}\\ &+ (kF)^\rho(k'F)^\sigma\frac{\partial^2\mathcal{L}}{\partial\mathcal{F}^2} + (k{\star}F)^\rho(k'{\star}F)^\sigma\frac{\partial^2\mathcal{L}}{\partial\mathcal{G}^2} + \Big[(k{\star}F)^\rho(k'F)^\sigma + (kF)^\rho(k'{\star}F)^\sigma\Big]\frac{\partial^2\mathcal{L}}{\partial\mathcal{F}\partial\mathcal{G}}\Bigg\}.\end{aligned} \tag{4.4}$$

Likewise, the third derivative of the Lagrangian is spanned by 20 independent tensor structures, corresponding to the basis elements of a fully symmetric rank-3 tensor. Hence, we obtain for the three-photon polarization tensor

$$\begin{aligned}\Pi^{\rho\sigma\eta}(k,k',k''|F) = -i\int_x \mathrm{e}^{i(k+k'+k'')x}\\ \times\Bigg\{&\Big[\big(kk'g^{\rho\sigma} - k^\sigma k'^\rho\big)(k''F)^\eta + \big(kk''g^{\rho\eta} - k^\eta k''^\rho\big)(k'F)^\sigma + \big(k'k''g^{\sigma\eta} - k'^\eta k''^\sigma\big)(kF)^\rho\Big]\frac{\partial^2\mathcal{L}}{\partial\mathcal{F}^2}\\ &- \Big[k_\mu k'_\nu\varepsilon^{\mu\nu\rho\sigma}(k''{\star}F)^\eta + k_\mu k''_\nu\varepsilon^{\mu\nu\rho\eta}(k'{\star}F)^\sigma + k'_\mu k''_\nu\varepsilon^{\mu\nu\sigma\eta}(k{\star}F)^\rho\Big]\frac{\partial^2\mathcal{L}}{\partial\mathcal{G}^2}\\ &+ \Big[\big(kk'g^{\rho\sigma} - k^\sigma k'^\rho\big)(k''{\star}F)^\eta + \big(kk''g^{\rho\eta} - k^\eta k''^\rho\big)(k'{\star}F)^\sigma + \big(k'k''g^{\sigma\eta} - k'^\eta k''^\sigma\big)(k{\star}F)^\rho\\ &- k_\mu k'_\nu\varepsilon^{\mu\nu\rho\sigma}(k''F)^\eta - k_\mu k''_\nu\varepsilon^{\mu\nu\rho\eta}(k'F)^\sigma - k'_\mu k''_\nu\varepsilon^{\mu\nu\sigma\eta}(kF)^\rho\Big]\frac{\partial^2\mathcal{L}}{\partial\mathcal{F}\partial\mathcal{G}}\\ &+ (kF)^\rho(k'F)^\sigma(k''F)^\eta\frac{\partial^3\mathcal{L}}{\partial\mathcal{F}^3} + (k{\star}F)^\rho(k'{\star}F)^\sigma(k''{\star}F)^\eta\frac{\partial^3\mathcal{L}}{\partial\mathcal{G}^3}\\ &+ \Big[(k{\star}F)^\rho(k'F)^\sigma(k''F)^\eta + (kF)^\rho(k'{\star}F)^\sigma(k''F)^\eta + (kF)^\rho(k'F)^\sigma(k''{\star}F)^\eta\Big]\frac{\partial^3\mathcal{L}}{\partial\mathcal{F}\partial\mathcal{F}\partial\mathcal{G}}\\ &+ \Big[(k{\star}F)^\rho(k'{\star}F)^\sigma(k''F)^\eta + (kF)^\rho(k'{\star}F)^\sigma(k''{\star}F)^\eta + (k{\star}F)^\rho(k'F)^\sigma(k''{\star}F)^\eta\Big]\frac{\partial^3\mathcal{L}}{\partial\mathcal{F}\partial\mathcal{G}\partial\mathcal{G}}\Bigg\}.\end{aligned} \tag{4.5}$$

The explicit representation of the Heisenberg-Euler effective Lagrangian, Eq. (F.7), can now be employed to calculate the derivatives with respect to $\mathcal{F}$ and $\mathcal{G}$. As detailed in the appendix F, for either purely electric or purely magnetic fields, or alternatively for orthogonal electric and magnetic fields the field invariant $\mathcal{G}$ vanishes and the proper

time integrations can be performed analytically. This allows explicit analytical insights into the polarization tensors in the strong-field limit (cf. also Refs. [28, 78, 121, 122]).

In this chapter, we will exclusively focus on the crossed-field case as it can be used to describe the electromagnetic fields delivered by high-intensity lasers. We employ the derivatives obtained from an expansion of the Heisenberg-Euler Lagrangian in the invariants $\mathcal{F}$ and $\mathcal{G}$, Eq. (F.8), reading

$$\begin{aligned}\left\{\frac{\partial^2\mathcal{L}}{\partial\mathcal{F}^2},\frac{\partial^2\mathcal{L}}{\partial\mathcal{G}^2},\frac{\partial^2\mathcal{L}}{\partial\mathcal{F}\partial\mathcal{G}}\right\}&=\{4,7,0\}\frac{\alpha}{45\pi}\left(\frac{e}{m^2}\right)^2+\mathcal{O}(\{\mathcal{F},\mathcal{G}\})\,,\\ \left\{\frac{\partial^3\mathcal{L}}{\partial\mathcal{F}^3},\frac{\partial^3\mathcal{L}}{\partial\mathcal{G}^3},\frac{\partial^3\mathcal{L}}{\partial\mathcal{F}\partial\mathcal{G}^2},\frac{\partial^3\mathcal{L}}{\partial\mathcal{F}^2\partial\mathcal{G}}\right\}&=-\{24,0,13,0\}\frac{4\alpha}{315\pi}\left(\frac{e}{m^2}\right)^4+\mathcal{O}(\{\mathcal{F},\mathcal{G}\})\,.\end{aligned}\tag{4.6}$$

For generic slowly-varying pump fields, neglecting higher-order expansion terms is equivalent to the weak-field limit $\mathcal{E}\ll\mathcal{E}_{\rm cr}$.[5] For the crossed field, however, both field invariants vanish identically and the lowest-order derivative terms in Eq. (4.6) constitute the full result within the LCFA. The reason is that for $\mathcal{F}=\mathcal{G}=0$ the higher-order contributions to the two-photon polarization tensor scale according to $\sim m^2\big[\big(\frac{e\mathcal{E}}{m^2}\big)^2\mathcal{O}\big(\frac{v^2}{m^2}\big)\big]^n$, with $n\in\mathbb{N}_+$ [121]; cf. also the appendix F.2. Likewise, the contributions for the three-photon polarization tensor scale as $\sim m\big(\frac{v}{m}\big)^3\frac{e\mathcal{E}}{m^2}\big[1+\mathcal{O}\big(\frac{v^2}{m^2}\big)\big]$ for the term linear in $\mathcal{E}$, and as $\sim m\frac{v}{m}\frac{e\mathcal{E}}{m^2}\big[\big(\frac{e\mathcal{E}}{m^2}\big)^2\mathcal{O}\big(\frac{v^2}{m^2}\big)\big]^n$ for higher powers of $\mathcal{E}$. As the LCFA adopted here neglects contributions $\sim\mathcal{O}\big(\frac{v^2}{m^2}\big)$, terms with $n>1$ are not accounted for in the corresponding two- and three-photon polarization tensors. Finally, in the limit $\mathcal{F}=\mathcal{G}=0$ we find

$$\begin{aligned}\Pi^{\rho\sigma}(k,k'|\mathbf{E}\perp\mathbf{B})&=\frac{\alpha}{45\pi}\int_x \mathrm{e}^{i(k+k')x}\left(\frac{e\mathcal{E}(x)}{m^2}\right)^2 c^{\rho\sigma}_{(2)}(k,k')\,,\\ \Pi^{\rho\sigma\eta}(k,k',k''|\mathbf{E}\perp\mathbf{B})&=i\frac{\alpha}{45\pi}\left(\frac{e}{m^2}\right)\int_x \mathrm{e}^{i(k+k'+k'')x}\\ &\quad\times\left\{\left(\frac{e\mathcal{E}(x)}{m^2}\right)c^{\rho\sigma\eta}_{(1)}(k,k',k'')-\frac{4}{7}\left(\frac{e\mathcal{E}(x)}{m^2}\right)^3 c^{\rho\sigma\eta}_{(3)}(k,k',k'')\right\}.\end{aligned}\tag{4.7}$$

The two-photon polarization tensor features only a component quadratic in the field amplitude $\mathcal{E}$, while the three-photon polarization tensor decomposes into components linear and cubic in $\mathcal{E}$. The corresponding tensorial coefficients read

$$c^{\rho\sigma}_{(2)}(k,k')=4(k\hat{F})^\rho(k'\hat{F})^\sigma+7(k^\star\hat{F})^\rho(k'^\star\hat{F})^\sigma\,,\tag{4.8}$$

[5] Working with Eqs. (F.8) and (4.6) corresponds to the same level of accuracy as has recently been used for a study of vacuum higher-harmonic generation in a slowly varying pump [123] or constant crossed-field pump in the shock regime [124] based on the quantum equations of motion.

as well as

$$\begin{aligned} c_{(1)}^{\rho\sigma\eta}(k,k',k'') = \; & 4\Big[\big(kk'g^{\rho\sigma} - k^\sigma k'^\rho\big)(k''\hat{F})^\eta + \big(kk''g^{\rho\eta} - k^\eta k''^\rho\big)(k'\hat{F})^\sigma \\ & + \big(k'k''g^{\sigma\eta} - k'^\eta k''^\sigma\big)(k\hat{F})^\rho\Big] \\ & - 7\Big[k_\mu k'_\nu \varepsilon^{\mu\nu\rho\sigma}(k''^\star\hat{F})^\eta + k_\mu k''_\nu \varepsilon^{\mu\nu\rho\eta}(k'^\star\hat{F})^\sigma + k'_\mu k''_\nu \varepsilon^{\mu\nu\sigma\eta}(k^\star\hat{F})^\rho\Big], \end{aligned} \tag{4.9}$$

and

$$\begin{aligned} c_{(3)}^{\rho\sigma\eta}(k,k',k'') = \; & 24(k\hat{F})^\rho(k'\hat{F})^\sigma(k''\hat{F})^\eta + 13\Big[(k^\star\hat{F})^\rho(k'^\star\hat{F})^\sigma(k''\hat{F})^\eta \\ & + (k\hat{F})^\rho(k'^\star\hat{F})^\sigma(k''^\star\hat{F})^\eta + (k^\star\hat{F})^\rho(k'\hat{F})^\sigma(k''^\star\hat{F})^\eta\Big]. \end{aligned} \tag{4.10}$$

Here, we have introduced the normalized field strength tensor $\hat{F}^{\mu\nu}$ by extracting the field strength amplitude, $F^{\mu\nu} = \mathcal{E}\hat{F}^{\mu\nu}$. For *unidirectional* fields, i.e. $\mathbf{E} = \hat{\mathbf{e}}_E\mathcal{E}(x)$ and $\mathbf{B} = \hat{\mathbf{e}}_B\mathcal{E}(x)$, the normalized field strength tensor is independent of x.[6]

The two-photon polarization tensor given by Eq. (4.7) together with Eq. (4.8) almost coincides with the weak-field expression of the polarization tensor for crossed pump fields obtained in the last chapter, cf. Eqs. (3.7) and (3.56). The main difference lies in the scope and range of applicability of the underlying procedures to arrive at the respective expressions: The formalism of the last chapter is not necessarily restricted to probe photons in the low-energy limit, and allows insights into effects related to higher orders in the pump field strength and even the nonperturbative strong-field limit. The trade-off is the restriction to only a few invariant polarization modes which preserve the Ward identity, and therefore the loss of information about processes which induce a change of the polarization properties of the probe photons. Contrarily, the procedure in the present chapter restricts the probe photons to the low-energy regime and, for crossed fields, only takes into account the lowest order in the pump field strength. On the upside, it is valid for probe photons of arbitrary polarization.

Equation (4.7) straightforwardly allows an analytical computation of the polarization tensors for pump field inhomogeneities $\mathcal{E}(x)$ for which we can calculate the Fourier transforms of $\mathcal{E}(x)$, $\mathcal{E}^2(x)$ and $\mathcal{E}^3(x)$. Taking, e.g., the constant pump field $\mathcal{E}(x) = \mathcal{E}$ yields delta functions $(2\pi)^4\delta^{(4)}(k + k')$ and $(2\pi)^4\delta^{(4)}(k + k' + k'')$, enforcing energy and momentum conservation. It is instructive to study the three-photon polarization tensor in the constant-field limit, for real ingoing and outgoing photons with four-mo-

[6] This is, e.g., the case for *linearly* polarized Gaussian laser beams in the paraxial approximation. Note, however, that for *circularly* polarized pump beams traveling, e.g., in the z direction the normalized field strength tensor is a function of $(\mathrm{z} - t)$. In this work we limit ourselves to the study of linearly polarized pump fields.

menta $k^2 = k'^2 = k''^2 = 0$. In this case all three photons propagate collinearly and the combination $\delta^{(4)}(-k+k'+k'')c_{(1)}^{\rho\sigma\eta}(-\hat{k},\hat{k}',\hat{k}'') = \delta^{(4)}(k-k'-k'')c_{(1)}^{\rho\sigma\eta}(\hat{k},-\hat{k}',-\hat{k}'')$ vanishes.[7] Consequentially, in the constant-field limit the lowest-order contributions to the three-photon polarization tensor are of $\mathcal{O}\big((\frac{e\mathcal{E}}{m^2})^3\big)$, which is a manifestation of the Adler-theorem [25]. First-order contributions, on the other hand, are only expected to become relevant for inhomogeneities facilitating an appreciable momentum transfer, such that the propagation directions of the photons notably differ from each other.

4.2. Amplitude for splitting and merging

In a straightforward generalization of Sect. 3.2.1, we can write down the amplitude $\mathcal{M}_{\text{Split}}^{p\to p'p''}(k',k'')$ for photons from a macroscopic probe photon field $a_\rho^{(p)}(q)$, with momentum q^μ and polarization vector $\epsilon_\rho^{(p)}(q)$, to split into two real photons with momenta $k'^\mu = (|\mathbf{k}'|,\mathbf{k}')$ and $k''^\mu = (|\mathbf{k}''|,\mathbf{k}'')$, and polarization vectors $\epsilon_\sigma^{*(p')}(k')$ and $\epsilon_\eta^{*(p'')}(k'')$ respectively,

$$\mathcal{M}_{\text{Split}}^{p\to p'p''}(k',k'') = \frac{\epsilon_\sigma^{*(p')}(k')}{\sqrt{2|\mathbf{k}'|}}\frac{\epsilon_\eta^{*(p'')}(k'')}{\sqrt{2|\mathbf{k}''|}}\int_q \Pi^{\rho\sigma\eta}(-q,k',k''|F)a_\rho^{(p)}(q)\,. \tag{4.11}$$

As before, p labels the two transverse photon polarizations. Likewise, the amplitude $\mathcal{M}_{\text{Merg}}^{p'p''\to p}(k)$ for merging photons from macroscopic probe fields to yield a single outgoing photon with momentum $k^\mu = (|\mathbf{k}|,\mathbf{k})$ and polarization vector $\epsilon_\rho^{*(p)}(k)$ reads

$$\mathcal{M}_{\text{Merg}}^{p'p''\to p}(k) = \frac{\epsilon_\rho^{*(p)}(k)}{\sqrt{2|\mathbf{k}|}}\int_{q'}\int_{q''}\Pi^{\rho\sigma\eta}(k,-q',-q''|F)a'_\sigma{}^{(p')}(q')a''^{(p'')}_\eta(q'')\,. \tag{4.12}$$

Here we accounted for the most generic situation, where the merged photons are originating from two distinct probe photon fields $a'_\sigma{}^{(p')}(q')$ and $a''^{(p'')}_\eta(q'')$ with polarizations p' and p'', respectively.

The most generic macroscopic photon field propagating on the light cone can be represented in momentum space via $a_\nu(k) = \frac{\mathfrak{E}}{2\omega}\epsilon_\nu^{(p)}(k)(2\pi)\delta(\omega-|\mathbf{k}|)a(\mathbf{k})$, with peak field strength $\mathfrak{E}$, frequency ω and arbitrary spectral composition $a(\mathbf{k})$.[8] The differential number $\mathrm{d}\mathcal{N}$ of induced photons from photon splitting or merging is obtained by Fermi's

[7] Here we have accounted for the relative sign for ingoing and outgoing photons, cf. Eqs. (4.11) and (4.12).

[8] The corresponding photon field in position space reads $a_\nu(x) = \int_{\mathbf{k}}\frac{\mathfrak{E}}{2\omega(\mathbf{k})}\epsilon_\nu^{(p)}(k)a(\mathbf{k})\mathrm{e}^{i(\mathbf{kx}-\omega t)}$.

Golden Rule,

$$\mathrm{d}^6\mathcal{N}^{\mathrm{Split}} = \frac{\mathrm{d}^3k'}{(2\pi)^3}\frac{\mathrm{d}^3k''}{(2\pi)^3}\left|\mathcal{M}^{\mathrm{Split}}(k',k'')\right|^2, \qquad \mathrm{d}^3\mathcal{N}^{\mathrm{Merg}} = \frac{\mathrm{d}^3k}{(2\pi)^3}\left|\mathcal{M}^{\mathrm{Merg}}(k)\right|^2, \quad (4.13)$$

resulting in

$$\mathrm{d}^6\mathcal{N}^{\mathrm{Split}}_{p\to p',p''} = \frac{\mathrm{d}^3k'}{(2\pi)^3}\frac{\mathrm{d}^3k''}{(2\pi)^3}\left|\mathfrak{E}\left(\int_{\mathbf{q}}\frac{a(\mathbf{q})}{2|\mathbf{q}|}\epsilon^{(p)}_\rho(q)\Pi^{\rho\sigma\eta}(-q,k',k'')\right)\frac{\epsilon^{*(p')}_\sigma(k')}{\sqrt{2\omega'}}\frac{\epsilon^{*(p'')}_\eta(k'')}{\sqrt{2\omega''}}\right|^2, \quad (4.14)$$

and

$$\mathrm{d}^3\mathcal{N}^{\mathrm{Merg}}_{p',p''\to p} = \frac{\mathrm{d}^3k}{(2\pi)^3}\left|\frac{\epsilon^{*(p)}_\rho(k)}{\sqrt{2\omega}}\,\mathfrak{E}'\mathfrak{E}''\int_{\mathbf{q}'}\int_{\mathbf{q}''}\frac{a(\mathbf{q}')}{2|\mathbf{q}'|}\frac{a(\mathbf{q}'')}{2|\mathbf{q}''|}\Pi^{\rho\sigma\eta}(k,-q',-q'')\epsilon^{(p')}_\sigma(q')\epsilon^{(p'')}_\eta(q'')\right|^2, \quad (4.15)$$

with $q^\mu = (|\mathbf{q}|,\mathbf{q})$. Equations (4.14) and (4.15) together with (4.5) allow the investigation of splitting and merging for arbitrary pump and probe beams subject to the low-energy approximation $\{\omega,\omega',\omega''\} \ll m$.

As in Chap. 3 we limit ourselves to incoming probe beams modeled as monochromatic and linearly polarized plane waves $a^{(p)}_\nu(x) = \frac{1}{2}\frac{\mathfrak{E}}{\omega}\epsilon^{(p)}_\nu(\hat{k})\,\mathrm{e}^{i\omega(\hat{k}x)}$. We can then express the field strength of the probe beams through the time averaged intensity $\mathfrak{E} = \sqrt{2\langle I\rangle}$, which in turn is related to the photon current density $J = \frac{\mathcal{N}}{\sigma T}$ (i.e. the number of photons $\mathcal{N}$ passing through an area σ in a certain time interval T) via $\langle I\rangle = \omega J$. Hence, the differential numbers of induced photons due to splitting and merging can be compactly written as

$$\mathrm{d}^6\mathcal{N}^{p\to p'p''}_{\mathrm{Split}} = J\frac{\mathrm{d}^3k'}{(2\pi)^3}\frac{\mathrm{d}^3k''}{(2\pi)^3}\left|\frac{\epsilon^{(p)}_\rho(k)}{\sqrt{2\omega}}\Pi^{\rho\sigma\eta}(-k,k',k'')\frac{\epsilon^{*(p')}_\sigma(k')}{\sqrt{2\omega'}}\frac{\epsilon^{*(p'')}_\eta(k'')}{\sqrt{2\omega''}}\right|^2, \quad (4.16)$$

$$\mathrm{d}^3\mathcal{N}^{p'p''\to p}_{\mathrm{Merg}} = J'\,J''\frac{\mathrm{d}^3k}{(2\pi)^3}\left|\frac{\epsilon^{*(p)}_\rho(k)}{\sqrt{2\omega}}\,\Pi^{\rho\sigma\eta}(k,-k',-k'')\frac{\epsilon^{(p')}_\sigma(k')}{\sqrt{2\omega'}}\frac{\epsilon^{(p'')}_\eta(k'')}{\sqrt{2\omega''}}\right|^2. \quad (4.17)$$

4.3. Polarization properties

In this section we discuss the polarization properties pertaining to photon splitting and merging for a unidirectional crossed pump field. Without loss of generality we assume $\hat{\mathbf{e}}_E = \cos\varphi\,\hat{\mathbf{e}}_\mathrm{x} + \sin\varphi\,\hat{\mathbf{e}}_\mathrm{y}$ and $\hat{\mathbf{e}}_B = \hat{\mathbf{e}}_E\big|_{\varphi\to\varphi+\frac{\pi}{2}}$, where the direction of the field vectors in the x-y plane is parametrized by the angle $\varphi \in [0,2\pi)$ (see Fig. 4.2). The normalized Poynting vector of the pump field (cf. Sect. (3.2.4)) is therefore given by

$\hat{\mathbf{s}} = \hat{\mathbf{e}}_z$. Switching to spherical polar coordinates, a probe photon's momentum points in the direction $\hat{\mathbf{k}} = (\cos\phi\sin\theta, \sin\phi\sin\theta, \cos\theta)$. Furthermore, we define its polarization four-vector for the polarization mode $p = 1$ as $\epsilon_\mu^{(1)}(k) = \big(0, \boldsymbol{\epsilon}^{(1)}(k)\big)$, with

$$\boldsymbol{\epsilon}^{(1)}(k) = \begin{pmatrix} \cos\theta\,\cos\phi\,\sin\gamma - \sin\phi\,\cos\gamma \\ \cos\theta\,\sin\phi\,\sin\gamma + \cos\phi\,\cos\gamma \\ -\sin\theta\,\sin\gamma \end{pmatrix}. \tag{4.18}$$

The corresponding second transverse polarization mode can be obtained by appropriately shifting γ: $\epsilon_\mu^{(2)}(k) = \epsilon_\mu^{(1)}(k)\big|_{\gamma\to\gamma-\frac{\pi}{2}}$. The photon's state is therefore completely characterized by its energy ω and the set of angles $\Phi := \{\theta, \phi, \gamma\}$.[9] Here, $\gamma \in [0, 2\pi)$ determines the orientation of the trihedron formed by $\hat{\mathbf{k}}$, $\boldsymbol{\epsilon}^{(1)}(k)$ and $\boldsymbol{\epsilon}^{(2)}(k)$, such that for $\gamma = 0$ the polarization vector $\boldsymbol{\epsilon}^{(1)}(k)$ lies in the x-y plane, while $\boldsymbol{\epsilon}^{(2)}(k)$ lies in the plane spanned by $\hat{\mathbf{e}}_z$ and $\hat{\mathbf{k}}$. For $\theta \in \{0, \pi\}$ both polarization vectors lie in the x-y plane. In the following it will suffice to perform the analysis exclusively for the choice $p = p' = p'' = 1$, as all other linear photon polarizations can be addressed by shifting γ, γ' and γ'' accordingly. In order to calculate contractions of the photon polarization tensor with the polarization vectors according to Eqs. (4.16) and (4.17), we define the *polarization overlap functions*

$$c_{(n)}^{pp'p''}(\Phi, \Phi', \Phi'', \varphi) := \epsilon_\rho^{(p)}(k)\epsilon_\sigma^{(p')}(k')\epsilon_\eta^{(p'')}(k'')c_{(n)}^{\rho\sigma\eta}(\hat{k}, \hat{k}', \hat{k}'')\,. \tag{4.19}$$

Recall, that the label n refers to the contributions linear ($n = 1$) and cubic ($n = 3$) in external field amplitude. We obtain

$$\begin{aligned} c_{(1)}^{111}(\Phi, \Phi', \Phi'', \varphi) =& 2\sin^2\frac{\theta''}{2}\Big(\big[(1 - \cos\theta\cos\theta')\cos(\phi - \phi') - \sin\theta\sin\theta'\big] \\ &\times \big[4\sin\delta''\cos(\gamma + \gamma') + 7\cos\delta''\sin(\gamma + \gamma')\big] \\ &+ (\cos\theta - \cos\theta')\sin(\phi - \phi') \\ &\times \big[4\sin\delta''\sin(\gamma + \gamma') - 7\cos\delta''\cos(\gamma + \gamma')\big]\Big) \\ &+ \text{cyclic perm. of } \Phi, \Phi', \Phi''\ , \end{aligned} \tag{4.20}$$

[9] In particular, this definition of the polarization four-vectors is independent of the orientation of the field strength vectors $\mathbf{E}$ and $\mathbf{B}$ of the pump field, as opposed to Eq. (B.22).

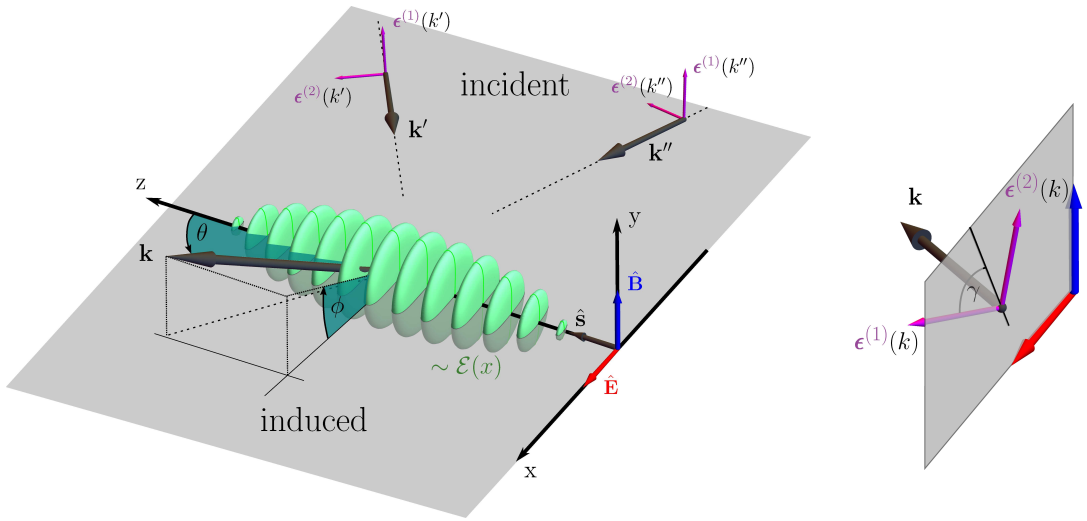

Figure 4.2.: **Left:** Geometry of photon merging in a localized pump field inhomogeneity with mutually perpendicular $\mathbf{E}$, $\mathbf{B}$ and $\hat{\mathbf{s}} \sim \hat{\mathbf{e}}_z$ for the particular choice of $\varphi = 0$. In this field configuration, two incoming probe photons with momenta $\mathbf{k}'$ and $\mathbf{k}''$ may merge into one photon with momentum $\mathbf{k}$. For photon splitting (not depicted) the roles are reversed: An incident photon with momentum $\mathbf{k}$ may split into two photons with momenta $\mathbf{k}'$ and $\mathbf{k}''$. The polarization degrees of freedom of the photons are spanned by the unit vectors $\boldsymbol{\epsilon}^{(1)}(q)$ and $\boldsymbol{\epsilon}^{(2)}(q)$, where $q \in \{k, k', k''\}$. This figure depicts the special case where the incident photons propagate in the x-z plane, and $\gamma' = \gamma'' = 0$. **Right:** The convention for the trihedron composed of $\hat{\mathbf{k}}$, $\boldsymbol{\epsilon}^{(1)}(k)$ and $\boldsymbol{\epsilon}^{(2)}(k)$ is such that for $\gamma = 0$ the polarization vector $\boldsymbol{\epsilon}^{(1)}(k)$ lies in the x-y plane (shaded area). (Both figures are taken from Ref. [45].)

and

$$c_{(3)}^{111}(\Phi, \Phi', \Phi'', \varphi) = -8 \sin^2\frac{\theta}{2} \sin^2\frac{\theta'}{2} \sin^2\frac{\theta''}{2} \Big(24 \sin\delta \sin\delta' \sin\delta'' + 13 \big[\sin\delta \cos\delta' \cos\delta'' + \cos\delta \sin\delta' \cos\delta'' + \cos\delta \cos\delta' \sin\delta'' \big] \Big) , \tag{4.21}$$

with $\delta := \varphi - \gamma - \phi$, and likewise for the primed quantities. As we are dealing with unidirectional pump fields, the polarization overlap functions are independent of the pump field profile $\mathcal{E}(x)$. The amplitude for photon splitting and merging thus decomposes into two independent factors: The polarization overlap function encodes all effects pertaining to the polarization of the incoming and outgoing photons, while the Fourier transform of the pump field profile encodes the momentum and energy transfers between the photons.

Examining Eqs. (4.20) and (4.21) more closely, we find that the polarization overlap

functions are symmetric with respect to Φ, Φ' and Φ''. Furthermore, if two photons, say Φ and Φ', propagate parallelly, the term proportional to $\sin^2 \frac{\theta''}{2}$ in $c_{(1)}^{pp'p''}$ vanishes, as then $\theta = \theta'$ and $\phi = \phi'$. Correspondingly, if the propagation directions of all three photons coincide, $c_{(1)}^{pp'p''}$ vanishes and, in accordance with the Adler-theorem, the three-photon amplitudes are cubic in the pump field strength. We also note that $c_{(1)}^{pp'p''}$ and $c_{(3)}^{pp'p''}$ differ with respect to photon propagation along the pump field's normalized Poynting vector $\hat{\mathbf{s}} = \hat{\mathbf{e}}_z$. Generically, $c_{(1)}^{pp'p''} \neq 0$ if at least one photon's propagation direction differs from $\hat{\mathbf{e}}_z$, while $c_{(3)}^{pp'p''}$ vanishes if at least one photon propagates along $\hat{\mathbf{e}}_z$. The latter property corresponds to the already discussed observation that photon propagation in constant-crossed pump fields is not modified if $(\hat{\mathbf{k}}, \hat{\mathbf{e}}_E, \hat{\mathbf{e}}_B)$ form the basis of a right-handed orthogonal coordinate system [28]. We find that the amplitudes for splitting and merging in the limit of constant crossed pump fields behave in a similar fashion, as in this limit they are determined by $c_{(3)}^{pp'p''}$ to leading order in the pump field strength.

The selection rules for the merging and splitting processes are a consequence of the structure of the Heisenberg-Euler Lagrangian, which in turn stems from CP invariance of QED. They determine the allowed interactions between ingoing and outgoing photons in the "slow" (s) and "fast" (f) modes. These modes correspond to the pump-field--dependent polarization four-vectors $(k^\star \hat{F})^\mu$ and $(k\hat{F})^\mu$: The polarization $a^\mu \sim (k^\star \hat{F})^\mu$ constitutes the slow mode of propagation, since the external field reduces the photon's phase velocity to $v_{\mathrm{ph}}^{(\mathrm{s})} \simeq 1 - \frac{14}{45}\frac{\alpha}{4\pi}\rho(\frac{\mathcal{E}}{\mathcal{E}_{\mathrm{cr}}})^2$ (where ρ is a purely geometrical factor [28]). Correspondingly, $(k\hat{F})^\mu$ describes the fast mode with $v_{\mathrm{ph}}^{(\mathrm{f})} \simeq 1 - \frac{8}{45}\frac{\alpha}{4\pi}\rho(\frac{\mathcal{E}}{\mathcal{E}_{\mathrm{cr}}})^2 \geq v_{\mathrm{ph}}^{(\mathrm{s})}$. In Table 4.1 we list the resulting selection rules. As merging and splitting are both inferred from the same tensor structures $c_{(n)}^{\rho\sigma\eta}(k, k', k'')$, they are governed by the same selection rules. For processes cubic in the pump field ($n = 3$), only those involving either three fast, or one fast and two slow photons are permitted. This coincides with the well-known selection rules for splitting and merging in constant-crossed fields [87]. However, inhomogeneous pump fields give rise to processes linear in the pump field strength ($n = 1$), possibly dominating over those cubic in the field strength. This generically lifts the selection rules set by $c_{(3)}^{\rho\sigma\eta}(k, k', k'')$, as the leading order is now determined by $c_{(1)}^{\rho\sigma\eta}(k, k', k'')$, see Table 4.1 (middle column).

Note that for the explicit calculations performed here we have employed the polarization four-vectors $\epsilon_\mu^{(p)}(k)$. In contrast to $(k^\star \hat{F})^\mu$ and $(k\hat{F})^\mu$, the $\epsilon_\mu^{(p)}(k)$ form a polarization basis which is independent of the pump field. By properly adjusting the orientation γ both sets of basis vectors can be brought into agreement. Generically, the appropriate choice of γ depends on the propagation direction $\mathbf{k}$ of the considered photon. An

(Splitting), (Merging)	Allowed?		In x-z plane, $\varphi = 0$
	$n = 1$	$n = 3$	$n = 1, 3$
(s $\to$ s′,s″) , (s′,s″ $\to$ s)	Yes	No	No
(f $\to$ f′,f″) , (f′,f″ $\to$ f)	Yes	Yes	Yes
(s $\to$ f′,f″) , (f′,f″ $\to$ s) (f $\to$ s′,f″) , (s′,f″ $\to$ f) (f $\to$ f′,s″) , (f′,s″ $\to$ f)	Yes	No	No
(s $\to$ s′,f″) , (s′,f″ $\to$ s) (f $\to$ s′,s″) , (s′,s″ $\to$ f) (s $\to$ f′,s″) , (f′,s″ $\to$ s)	Yes	Yes	Yes

Table 4.1.: Selection rules for photon splitting and merging for generic propagation directions (middle column), as well as the special case where all photons propagate in the x-z plane and the choice $\varphi = 0$ for the pump field polarization (right column). These selection rules can be inferred from the tensor structures $c_{(n)}^{\rho\sigma\eta}(k, k', k'')$ in Eqs. (4.20) and (4.21). Here, "s" ("f") denotes probe photons polarized in the "slow" ("fast") polarization mode in the pump field. Photon splitting and merging are governed by the same selection rules. The selection rules for processes which are cubic in the pump field strength ($n = 3$) agree with the well-known rules valid in the constant-field limit [87]. By contrast, first-order processes ($n = 1$) generically lift the restrictions for the $n = 3$ case, unless the wave vectors of all probe photons are confined to the x-z plane, i.e., for $\phi, \phi', \phi'' \in \{0, \pi\}$, and $\varphi = 0$ (right column). For this special case we have $\epsilon_\mu^{(1)}(k)|_{\phi\in\{0,\pi\},\gamma=0} \sim (k^\star \hat{F})_\mu$ and $\epsilon_\mu^{(1)}(k)|_{\phi\in\{0,\pi\},\gamma=\frac{\pi}{2}} \sim (k\hat{F})_\mu$, such that the "s" ("f") polarization mode corresponds to the choice of $\gamma = 0$ ($\gamma = \frac{\pi}{2}$), cf. the main text.

exception is given by restricting photon propagation to the x-z plane and specializing to $\varphi = 0$. This scenario corresponds to the one depicted in Fig. 4.2. Then we find that the choice $\gamma = 0$ corresponds to the slow photon mode, $\epsilon_\mu^{(1)}(k)|_{\phi\in\{0,\pi\},\gamma=0} \sim (k^\star \hat{F})_\mu$, and $\gamma = \frac{\pi}{2}$ to the fast mode, $\epsilon_\mu^{(1)}(k)|_{\phi\in\{0,\pi\},\gamma=\frac{\pi}{2}} \sim (k\hat{F})_\mu$. Most notably, for this special scenario the selection rules for $n = 1$ and $n = 3$ coincide, cf. Table 4.1 (right column).

4.4. Towards experimental estimates

In analogy to Sect. 3.2.6 we estimate the number of induced photons due to splitting and merging for a spatially localized pump field profile resembling the focal spot of a high-intensity laser pulse. As our formalism allows the investigation of 3+1 dimensional inhomogeneities, we extend the unidirectional pump field profile (3.101) considered for quantum reflection to

$$\left(\frac{e\mathcal{E}(x)}{m^2}\right) = \left(\frac{e\mathcal{E}}{m^2}\right) \mathrm{e}^{-\left(\frac{2r}{w_0}\right)^2} \mathrm{e}^{-\left(\frac{2\mathrm{z}}{w_\mathrm{z}}\right)^2} \mathrm{e}^{-\left(\frac{2(\mathrm{z}-t)}{\tau}\right)^2} \cos\bigl(\Omega(\mathrm{z}-t)\bigr)\,, \tag{4.22}$$

where $r = \sqrt{\mathrm{x}^2+\mathrm{y}^2}$ and the transversal $\frac{1}{e}$-width has been labeled w_0. Similar to the experimental investigation of quantum reflection, we have adopted a simplified field profile by neglecting beam widening effects and substituting the longitudinal Lorentz profile of a Gaussian beam by an exponential profile, cf. Sect. 3.2.6. This has been done to obtain more compact formulae due to the appearance of Gaussian integrals in Eq. (4.7). Plugging the field profile (4.22) into the polarization tensor, and inserting the resulting expression into Eqs. (4.16) and (4.17), we find for the differential number of induced photons due to splitting and merging

$$\begin{aligned}\begin{Bmatrix} \mathrm{d}^6\mathcal{N}^{p\to p'p''}_{\text{Split}} \\ \mathrm{d}^3\mathcal{N}^{p'p''\to p}_{\text{Merg}} \end{Bmatrix} \;=\; & \begin{Bmatrix} \frac{J}{(2\pi)^3}\mathrm{d}^3k'\mathrm{d}^3k'' \\ J'J''\mathrm{d}^3k \end{Bmatrix} \frac{w_0^4 w_\mathrm{z}^2\tau^2\alpha^2}{11520^2\pi} \left(\frac{e\mathcal{E}}{m^2}\right)^2 \left(\frac{e}{m^2}\right)^2 \omega\omega'\omega'' \\ & \times \Bigg| c^{pp'p''}_{(1)}(\Phi,\Phi',\Phi'',\varphi) \sum_{\ell=\pm1} \mathrm{e}^{-\frac{1}{16}\left[w_0^2(q_\mathrm{x}^2+q_\mathrm{y}^2)+w_\mathrm{z}^2(q^0-q_\mathrm{z})^2+\tau^2(q^0+\ell\Omega)^2\right]} \\ & \quad -\frac{1}{63}\left(\frac{e\mathcal{E}}{m^2}\right)^2 c^{pp'p''}_{(3)}(\Phi,\Phi',\Phi'',\varphi) \\ & \quad \times \sum_{\ell=0}^{3}[1+\ell(3-\ell)]\mathrm{e}^{-\frac{1}{48}\left[w_0^2(q_\mathrm{x}^2+q_\mathrm{y}^2)+w_\mathrm{z}^2(q^0-q_\mathrm{z})^2+\tau^2(q^0+(3-2\ell)\Omega)^2\right]}\Bigg|^2 . \end{aligned} \tag{4.23}$$

Here, $q^\mu := k^\mu - k'^\mu - k''^\mu$ denotes the four-momentum exchange of the probe and signal photons, measuring the deviation from the four-momentum conservation law in constant pump fields, $q^\mu|_{\text{const. pump}} = 0$. Equation (4.23) is composed of contributions linear and cubic in the pump field strength. The former entails processes where the probe photon beam exchanges a single photon of frequency Ω with the pump field, while the latter encodes energy transfers $\{3\Omega, \Omega, -\Omega, -3\Omega\}$. On the level of the amplitude, the cubic process is generally suppressed by a factor $\left(\frac{e\mathcal{E}}{m^2}\right)^2$ compared to the linear process. However, the exponential momentum suppression for the cubic process is

smaller than for the linear process (as observed by the prefactors in the exponentials, $\frac{1}{48}$ vs. $\frac{1}{16}$), therefore allowing for kinematic situations where cubic processes dominate over linear ones.

The emission characteristics for splitting and merging are determined by both the exponential terms in Eq. (4.23) as well as the polarization overlap functions. As mentioned before, the former encode momentum and energy conservation, and a maximum of induced signal photons will occur for those parameters which lead to the vanishing of all arguments of the exponential functions. For this, the interacting photons must necessarily fulfill $\omega - \omega' - \omega'' + \ell\Omega = 0$, with $\ell \in \{-3, -1, 1, 3\}$. A specific set of energies then results in a relation for the corresponding polar angles $\{\theta, \theta', \theta''\}$: $\omega \cos\theta + \ell\Omega = \omega' \cos\theta' + \omega'' \cos\theta''$ from z-momentum conservation. The emission characteristics in the x-y plane are determined by $k_\mathrm{x} - k'_\mathrm{x} - k''_\mathrm{x} = 0$ and $k_\mathrm{y} - k'_\mathrm{y} - k''_\mathrm{y} = 0$. These relations enable us to obtain estimates of the incidence directions of the probe photons maximizing the signal for certain directions of the outgoing photons, similar to Fig. 3.10. As we are dealing with a pump beam of finite spatial and temporal extent, the spread of the signal will furthermore be determined by the focussing parameters $\{w_0, w_\mathrm{z}\}$ and the pulse duration τ of the pump beam.

The microscopic amplitudes for splitting and merging are fully determined by the three-photon polarization tensor. The macroscopic number of induced photons, however, scales differently for splitting and merging: The former is linear in the macroscopic probe photon field, while the latter is quadratic. From the parametric analysis in Sect. F.2, we find that to linear order in the pump field strength the ratio of $\mathcal{N}_\mathrm{Split}$ to $\mathcal{N}_\mathrm{Merg}$ scales as $\frac{\mathcal{N}_\mathrm{Split}}{\mathcal{N}_\mathrm{Merg}} \sim \left(\frac{v}{m}\right)^4 \left(\frac{e\mathfrak{E}}{m^2}\right)^{-2}$, assuming identical field strengths $\mathfrak{E}$ for the probe photon fields. Set-ups with high-intensity optical lasers ($\frac{v}{m} \ll 1$) as considered here therefore strongly favor the merging process. In fact, employing parameters for a typical set-up consisting of state-of-the-art optical high-intensity lasers, we find $\frac{\mathcal{N}_\mathrm{Split}}{\mathcal{N}_\mathrm{Merg}} \sim \frac{\omega^4_\mathrm{probe}}{\mathfrak{E}^2} \sim 10^{-16}$.

In the experimental analysis to follow, we will therefore solely focus on photon merging. It should be noted that our formalism is then a generalization of the four-wave mixing scenario suggested in Refs. [125, 126]. The latter scenario focusses on the mixing of three incident photon waves from the outset to address elastic photon-photon scattering with high-power lasers. Both scenarios have the use of high-intensity lasers in common as well as the same underlying set of Feynman diagrams. However, with the help of the formalism developed in this work we may consider the merging of two photon waves in a pump field inhomogeneity which is not restricted to the electromagnetic field of a propagating laser beam. Our formalism generalizes straightforwardly to any

Set-up	$W_{\text{pump}}/W_{\text{probe}}$[J]	$\lambda_{\text{pump}}/\lambda_{\text{probe}}$[nm]	$\tau_{\text{pump}}/\tau_{\text{probe}}$[fs]
(a) POLARIS+JETI	150 / 2×2	1030 / 800	150 / 20
(b) Vulcan 1PW (SHG)	250 / 2×62.5	1053 / 526.5	500 / 500
(c) ELI-NP 2×1PW (SHG)	25 / 2×6.25	800 / 400	25 / 25

Table 4.2.: Design parameters for the pump-probe set-ups considered in this section to investigate photon merging (see the main text for more details).

inhomogeneous pump field. As such, in our approach we can naturally make contact with the constant crossed-field limit for the pump field configuration as well as read off the various selection rules which govern the photon merging process, cf. Sect 4.3.

We analyze photon merging for the Set-ups (a)-(c) consisting of high-intensity optical lasers, listed in Table 4.2. They are similar to the Set-ups (1), (3) and (4) which have been employed for the experimental analysis of quantum reflection (cf. Table 3.1). Set-up (a) employs the POLARIS laser as pump, and the JETI200 laser is split into two beams of equal power to constitute the probe beams. For Set-up (b) we split the 1PW beam from the Vulcan laser into a pump and a probe beam of equal power. The probe beam is then again split into two beams of equal power, which are each then frequency doubled. The energy loss Q due to conversion to the SHG is estimated as $Q = 0.5$, while the pulse length is assumed to be unaffected by the frequency doubling process. Set-up (c) consists of one 1PW beam as pump, and the other 1PW beam split into two frequency doubled beams of equal power. Note that for the last two set-ups employing frequency doubled beams is a necessary requirement to obtain a sizable number of merged photons for the set-ups under consideration below, as the relations pertaining to the conservation of energy and momentum cannot be simultaneously fulfilled for pump and probe beams with equal wavelengths.

Employing the values listed in Table 4.2, we use the same relations as detailed in Sect. 3.2.6 to determine the parameters appearing in Eq. (4.23): $w_0 = 2\lambda_{\text{pump}}$, $w_z = 2\pi\lambda_{\text{pump}}$, $\Omega = 2\pi/\lambda_{\text{pump}}$, $\tau = \tau_{\text{pump}}$ and $\omega' = \omega'' = \omega_{\text{probe}} = 2\pi/\lambda_{\text{probe}}$. Likewise, we use Eq. (3.104) to determine the maximum pump field strength $\mathcal{E}$. In contrast to Sect. 3.2.6, in this section we do not limit ourselves to probes with f-numbers $f^{\#} = 1$. Rather, we assume the probe beam's focal area to be $\sigma = \pi\rho^2\lambda_{\text{probe}}^2$, where we have introduced the focus parameter ρ measuring the beam waist in units of the wavelength. The diffraction limit is then given for $\rho = 1$. The photon currents associated with

incident probe beams are then estimated from

$$J = \frac{0.86}{2\pi^2} \frac{W_{\text{probe}}}{\tau_{\text{probe}} \rho^2 \lambda_{\text{probe}}} \min\left\{1, \frac{\tau_{\text{probe}}}{\tau_{\text{pump}}}\right\} \min\left\{1, \frac{\rho^2 \lambda_{\text{probe}}^2}{\lambda_{\text{pump}}^2}\right\}. \tag{4.24}$$

Here, we have introduced correction factors taking into account the finite temporal and spatial overlap between the pump and the probe beams, which become important if the probe is of shorter duration and/or has a smaller spot size than the pump.[10]

For simplicity, we limit ourselves to pump and probe beam propagation in the x-z

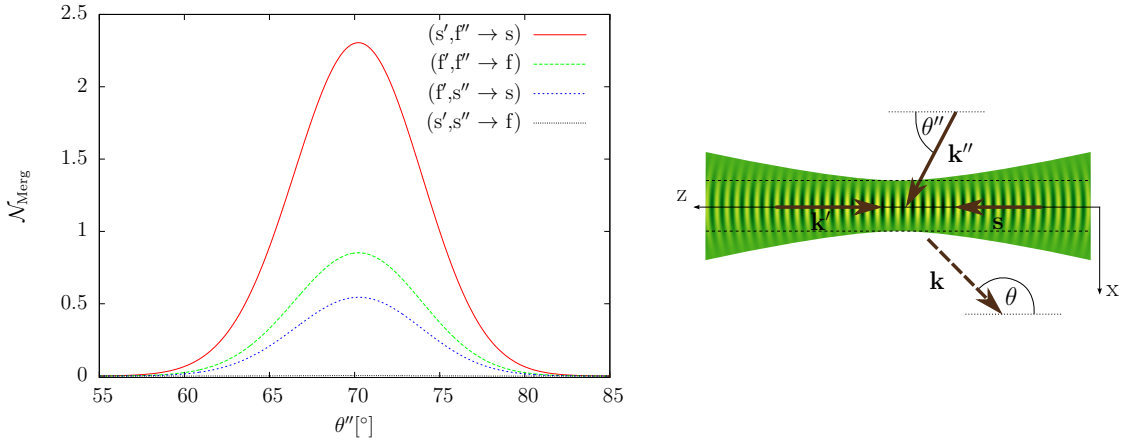

Figure 4.3.: **Left:** Total number of merged photons $\mathcal{N}_{\text{Merg}}$ for Set-up (c) as a function of the angle $\theta'' = \sphericalangle(\mathbf{k}'', \hat{\mathbf{e}}_z)$ attainable for the beam configuration sketched on the right panel. In the vicinity of the focal spot of a Gaussian beam, curvature effects can be neglected, justifying the simpler pump beam profile (4.22) employed in this work (indicated by the dashed lines). The result is obtained by an integration over the complete energy range and the full solid angle of the induced merged photons. We considered probe beams with focus parameters $\rho', \rho'' \leq 2$ propagating in the x-z plane, i.e. $\phi' = 0$, $\phi'' = 0$, and $\theta' = \pi$ (cf. also Fig. 4.2). The polarization of the pump beam is chosen as $\varphi = 0$. The plot depicts the number of merged photons for various polarization assignments of the probe photons, allowed according to the selection rules in Table 4.1 (right).

[10] It can be assumed that the principal contribution to the merging of photons comes from the region close to the peak of the pump beam. That means that for tightly focussed probe beams whose focal spots occupy an area smaller than the focal spot of the pump beam, and good temporal and spatial synchronization between pump and probe, the majority of incident probe photons will interact with the pump in the relevant region close the peak of the pump field. Therefore, the corrections introduced in (4.24) are rather conservative estimates of the interaction between the probe and pump beam. In particular, the spatial corrections introduced here will lead to values smaller than those obtained in Ref. [45], where such corrections have not been taken into account. To obtain a more precise estimate of the number of merged photons requires the modeling of the probe beams as temporally and spatially localized pulses. A recent analytical study in the context of vacuum birefringence can be found in Ref. [127].

plane, cf. Fig. 4.2 as well as Table 4.1 (last column). Furthermore, we choose the polarization of the pump beam as $\varphi = 0$. At first let us have a detailed look at only Set-up (c), where both probe beams are assumed to be focussed down to $\rho', \rho'' \leq 2$. The left panel of Fig. 4.3 shows the total number of merged photons for the geometry depicted on right panel. Here, the probe beam with $\mathbf{k}'$ counterpropagates with the pump beam, and the second probe beam hits the interaction area under an angle θ''. We see that a sizable number of merged photons is induced for the optimum angle $\theta''_{\max} \approx 70.5°$. Furthermore, the number of merged photons depends strongly on the polarization modes of the probe photons, with a maximum given for $\gamma = 0$, $\gamma' = 0$ and $\gamma'' = \frac{\pi}{2}$ (corresponding to the process $\mathrm{s}', \mathrm{f}'' \to \mathrm{s}$).

Figure 4.4 displays the emission characteristics for the optimum geometry with $\theta'' = \theta''_{\max} = 70.5°$, as shown in the right panel of Fig. 4.3. The top left panel shows the distribution of merged photons as a function of the polar angle θ, and the top right panel as a function of ϕ. In both cases the integrals for the remaining parameters have been performed over the entire parameter regime. From these plots we infer that the merged signal photons are predominantly emitted in the x-z plane, at an outgoing polar angle of $\theta_{\max} \approx 140.9°$. This result is also indicated in the right panel of Fig. 4.3, where the direction of the dashed arrow has been chosen accordingly. The divergence Θ of the induced photon number $\mathrm{d}\mathcal{N}_{\mathrm{Merg}}(\theta)$ is defined as half the $1/\mathrm{e}^2$-width, and can be read off from the top left panel of Fig. 4.4. For the process $\mathrm{s}', \mathrm{f}'' \to \mathrm{s}$ it has the value $\Theta \approx 3.9°$. This is much lower than, e.g., the divergence of a Gaussian beam focussed down to the diffraction limit. Note, however, that for more realistically modeled probe beams the divergence Θ of the signal is expected to increase, as the plane wave approximation adopted here does not take into account the divergence of the probe photons.

The bottom panel of Fig. 4.4 shows a logarithmic plot of the energy spectrum $\mathrm{d}\mathcal{N}_{\mathrm{Merg}}(\omega)$ of merged photons emitted into the full solid angle. Visible are the two contributions at $2\omega_{\mathrm{probe}} \pm \Omega$. The maximum at $\approx 4.65\mathrm{eV}$ stems from the process linear in the pump field strength, where the merged photon transfers an energy Ω to the pump field. However, moving away from the maximum we find a transition region at $\approx 4.6 \pm 0.4\mathrm{eV}$ beyond which the process cubic in the pump field strength dominates over the linear one. Hence, the second maximum at $\approx 7.65\mathrm{eV}$ is determined by the process cubic in the pump field strength, where the pump field supplies an energy Ω to the merged photon. Correspondingly, as the polarization properties at this maximum are governed by $c^{pp'p''}_{(3)}$, we find that the process yielding the largest number of merged photons is actually the one with $\mathrm{f}', \mathrm{f}'' \to \mathrm{f}$.

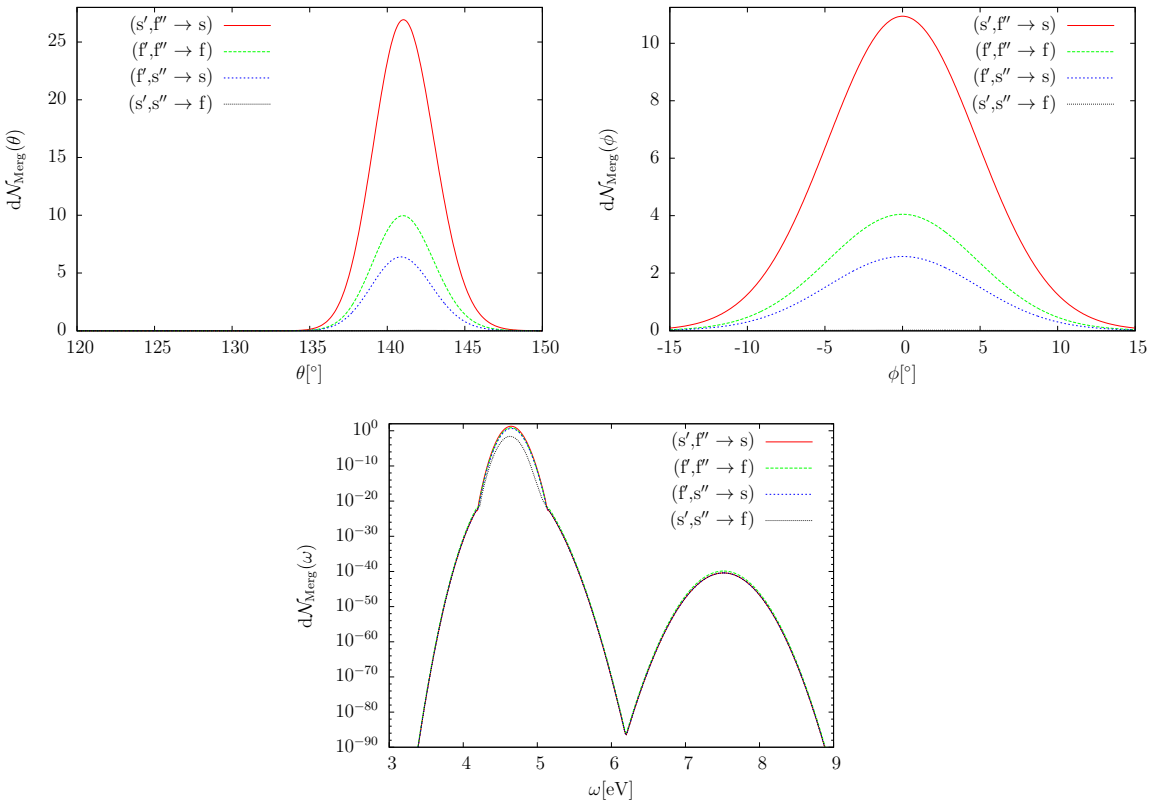

Figure 4.4.: Emission characteristics of the attainable number of merged photons for Set-up (c). The parameters of the incoming beams are chosen as $\theta' = \pi$, $\phi' = 0°$, $\theta'' = 70.5°$ and $\phi'' = 0$; the polarization of the pump beam is $\varphi = 0$. **Top left:** Differential photon number $\mathrm{d}\mathcal{N}_{\mathrm{Merg}}(\theta)$ as a function of the polar angle θ. **Top right:** $\mathrm{d}\mathcal{N}_{\mathrm{Merg}}(\phi)$ as a function of the polar angle ϕ. **Bottom:** Logarithmic plot of the energy spectrum $\mathrm{d}\mathcal{N}_{\mathrm{Merg}}(\omega)$. For each plot the integrations over the corresponding remaining parameters have been performed over the full parameter regime.

It should be noted that the experimental proposal shown in Fig. 4.3 is quite favorable for optimizing the signal-to-noise ratio as it induces a maximum of signal photons into regions where both the fields generated by the pump as well as the probe beams have decreased by several orders of magnitude from their peak value. This is illustrated in Fig. 4.5, which shows a logarithmic plot of the differential numbers of induced photons due to photon merging, $\frac{\mathrm{d}\mathcal{N}_{\mathrm{Merg}}}{\mathrm{d}\cos\theta}(\theta)$, and the differential number of photons originating from the pump and probe beams. The latter are collectively denoted by $\frac{\mathrm{d}\mathcal{N}_{\mathrm{bg}}}{\mathrm{d}\cos\theta}(\theta)$, and constitute the background noise. The probe beams have been modeled as Gaussian beams,[11] and the plot shows $\frac{\mathrm{d}\mathcal{N}_{\mathrm{bg}}}{\mathrm{d}\cos\theta}(\theta)$ for probe beams focussed down to the diffraction limit $\rho' = \rho'' = 1$ (brown curves), as well as for weaker focussing $\rho' = \rho'' = 2$ (violet

[11] More details are given in the appendix G.

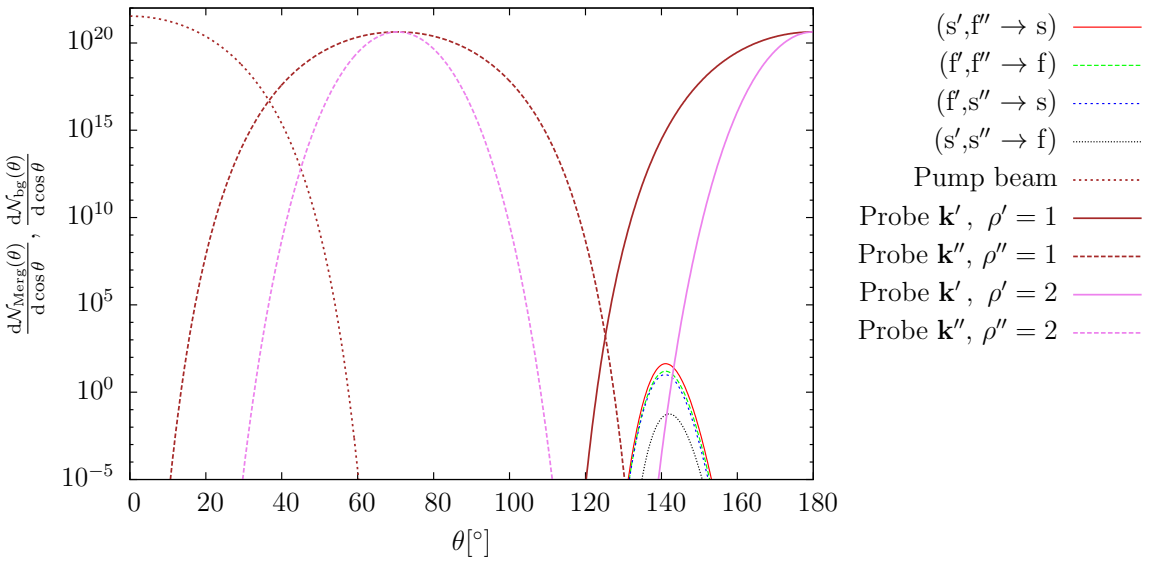

Figure 4.5.: Logarithmic plot of the differential number of induced photons $\frac{d\mathcal{N}_{Merg}}{d\cos\theta}(\theta)$ for the various polarization modes for Set-up (c), as well as the number of photons originating from the pump and the probe beams, $\frac{d\mathcal{N}_{bg}}{d\cos\theta}(\theta)$, as a function of the outgoing angle θ. The number of probe photons has been plotted for the focus parameters $\rho' = \rho'' = 1$ (brown), as well as $\rho' = \rho'' = 2$ (violet). In order to apply polarization filtering techniques, the polarization of the probe photons emitted around θ_{max} has to differ from the signal photons' polarization. This is the case for the configurations (f′,s″ → s) and (s′,s″ → f).

curves). For $\rho' = \rho'' = 1$, we find that the induced number of photons due to merging is generically lower than the number of probe photons in the same angular region. However, for $\rho' = \rho'' = 2$ the spread of the probe beams is smaller and we observe that there exists a small region where the number of merged photons is partially larger than the number of background photons.

To perform a more quantitative analysis, let us define the number of signal photons emitted into the angle interval $\theta_{max} - \Theta ... \theta_{max} + \Theta$ around the maximum emission direction θ_{max} of the signal photons as

$$\mathcal{N}^{p'p''\to p}_{\text{Merg},<\Theta} := \int_{\theta_{max}-\Theta}^{\theta_{max}+\Theta} \frac{d\mathcal{N}^{p'p''\to p}_{\text{Merg}}}{d\theta}(\theta)d\theta\,. \tag{4.25}$$

Similarly, let

$$\mathcal{N}^{p'}_{<\Theta} := \int_{\theta_{max}-\Theta}^{\theta_{max}+\Theta} \frac{d\mathcal{N}^{p'}_{<\Theta}}{d\theta}(\theta)d\theta \tag{4.26}$$

denote the number of photons belonging to the probe beam $\mathbf{k}'$ with polarization p',

emitted into the same angular region (and likewise for the probe beam with $\mathbf{k}''$ and p''). Together with the pump beam photons, whose polarization we denote by $\tilde{p}$, they constitute the total background noise $\mathcal{N}_{\mathrm{bg}}^{<\Theta}$. Let us introduce the ratio $r_{<\Theta}^{(\parallel)}$ ($r_{<\Theta}^{(\perp)}$) of signal photons of a certain polarization p and background photons of the same (perpendicular) polarization emitted into the angular region $\theta_{\max}-\Theta ... \theta_{\max}+\Theta$ as

$$\begin{aligned} r_{<\Theta}^{(\parallel)} &:= \frac{\mathcal{N}_{\mathrm{Merg},<\Theta}^{p'p''\to p}}{\delta_{p'p}\,\mathcal{N}_{<\Theta}^{p'}+\delta_{p''p}\,\mathcal{N}_{<\Theta}^{p''}+\delta_{\tilde{p}p}\,\mathcal{N}_{<\Theta}^{\tilde{p}}}\,, \qquad \text{and} \\ r_{<\Theta}^{(\perp)} &:= \frac{\mathcal{N}_{\mathrm{Merg},<\Theta}^{p'p''\to p}}{(1-\delta_{p'p})\,\mathcal{N}_{<\Theta}^{p'}+(1-\delta_{p''p})\,\mathcal{N}_{<\Theta}^{p''}+(1-\delta_{\tilde{p}p})\,\mathcal{N}_{<\Theta}^{\tilde{p}}}\,. \end{aligned} \tag{4.27}$$

In principle, an experimental detection of the induced merging signal is only possible for configurations for which the ratio $r_{<\Theta}^{(\parallel)}$ is larger than the filtering efficiency achievable by means of frequency filtering techniques.[12] Otherwise, the signal is drowned by background photons of identical polarization as the signal.

For simplicity, in this work we restrict ourselves to configurations featuring ratios $r_{<\Theta}^{(\parallel)} \gg 1$, i.e. those for which the number of background photons of identical polarization as the signal is negligible with respect to the signal. Referring to Fig. 4.5 we find that the dominant source of background photons around $\theta_{\max}$ stems from the beam $\mathbf{k}'$, and therefore the processes (f′,s″ → s) and (s′,s″ → f) feature ratios $r_{<\Theta}^{(\parallel)} \gg 1$. For probe beams focussed down to the diffraction limit, $\rho' = \rho'' = 1$, we find $\mathcal{N}_{\mathrm{Merg},<\Theta}^{\mathrm{f}',\mathrm{s}''\to\mathrm{s}} \approx 0.52$ merged photons per laser shot and a signal-to-noise ratio of $r_{<\Theta}^{(\perp)} \approx 2.0\cdot 10^{-15}$, making the signal undetectable.[13] However, employing a weaker focussing of the probe beams significantly increases the signal-to-noise ratio, as the probe beam's divergence decreases. For example, increasing the focussing to $\rho' = 2$ and $\rho'' = 2$ yields the same number of merged signal photons, $\mathcal{N}_{\mathrm{Merg},<\Theta}^{\mathrm{f}',\mathrm{s}''\to\mathrm{s}} \approx 0.52$ (cf. Eq. (4.24) and the associated footnote), but an increased ratio of $r_{<\Theta}^{(\perp)} \approx 0.043$. Employing linear polarizers this should already allow for a separation of the signal from the background beam. For configurations with even larger focus parameters the ratio $r_{<\Theta}^{(\perp)}$ may increase further, but this generally has to be paid for with a lower signal photon yield, since a smaller

[12] Recall that the signal photon is an odd harmonic of the probe.

[13] Commercially available linear polarizers for beams in the near-UV energy range based on birefringent crystals, e.g. BBO, feature extinction ratios of 100,000:1, with transmission rates around $85-90\%$, see, e.g., Ref. [128]. Note that in this work we do not discuss additional noise sources such as those stemming from, e.g., an imperfect polarization of the probe beams or an imperfect vacuum in the interaction area. The latter has been discussed in Refs. [125, 126], finding that for a vacuum of 10^{-9}Torr the noise signal due to Compton scattering is several orders of magnitudes below the merged photon signal. Additional noise sources can be included in Eq. (4.27) by adding a term $\mathcal{N}_{<\Theta}^{\mathrm{noise}}$ to the denominators of $r_{<\Theta}^{(\parallel)}$ and $r_{<\Theta}^{(\perp)}$, thereby limiting their maximum values.

Set-up	$\theta''_{\max}$ [°]	$\theta_{\max}$ [°]	$\omega_{\max}$ [eV]	$\Theta(\frac{1}{e^2})$ [°]	$\Delta\omega(\frac{1}{e^2})$ [eV]
(a)	41.7	147.3	1.9	6.3	0.035
(b)	70.5	140.9	3.5	2.9	0.011
(c)	70.5	140.9	4.6	3.9	0.18

Table 4.3.: Comparison of the emission characteristics for the Set-ups (a)-(c) listed in Table 4.2, for the counterpropagating configuration shown in the right panel of Fig. 4.3.

fraction of probe photons traverses the interaction area. Correspondingly, employing probe beams with focus parameters $\rho' = 3$ and $\rho'' = 2$ yields $\mathcal{N}^{\mathrm{f}',\mathrm{s}''\to\mathrm{s}}_{\mathrm{Merg},<\Theta} \approx 0.23$ merged photons per laser shot and a ratio of $r^{(\perp)}_{<\Theta} \gg 1$, i.e. the signal is emitted into the background-free field region. Therefore, by appropriately varying the focussing of the probe beams we can identify configurations featuring signal-to-background ratios which, after employing polarization-discriminating filtering, allow for the use of sensitive single-photon detection schemes. On top of this, frequency filtering may additionally be used to further enhance the signal-to-background ratio.

To complete the discussion of the experimental detection of photon merging we compare the total number of merged photons for the Set-ups (a) - (c), listed in Table 4.2. For simplicity, we only look at the configuration shown in the right panel of Fig. 4.3, where one probe beam counterpropagates with the pump beam ($\theta' = \pi, \phi' = 0$) and the second probe beam enters under the angle θ'' from the upper half space ($\phi'' = 0$). The signal photons are then emitted into the lower half space, i.e. they are centered around $\phi = 0$ (cf. upper right panel of Fig. 4.4). The emission characteristics for the three set-ups are collected in Table 4.3. For probe beams of equal energy $\omega' = \omega''$ the values of the incidence and outgoing angles maximizing the photon merging signal depend only on the combination $\ell\frac{\Omega}{\omega'}$. Therefore, Set-ups (b) and (c) in Table 4.4 have identical values for $\theta''_{\max}$ and $\theta_{\max}$. Table 4.4 compares the numbers of merged photons and the signal-to-background ratio for Set-ups (a)-(c), employing various focussing parameters ρ' and ρ''. We concentrate only on the processes (f',s'' $\to$ s) and (s',s'' $\to$ f), as for these the polarization of the signal and background photons in the relevant region around $\theta_{\max}$ differ and we find $r^{(\parallel)}_{<\Theta} \gg 1$.

Set-up (a) features rather low numbers of merged photons, accompanied with low values for $r^{(\perp)}_{<\Theta}$. The latter is both a consequence of the rather large divergence Θ as well as the larger outgoing angle $\theta_{\max}$ of the signal beam, cf. Table 4.3, leading to an increased overlap of the signal and probe beam $\mathbf{k}'$.

Set-up (b), on the other hand, features numbers of merged photons which are comparable to Set-up (c), although the peak laser power for Set-up (b) is actually smaller

Focus parameters		$\rho' = 1$ $\rho'' = 1$	$\rho' = 2$ $\rho'' = 2$	$\rho' = 3$ $\rho'' = 3$	$\rho' = 3$ $\rho'' = 2$
Set-up (a)					
f′,s″ → s:	$\mathcal{N}_{\mathrm{Merg},<\Theta}$	0.0029	$4.9 \cdot 10^{-4}$	$9.7 \cdot 10^{-5}$	$2.2 \cdot 10^{-4}$
	$r_{<\Theta}^{(\perp)}$	$9.0 \cdot 10^{-20}$	$1.3 \cdot 10^{-13}$	0.0022	0.0049
s′,s″ → f:	$\mathcal{N}_{\mathrm{Merg},<\Theta}$	$4.7 \cdot 10^{-4}$	$8.0 \cdot 10^{-5}$	$1.6 \cdot 10^{-5}$	$3.6 \cdot 10^{-5}$
	$r_{<\Theta}^{(\perp)}$	$1.5 \cdot 10^{-20}$	$2.1 \cdot 10^{-14}$	$3.5 \cdot 10^{-4}$	$7.9 \cdot 10^{-4}$
Set-up (b)					
f′,s″ → s:	$\mathcal{N}_{\mathrm{Merg},<\Theta}$	0.65	0.65	0.13	0.29
	$r_{<\Theta}^{(\perp)}$	$4.4 \cdot 10^{-16}$	0.095	$\gg 1$	$\gg 1$
s′,s″ → f:	$\mathcal{N}_{\mathrm{Merg},<\Theta}$	0.0033	0.0033	$6.5 \cdot 10^{-4}$	0.0015
	$r_{<\Theta}^{(\perp)}$	$2.2 \cdot 10^{-18}$	$4.8 \cdot 10^{-4}$	$\gg 1$	$\gg 1$
Set-up (c)					
f′,s″ → s:	$\mathcal{N}_{\mathrm{Merg},<\Theta}$	0.52	0.52	0.10	0.23
	$r_{<\Theta}^{(\perp)}$	$2.0 \cdot 10^{-15}$	0.043	$\gg 1$	$\gg 1$
s′,s″ → f:	$\mathcal{N}_{\mathrm{Merg},<\Theta}$	0.0027	0.0027	$5.3 \cdot 10^{-4}$	0.0012
	$r_{<\Theta}^{(\perp)}$	$1.1 \cdot 10^{-17}$	$2.2 \cdot 10^{-4}$	$\gg 1$	$\gg 1$

Table 4.4.: Comparison of the numbers of merged photons $\mathcal{N}_{\mathrm{Merg},<\Theta}$ and the signal-to-background ratio $r_{<\Theta}^{(\perp)}$ for the Set-ups (a)-(c), for varying focus parameters ρ' and ρ'' of the probe beams. For simplicity, we employed the counterpropagating configuration depicted in the right panel of Fig. 4.3 and the parameters $\theta'' = \theta''_{\max}$ and $\theta = \theta_{\max}$ listed in Table 4.3, maximizing the total photon yield. Listed are the values for the processes (f′,s″ → s) and (s′,s″ → f), as for these the polarizations of the signal and background beam differ, thus allowing for an efficient filtering of the signal from the background by means of linear polarizers.

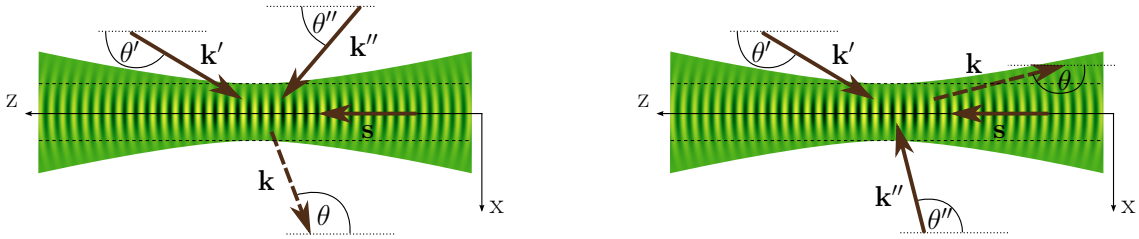

Figure 4.6.: Alternative configurations employing the laser parameters of Set-up (c), with $\theta' = 145°$ and $\phi' = 0$. The configuration in the left panel yields lower numbers of merged photons than the configuration in the right panel and the one depicted in Fig. 4.3, but completely avoids counterpropagating pump, probe and signal beams. The configuration in the right panel yields large numbers of signal photons, which are however almost counterpropagating with the pump beam.

than for Set-up (c). This is a consequence of the larger pulse energy of the Vulcan laser, leading to a greater number of photons available for probing. Additionally, the Vulcan laser's long pulse duration induces a signal photon beam which is more tightly focussed and whose energy spread is about an order of magnitude smaller than for the signal beam from Set-up (c). Hence, also the signal-to-background ratios for Set-up (b) and (c) are of comparable size. For both Set-ups (b) and (c), widening the probe beam $\mathbf{k}'$ to $\rho' = 3$ leads to the signal photons being emitted entirely into the background-free field region, i.e. $r^{(\perp)}_{<\Theta} \gg 1$, and they should hence be accessible to an experimental detection.

Let us mention that from an experimental viewpoint it might prove challenging to employ two exactly counterpropagating lasers as considered here. To this end, employing the parameters of Set-up (c), in Fig. 4.6 we depict two alternative configurations. Instead of the probe beam $\mathbf{k}'$ counterpropagating with the pump we let it enter under an angle of, e.g., $\theta' = 145°$ and $\phi' = 0$. A maximum of photons is then induced for two configurations: The first one is depicted in the left panel of Fig. 4.6 and has $\phi'' = 0$, $\theta''_{\max} = 49.3°$ and $\theta_{\max} = 116.5°$. The divergence of the outgoing beam for this configuration is $\Theta \approx 2.8°$. For a focussing of $\rho' = 3$ and $\rho'' = 2$ we find $\mathcal{N}^{\mathrm{f}',\mathrm{s}''\to\mathrm{s}}_{\mathrm{Merg},<\Theta} \approx 0.06$ and $r^{(\perp)}_{<\Theta}(\mathrm{s}', \mathrm{s}'' \to \mathrm{f}) \approx 0.02$.

The second configuration yielding a maximum number of photons is depicted in the right panel of Fig. 4.6. It has the parameters $\phi'' = \pi$ and $\theta''_{\max} = 96.5°$, and the signal beam is emitted at around $\theta_{\max} = 163.4°$ with a divergence of $\Theta \approx 5.4°$. Focussing the probe beams to $\rho' = \rho'' = 2$, we find $\mathcal{N}^{\mathrm{f}',\mathrm{s}''\to\mathrm{s}}_{\mathrm{Merg},<\Theta} \approx 1.54$ and $r^{(\perp)}_{<\Theta}(\mathrm{s}', \mathrm{s}'' \to \mathrm{f}) \gg 1$, i.e. the merged photons are induced into an area essentially free of background photons originating from the probe beams. However, they also have the downside of being emitted at a shallow angle with respect to the z-axis and having a larger divergence Θ

than most of the other configurations considered in this section. This might necessitate the use of beam splitters along z, lowering the available pump laser power.[14]

In conclusion, we find that photon merging facilitates a variety of experimental realizations without fine-tuning requirements, making it an ideal candidate to experimentally verify the nonlinear nature of the quantum vacuum. It should be noted that the laser parameters employed in this section resemble parameters of high-intensity laser facilities *currently* in operation. At the same time, the parameters for Set-up (c) are very conservative estimates for the design parameters of the future laser facility ELI-NP, which plans to operate two 10PW lasers instead of the two 1PW lasers considered here (cf. the appendix E). As the number of merged signal photons scales as $\sim W_{\mathrm{beam}}^3$, we can rescale our results straightforwardly to the design parameters of ELI-NP featuring two 10PW lasers by multiplying our results with a factor of 1000. Further facilities with comparably intense laser beams are being projected and developed (see, e.g., Refs. [109, 110, 129, 130]).

[14] Note that a similar configuration has also been discussed in [125, 126].

5. Conclusion

This work has dealt in detail with some of the nonlinear optical properties of the quantum vacuum under the influence of strong electromagnetic fields. In the first part we have introduced "optical quantum reflection" as a novel signature of the quantum vacuum nonlinearity. We have shown that the quantum vacuum subject to a strong electromagnetic field acts as an effective, attractive potential for traversing probe photons, which may experience above-the-barrier scattering. Our approach relied heavily on analytical insights into the two-photon polarization tensor in homogeneous electromagnetic pump fields. Employing a locally-constant field approximation we implemented the inhomogeneity *a posteriori* and examined quantum reflection in the weak-field limit $\mathcal{E} \ll \mathcal{E}_{\mathrm{cr}}$ for a large class of pump field configurations. In order to satisfy the Ward identity within our approximation scheme, we limited ourselves to scenarios where the polarization of the probe photons is conserved. Furthermore, we were able to derive a representation of the two-photon polarization tensor for a one-dimensional Lorentz profile valid for arbitrary field strengths, allowing an analytical investigation of quantum reflection in the strong-field limit. In the context of pump-probe type experiments employing high-intensity lasers we gave fully analytical estimates for the number of photons undergoing quantum reflection. The results show that the experimental verification of *pure* quantum reflection will be very challenging, as the large majority of induced photons is emitted along directions where the background field dominates. Nevertheless, the inhomogeneity profile of the pump field plays an important role for some proposed laser-based set-ups, as the scattering of induced photons out of the cone of divergence of the pump field may significantly enhance the signal-to-background ratio.

Next we have investigated photon merging and splitting in electromagnetic field inhomogeneities. Following from the Heisenberg-Euler effective action, we have derived an analytical expression for the three-photon polarization tensor in slowly-varying, but otherwise arbitrary pump field inhomogeneities. This expression allowed us to analyze in detail the selection rules for splitting and merging in crossed fields. We have also been able to demonstrate how the well-established restrictions arising from selection

rules in constant pump fields are lifted in inhomogeneous pump fields. The relevance of inhomogeneities is furthermore highlighted by the fact that splitting and merging in constant pump fields scale as $(\mathcal{E}/\mathcal{E}_{\mathrm{cr}})^6$, whereas in inhomogeneous pump fields the suppression is generically reduced to $(\mathcal{E}/\mathcal{E}_{\mathrm{cr}})^2$.

With the help of fully analytical expressions for the number of merged photons in a localized field inhomogeneity resembling the focal spot of a high-intensity laser, we gave experimental estimates for the detectable number of merged photons. We found that employing exemplary parameters for even already existing state-of-the-art high-intensity laser systems yields a decent amount of merged photons per laser shot, whose emission characteristics allow for polarization and frequency-based filtering techniques, and should give rise to a successful implementation of sensitive single-photon detection schemes. Hence, we believe that photon merging is an ideal candidate to experimentally verify the optical nonlinear nature of the quantum vacuum.

In this work we have obtained *analytical* expressions for the number of quantum reflected photons as well as those originating from photon splitting and merging. This is very desirable as they allow a straightforward systematic study of the influence of the various features of the pump field inhomogeneity, as has been performed in Chap. 3. In order to arrive at more accurate predictions we eventually have to move away from the plane-wave approximation for the probe beams, and model them too as spatially and temporally localized pulses. Note that in the context of vacuum birefringence, an analytical study has been recently performed where both the probe and pump beams have been modeled as Gaussian beams [127]. The formalism of Chap. 4 for photon splitting and merging straightforwardly allows for a similar generalization, cf. Eqs. (4.14) and (4.15). It is unclear, however, whether the resulting momentum integrals in Eq. (4.15) can still be solved analytically for more complicated probe photon fields, or whether solutions can only be obtained by means of numerical methods. This question is a subject of ongoing research.

Bibliography

[1] R. Hardie and R. Gaye, *The Works of Aristotle*, Oxford University Press, 1930.

[2] R. Descartes, *Principia philosophiae*, 1644.

[3] A. Michelson and E. Morley, *On the Relative Motion of the Earth and the Luminiferous Ether*, Amer. Journ. of Sc. **34**, 333 (1887).

[4] A. Einstein, *Zur Elektrodynamik bewegter Körper*, Annalen der Physik **322**, 891 (1905).

[5] P. A. M. Dirac, *The quantum theory of the electron*, Proc. Roy. Soc. Lond. **A117**, 610 (1928).

[6] P. A. M. Dirac, *Theory of the positron*, Report to 7th Solvay Conference (1933).

[7] R. Karplus and M. Neuman, *Non-Linear Interactions between Electromagnetic Fields*, Phys. Rev. **80**, 380 (1950).

[8] W. Heisenberg and H. Euler, *Consequences of Dirac's theory of positrons*, Z. Phys. **98**, 714 (1936).

[9] V. Weisskopf, *The electrodynamics of the vacuum based on the quantum theory of the electron*, Kong. Dan. Vid. Sel. Mat. Fys. Med. **14N6**, 1 (1936).

[10] J. S. Schwinger, *On gauge invariance and vacuum polarization*, Phys. Rev. **82**, 664 (1951).

[11] S. Z. Akhmadaliev et al., *Delbruck scattering at energies of 140-450 MeV*, Phys. Rev. **C58**, 2844 (1998).

[12] S. Z. Akhmadaliev et al., *Experimental investigation of high-energy photon splitting in atomic fields*, Phys. Rev. Lett. **89**, 061802 (2002).

[13] L. Meitner and H. Kösters, *Über die Streuung kurzwelliger Gammastrahlen*, Zeitschrift für Physik **84**, 137 (1933).

[14] H. Bethe and F. Rohrlich, *Small Angle Scattering of Light by a Coulomb Field*, Phys. Rev. **86**, 10 (1952).

[15] S. L. Adler, J. N. Bahcall, C. G. Callan, and M. N. Rosenbluth, *Photon splitting in a strong magnetic field*, Phys. Rev. Lett. **25**, 1061 (1970).

[16] R. N. Lee, A. I. Milstein, and V. M. Strakhovenko, *High-energy photon splitting on heavy atoms*, Phys. Rev. **A57**, 2325 (1998).

[17] S. K. Lamoreaux, *Demonstration of the Casimir Force in the 0.6 to* $6\mu m$ *Range*, Phys. Rev. Lett. **78**, 5 (1997).

[18] U. Mohideen and A. Roy, *Precision Measurement of the Casimir Force from 0.1 to* $0.9\mu m$, Phys. Rev. Lett. **81**, 4549 (1998).

[19] G. Bressi, G. Carugno, R. Onofrio, and G. Ruoso, *Measurement of the Casimir Force between Parallel Metallic Surfaces*, Phys. Rev. Lett. **88**, 041804 (2002).

[20] H. Euler and B. Kockel, *Ueber die Streuung von Licht an Licht nach der Diracschen Theorie*, Naturwiss. **23**, 246 (1935).

[21] R. Karplus and M. Neuman, *The scattering of light by light*, Phys. Rev. **83**, 776 (1951).

[22] J. S. Toll, *The Dispersion relation for light and its application to problems involving electron pairs*, PhD thesis, Princeton U., 1952, (Unpublished).

[23] R. Baier and P. Breitenlohner, *Photon Propagation in External Fields*, Acta Phys. Austriaca **25**, 212 (1967).

[24] Z. Bialynicka-Birula and I. Bialynicki-Birula, *Nonlinear effects in Quantum Electrodynamics. Photon propagation and photon splitting in an external field*, Phys. Rev. **D2**, 2341 (1970).

[25] S. L. Adler, *Photon splitting and photon dispersion in a strong magnetic field*, Annals Phys. **67**, 599 (1971).

[26] V. P. Yakovlev, *Incoherent Electromagnetic Wave Scattering In a Coulomb Field*, Zh. Eksp. Teor. Fiz. **51**, 619 (1966), English translation available at Sov. Phys. JETP **24**, 411 (1967).

[27] F. Sauter, *Uber das Verhalten eines Elektrons im homogenen elektrischen Feld nach der relativistischen Theorie Diracs*, Zeitschrift für Physik **69**, 742 (1931).

[28] W. Dittrich and H. Gies, *Probing the quantum vacuum. Perturbative effective action approach in quantum electrodynamics and its application*, Springer Tracts Mod. Phys. **166**, 1 (2000).

[29] M. Marklund and J. Lundin, *Quantum Vacuum Experiments Using High Intensity Lasers*, Eur. Phys. J. **D55**, 319 (2009).

[30] G. V. Dunne, *New Strong-Field QED Effects at ELI: Nonperturbative Vacuum Pair Production*, Eur. Phys. J. **D55**, 327 (2009).

[31] A. Di Piazza, C. Muller, K. Z. Hatsagortsyan, and C. H. Keitel, *Extremely high-intensity laser interactions with fundamental quantum systems*, Rev. Mod. Phys. **84**, 1177 (2012).

[32] R. Battesti and C. Rizzo, *Magnetic and electric properties of quantum vacuum*, Rept. Prog. Phys. **76**, 016401 (2013).

[33] B. King and T. Heinzl, *Measuring vacuum polarization with high-power lasers*, High Power Laser Science and Engineering **4** (2016).

[34] Y. J. Ding and A. E. Kaplan, *Nonlinear magneto-optics of vacuum: Second-harmonic generation*, Phys. Rev. Lett. **63**, 2725 (1989).

[35] N. N. Rozanov, *Reflection from a Barrier in the Quasi-Classical Approximation*, Sov. Phys. JETP **76**, 991 (1993).

[36] F. Moulin and D. Bernard, *Four-wave interaction in gas and vacuum: definition of a third-order nonlinear effective susceptibility in vacuum:* $\chi^{(3)}_{\text{vacuum}}$, Optics Communications **164**, 137 (1999).

[37] B. King, A. Di Piazza, and C. H. Keitel, *Double-slit vacuum polarization effects in ultraintense laser fields*, Phys. Rev. A **82**, 032114 (2010).

[38] B. King and C. Keitel, *Photon–photon scattering in collisions of intense laser pulses*, New Journal of Physics **14**, 103002 (2012).

[39] B. King, A. Di Piazza, and C. H. Keitel, *A matterless double slit*, Nature Photon. **4**, 92 (2010).

[40] D. Tommasini and H. Michinel, *Light by light diffraction in vacuum*, Phys. Rev. A **82**, 011803 (2010).

[41] G. Y. Kryuchkyan and K. Z. Hatsagortsyan, *Bragg Scattering of Light in Vacuum Structured by Strong Periodic Fields*, Phys. Rev. Lett. **107**, 053604 (2011).

[42] B. Döbrich and H. Gies, *Axion-like-particle search with high-intensity lasers*, Journal of High Energy Physics **2010**, 22 (2010).

[43] H. Gies, F. Karbstein, and N. Seegert, *Quantum Reflection as a New Signature of Quantum Vacuum Nonlinearity*, New J. Phys. **15**, 083002 (2013).

[44] H. Gies, F. Karbstein, and N. Seegert, *Quantum reflection of photons off spatio-temporal electromagnetic field inhomogeneities*, New J. Phys. **17**, 043060 (2015).

[45] H. Gies, F. Karbstein, and N. Seegert, *Photon merging and splitting in electromagnetic field inhomogeneities*, Phys. Rev. **D93**, 085034 (2016).

[46] M. Peskin and D. Schroeder, *An Introduction to Quantum Field Theory*, Advanced book classics, Addison-Wesley Publishing Company, 1995.

[47] L. Ryder, *Quantum Field Theory*, Cambridge University Press, 1985.

[48] W. Greiner and J. Reinhardt, *Quantum Electrodynamics*, Physics and Astronomy, Springer Berlin Heidelberg, 2008.

[49] H. Gies, *Physics of the quantum vacuum*, Friedrich-Schiller-Universität Jena, 2012, Lecture notes taken by the author.

[50] H. Gies, *Introduction to the Functional RG and Applications to Gauge Theories*, pages 287–348, Springer Berlin Heidelberg, Berlin, Heidelberg, 2012.

[51] L. Brown, *Quantum Field Theory*, Cambridge University Press, 1994.

[52] W. H. Furry, *A Symmetry Theorem in the Positron Theory*, Phys. Rev. **51**, 125 (1937).

[53] D. Galtsov and V. Skobelev, *Photons creation by an external field*, Phys. Lett. **B36**, 238 (1971).

[54] F. Karbstein and R. Shaisultanov, *Stimulated photon emission from the vacuum*, Phys. Rev. **D91**, 113002 (2015).

[55] R. Baier and P. Breitenlohner, *The Vacuum refraction Index in the presence of External Fields*, Nuovo Cim. **B47**, 117 (1967).

[56] G. Cantatore, *Recent results from the PVLAS experiment on the magnetized vacuum*, Lect. Notes Phys. **741**, 157 (2008).

[57] E. Zavattini et al., *New PVLAS results and limits on magnetically induced optical rotation and ellipticity in vacuum*, Phys. Rev. D **77**, 032006 (2008).

[58] F. D. Valle, U. Gastaldi, G. Messineo, E. Milotti, R. Pengo, L. Piemontese, G. Ruoso, and G. Zavattini, *Measurements of vacuum magnetic birefringence using permanent dipole magnets: the PVLAS experiment*, New Journal of Physics **15**, 053026 (2013).

[59] F. Della Valle, A. Ejlli, U. Gastaldi, G. Messineo, E. Milotti, R. Pengo, G. Ruoso, and G. Zavattini, *The PVLAS experiment: measuring vacuum magnetic birefringence and dichroism with a birefringent Fabry–Perot cavity*, Eur. Phys. J. **C76**, 24 (2016).

[60] P. Berceau, R. Battesti, M. Fouche, and C. Rizzo, *The vacuum magnetic birefringence experiment: A test for quantum electrodynamics*, Can. J. Phys. **89**, 153 (2011).

[61] P. Berceau, M. Fouché, R. Battesti, and C. Rizzo, *Magnetic linear birefringence measurements using pulsed fields*, Phys. Rev. A **85**, 013837 (2012).

[62] A. Cadène, P. Berceau, M. Fouché, R. Battesti, and C. Rizzo, *Vacuum magnetic linear birefringence using pulsed fields: status of the BMV experiment*, Eur. Phys. J. **D68**, 16 (2014).

[63] G. Zavattini, F. Della Valle, A. Ejlli, and G. Ruoso, *A polarisation modulation scheme for measuring vacuum magnetic birefringence with static fields*, Eur. Phys. J. **C76**, 294 (2016).

[64] T. Heinzl, B. Liesfeld, K.-U. Amthor, H. Schwoerer, R. Sauerbrey, and A. Wipf, *On the observation of vacuum birefringence*, Opt. Commun. **267**, 318 (2006).

[65] A. Di Piazza, K. Z. Hatsagortsyan, and C. H. Keitel, *Light diffraction by a strong standing electromagnetic wave*, Phys. Rev. Lett. **97**, 083603 (2006).

[66] T. Heinzl and A. Ilderton, *Exploring high-intensity QED at ELI*, Eur. Phys. J. **D55**, 359 (2009).

[67] V. Dinu, T. Heinzl, A. Ilderton, M. Marklund, and G. Torgrimsson, *Vacuum refractive indices and helicity flip in strong-field QED*, Phys. Rev. **D89**, 125003 (2014).

[68] V. Dinu, T. Heinzl, A. Ilderton, M. Marklund, and G. Torgrimsson, *Photon polarization in light-by-light scattering: Finite size effects*, Phys. Rev. **D90**, 045025 (2014).

[69] G. Zavattini and E. Calloni, *Probing for new physics and detecting non-linear vacuum QED effects using gravitational wave interferometer antennas*, The European Physical Journal C **62**, 459 (2009).

[70] B. Döbrich and H. Gies, *Interferometry of light propagation in pulsed fields*, EPL (Europhysics Letters) **87**, 21002 (2009).

[71] H. Grote, *On the possibility of vacuum QED measurements with gravitational wave detectors*, Phys. Rev. D **91**, 022002 (2015).

[72] I. A. Batalin and A. E. Shabad, *Photon green function in a stationary homogeneous field of the most general form*, Sov. Phys. JETP **33**, 483 (1971).

[73] G. K. Artimovich, *Properties of the photon polarization operator in an electric field: Effective charge of the electron in an external field*, Sov. Phys. JETP **70**, 787 (1990), [Zh. Eksp. Teor. Fiz. **97**, 1393 (1990)].

[74] C. Schubert, *Vacuum polarisation tensors in constant electromagnetic fields: Part I*, Nuclear Physics B **585**, 407 (2000).

[75] A. Minguzzi, *Non-linear effects in the vacuum polarization*, Il Nuovo Cimento (1955-1965) **4**, 476 (1956).

[76] D. H. Constantinescu, *Vacuum polarization in magnetic field*, Nucl. Phys. **B36**, 121 (1972).

[77] W.-y. Tsai and T. Erber, *Photon Pair Creation in Intense Magnetic Fields*, Phys. Rev. **D10**, 492 (1974).

[78] W.-y. Tsai and T. Erber, *The Propagation of Photons in Homogeneous Magnetic Fields: Index of Refraction*, Phys. Rev. **D12**, 1132 (1975).

[79] W.-y. Tsai and T. Erber, *The Propagation of Photons in Homogeneous Magnetic Fields. 2. Dispersion Relations and Propagation Modes*, Acta Phys. Austriaca **45**, 245 (1976).

[80] N. Narozhnyi, *Propagation of Plane Electromagnetic Waves in a Constant Field*, Sov. Phys. JETP **28**, 371 (1969).

[81] V. I. Ritus, *Radiative corrections in quantum electrodynamics with intense field and their analytical properties*, Annals Phys. **69**, 555 (1972).

[82] V. N. Baier, A. I. Milshtein, and V. M. Strakhovenko, *Interaction Between a Photon and a High Intensity Electromagnetic Wave*, Zh. Eksp. Teor. Fiz. **69**, 1893 (1975).

[83] W. Becker and H. Mitter, *Vacuum polarization in laser fields*, J. of Phys. A **8**, 1638 (1975).

[84] S. Meuren, C. H. Keitel, and A. Di Piazza, *Polarization operator for plane-wave background fields*, Phys. Rev. **D88**, 013007 (2013).

[85] R. J. Stoneham, *Photon splitting in the magnetised vacuum*, J. of Phys. A **12**, 2187 (1979).

[86] V. O. Papanyan and V. I. Ritus, *Vacuum polarization and photon splitting in an intense field*, Zh. Eksp. Teor. Fiz. **61**, 2231 (1971).

[87] V. O. Papanyan and V. I. Ritus, *Three-photon interaction in an intense field and scaling invariance*, Zh. Eksp. Teor. Fiz. **65**, 1756 (1973).

[88] V. L. Pokrovskii, S. K. Sawinykh, and F. R. Ulinich, *Reflection from a Barrier in the Quasi-Classical Approximation*, Sov. Phys. JETP **7**, 879 (1958).

[89] V. L. Pokrovskii, S. K. Sawinykh, and F. R. Ulinich, *Reflection from a Barrier in the Quasi-Classical Approximation II*, Sov. Phys. JETP **7**, 1119 (1958).

[90] C. Henkel, C. I. Westbrook, and A. Aspect, *Quantum reflection: atomic matter-wave optics in an attractive exponential potential*, J. Opt. Soc. Am. B **13**, 233 (1996).

[91] V. Druzhinina and M. DeKieviet, *Experimental Observation of Quantum Reflection far from Threshold*, Phys. Rev. Lett. **91**, 193202 (2003).

[92] B. S. Zhao, G. Meijer, and W. Schöllkopf, *Quantum reflection of* He_2 *several nanometers above a grating surface*, Science **331**, 892 (2011).

[93] H. B. G. Casimir and D. Polder, *The Influence of Retardation on the London-van der Waals Forces*, Phys. Rev. **73**, 360 (1948).

[94] F. London, *The general theory of molecular forces*, Trans. Faraday Soc. **33**, 8b (1937).

[95] F. Shimizu, *Specular Reflection of Very Slow Metastable Neon Atoms from a Solid Surface*, Phys. Rev. Lett. **86**, 987 (2001).

[96] C. Carraro and M. W. Cole, *Sticking coefficient at ultralow energy: Quantum reflection*, Progress in Surface Science **57**, 61 (1998).

[97] Doak, R. B. and Chizmeshya, A. V. G., *Sufficiency conditions for quantum reflection*, Europhys. Lett. **51**, 381 (2000).

[98] H. Oberst, Y. Tashiro, K. Shimizu, and F. Shimizu, *Quantum reflection of* He^* *on silicon*, Phys. Rev. A **71**, 052901 (2005).

[99] D. Kouznetsov, H. Oberst, A. Neumann, Y. Kuznetsova, K. Shimizu, J.-F. Bisson, K. Ueda, and S. R. J. Brueck, *Ridged atomic mirrors and atomic nanoscope*, J. of Phys. B **39**, 1605 (2006).

[100] F. Karbstein, *Photon polarization tensor in a homogeneous magnetic or electric field*, Phys. Rev. **D88**, 085033 (2013).

[101] H. Gies and L. Roessler, *Vacuum polarization tensor in inhomogeneous magnetic fields*, Phys. Rev. **D84**, 065035 (2011).

[102] I. S. Gradshteyn and I. M. Ryzhik, *Table of integrals, series, and products*, Elsevier/Academic Press, Amsterdam, seventh edition, 2007, Translated from Russian.

[103] A. Siegman, *Lasers*, University Science Books, 1986.

[104] I. Bassett, *Limit to Concentration by Focusing*, Optica Acta: International Journal of Optics **33**, 279 (1986).

[105] I. Gonoskov, A. Aiello, S. Heugel, and G. Leuchs, *Dipole pulse theory: Maximizing the field amplitude from* 4π *focused laser pulses*, Phys. Rev. A **86**, 053836 (2012).

[106] Website of the Helmholtz Institute Jena, http://www.hi-jena.de/en/, [Online; accessed 25. Aug. 2016].

[107] M. Hornung et al., *High-intensity, high-contrast laser pulses generated from the fully diode-pumped Yb:glass laser system POLARIS*, Opt. Lett. **38**, 718 (2013).

[108] M. Hornung et al., *The all-diode-pumped laser system POLARIS – an experimentalist's tool generating ultra-high contrast pulses with high energy*, High Power Laser Science and Engineering **2** (2014).

[109] Website of the Central Laser Facility, UK, http://www.stfc.ac.uk/CLF/Facilities/Vulcan/The+Vulcan+10+Petawatt+Project/14684.aspx, [Online; accessed 25. Aug. 2016].

[110] Website of the Extreme Light Infrastructure, https://eli-laser.eu/, [Online; accessed 25. Aug. 2016].

[111] Website of the HIBEF project, http://www.hzdr.de/db/Cms?pOid=35325&pNid=3214, [Online; accessed 25. Aug. 2016].

[112] H.-P. Schlenvoigt, T. Heinzl, U. Schramm, T. E. Cowan, and R. Sauerbrey, *Detecting vacuum birefringence with x-ray free electron lasers and high-power optical lasers: a feasibility study*, Physica Scripta **91**, 023010 (2016).

[113] B. Marx et al., *Determination of high-purity polarization state of X-rays*, Optics Communications **284**, 915 (2011).

[114] B. Marx et al., *High-Precision X-Ray Polarimetry*, Phys. Rev. Lett. **110**, 254801 (2013).

[115] F. Karbstein, H. Gies, M. Reuter, and M. Zepf, *Vacuum birefringence in strong inhomogeneous electromagnetic fields*, Phys. Rev. **D92**, 071301 (2015).

[116] V. N. Baier, A. I. Milshtein, and R. Z. Shaisultanov, *Photon Splitting in a Strong Electromagnetic Field*, Sov. Phys. JETP **63**, 665 (1986), [Zh. Eksp. Teor. Fiz. **90**, 1141 (1986)].

[117] S. L. Adler and C. Schubert, *Photon Splitting in a Strong Magnetic Field: Recalculation and Comparison with Previous Calculations*, Phys. Rev. Lett. **77**, 1695 (1996).

[118] A. Di Piazza, A. I. Milstein, and C. H. Keitel, *Photon splitting in a laser field*, Phys. Rev. **A76**, 032103 (2007).

[119] A. Di Piazza, K. Z. Hatsagortsyan, and C. H. Keitel, *Non-perturbative vacuum-polarization effects in proton-laser collisions*, Phys. Rev. Lett. **100**, 010403 (2008).

[120] H. Gies, F. Karbstein, and R. Shaisultanov, *Laser photon merging in an electromagnetic field inhomogeneity*, Phys. Rev. **D90**, 033007 (2014).

[121] F. Karbstein and R. Shaisultanov, *Photon propagation in slowly varying inhomogeneous electromagnetic fields*, Phys. Rev. **D91**, 085027 (2015).

[122] W. Dittrich and M. Reuter, *Effective Lagrangians in Quantum Electrodynamics*, Lect. Notes Phys. **220**, 1 (1985).

[123] B. King, P. Böhl, and H. Ruhl, *Interaction of photons traversing a slowly varying electromagnetic background*, Phys. Rev. D **90**, 065018 (2014).

[124] P. Böhl, B. King, and H. Ruhl, *Vacuum high-harmonic generation in the shock regime*, Phys. Rev. A **92**, 032115 (2015).

[125] E. Lundstrom, G. Brodin, J. Lundin, M. Marklund, R. Bingham, J. Collier, J. T. Mendonca, and P. Norreys, *Using high-power lasers for detection of elastic photon-photon scattering*, Phys. Rev. Lett. **96**, 083602 (2006).

[126] J. Lundin, M. Marklund, E. Lundstrom, G. Brodin, J. Collier, R. Bingham, J. T. Mendonca, and P. Norreys, *Detection of elastic photon-photon scattering through four-wave mixing using high power lasers*, Phys. Rev. **A74**, 043821 (2006).

[127] F. Karbstein and C. Sundqvist, *Probing vacuum birefringence using x-ray free electron and optical high-intensity lasers*, Phys. Rev. **D94**, 013004 (2016).

[128] Thorlabs website, https://www.thorlabs.de/NewGroupPage9.cfm?ObjectGroup_ID=5093, [Online; accessed 21. Aug. 2016].

[129] Website of the Omega Facility, USA, http://www.lle.rochester.edu/omegafacility/omegaep/, [Online; accessed 25. Aug. 2016].

[130] Website of the XCELS Project, Russia, http://www.xcels.iapras.ru/, [Online; accessed 25. Aug. 2016].

[131] Z. Bern and D. A. Kosower, *Efficient calculation of one loop QCD amplitudes*, Phys. Rev. Lett. **66**, 1669 (1991).

[132] Z. Bern and D. A. Kosower, *The Computation of loop amplitudes in gauge theories*, Nucl. Phys. **B379**, 451 (1992).

[133] H. Gies and K. Langfeld, *Loops and loop clouds: A Numerical approach to the worldline formalism in QED*, Int. J. Mod. Phys. **A17**, 966 (2002).

[134] H. Gies and K. Langfeld, *Quantum diffusion of magnetic fields in a numerical worldline approach*, Nucl. Phys. **B613**, 353 (2001).

[135] K. Langfeld, L. Moyaerts, and H. Gies, *Fermion induced quantum action of vortex systems*, Nucl. Phys. **B646**, 158 (2002).

[136] D. Mazur and J. S. Heyl, *Casimir interactions between magnetic flux tubes in a dense lattice*, Phys. Rev. D **91**, 065019 (2015).

[137] L. F. Urrutia, *Vacuum Polarization in Parallel Homogeneous Electric and Magnetic Fields*, Phys. Rev. **D17**, 1977 (1978).

[138] F. Karbstein, L. Roessler, B. Dobrich, and H. Gies, *Optical Probes of the Quantum Vacuum: The Photon Polarization Tensor in External Fields*, Int. J. Mod. Phys. Conf. Ser. **14**, 403 (2012).

[139] K.-I. Ishikawa, D. Kimura, K. Shigaki, and A. Tsuji, *A numerical evaluation of vacuum polarization tensor in constant external magnetic fields*, Int. J. Mod. Phys. **A28**, 1350100 (2013).

[140] B. Döbrich, H. Gies, N. Neitz, and F. Karbstein, *Magnetically amplified light-shining-through-walls via virtual minicharged particles*, Phys. Rev. **D87**, 025022 (2013).

[141] M. Born and E. Wolf, *Principles of Optics: Electromagnetic Theory of Propagation, Interference and Diffraction of Light*, Elsevier Science, 1980.

[142] E. Brezin and C. Itzykson, *Pair production in vacuum by an alternating field*, Phys. Rev. **D2**, 1191 (1970).

[143] M. S. Marinov and V. S. Popov, *Electron-Positron Pair Creation from Vacuum Induced by Variable Electric Field*, Fortsch. Phys. **25**, 373 (1977).

[144] R. Dabrowski and G. V. Dunne, *Superadiabatic particle number in Schwinger and de Sitter particle production*, Phys. Rev. **D90**, 025021 (2014).

[145] A. Di Piazza, K. Z. Hatsagortsyan, and C. H. Keitel, *Laser photon merging in proton-laser collisions*, Phys. Rev. **A78**, 062109 (2008).

[146] A. Di Piazza, *On refractive processes in strong laser field quantum electrodynamics*, Annals Phys. **338**, 302 (2013).

[147] D. Strickland and G. Mourou, *Compression of amplified chirped optical pulses*, Optics Communications **55**, 447 (1985).

[148] R. Danielius, A. Piskarskas, A. Stabinis, G. P. Banfi, P. D. Trapani, and R. Righini, *Traveling-wave parametric generation of widely tunable, highly coherent femtosecond light pulses*, J. Opt. Soc. Am. B **10**, 2222 (1993).

[149] Website of the International Committee on Ultra-High Intensity Lasers (ICUIL), http://www.icuil.org/activities/laser-labs.html, [Online; accessed 15. Sept. 2016].

[150] Cf. the annual report 2015 of the Helmholtz Institute Jena, https://www.hi-jena.de/files/annual_reports/HI_Jena_Annual_Report_2015.pdf, [Online; accessed 16. Sept. 2016].

[151] Website of the Berkeley Lab, USA, http://bella.lbl.gov/facilities/bella-center-facilities-bella-laser/, [Online; accessed 15. Sept. 2016].

[152] V. P. Gusynin and I. A. Shovkovy, *Derivative expansion of the effective action for QED in (2+1)-dimensions and (3+1)-dimensions*, J. Math. Phys. **40**, 5406 (1999).

[153] A. M. Ostrowski, *On some generalizations of the Cauchy-Frullani integral*, Proceedings of the National Academy of Sciences of the United States of America **35**, 612 (1949).

[154] S. K. Blau, M. Visser, and A. Wipf, *Analytical Results for the effective action*, International Journal of Modern Physics A **06**, 5409 (1991).

[155] J. W. L. Glaisher, *On the product* $1^1 2^2 ... n^n$, Messenger Math. **7**, 43 (1878).

[156] H. Kinkelin, *Über eine mit der Gammafunktion verwandte Transcendente und deren Anwendung auf die Integralrechnung*, J. reine angew. Math. **57**, 122 (1860).

A. Notation, conventions and units

In this thesis we exclusively work in the Heaviside-Lorentz system and employ natural units, defined by $\hbar \equiv c \equiv 1$. The unit of electric charge e is then related to the fine structure α by

$$e = \sqrt{4\pi\alpha} \approx 0.303\,. \tag{A.1}$$

Furthermore, our convention for the Minkowski metric is

$$g_{\mu\nu} = g^{\mu\nu} = \text{diag}\,(-1, 1, 1, 1)\,. \tag{A.2}$$

Lorentz indices are denoted by Greek letters, and run from $\mu = 0, \ldots, 3$. Latin indices run from $i = 1, \ldots, 3$. According to Einstein's summation rule, indices appearing twice in a term are being summed over. k^μ denotes a momentum four-vector in Minkowski space, with elements $k^\mu = (\omega, k_\mathrm{x}, k_\mathrm{y}, k_\mathrm{z}) = (\omega, \mathbf{k})$. Accordingly, for spatio-temporal four-vectors x^μ we use Roman letters to denote their spatial components, i.e. $x^\mu = (t, \mathrm{x}, \mathrm{y}, \mathrm{z}) = (t, \mathbf{x})$. Bold quantities represent Euclidean vectors in three-space. Unit vectors in three-space are denoted by a hat, e.g. the unit vectors along the three principal orthogonal directions of Euclidean space read $\hat{\mathbf{e}}_\mathrm{x}$, $\hat{\mathbf{e}}_\mathrm{y}$ and $\hat{\mathbf{e}}_\mathrm{z}$. The product of two four-vectors is given by

$$kx = -\omega t + \mathbf{k}\cdot\mathbf{x} = -\omega t + k_\mathrm{x}\mathrm{x} + k_\mathrm{y}\mathrm{y} + k_\mathrm{z}\mathrm{z}\,. \tag{A.3}$$

By definition the γ-matrices, which in standard representation are given by

$$\gamma^0 = \begin{pmatrix} 1 & 0 \\ 0 & -1 \end{pmatrix} \qquad \text{and} \qquad \gamma^i = \begin{pmatrix} 0 & \sigma^i \\ -\sigma^i & 0 \end{pmatrix}, \tag{A.4}$$

satisfy the anti-commutation relations $\left\{\gamma^\mu, \gamma^\nu\right\} = -2g^{\mu\nu}$. The given representation employs the Pauli matrices

$$\sigma^1 = \begin{pmatrix} 0 & 1 \\ 1 & 0 \end{pmatrix}, \qquad \sigma^2 = \begin{pmatrix} 0 & -i \\ i & 0 \end{pmatrix}, \quad \text{and} \quad \sigma^3 = \begin{pmatrix} 1 & 0 \\ 0 & -1 \end{pmatrix}. \tag{A.5}$$

Furthermore, in the appendix F we have employed the matrices $\sigma^{\mu\nu}$, which are defined by

$$\sigma^{\mu\nu} := \frac{i}{2}\big[\gamma^\mu, \gamma^\nu\big] \,. \tag{A.6}$$

The Feynman slash is a commonly employed notation in quantum field theory, and denotes a contraction of a four-vector with γ-matrices, i.e.

$$\not{a} = \gamma_\mu a^\mu = -\gamma^0 a^0 + \gamma^i a^i \,. \tag{A.7}$$

Field strength tensor

In our metric the electromagnetic field strength tensor $F^{\mu\nu} = \partial^\mu a^\nu - \partial^\nu a^\mu$ is given by

$$F^{\mu\nu} = \begin{pmatrix} 0 & E_1 & E_2 & E_3 \\ -E_1 & 0 & B_3 & -B_2 \\ -E_2 & -B_3 & 0 & B_1 \\ -E_3 & B_2 & -B_1 & 0 \end{pmatrix} . \tag{A.8}$$

Lowering the Lorentz indices corresponds to replacing $E_i \to -E_i$. The dual field strength tensor is defined by ${}^\star F = \frac{1}{2}\varepsilon^{\mu\nu\alpha\beta}F_{\alpha\beta}$, with the total antisymmetric Levi-Civita symbol $\varepsilon^{\mu\nu\alpha\beta}$. Here, we choose $\varepsilon^{0123} = 1$. Often, we employ the shorthand notation $(kF)^\mu \equiv k_\nu F^{\nu\mu}$ for the contraction of the momentum four-vector k^μ with the field strength tensor, and likewise with the dual field strength tensor. Additionally, we employ $(F^2 k)^\mu \equiv F^{\mu\nu}F_{\nu\alpha}k^\alpha$. The antisymmetric field strength tensor allows the construction of two Lorentz invariants, namely

$$\mathcal{F} = \frac{1}{4}F_{\mu\nu}F^{\mu\nu} = \frac{1}{2}(\mathbf{B}^2 - \mathbf{E}^2) \qquad \text{and} \qquad \mathcal{G} = \frac{1}{4}F_{\mu\nu}{}^\star F^{\mu\nu} = -\mathbf{E}\cdot\mathbf{B} \,, \tag{A.9}$$

the first of which is CP-even and the second is CP-odd. Another set of invariants is given by the secular invariants

$$a = \left(\sqrt{\mathcal{F}^2 + \mathcal{G}^2} - \mathcal{F}\right)^{\frac{1}{2}} \qquad \text{and} \qquad b = \left(\sqrt{\mathcal{F}^2 + \mathcal{G}^2} + \mathcal{F}\right)^{\frac{1}{2}} . \tag{A.10}$$

In fact, the quantities $\pm ia$ and $\pm b$ are the eigenvalues of the field strength tensor $F_{\mu\nu}$ for constant electric and magnetic fields.

Integrations and Fourier transformations

When integrating over momentum space, we often employ the shorthand notation $\int_k \equiv \int_{-\infty}^{\infty} \frac{\mathrm{d}^4k}{(2\pi)^4}$. Likewise, we denote momentum integrals over only the spatial components by $\int_{\mathbf{k}} \equiv \int_{-\infty}^{\infty} \frac{\mathrm{d}^3k}{(2\pi)^3}$. Analogously, integrals in position space over the entire Minkowski space are abbreviated by $\int_x = \int_{-\infty}^{\infty} \mathrm{d}^4x$, and integrals over the Euclidean space by $\int_{\mathbf{x}} = \int_{-\infty}^{\infty} \mathrm{d}^3x$. Furthermore, we employ the following antisymmetric conventions for Fourier transformations from momentum to position space:

$$a_\nu(x) = \int_k a_\nu(k) \mathrm{e}^{ikx} \qquad \text{and} \qquad \Pi^{\mu\nu}(x,x') = \int_k \int_{k'} \mathrm{e}^{ikx}\, \Pi^{\mu\nu}(k,k')\, \mathrm{e}^{ik'x'} \,. \tag{A.11}$$

Note that we employ the same symbol for a given quantity in both momentum and position space, and indicate its momentum or position space representation merely by its argument being either a momentum or position coordinate. Accordingly, the definitions for the inverse Fourier transformations read

$$a_\nu(k) = \int_x a_\nu(x) \mathrm{e}^{-ikx} \qquad \text{and} \qquad \Pi^{\mu\nu}(k,k') = \int_x \int_{x'} \mathrm{e}^{-ikx}\, \Pi^{\mu\nu}(x,x')\, \mathrm{e}^{-ik'x'} \,. \tag{A.12}$$

Conversion from SI units

The following table gives the conversion factors between SI-units and natural units:

Quantity	SI-unit	Natural unit
Length	$1\,\mathrm{m}$	$5.07 \cdot 10^{6}\ \mathrm{eV}^{-1}$
Time	$1\,\mathrm{s}$	$1.52 \cdot 10^{15}\ \mathrm{eV}^{-1}$
Mass	$1\,\mathrm{kg}$	$5.61 \cdot 10^{35}\ \mathrm{eV}$
Energy	$1\,\mathrm{J}$	$6.24 \cdot 10^{18}\ \mathrm{eV}$
Intensity	$1\,\mathrm{W/cm^2}$	$1.59 \cdot 10^{-6}\ \mathrm{eV}^4$
Power	$1\,\mathrm{W}$	$4.11 \cdot 10^{3}\ \mathrm{eV}^2$
Magnetic field strength	$1\,\mathrm{T}$	$195.5\ \mathrm{eV}^2$
Electric field strength	$1\mathrm{V/m}$	$6.5 \cdot 10^{-7}\ \mathrm{eV}^2$

Both the critical electric and magnetic field strength, which in SI-units are given by $\mathcal{E}_{\mathrm{cr}} = \frac{m^2c^3}{e\hbar} \approx 1.3 \cdot 10^{18}\mathrm{V/m}$ and $\mathcal{B}_{\mathrm{cr}} = \frac{m^2c^2}{e\hbar} \approx 4 \cdot 10^{9}\mathrm{T}$ respectively, have the same value in natural units: $\mathcal{E}_{\mathrm{cr}} = \mathcal{B}_{\mathrm{cr}} \approx 9 \cdot 10^{11}\mathrm{eV}^2$. Throughout this work, $m \approx 9.1 \cdot 10^{-31}\mathrm{kg} \simeq 511\mathrm{keV}$ denotes the rest mass of the electron. The typical spatial extension and lifetime of an electron-positron loop are entirely determined by the electron's mass, and are given by the (reduced) Compton wavelength $\lambda_c = \frac{\hbar}{mc} \approx 3.9 \cdot 10^{-13}\mathrm{m}$ and the Compton

time $\tau_c = \frac{\hbar}{mc^2} \approx 1.3 \cdot 10^{-21}$s respectively. In natural units both read $\lambda_c = \tau_c \approx 2.0 \cdot 10^{-6}\text{eV}^{-1}$. Note that the critical electric field strength $\mathcal{E}_{\text{cr}}$ is precisely the field strength which is needed to supply an electron with its rest-mass energy mc^2 over a spatial distance of the Compton wavelength.

B. The photon polarization tensor in constant fields

In this appendix we provide a short overview of the photon polarization tensor in arbitrary constant electromagnetic pump fields. We give expressions for the tensors in purely magnetic as well as crossed pump fields together with the respective weak-field expansions, as they are needed for the investigation of quantum reflection in Chap. 3.

As a start, let us consider photon propagation in vacuum without external fields. The photon polarization tensor is also known as the "photon self energy", and describes the modified propagation of photons through vacuum due to virtual electron-positron fluctuations.[1] Formally, the photon polarization tensor $\Pi^{\mu\nu}(k)$ is defined as the sum of all one-particle irreducible diagrams (1PI) without external legs contributing to the full photon propagator $G_A^{\mu\nu}(k)$, or photon two-point function, in vacuum. Hence,

$$
\begin{aligned}
i\Pi^{\mu\nu}(k) :=\quad & \mu \;\times\!\!\bigcirc\!\!\text{1PI}\!\!\times\; \nu \\
=\quad & \mu \;\times\!\!\bigcirc\!\!\times\; \nu + \mu \;\times\!\!\sim\!\!\times\; \nu + \mu \;\times\!\!\sim\!\!\times\; \nu + \mu \;\times\!\!\sim\!\!\times\; \nu + \mathcal{O}\big(e^6\big)\,,
\end{aligned}
\tag{B.1}
$$

where the direction of the momentum has been omitted. Denoting by $D^{\mu\nu}(k) = \frac{i}{k^2}\left(\delta^{\mu\nu} + (\alpha-1)\frac{k^\mu k^\nu}{k^2}\right)$ the photon propagator for the noninteracting theory in either Landau gauge ($\alpha = 0$) or Feynman gauge ($\alpha = 1$), the full photon two-point function is given by the geometric series

$$
\begin{aligned}
G_A^{\mu\nu}(k) =\quad & \mu \;\sim\!\sim\!\sim\; \nu + \quad \mu \;\sim\!\!\text{1PI}\!\!\sim\; \nu \quad + \quad \mu \;\sim\!\!\text{1PI}\!\!\text{1PI}\!\!\sim\; \nu \quad + \ldots \\
=\quad & D^{\mu\nu} + D^\mu_\kappa i\Pi^{\kappa\lambda} D^\nu_\lambda + D^\mu_\kappa i\Pi^{\kappa\lambda} D_{\lambda\delta}\Pi^{\delta\beta} D^\nu_\beta + \ldots\ .
\end{aligned}
\tag{B.2}
$$

[1] For electron propagation in vacuum, the analogous quantity is the "mass operator" Σ.

Employing the invariance of the generating functional of QED under gauge transformations, it can be shown that $k_\mu G_A^{\mu\nu}(k) = k_\mu D^{\mu\nu}(k)$ holds. Correspondingly, quantum fluctuations do not affect the longitudinal contributions to the full photon propagator. As these fluctuations are encoded in the free-field photon polarization tensor, it follows that it must be transverse and hence of the form

$$\Pi^{\mu\nu}(k) = \left(k^2 g^{\mu\nu} - k^\mu k^\nu\right)\Pi(k) = k^2\, P_T^{\mu\nu}(k)\Pi(k)\,, \tag{B.3}$$

with the transversal projector $P_T^{\mu\nu}(k) = \left(g^{\mu\nu} - \frac{k^\mu k^\nu}{k^2}\right)$. This structure is the manifestation of the Ward identity. Accordingly, also the polarization tensor in external fields may only span the transverse subspace and its tensor structure must reduce to Eq. (B.3) in the limit of vanishing fields. Derivations of the free-field photon polarization tensor to one-loop order can be found in textbooks, e.g. Ref. [46].

B.1. Arbitrary constant fields

External fields may couple to the virtual particle-antiparticle fluctuations, and thus influence the propagation of photons in these fields. As of today, obtaining an exact analytical representation of the photon polarization tensor in arbitrary pump fields even to one-loop order is still an unsolved task.[2] For a constant electromagnetic field with arbitrary orientations of the electric and magnetic components, the polarization tensor to one-loop order has been first derived by Batalin and Shabad in 1971 [72], taking into account the coupling of the external field to the electron-positron loop to all orders. Based on the polarization tensor for parallel electric and magnetic fields obtained by Urrutia [137], a lucid derivation for arbitrary constant fields can be found in Ref. [28]. There, use has been made of the existence of a one-to-one correspondence between the dynamical variables in the polarization tensor for the parallel configuration, Ref. [137], and a complete set of linearly independent Lorentz and gauge invariants, allowing the reconstruction of the Lorentz invariant form of the polarization tensor valid for constant arbitrary field configurations. The representation of the polarization tensor given in Ref. [28] employs the secular invariants[3] $a = \left(\sqrt{\mathcal{F}^2 + \mathcal{G}^2} - \mathcal{F}\right)^{\frac{1}{2}}$ and $b = \left(\sqrt{\mathcal{F}^2 + \mathcal{G}^2} + \mathcal{F}\right)^{\frac{1}{2}}$, as well as $z_k = -(kF)^\mu (kF)_\mu$. Furthermore, defining the

[2] Employing the world-line (or string-inspired) formalism [131, 132] is one possible way to obtain access to the polarization tensor in general external fields, which, however, presents formidable difficulties and may require dedicated numerical efforts; some examples and details can be looked up in Refs. [101, 133–136].

[3] Note that in order to keep a consistent notation in this work, we have relabeled $a \leftrightarrow b$ with respect to Ref. [28].

Lorentz tensors

$$v_\parallel^\mu = \frac{1}{a^2+b^2}\Big(b\,(k^\star F)^\mu - a\,(kF)^\mu\Big) \qquad \text{and} \qquad v_\perp^\mu = \frac{1}{a^2+b^2}\Big(a\,(k^\star F)^\mu + b\,(kF)^\mu\Big)\,, \tag{B.4}$$

and the projectors

$$\begin{aligned} P_0^{\mu\nu} =& \frac{1}{k^2\left[2\mathcal{F}z_k/k^2+\mathcal{G}^2-(z_k/k^2)^2\right]}\left((F^2k)^\mu+\frac{z_k}{k^2}k^\mu\right)\left((F^2k)^\nu+\frac{z_k}{k^2}k^\nu\right)\,,\\ P_\parallel^{\mu\nu} =& \frac{v_\parallel^\mu v_\parallel^\nu}{v_\parallel^2}\,, \qquad \text{and} \qquad P_\perp^{\mu\nu} = \frac{v_\perp^\mu v_\perp^\nu}{v_\perp^2}\,, \end{aligned} \tag{B.5}$$

the polarization tensor can be conveniently given by

$$\Pi^{\mu\nu}(k|\mathbf{E},\mathbf{B}) = \Pi_0(k)P_0^{\mu\nu} + \Pi_\parallel(k)P_\parallel^{\mu\nu} + \Pi_\perp(k)P_\perp^{\mu\nu} + \Theta(k)Q^{\mu\nu}\,. \tag{B.6}$$

The off-diagonal elements are proportional to $Q^{\mu\nu} = v_\parallel^\mu v_\perp^\nu + v_\perp^\mu v_\parallel^\nu$, which does not have projector properties. The scalar coefficients are given in terms of a double-parameter integral,

$$\begin{Bmatrix}\Pi_0\\ \Pi_\parallel\\ \Pi_\perp\\ \Theta\end{Bmatrix} = \frac{\alpha}{2\pi}\int_0^\infty \frac{\mathrm{d}s}{s}\int_{-1}^1 \frac{\mathrm{d}\nu}{\nu}\left(\mathrm{e}^{-is\phi_0}\frac{eas\,ebs}{\sin ebs\,\sinh eas}\begin{Bmatrix} k^2N_0\\ N_0v_\perp^2 - N_1v_\parallel^2\\ N_2v_\perp^2 - N_0v_\parallel^2\\ -N_3\end{Bmatrix} + \text{c.t.}\right). \tag{B.7}$$

The contact term

$$\text{c.t.} = -\mathrm{e}^{-im^2s}k^2(1-\nu^2) \tag{B.8}$$

only contributes to the Π_i's, but not to the coefficient Θ. It assures the proper renormalization of the polarization tensor such that it vanishes in the combined limit of vanishing fields and photons on the light cone, $k^2 = 0$. The functions N_i and ϕ_0 read

$$\begin{aligned} \phi_0 &= m^2 - \frac{v_\parallel^2}{2}\frac{\cosh eas - \cosh\nu eas}{eas\,\sinh eas} + \frac{v_\perp^2}{2}\frac{\cos\nu ebs - \cos ebs}{ebs\sin ebs}\,,\\ N_0 &= \cosh\nu eas\cos\nu ebs - \sinh\nu eas\sin\nu ebs\cot ebs\coth eas\,,\\ N_1 &= 2\cos ebs\frac{\cosh eas - \cosh\nu eas}{\sinh^2 eas}\,,\\ N_2 &= 2\cosh eas\frac{\cos\nu ebs - \cos ebs}{\sin^2 ebs}\,,\\ N_3 &= -\frac{1-\cos ebs\cos\nu ebs}{\sin ebs}\frac{\cosh\nu eas\cosh eas - 1}{\sinh eas} + \sin\nu ebs\sinh\nu eas\,. \end{aligned} \tag{B.9}$$

In the integral representation of the scalar functions (B.7) and all subsequent discussions of the polarization tensor, the substitution $m \to m - i0^+$ is implicitly assumed. While the ν integration corresponds to the momentum integration within the electron-positron loop, the s integration stems from employing a convenient integral representation of the inverse Dirac operator. Note that the polarization tensor as given by Eq. (B.6) fulfills the Ward identity $k_\mu \Pi^{\mu\nu}(k) = 0$, as can be quickly verified.

B.2. Constant magnetic field

The polarization tensor, Eq. (B.6), simplifies significantly if the electric field component vanishes, implying $a \to 0$. Most importantly, in this limit the off-diagonal contribution Θ vanishes and the representation of the polarization tensor becomes diagonal. Hence, the eigenvalues $\Pi_0, \Pi_\parallel$ and $\Pi_\perp$ directly correspond to the various modes of propagation of a photon in an external magnetic field. A uni-directional magnetic field provides a global spatial reference direction $\hat{\mathbf{e}}_B$, with respect to which tensors can be decomposed into parallel and perpendicular components: The photon momentum is split up according to $k^\mu = k_\parallel^\mu + k_\perp^\mu$, with $k_\parallel^\mu = (\omega, \mathbf{k}_\parallel)$ and $k_\perp^\mu = (0, \mathbf{k}_\perp)$. The parallel component of the spatial momentum vector is the projection of the momentum onto the direction of the magnetic field, $\mathbf{k}_\parallel = (\mathbf{k} \cdot \hat{\mathbf{e}}_B)\hat{\mathbf{e}}_B$. Likewise, the perpendicular component is the part of the spatial momentum perpendicular to the field, $\mathbf{k}_\perp = \mathbf{k} - \mathbf{k}_\parallel$. In the same way tensors can be decomposed, e.g. $g^{\mu\nu} = g_\parallel^{\mu\nu} + g_\perp^{\mu\nu}$.

From Eq. (B.7), we see that the polarization tensor in the limit $a \to 0$ reduces to

$$\Pi^{\mu\nu}(k|\mathbf{B}) = P_0^{\mu\nu}\Pi_0(k|\mathbf{B}) + P_\parallel^{\mu\nu}\Pi_\parallel(k|\mathbf{B}) + P_\perp^{\mu\nu}\Pi_\perp(k|\mathbf{B})\,, \tag{B.10}$$

with

$$\begin{Bmatrix}\Pi_0\\ \Pi_\parallel\\ \Pi_\perp\end{Bmatrix} = \frac{\alpha}{2\pi}\int_0^\infty \frac{\mathrm{d}s}{s}\int_{-1}^1 \frac{\mathrm{d}\nu}{2}\left(\frac{e\mathcal{B}s}{\sin e\mathcal{B}s}e^{-is\phi_0}\begin{Bmatrix}k^2 & N_0\\ N_0k_\perp^2 + N_1k_\parallel^2\\ N_2k_\perp^2 + N_0k_\parallel^2\end{Bmatrix} - e^{-im^2s}k^2(1-\nu^2)\right), \tag{B.11}$$

where $\mathcal{B}$ denotes the magnetic field strength. The functions N_i, Eq. (B.9), have reduced to

$$\begin{aligned} &N_0 \to \cos\nu z - \nu\sin\nu z\cot z\,, \quad N_1 \to (1-\nu^2)\cos z\,, \quad N_2 \to 2\frac{\cos\nu z - \cos z}{\sin^2 z}\,,\\ &\text{and} \qquad \phi_0 \to m^2 + \frac{1-\nu^2}{4}k_\parallel^2 + \frac{1}{2}\frac{\cos\nu z - \cos z}{z\sin z}k_\perp^2\,. \end{aligned} \tag{B.12}$$

We have employed the shorthand notation $z = e\mathcal{B}s$. The parallel and the perpendicular projectors are now given by

$$P_{\parallel}^{\mu\nu}(k) = g_{\parallel}^{\mu\nu} - \frac{k_{\parallel}^{\mu} k_{\parallel}^{\nu}}{k_{\parallel}^{2}} \quad \text{and} \quad P_{\perp}^{\mu\nu}(k) = g_{\perp}^{\mu\nu} - \frac{k_{\perp}^{\mu} k_{\perp}^{\nu}}{k_{\perp}^{2}} \,. \tag{B.13}$$

The longitudinal projector $P_0^{\mu\nu}(k)$ spans the remaining subspace orthogonal to $k^\mu k^\nu$, and is best represented via

$$P_0^{\mu\nu}(k) = g^{\mu\nu} - \frac{k^\mu k^\nu}{k^2} - P_{\parallel}^{\mu\nu}(k) - P_{\perp}^{\mu\nu}(k) \,. \tag{B.14}$$

In contrast to light propagation in field-free vacuum, the presence of an external magnetic field generically allows for the existence of three distinct and independent photon polarization modes, which are each associated with one of the projectors given by Eqs. (B.13) and (B.14). As long as the propagation direction of the photon does not coincide with the orientation of the magnetic field, i.e. if we have $\mathbf{k} \nparallel \mathbf{B}$, $P_{\parallel}^{\mu\nu}$ and $P_{\perp}^{\mu\nu}$ project onto polarization modes parallel and perpendicular to the plane spanned by $\mathbf{k}$ and $\mathbf{B}$. These two polarization modes can also be continuously related to the corresponding two orthogonal modes which exist in the limit of a vanishing magnetic field. The polarization mode described by $P_0^{\mu\nu}$ does not prevail in the free-field limit. An exception is given by the special case in which the photon's propagation direction coincides with the orientation of the magnetic field, i.e. $\mathbf{k} \parallel \mathbf{B}$. Now, only one externally set reference direction is left, and the projectors $P_0^{\mu\nu}$ and $P_{\perp}^{\mu\nu}$ correspond to the two polarization modes in the limit of vanishing magnetic field strength [138].

Analytical evaluations of the double parameter integral in Eq. (B.11) can be performed for low phase velocity shifts, i.e. $\omega/|\mathbf{k}| \simeq 1$, which should occur for moderate frequencies $0 \leq \omega \leq \mathcal{O}(m)$ and moderate magnetic field strengths $0 \leq \mathcal{B} \leq \mathcal{O}(\mathcal{B}_{\text{cr}})$ [28]. Likewise, analytical expressions for the absorption rate of high-frequency photons, $\omega \gg m$, in weak magnetic fields can be obtained from the parameter integral. A detailed analytical analysis of the polarization tensor in constant magnetic or electric fields for various physical parameter regimes has been performed in Ref. [100]. Additionally, a numerical study for purely magnetic fields can be found in Ref. [139].

Weak-field expansion

For the purposes of examining quantum reflection in Chap. 3, it mainly suffices to evaluate the photon polarization tensor in the limit of weak magnetic fields. By means of the procedure (3.4), this allows analytical insights into nonlinear processes for inho-

mogeneous magnetic pump fields. To this end, we perform a perturbative expansion of the polarization tensor in the field strength $e\mathcal{B}$, reading

$$\begin{aligned}\Pi^{\mu\nu}(k|\mathbf{B}) &= \sum_{n=0}^{\infty} \Pi^{\mu\nu}_{(2n)}(k)\,(e\mathcal{B})^{2n} \\ &= \Pi^{\mu\nu}_{(0)}(k) + \Pi^{\mu\nu}_{(2)}(k)\,(e\mathcal{B})^2 + \mathcal{O}\left[(e\mathcal{B})^4\right] .\end{aligned} \tag{B.15}$$

Due to Furry's theorem, this expansion is in even powers of the field strength only. The expansion coefficients can be generated from Eq. (B.11). After a substitution $s \to s/e\mathcal{B}$, the exponential term in Eq. (B.11) becomes $\mathrm{e}^{-is\phi_0} \to \mathrm{e}^{-is\frac{\phi_0}{e\mathcal{B}}}$. In the limit $\frac{e\mathcal{B}}{\phi_0} \ll 1$, the main contribution to the propertime integral stems from small s, such that the functions N_i can be substituted with their asymptotic expressions for $s \to 0$. A rigorous analysis can be found in Ref. [100], where it is shown that in order to only retain the leading-order expansion terms in Eq. (B.15) the additional condition $\frac{e\mathcal{B}}{\phi_0}\frac{k_\perp^2}{\phi_0} \ll 1$ has to be met.

The lowest-order coefficient corresponds to the zero-field limit, and is given by

$$\Pi_{p,(0)}(k) = \left(k^2\right)^2 \frac{\alpha}{4\pi} \int_0^1 d\nu \left(\frac{\nu^2}{3} - 1\right) \frac{\nu^2}{\phi_0} , \tag{B.16}$$

with

$$\phi_0 \to m^2 + \frac{1-\nu^2}{4}\, k^2 . \tag{B.17}$$

The label p refers to the three different polarization modes $p = 0, \parallel, \perp$. Naturally, in the zero-field limit the Π_p are identical for all polarization modes p, such that the tensor structure indicated in Eq. (B.3) is recovered. The second order can be calculated analogously and reads (see, e.g., [100, 140])

$$\begin{aligned}\Pi_{p,(2)}(k) = &-\frac{\alpha}{12\pi} \\ &\times \int_0^1 d\nu \frac{(1-\nu^2)^2}{\phi_0^2} \left[\begin{Bmatrix} 1 \\ -\frac{2}{1-\nu^2} \\ 1 \end{Bmatrix} k_\parallel^2 + \left(\begin{Bmatrix} 1 \\ 1 \\ \frac{5-\nu^2}{2(1-\nu^2)} \end{Bmatrix} - \frac{k^2(1-\nu^2)}{4\phi_0} \right) k_\perp^2 \right] ,\end{aligned} \tag{B.18}$$

with ϕ_0 given by Eq. (B.17). On the light cone, a truncation of the expansion (B.15) is limited to the parameter regime $\left\{\frac{e\mathcal{B}}{m^2}, \frac{e\mathcal{B}}{m^2}\frac{k_\perp^2}{m^2}\right\} \ll 1$. In this case, the remaining parameter integral in Eq. (B.18) can be performed in closed form, serving as the starting point in Sect. (3.2.2) for the analysis of quantum reflection in a purely magnetic field in the weak-field limit.

B.3. Constant crossed field

Another configuration is of great interest with respect to experimental scenarios featuring high-intensity lasers. This is the so-called "crossed-field" configuration, characterized by $\mathbf{E}\cdot\mathbf{B}=0$ and $|\mathbf{E}|=|\mathbf{B}|=:\mathcal{E}$, i.e. featuring orthogonal electric and magnetic fields of equal amplitude. The photon polarization tensor in crossed fields has been first studied by Narozhnyi [80] and Ritus [81]. In this limit, both field invariants $\mathcal{F}$ and $\mathcal{G}$ and, correspondingly, also the secular invariants a and b vanish. The entire field dependence is therefore carried by the invariant z_k. As detailed in Ref. [28], the correct expression for the polarization tensor in constant crossed fields can be obtained from the general expression (B.6) by first setting $a=b$, and then taking the limit $(a=b)\to 0$.[4]

The polarization tensor in the crossed-field configuration can be decomposed according to

$$\Pi^{\mu\nu}(k|\mathbf{E}\perp\mathbf{B}) = P_0^{\mu\nu}\Pi_0(k) + P_1^{\mu\nu}\Pi_1(k) + P_2^{\mu\nu}\Pi_2(k)\,, \tag{B.19}$$

with

$$\begin{Bmatrix}\Pi_0\\ \Pi_1\\ \Pi_2\end{Bmatrix} = \frac{\alpha}{2\pi}\int_0^\infty \frac{ds}{s}\int_{-1}^1 \frac{d\nu}{2}(1-\nu^2)\left(e^{-is\phi_1}\begin{Bmatrix}k^2\\ k^2+\frac{(es)^2}{6}(3-\nu^2)z_k\\ k^2+\frac{(es)^2}{12}(3+\nu^2)z_k\end{Bmatrix} - k^2\,e^{-im^2 s}\right), \tag{B.20}$$

where

$$\begin{aligned}\phi_1 &:= m^2+\frac{k^2}{4}(1-\nu^2)+\frac{(es)^2}{48}z_k(1-\nu^2)^2\,,\\ z_k &= (\mathbf{k}\times\mathbf{B})^2+(\mathbf{k}\times\mathbf{E})^2-(\mathbf{k}^2-\omega^2)\mathcal{E}^2-2\omega\mathcal{E}^2\,\mathbf{k}\cdot\hat{\mathbf{s}}\,.\end{aligned} \tag{B.21}$$

Here, we have defined the normalized Poynting vector of the pump field $\hat{\mathbf{s}}=\hat{\mathbf{e}}_E\times\hat{\mathbf{e}}_B$. Most importantly, as has been the case for purely magnetic fields, also for constant crossed fields the off-diagonal elements which are present in Eq. (B.6) vanish. The remaining projectors form an orthonormal system and are given by $P_p^{\mu\nu}=u_p^\mu u_p^\nu$, with

[4] Setting one of the secular invariants to zero first, and then taking the limit to zero for the remaining one, recovers the trivial vacuum $F^{\mu\nu}=0$. In contrast, setting $a=b$ first, the subsequent limit $(a=b)\to 0$ only affects the orientation of the electric and magnetic field, and not their magnitude.

$p \in \{0,1,2\}$. We have defined the normalized polarization vectors u_p^μ as

$$\begin{aligned} u_0^\mu &= \frac{(F^2k)^\mu + \frac{z_k}{k^2}k^\mu}{\sqrt{-z_k^2/k^2}}\,, \qquad u_1^\mu = \frac{(k^\star F)^\mu}{\sqrt{z_k}} = \frac{1}{\sqrt{z_k}}(\mathbf{kB},\ -\mathbf{k}\times\mathbf{E}+\omega\mathbf{B})\,, \\ u_2^\mu &= \frac{(kF)^\mu}{\sqrt{z_k}} = \frac{1}{\sqrt{z_k}}(\mathbf{kE},\ \mathbf{k}\times\mathbf{B}+\omega\mathbf{E})\,. \end{aligned} \tag{B.22}$$

The projectors $P_1^{\mu\nu}$ and $P_2^{\mu\nu}$ project onto the physical photon polarization modes in the case of a vanishing background field. In fact, the resulting electric field vectors of the probe field are

$$\begin{aligned} \mathbf{e}_1 &= k^0\mathbf{a}_1 - a_1^0\mathbf{k} \sim \omega(\mathbf{E}\times\mathbf{k}) + \omega^2\mathbf{B} - (\mathbf{kB})\mathbf{k}\,, \\ \mathbf{e}_2 &= k^0\mathbf{a}_2 - a_2^0\mathbf{k} \sim -\omega(\mathbf{B}\times\mathbf{k}) + \omega^2\mathbf{E} - (\mathbf{kE})\mathbf{k}\,. \end{aligned} \tag{B.23}$$

The electric field component associated with the photon polarization mode $p = 1$ is perpendicular to the pump field electric component, and in the plane spanned by $\mathbf{k}$ and the magnetic component of the pump field. For the electric field component belonging to the photon polarization mode $p = 2$, the roles of electric and magnetic pump field component are reversed.

Note that for weak field strengths the shift of the phase velocity $\omega/|\mathbf{k}|$ can be assumed to be small, i.e. $\omega/|\mathbf{k}| \simeq 1$, and the invariant z_k becomes

$$z_k = |\mathbf{k}|^2\mathcal{E}^2\Big(1 - (\hat{\mathbf{e}}_k\cdot\hat{\mathbf{s}})\Big)^2\,. \tag{B.24}$$

Consequentially, weak crossed pump fields do not affect the propagation of light if $(\hat{\mathbf{e}}_k, \hat{\mathbf{e}}_E, \hat{\mathbf{e}}_B)$ form the basis of an ortho-normalized coordinate system [28]. Let us remark that this behavior also persists for quantum reflection in the limit of strong crossed fields, as quantum reflection requires an evaluation of the polarization tensor on the light cone, i.e. $k^2 = 0$; cf. Sect. 3.2.5.

Weak-field expansion

A perturbative expansion of the polarization tensor in a constant crossed field in the field strength $e\mathcal{E}$ reads

$$\begin{aligned} \Pi^{\mu\nu}(k|\mathbf{E}\perp\mathbf{B}) &= \sum_{n=0}^{\infty}\Pi_{(2n)}^{\mu\nu}(k)\,(e\mathcal{E})^{2n} \\ &= \Pi_{(0)}^{\mu\nu}(k) + \Pi_{(2)}^{\mu\nu}(k)\,(e\mathcal{E})^2 + \mathcal{O}\left[(e\mathcal{E})^4\right]. \end{aligned} \tag{B.25}$$

The lowest-order expansion coefficient is just the limit of Eq. (B.19) for vanishing field strength, and hence identical to the corresponding expression (B.16) given in Sect. B.2. The second order reads

$$\Pi_{p,(2)}(k) = -\frac{\alpha\tilde{z}_k}{12\pi}\int_0^1 d\nu \frac{(1-\nu^2)}{\phi_0^2}\left(\left\{\begin{matrix} 3-\nu^2 \\ \frac{3+\nu^2}{2}\end{matrix}\right\} + k^2\frac{(1-\nu^2)^2}{4\phi_0}\right). \tag{B.26}$$

Here, we have extracted the field strength from the invariant z_k, and defined $\tilde{z}_k = z_k/\mathcal{E}^2$. Furthermore, the phase $\phi_0(k)$ is given by Eq. (B.17). As has been the case for the purely magnetic pump field, for $k^2 = 0$ the parameter integral in Eq. (B.26) can be easily performed.

From Eq. (B.20) it is apparent that an expansion in $e\mathcal{E}$ automatically corresponds to an expansion in the invariant z_k. Correspondingly, for a truncation of the expansion (B.25) to be a good approximation, we require $z_k \ll 1$. For on-the-light-cone dynamics, this condition becomes $\left(\frac{e\mathcal{E}}{m^2}\right)^2 \omega^2\left(1-(\hat{\mathbf{e}}_k\cdot\hat{\mathbf{s}})\right)^2 \ll 1$.

C. The reflection coefficient in the transfer matrix formalism

In this appendix we detail the calculation of the one-dimensional reflection coefficient in a smooth and spatially localized potential $V(\mathrm{x}) < 0$, employing the transfer-matrix formalism. This approach is a successful method applied in optics to calculate reflection and transmission in layered media [141]. Besides quantum reflection processes, one-dimensional above-the-barrier scattering plays an important role, e.g., in the context of electron-positron pair production in vacuum for purely temporally varying electric fields. There, computing pair production rates basically amounts to calculating above-the-barrier scattering coefficients, as the pair production process reduces to a one-dimensional Schrödinger equation in the time domain; see, e.g. [142–144].

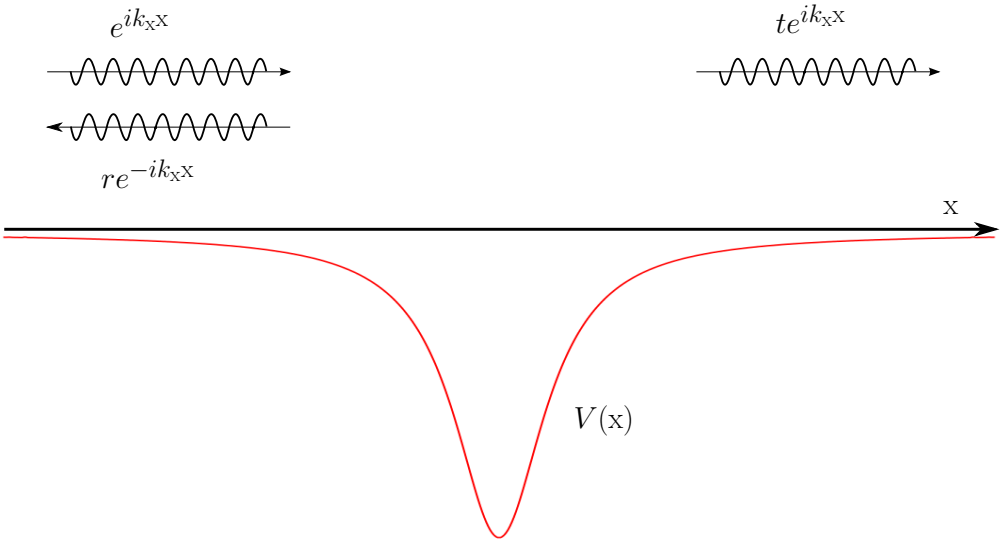

Figure C.1.: Above-the-barrier scattering for an exemplary one-dimensional smooth and spatially localized attractive potential $V(\mathrm{x}) < 0$. A normalized incident matter wave with positive energy and wave vector k_{x} for asymptotic distances $|\mathrm{x}| \to \infty$ experiences partial reflection and transmission at the inhomogeneous profile. The asymptotic reflection and transmission amplitudes are denoted by r and t respectively.

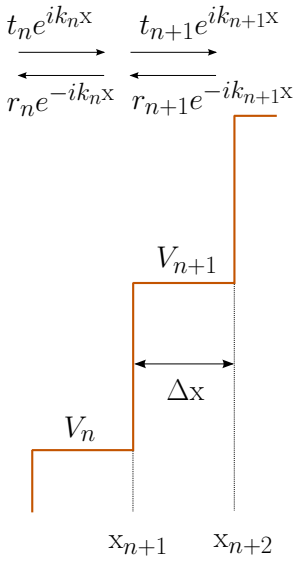

Figure C.2: Discretization of the smooth potential $V(\mathrm{x})$ depicted in Fig. C.1 into constant segments $V_n = V(n\Delta \mathrm{x})$ of equal length $\Delta \mathrm{x}$. The forward and backward traveling waves for each segment propagate with wave vector k_n and amplitudes r_n and t_n respectively.

As shown in Fig. C.1, we consider an incident normalized matter wave with positive energy eigenvalue E approaching the region of the inhomogeneity from $\mathrm{x} \to -\infty$, and with the asymptotic wave vector k_x. To calculate the reflection coefficient, the smooth potential is discretized and substituted by a piecewise continuous step potential $V_n = V(n\Delta \mathrm{x})$ for $\mathrm{x} \in [n\Delta \mathrm{x}, (n+1)\Delta \mathrm{x})$, with $n \in \mathbb{Z}$, and the transfer matrix is then computed for each potential step, cf. Fig. C.2. In the end, the continuous limit can be retrieved by taking $\Delta \mathrm{x} \to 0$.

For each segment V_n of the potential the Schrödinger equation features the plane-wave solutions $r_n \mathrm{e}^{-ik_n \mathrm{x}_n}$ and $t_n \mathrm{e}^{ik_n \mathrm{x}_n}$, corresponding to left and right-moving contributions with constant wave vector $k_n = \sqrt{E - V_n}$ and reflection and transmission amplitudes r_n and t_n respectively. The requirement of continuity of the wave function itself and its first derivative at the potential step at $\mathrm{x}_{n+1} = (n+1)\Delta \mathrm{x}$ leads to

$$\begin{aligned} t_n \mathrm{e}^{ik_n \mathrm{x}_{n+1}} + r_n \mathrm{e}^{-ik_n \mathrm{x}_{n+1}} &= t_{n+1} \mathrm{e}^{ik_{n+1} \mathrm{x}_{n+1}} + r_{n+1} \mathrm{e}^{-ik_{n+1} \mathrm{x}_{n+1}} \,, \\ k_n \left(t_n \mathrm{e}^{ik_n \mathrm{x}_{n+1}} - r_n \mathrm{e}^{-ik_n \mathrm{x}_{n+1}} \right) &= k_{n+1} \left(t_{n+1} \mathrm{e}^{ik_{n+1} \mathrm{x}_{n+1}} - r_{n+1} \mathrm{e}^{-ik_{n+1} \mathrm{x}_{n+1}} \right) \,. \end{aligned} \tag{C.1}$$

Employing matrix formalism, Eq. (C.1) can be rewritten according to

$$\begin{pmatrix} t_n \\ r_n \end{pmatrix} = \begin{pmatrix} \frac{1}{2}(1 + \frac{k_{n+1}}{k_n}) \mathrm{e}^{i(k_{n+1} - k_n)\mathrm{x}_{n+1}} & \frac{1}{2}(1 - \frac{k_{n+1}}{k_n}) \mathrm{e}^{-i(k_{n+1} + k_n)\mathrm{x}_{n+1}} \\ \frac{1}{2}(1 - \frac{k_{n+1}}{k_n}) \mathrm{e}^{i(k_{n+1} + k_n)\mathrm{x}_{n+1}} & \frac{1}{2}(1 + \frac{k_{n+1}}{k_n}) \mathrm{e}^{-i(k_{n+1} - k_n)\mathrm{x}_{n+1}} \end{pmatrix} \begin{pmatrix} t_{n+1} \\ r_{n+1} \end{pmatrix} \,. \tag{C.2}$$

Next, we substitute $(k_{n+1} - k_n)/\Delta \mathrm{x} =: k'_n$, where k'_n denotes the discretized version of the first derivative of the wave vector k_n. Hence, the continuity condition (C.2) can

be cast into

$$\begin{aligned}\begin{pmatrix} t_n \\ r_n \end{pmatrix} &= \begin{pmatrix} \left(1+\frac{k_n'}{2k_n}\Delta\mathrm{x}\right)\mathrm{e}^{ik_n'\mathrm{x}_{n+1}\Delta\mathrm{x}} & -\frac{k_n'}{2k_n}\Delta\mathrm{x}\,\mathrm{e}^{-ik_n'\mathrm{x}_{n+1}\Delta\mathrm{x}}\mathrm{e}^{-i2k_n\mathrm{x}_{n+1}} \\ -\frac{k_n'}{2k_n}\Delta\mathrm{x}\,\mathrm{e}^{ik_n'\mathrm{x}_{n+1}\Delta\mathrm{x}}\mathrm{e}^{i2k_n\mathrm{x}_{n+1}} & \left(1+\frac{k_n'}{2k_n}\Delta\mathrm{x}\right)\mathrm{e}^{-ik_n'\mathrm{x}_{n+1}\Delta\mathrm{x}} \end{pmatrix} \begin{pmatrix} t_{n+1} \\ r_{n+1} \end{pmatrix} \\ &=: \begin{pmatrix} A_{11}(n,n+1) & A_{12}(n,n+1) \\ A_{12}^*(n,n+1) & A_{11}^*(n,n+1) \end{pmatrix} \begin{pmatrix} t_{n+1} \\ r_{n+1} \end{pmatrix} . \end{aligned} \tag{C.3}$$

Up to now, all orders of $\Delta\mathrm{x}$ have been taken into account. The transfer matrix in Eq. (C.3) encodes the continuity conditions for the potential step between the segments n and $n+1$. Successive multiplication for m adjacent potential steps results in

$$\begin{pmatrix} t_n \\ r_n \end{pmatrix} = \begin{pmatrix} A_{11}(n,n+m) & A_{12}(n,n+m) \\ A_{12}^*(n,n+m) & A_{11}^*(n,n+m) \end{pmatrix} \begin{pmatrix} t_{n+m} \\ r_{n+m} \end{pmatrix} . \tag{C.4}$$

with the matrix elements

$$\begin{aligned} A_{11}(n,n+m) &= 1+\Delta\mathrm{x}\sum_{j=n}^{n+m}\left(\frac{k_j'}{2k_j}+ik_jx_{j+1}\right)+\mathcal{O}(\Delta\mathrm{x}^2)\,, \\ A_{12}(n,n+m) &= -\sum_{j=n}^{n+m}\frac{k_j'}{2k_j}\mathrm{e}^{-i2k_j\mathrm{x}_{j+1}}+\mathcal{O}(\Delta\mathrm{x}^2)\,. \end{aligned}$$

Only terms up to first order in $\Delta\mathrm{x}$ have been retained. The combined limit of $\Delta\mathrm{x}\to 0$ and $m\to\infty$, such that their product $m\Delta\mathrm{x} =: \mathrm{x}-\mathrm{y}$ remains finite, recovers the limit of a continuous potential and establishes a relation between the transmission and reflection amplitudes at positions x and y. Taking the limit we obtain

$$\begin{pmatrix} t(x) \\ r(x) \end{pmatrix} = \begin{pmatrix} A_{11}(\mathrm{x},\mathrm{y}) & A_{12}(\mathrm{x},\mathrm{y}) \\ A_{12}^*(\mathrm{x},\mathrm{y}) & A_{11}^*(\mathrm{x},\mathrm{y}) \end{pmatrix} \begin{pmatrix} t(y) \\ r(y) \end{pmatrix} , \tag{C.5}$$

with matrix coefficients

$$\begin{aligned} A_{11}(\mathrm{x},\mathrm{y}) &= 1+\int_{\mathrm{x}}^{\mathrm{y}}\mathrm{d}\tilde{\mathrm{x}}\left(\frac{k'(\tilde{\mathrm{x}})}{2k(\tilde{\mathrm{x}})}+i\,k'(\tilde{\mathrm{x}})\tilde{\mathrm{x}}\right) , \\ A_{12}(\mathrm{x},\mathrm{y}) &= -\int_{\mathrm{x}}^{\mathrm{y}}\mathrm{d}\tilde{\mathrm{x}}\,\frac{k'(\tilde{\mathrm{x}})}{2k(\tilde{\mathrm{x}})}\mathrm{e}^{-2ik(\tilde{\mathrm{x}})\tilde{\mathrm{x}}}\,. \end{aligned}$$

Here, $k(\mathrm{x}) = \sqrt{E-V(\mathrm{x})}$ and $k'(\mathrm{x}) = \frac{\mathrm{d}}{\mathrm{dx}}k(\mathrm{x})$. Scattering above-the-barrier implies $k(\mathrm{x})>0$ for all x. The reflection coefficient R at asymptotic negative distance follows

from $R = |r(\mathrm{x} \to -\infty)|^2$. The boundary conditions for t and r can be inferred from the fact that we deal with a localized potential as depicted in Fig. C.1: Assuming a normalized beam traveling towards the inhomogeneity, we take $t(\mathrm{x} \to -\infty) = 1$. Furthermore, no reflected contributions can be expected at ∞, which implies $r(\mathrm{x} \to \infty) = 0$. With the aid of these boundary conditions, a formula for the reflection coefficient can be straightforwardly determined from Eq. (C.5), reading

$$R = \left| \frac{\int_{-\infty}^{\infty} \mathrm{d}\tilde{\mathrm{x}}\, \frac{k'(\tilde{\mathrm{x}})}{2k(\tilde{\mathrm{x}})} \mathrm{e}^{-2ik(\tilde{\mathrm{x}})\tilde{\mathrm{x}}}}{1 + \int_{-\infty}^{\infty} \mathrm{d}\tilde{\mathrm{x}} \left(\frac{k'(\tilde{\mathrm{x}})}{2k(\tilde{\mathrm{x}})} + i\, k'(\tilde{\mathrm{x}})\tilde{\mathrm{x}} \right)} \right|^2 . \tag{C.6}$$

This is the formula given in Eq. (3.52).

D. Quantum reflection in a plane-wave pump field

In this appendix we sketch out an alternative way to arrive at the scattering coefficients (3.65) for quantum reflected photons in the presence of a $2+1$-dimensional inhomogeneity, featuring a localized transversal field profile $\mathcal{E}(\mathrm{x})$ and a longitudinal profile $\propto \cos\big(\Omega(\mathrm{y}-t)\big)$. To this end, we employ the explicit representation of the photon polarization tensor in a generic, elliptically polarized monochromatic plane-wave field [82, 83] parametrized by the gauge potential in Coulomb-Weyl gauge

$$A_\mu(x) = \hat{\varepsilon}_{1\mu}\frac{\mathcal{E}_1}{\Omega}\cos(\Omega\,\hat{s}x) + \hat{\varepsilon}_{2\mu}\frac{\mathcal{E}_2}{\Omega}\sin(\Omega\,\hat{s}x)\,, \tag{D.1}$$

constituting the pump photons of four-momentum $\Omega\hat{s}^\mu$, where $\hat{s}^\mu = (1, \mathbf{e}_\mathrm{y})$ is the normalized Poynting vector of the pump field. The unit four-vectors $\hat{\varepsilon}_i^\mu = (0, \hat{\boldsymbol{\varepsilon}}_i)$ are independent of x^μ and span the transversal polarization modes of the pump photons; they fulfill $\hat{\varepsilon}_1\hat{\varepsilon}_2 = \hat{\varepsilon}_1\hat{s} = \hat{\varepsilon}_2\hat{s} = 0$, $\hat{\varepsilon}_1^2 = \hat{\varepsilon}_2^2 = 1$. The associated amplitudes can be parameterized by the two electric field strengths $\mathcal{E}_1$ and $\mathcal{E}_2$ divided by the pump photon energy Ω. By varying the ratio of the amplitudes $\mathcal{E}_1$ and $\mathcal{E}_2$ any elliptical polarization mode is attainable.

Plane-wave polarization tensor

The plane-wave polarization tensor already mediates between two probe photon momenta k and k'. It can be expanded in multiples of the momentum transfer $2\Omega\hat{s}^\mu$ [82, 120], reading[1]

$$\Pi^{\mu\nu}(k,k'|A) = (2\pi)^4\sum_{n\in\mathbb{Z}}\delta^{(4)}\big(k+k'-2n\Omega\hat{s}\big)\Pi_n^{\mu\nu}(k,-k')\,. \tag{D.2}$$

[1] The signs of the momenta k and k' in the polarization tensor (D.2) have been adapted to the particular convention of the Fourier transform employed in this work, see the appendix A, and therefore slightly differ from the expressions given in Refs. [82, 120].

Positive n (negative n) are associated with the absorption (emission) of $2|n|$ pump laser photons by the incoming probe photon with k'. The expansion coefficients are given by[2]

$$\Pi_n^{\mu\nu}(k,k'|A) = -m^2\frac{\alpha}{\pi}\left\{\Lambda_1^\mu\Lambda_2^\nu G_1^n + \Lambda_2^\mu\Lambda_1^\nu G_2^n + \Lambda_1^\mu\Lambda_1^\nu G_3^n + \Lambda_2^\mu\Lambda_2^\nu G_4^n + \Lambda_3^\mu\Lambda_4^\nu G_5^n\right\}. \quad \text{(D.3)}$$

Their tensor structure is composed of the four vectors

$$\Lambda_i^\mu = \hat{\varepsilon}_i^\mu - \frac{k\hat{\varepsilon}_i}{k\hat{s}}\hat{s}^\mu\,, \qquad \Lambda_3^\mu = \frac{\hat{s}^\mu k^2 - k^\mu(\hat{s}k)}{(\hat{s}k)\sqrt{-k^2}}\,, \qquad \Lambda_4^\mu = \frac{\hat{s}^\mu k'^2 - k'^\mu(\hat{s}k)}{(\hat{s}k)\sqrt{-k'^2}}\,, \quad \text{(D.4)}$$

with $i = 1, 2$. They fulfill $\Lambda_1^2 + \Lambda_2^2 + \Lambda_3^2 + \Lambda_4^2 = 1$. The polarization four-vector Λ_1 (Λ_2) projects onto the probe photon polarization mode whose electric field lies in the plane spanned by $\mathbf{k}$ and $\hat{\boldsymbol{\varepsilon}}_1$ ($\hat{\boldsymbol{\varepsilon}}_2$); in Coulomb-Weyl gauge the vectors $\hat{\boldsymbol{\varepsilon}}_1$ and $\hat{\boldsymbol{\varepsilon}}_2$ constitute the spatial directions of the electric field vector associated with the pump field $\mathcal{E}_1$ and $\mathcal{E}_2$, respectively.

The scalar coefficients G_j^n in Eq. (D.3) can be represented in terms of a double-parameter integral,

$$G_j^n = \int_{-1}^{1} d\nu \int_0^\infty \frac{d\rho}{\rho} e^{-i\varphi_0\rho}\; g_j^n\; e^{-iY}\,, \quad \text{(D.5)}$$

where the coefficients g_j^n in the integrand are given by

$$\begin{aligned}
g_1^n &= \xi_1\xi_2\left(2\,\mathrm{sign}(\lambda)\frac{1+\nu^2}{1-\nu^2}\rho\,\mathfrak{a}_0 - \mathfrak{a}_1\frac{n}{Z}\right) i^n J_n(Z)\,,\\
g_2^n &= g_1^n(\mathfrak{a}_0 \to -\mathfrak{a}_0)\,,\\
g_3^n &= \left(\xi_1^2\,\mathfrak{a}_1 - \frac{\xi_1^2-\xi_2^2}{1-\nu^2}\sin^2\rho\right) i^n[J_n(Z) - iJ_n'(Z)] + \xi_1^2\frac{1+\nu^2}{1-\nu^2}\sin^2\rho\; i^n J_n(Z)\\
&\qquad + \frac{1}{4}\left(\frac{kk'}{m^2} - \frac{i|\lambda|(1-\nu^2)}{\rho}\right) i^n[J_n(Z) - \delta_{n0}e^{iY}]\,,\\
g_4^n &= g_3^n(\xi_1^2 \leftrightarrow \xi_2^2)(-1)^n\,,\\
g_5^n &= -\frac{\sqrt{k^2k'^2}}{4m^2}(1-\nu^2)i^n[J_n(Z) - \delta_{n0}e^{iY}]\,,
\end{aligned} \quad \text{(D.6)}$$

[2] To have uniform conventions throughout this work we have introduced an additional factor of i with respect to the definition of the expansion coefficients in Ref. [120].

and we have furthermore employed the definitions

$$\begin{aligned}
\mathfrak{a} &= \frac{1}{2}\left(1 - \frac{\sin^2\rho}{\rho^2}\right), \quad \mathfrak{a}_0 = \frac{1}{2}\rho(\partial_\rho \mathfrak{a}), \quad \mathfrak{a}_1 = \mathfrak{a} + 2\,\mathfrak{a}_0, \\
Z &= \frac{2(\xi_1^2 - \xi_2^2)}{|\lambda|(1-\nu^2)}\rho\,\mathfrak{a}_0, \quad Y = \frac{2(\xi_1^2 + \xi_2^2)}{|\lambda|(1-\nu^2)}\rho\,\mathfrak{a}, \\
\varphi_0 &= \frac{2}{|\lambda|(1-\nu^2)}\left[1 - i0^+ + \frac{kk'}{4m^2}(1-\nu^2)\right].
\end{aligned} \tag{D.7}$$

Here, $J_n(Z)$ denotes the Bessel function of the first kind. The scalar coefficients G_j^n of the off-shell plane wave polarization tensor are fully governed by the Lorentz-invariant parameters

$$\frac{kk'}{4m^2}, \qquad \xi_1 = \frac{e\mathcal{E}_1}{m\Omega}, \qquad \xi_2 = \frac{e\mathcal{E}_2}{m\Omega}, \qquad \text{and} \qquad \lambda = -\frac{\Omega\,\hat{s}k}{2m^2}. \tag{D.8}$$

To make contact with the weak-field limit considered in Sect. 3.2.4, we perform an expansion in the field strength ratios $\frac{e\mathcal{E}_i}{m^2}$. Following [120], this can formally be achieved by an expansion in the intensity parameters ξ_i. Although state-of-the-art optical high-intensity lasers actually feature intensity parameters $\xi_i \gg 1$, thereby suggesting the invalidity of such an expansion, we find that after a substitution $\rho \to |\lambda|^3\rho$ in Eq. (D.5) the intensity parameters appear in the definitions of Z and Y (Eq. (D.7)) only in combination with λ according to

$$\xi_i^2\lambda^2 = \left(\frac{e\mathcal{E}_i}{m^2}\right)^2 \frac{(\hat{s}k)^2}{4m^2}. \tag{D.9}$$

This approach therefore has a greater range of validity as could be expected from a "naive" expansion in the intensity parameter [120], see also [145, 146]. Hence, the quantities $Y, Z \propto |\lambda|^2\xi^2 \ll 1$ can be considered small, such that we can make use of the expansion of the Bessel function

$$\begin{aligned}
J_n(Z) &\sim \left(\frac{1}{2}Z\right)^n \frac{1}{\Gamma(n+1)} + \left(\frac{1}{2}Z\right)^n \frac{\left(-\frac{1}{4}Z^2\right)}{\Gamma(n+2)} + \mathcal{O}(Z^{n+4}), \\
J_n'(Z) &\sim \frac{n\frac{1}{2^n}Z^{n-1}}{\Gamma(n+1)} - \frac{2+n}{\Gamma(n+2)}\left(\frac{1}{2}Z\right)^{n+1} + \mathcal{O}(Z^{n+3}).
\end{aligned} \tag{D.10}$$

Correspondingly, for $n \neq 0$ the scalar coefficients scale as $G_j^n \propto \left(\frac{e\mathcal{E}_i}{m^2}\right)^{2|n|}$, and contributions with $|n| \geq 2$ are suppressed by additional powers of the pump field strength

ratios. The scalar coefficients for the relevant contributions are then given by

$$G_j^n = \int_{-1}^{1} d\nu \int_0^\infty \frac{d\rho}{\rho} e^{-i\varphi_0\rho}\, \tilde{g}_j^n \,, \tag{D.11}$$

with the $n = 0$ terms (i.e. no net energy/momentum exchange between pump field and probe photons)

$$\begin{aligned}
\tilde{g}_1^0 &= 2\xi_1\xi_2\,\mathrm{sign}(\lambda)\frac{1+\nu^2}{1-\nu^2}\rho\,\mathfrak{a}_0\,,\\
\tilde{g}_2^0 &= -2\xi_1\xi_2\,\mathrm{sign}(\lambda)\frac{1+\nu^2}{1-\nu^2}\rho\,\mathfrak{a}_0\,,\\
\tilde{g}_3^0 &= \xi_1^2\,\mathfrak{a}_1 + \frac{\xi_1^2\nu^2+\xi_2^2}{1-\nu^2}\sin^2\rho - \frac{i}{2|\lambda|}\frac{\xi_1^2+\xi_2^2}{1-\nu^2}\rho\,\mathfrak{a}\frac{kk'}{m^2} - \frac{\xi_1^2+\xi_2^2}{2}\,\mathfrak{a}\,,\\
\tilde{g}_4^0 &= \xi_2^2\,\mathfrak{a}_1 + \frac{\xi_2^2\nu^2+\xi_1^2}{1-\nu^2}\sin^2\rho - \frac{i}{2|\lambda|}\frac{\xi_1^2+\xi_2^2}{1-\nu^2}\rho\,\mathfrak{a}\frac{kk'}{m^2} - \frac{\xi_1^2+\xi_2^2}{2}\,\mathfrak{a}\,,\\
\tilde{g}_5^0 &= \frac{\sqrt{k^2k'^2}}{2m^2|\lambda|}i(\xi_1^2+\xi_2^2)\rho\,\mathfrak{a}\,,
\end{aligned} \tag{D.12}$$

and the $|n| = 1$ terms (i.e. the pump field either picking up or transferring the four-momentum $2\Omega\hat{s}^\mu$ from/onto the probe photons)

$$\begin{aligned}
\tilde{g}_1^1 &= -\tilde{g}_1^{-1} = -\frac{i}{2}\xi_1\xi_2\,\mathfrak{a}_1\,,\\
\tilde{g}_2^1 &= -\tilde{g}_2^{-1} = -\frac{i}{2}\xi_1\xi_2\,\mathfrak{a}_1\,,\\
\tilde{g}_3^1 &= \tilde{g}_3^{-1} = \frac{1}{2}\xi_1^2\,\mathfrak{a}_1 - \frac{1}{2}\frac{\xi_1^2-\xi_2^2}{1-\nu^2}\sin^2\rho + \frac{i}{4|\lambda|}\frac{\xi_1^2-\xi_2^2}{1-\nu^2}\rho\,\mathfrak{a}_0\frac{k_1k_2}{m^2} + \frac{\xi_1^2-\xi_2^2}{4}\,\mathfrak{a}_0\,,\\
\tilde{g}_4^1 &= \tilde{g}_4^{-1} = -\frac{1}{2}\xi_2^2\,\mathfrak{a}_1 - \frac{1}{2}\frac{\xi_1^2-\xi_2^2}{1-\nu^2}\sin^2\rho + \frac{i}{4|\lambda|}\frac{\xi_1^2-\xi_2^2}{1-\nu^2}\rho\,\mathfrak{a}_0\frac{k_1k_2}{m^2} + \frac{\xi_1^2-\xi_2^2}{4}\,\mathfrak{a}_0\,,\\
\tilde{g}_5^1 &= \tilde{g}_5^{-1} = -\frac{\sqrt{k^2k'^2}}{4m^2|\lambda|}i(\xi_1^2-\xi_2^2)\rho\,\mathfrak{a}_0\,.
\end{aligned} \tag{D.13}$$

Identifying an invariant projector

The tensor structure of the plane-wave polarization tensor is spanned by projectors of the kind $P_{ij}^{\mu\nu} = \Lambda_i^\mu\Lambda_j^\nu$. The left-hand side of the equation of motion (3.3) governing photon propagation in an inhomogeneous pump field can be decomposed in terms of these projectors according to

$$k^2\Big(P_{11}^{\mu\nu} + P_{22}^{\mu\nu} + P_{33}^{\mu\nu}\Big)\,a_\nu(k) = -\int_{k'} \tilde{\Pi}^{\mu\nu}(k,-k'|A)\,a_\nu(k')\,. \tag{D.14}$$

We adopt the configuration from Sect. 3.2.4 by choosing $\hat{s}^\mu = (1, \hat{\mathbf{e}}_\mathrm{y})$ for the pump field inhomogeneity and restricting the probe beam to propagation in the x-y plane. Furthermore, we consider a linearly polarized pump field by setting $\xi_1 = 0$, leading to the vanishing of $G_2^{0,\pm1}$.[3] As in Sections 3.2.2 and 3.2.4 our goal is to identify scenarios for which, after implementing an additional pump field inhomogeneity profile $\xi_2 \to \xi_2(x)$ into the plane wave polarization tensor by means of procedure (3.4), at least one invariant projector $\tilde{P}_p^{\mu\nu}$ exists. To this end we note that in plane-wave fields the four-momentum conservation law $k^\mu = k'^\mu + C\hat{s}^\mu$, with some constant $C \in \mathbb{R}$, holds by virtue of the delta functions in Eq. (D.2). Correspondingly, we find both

$$k'\hat{s} = k\hat{s} \qquad \text{and} \qquad \hat{\varepsilon}_i k = \hat{\varepsilon}_i k' \,, \tag{D.15}$$

such that Λ_1 and Λ_2 may be evaluated at either momentum k^μ or k'^μ, cf. Eq. (D.4). As the projectors are composed of the Λ's, an invariant projector may only exist for scenarios featuring ingoing and outgoing four-momenta k and k' which fulfill the conditions (D.15) for at least one of the polarization vectors $\hat{\varepsilon}_i^\mu$.

Correspondingly, we find that the left side of the conditions (D.15) is fulfilled if the inhomogeneity only varies along the x direction, i.e., $\xi_2 \to \xi_2(\mathrm{x})$. As the probe photons pick up extra momentum along x, we have two choices to be in accordance with the right side of (D.15): For $\hat{\varepsilon}_1^\mu = (0, \hat{\mathbf{e}}_\mathrm{z})$ the projector $P_{11}^{\mu\nu} = \tilde{P}_{11}^{\mu\nu}$ constitutes an invariant projector. As for this choice the electric component of the pump field points along $\hat{\mathbf{e}}_\mathrm{z}$, the scenario can be identified with the one labeled $p = 1$ in Sect. 3.2.4; cf. Eq. (3.61). Likewise, choosing for $\hat{\varepsilon}_2^\mu = (0, \hat{\mathbf{e}}_\mathrm{z})$ the projector $P_{22}^{\mu\nu} = \tilde{P}_{22}^{\mu\nu}$ is invariant, and this choice corresponds with the scenario labeled $p = 2$.

A contraction of the plane-wave polarization tensor (D.2), after the inhomogeneity has been implemented by means of the scheme (3.4), with the global projectors identified above should filter out those Lorentz components which obey the Ward identity. However, we see that after a contraction with the projector $P_{11}^{\mu\nu}$ the tensor structure still contains $P_{12}^{\mu\nu}$, which is not a global projector.[4] Therefore, the resulting equation of motion will not be gauge invariant. In conclusion, it is not possible with our procedure to reliably and unambiguously implement the inhomogeneity $\xi_2(\mathrm{x})$ for the scenario $p = 1$. Note, that for the other scenario, $p = 2$, this problem does not appear since after a contraction of the polarization tensor with $P_{22}^{\mu\nu}$ it is proportional to this global projector, i.e. $\Pi^{\mu\nu} \sim P_{22}^{\mu\nu}$.

[3] By choosing $\xi_1 = 0$ instead of $\xi_2 = 0$, we ensure that in the limit $\Omega \to 0$ the constant-field case is recovered.

[4] Note that $(P_{11})_{\mu\alpha} P_{12}^{\alpha\nu} = P_{12}^{\mu\nu}$.

Result

Consequentially, in what follows we restrict ourselves to the scenario $p = 2$. In accordance with Chap. 3, the equation of motion (D.14) can be reduced to a scalar equation by contracting it with the projector $P_{22}^{\mu\nu}$. The inhomogeneity $\xi_2(\mathrm{x})$ is implemented in the weak-field expansion of the plane-wave polarization tensor according to the procedure (3.4). The induced photon field can then be straightforwardly calculated from Eq. (3.21). Assuming an incoming plane-wave probe photon beam with four-momentum $k_{\mathrm{in}}^{\mu} = \omega_{\mathrm{in}}(1, \cos\beta, \sin\beta, 0)$ and amplitude $a(\omega_{\mathrm{in}})$, we finally obtain for the induced photon field

$$a_2^{\mathrm{ind}}(x) = -ia(\omega_{\mathrm{in}})\frac{m^2\alpha}{2\pi}\sum_{n=-1}^{1}\Theta\big(k_{\mathrm{x},2n}^2\big)\frac{\hat{G}_4^n(\lambda)}{|k_{\mathrm{x},2n}|}\mathrm{e}^{i[|k_{\mathrm{x},2n}|\mathrm{x}+(\omega_{\mathrm{in}}\sin\beta-2n\Omega)\mathrm{y}-(\omega_{\mathrm{in}}-2n\Omega)t]}$$
$$\times\left\{\int\mathrm{dx}'\mathrm{e}^{i(\omega_{\mathrm{in}}\cos\beta-|k_{\mathrm{x},2n}|)\mathrm{x}'}\xi_2^2(\mathrm{x}')+\mathrm{e}^{-2i|k_{\mathrm{x},2n}|\mathrm{x}}\int\mathrm{dx}'\mathrm{e}^{i(\omega_{\mathrm{in}}\cos\beta+|k_{\mathrm{x},2n}|)\mathrm{x}'}\xi_2^2(\mathrm{x}')\right\}+\mathcal{O}\left(\xi_2^4\right)\,. \tag{D.16}$$

Here, the functions $\hat{G}_4^n(\lambda)$ are given by

$$\hat{G}_4^0(\lambda) := \int_{-1}^{1}\frac{d\nu}{8\lambda^2(1-\nu^2)^2}\Big\{\lambda^2(1-\nu^2)^2-4\lambda(1-\nu^2)\,\mathrm{artanh}\Big(\lambda(1-\nu^2)\Big) \\ +\Big(-3+\lambda^2(1-\nu^4)\Big)\log\Big(1-\lambda^2(1-\nu^2)^2\Big)\Big\} \tag{D.17}$$

for the elastic contribution $n = 0$, and

$$\hat{G}_4^n(\lambda) := \int_{-1}^{1}\frac{d\nu}{16\lambda^2(1-\nu^2)^2}\Big\{\lambda^2(1-\nu^2)^2+(2+4n\lambda)\lambda(1-\nu^2)\mathrm{artanh}\Big(\lambda(1-\nu^2)\Big) \\ +\Big(3+4n\lambda+2\lambda^2\nu^2(1-\nu^2)\Big)\log\Big(1-\lambda^2(1-\nu^2)^2\Big)\Big\} \tag{D.18}$$

for the inelastic $n = \pm 1$ contributions. The parameter λ reads

$$\lambda = \frac{\omega_{\mathrm{in}}\Omega}{2m^2}(1-\sin\beta)\,, \tag{D.19}$$

while the x component $k_{\mathrm{x},2n}$ of the momentum of the outgoing photon beam is the same as given in Sect. (3.2.4), under Eq. (3.63). The result for the induced photon field obtained in this section is very similar to Eq. (3.64), which has been obtained by starting from the polarization tensor in constant fields. In fact, by observing that in the limit $\lambda \to 0$ the functions $\hat{G}_4^n(\lambda)$ become

$$\hat{G}_4^0(\lambda) \sim -\frac{8\lambda^2}{45} \qquad \text{and} \qquad \hat{G}_4^{\pm 1}(\lambda) \sim -\frac{4\lambda^2}{45}\,, \tag{D.20}$$

the induced photon field (D.16) obtained here coincides with Eq. (3.64) for the polarization mode $p = 2$ and the soft-photon regime.

The results of this appendix are limited to the polarization mode $p = 2$. In contrast to Sect. 3.2.4, however, they are not limited to pump fields with longitudinal modulations fulfilling $\Omega \ll m$. Correspondingly, Eq. (D.16) allows insights into quantum reflection for inhomogeneous pump fields consisting of high-energy photons, i.e. in the hard X-ray and Gamma regime.[5] To this end, Fig. D.1 shows plots of the real and imaginary part of $\hat{G}_4^n(\lambda)$ as functions of λ. For $\lambda < 1$, the $\hat{G}_4^n(\lambda)$ are strictly real and negative, and their low-frequency behavior is given by Eq. (D.20). For $\lambda > 1$, they

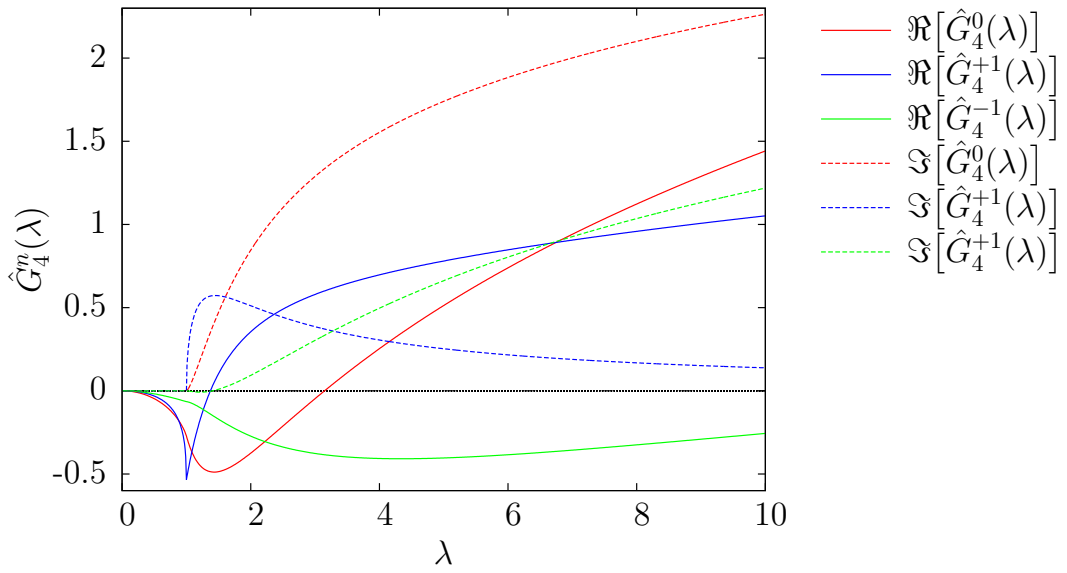

Figure D.1.: Plots of $\hat{G}_4^n(\lambda)$ for $n = 0, \pm 1$, as a function of the parameter λ. For $\lambda \to 0$, the real parts (solid lines) behave like $\sim -\lambda^2$. For $\lambda > 1$, the functions generate an imaginary part (dashed lines). With the exception of $\Im\big[G_4^{+1}\big]$, which approaches zero for $\lambda \to \infty$, all graphs go to ∞ for $\lambda \to \infty$.

[5] While in general $\lambda \ll 1$ is not required, the parameter λ is restricted to such values which fulfill $\xi_i^2 \lambda^2 \ll 1$ for a given pump field strength.

develop an imaginary part which signals the onset of absorptive effects by means of electron-positron pair production. The real parts for $n = 0, \pm 1$ show qualitatively similar behavior: They each have a single negative maximum, before they finally approach positive infinity for $\lambda \to \infty$. The imaginary parts are strictly positive, and for $\lambda \to \infty$ also approach positive infinity with the exception of $\Im\big[G_4^{+1}\big]$, which goes to zero in this limit.

The numbers of induced photons and hence the coefficients for reflection and forward scattering, which can be inferred from Eq. (D.16), do not only depend on the functions $\hat{G}_4^n(\lambda)$ but also feature the generic exponential suppression in the transferred momentum between the pump and probe photons which is typical for quantum reflection processes. Consequentially, when employing high-energy probe and pump photons only the contribution in Eq. (D.16) belonging to elastic scattering in the forward direction features a nonnegligible number of induced photons. In fact the coefficient for elastic forward scattering,[6] $R_{\parallel,0}^{(+)}$, scales with respect to the pump and probe photon frequencies according to $R_{\parallel,0}^{(+)} \sim \frac{|\hat{G}(\lambda)|^2 \omega_{\text{in}}^2}{\lambda^4}$. Hence, keeping Ω fixed and increasing the probe photon frequency ω_{in} leads to an increase of $R_{\parallel,0}^{(+)}$ until $\lambda \simeq 1.2$, after which point the coefficient decreases and approaches zero for $\lambda \to \infty$. As our formalism is restricted to configurations conserving the polarization of the probe photon beam, the forward scattered elastic contributions referred to here are by default indistinguishable from the background beam, cf. also Sect. 3.2.6.[7]

[6] Cf. Sections 3.2.4 and 3.2.2 for the notation employed here.

[7] However, the larger cross section of nonlinear vacuum effects when moving to high-frequency probe beams (compared to probe beams in the optical frequency range) is at the heart of Laser-based proposals to detect vacuum birefringence, see [64]. By employing counterpropagating pump and probe beams the detection of induced photons with flipped polarization, constituting the signal, needs to take place essentially in forward direction [115].

E. Design parameters of some current and future high-intensity lasers

At present, the highest electric field strengths which can be achieved in a laboratory setting are those generated in the focal spots of pulsed high-intensity lasers. To achieve large intensities $\langle I \rangle = W/(\tau\sigma)$ requires one to employ pulses with high energy W, and temporally and spatially compress them to short pulse durations τ and small focal areas σ. Since the invention of the laser, for a long time maximum intensities were limited by the nonlinear response and damage thresholds of the gain medium and other optical components. The invention of "chirped pulse amplification" (CPA) in 1985 circumvented these limitations [147]: Employing dispersive elements a short broadband "seed" laser pulse is stretched in time by a factor of up to 10^6 before being amplified in a gain medium by several orders of magnitudes. As this happens at comparatively low intensities, the integrity of the optical components is preserved. Alternatively, the amplification of the stretched laser pulse is achieved by "optical parametric CPA" (OPCPA), where nonlinear wave-mixing effects in the pump medium are utilized to transfer energy from a pump to the laser pulse [148]. In the end the laser pulse is then re-compressed to its original pulse duration, and hence to a greatly increased intensity. Modern high-intensity laser systems usually employ several stages of amplification combining both CPA and OPCPA.

With the help of these techniques the maximum peak intensity of laser systems has steadily risen over the last decades. Currently, the highest reported laser powers are around $P = 1\text{PW}$, with corresponding intensities in the range of $\langle I \rangle \approx 10^{21} \ldots 10^{22}\text{W/cm}^2$. Several laser facilities aimed at the generation of pulses with powers of $P = 10\text{PW}$ are being projected, or already under construction.

In Table E.1 we list the design parameters of a selection of current state-of-the-art high-intensity laser facilities, and some facilities planned to be constructed and/or com-

Laser facility	W[J]	λ[nm]	τ[fs]	P[PW]	$\langle I\rangle$[W/cm^2]
JETI200	4	800	20	0.2	$8.6 \cdot 10^{21}$
Omega EP	2500	1053	10000	0.25	$6.2 \cdot 10^{21}$
BELLA	40	1075	40	1	$2.4 \cdot 10^{22}$
POLARIS	150	1030	150	1	$2.6 \cdot 10^{22}$
Vulcan	500	1053	500	1	$2.5 \cdot 10^{22}$
Vulcan 10PW	300	1053	30	10	$2.5 \cdot 10^{23}$
ELI-NP	2×250	800	25	2×10	$2 \times 4.3 \cdot 10^{23}$
XCELS	12×400	910	25	12×15	$12 \times 5.3 \cdot 10^{23}$

Table E.1.: Design parameters of a selection of high-intensity laser systems which are either currently in operation or projected for the near-future. Listed are the pulse energy W per shot, laser wavelength λ, pulse duration τ, pulse power P as well as the cycle-averaged pulse intensity $\langle I\rangle$, assuming the laser pulse has been focussed down to the diffraction limit.

pleted in the near-future.[1] The JETI200 and POLARIS laser systems are both located at the Helmholtz Institute of Jena, Germany. The JETI200 laser is a system based on Ti:sapphire, featuring pulses with an on-target energy of 4J and pulse durations as low as 17fs [106]. The POLARIS laser [107, 108] is an experimental diode-pumped solid-state CPA laser system. A recent upgrade has increased its pulse energy to above 50J [150], which are the highest pulse energies delivered by a diode-pumped laser in the world at the moment. These, however, are still well below the design parameters listed in Table E.1 which have been employed in Sects. 3.2.6 and 4.4 to obtain experimental estimates for the numbers of quantum reflected and merged photons.

The BELLA laser at the Berkeley Lab, USA, is a CPA laser based on Ti:sapphire, delivering short pulses with peak powers of 1PW, and is mainly used for electron acceleration experiments [151]. The Vulcan laser, located at the Central Laser Facility in the UK, reaches similar peak powers by generating pulses with comparatively long pulse durations and large pulse energies [109]. At the moment, these two facilities belong among the most powerful fully operational high-intensity laser systems.

Several high-intensity laser facilities featuring even greater peak powers are being developed at the moment. The most prominent examples are the 10PW extension of the Vulcan laser, as well as the laser facility at the Nuclear Physics Research Center of the European "Extreme Light Infrastructure" (ELI-NP) [110], located in Romania. The latter will feature two 10PW laser arms, and is set to be commissioned in 2018. Additionally, the Exawatt Center for Extreme Light studies (XCELS) in Russia [130]

[1] Note that such a selection necessarily has to be incomplete. An overview of many existing high-intensity laser facilities around the world can be found, e.g., in Ref. [149].

ambitiously plans to generate even more powerful laser pulses by coherently adding a large number of ultra-high power laser beams, aimed at reaching peak powers in the Exawatt regime in the not-too-far future.

Lastly, let us add that currently the highest laser pulse energies are actually achieved in research facilities used to explore nuclear fusion by means of initial confinement fusion, of which the world's largest facility is the National Ignition Facility (NIF) in the USA. In Table E.1 we have listed the design parameters for another such facility, the OMEGA EP (extended performance) laser system. The laser pulses generated there will have energies in the kJ-regime and pulse durations in the picosecond regime. Hence, despite their enormous pulse energy the generated peak power is actually comparable (or less) to the smaller laser systems listed here.

F. The Heisenberg-Euler effective Lagrangian

In this section we briefly outline the derivation of the Heisenberg-Euler effective action, starting from the one-loop effective action (2.10). For simplicity we restrict ourselves to purely magnetic fields, and later simply state the result for arbitrary constant electric and magnetic fields.[1] The derivation closely follows Ref. [49].

As a first step the functional determinant appearing in Eq. (2.10) can be rewritten as

$$\Gamma^{(1)} = -\frac{i}{2}\mathrm{Tr}\left[\ln\left(\not{D}^2 + m^2\right)\right], \tag{F.1}$$

where use has been made of the operator relation $\ln\left[\det(\dots)\right] = \mathrm{Tr}\left[\ln(\dots)\right]$. A straightforward technique to deal with the logarithm is to employ Frullani's integral [153] to arrive at the proper time representation[2,3]

$$\Gamma^{(1)} = \frac{i}{2}\int_{\frac{1}{\Lambda^2}}^{\infty}\frac{\mathrm{d}T}{T}\mathrm{e}^{-m^2T}\mathrm{Tr}\left[\mathrm{e}^{-\left(-D^2-\frac{e}{2}\sigma^{\mu\nu}F_{\mu\nu}\right)T}\right]. \tag{F.2}$$

To deal with the divergence at $T \to 0$, a UV cut-off $1/\Lambda^2 > 0$ has been introduced at the lower bound. This expression for the one-loop correction of the effective action is still valid for arbitrary electromagnetic fields.

The evaluation of Eq. (F.2) is greatly simplified for constant purely magnetic fields, as the spectrum of the differential operator $-D^2$ is then composed of Landau levels. Let us consider a constant magnetic field $\mathbf{B} = \mathcal{B}\mathbf{e}_\mathrm{z}$ pointing along the z direction. The eigenvalues of the operator $-D^2$ then read

$$-\omega^2 + p_\mathrm{z}^2 + e\mathcal{B}(2n+1), \tag{F.3}$$

[1] Some generalizations to inhomogeneous fields have been obtained by means of derivative expansions, see, e.g., Ref. [152].

[2] The version of Frullani's integral employed here is $\ln\frac{A}{B} = -\int_0^\infty \frac{\mathrm{d}T}{T}\left(\mathrm{e}^{-AT} - \mathrm{e}^{-BT}\right)$, with $B = 0$.

[3] An alternative approach to calculate the effective action (F.1) uses zeta-function regularization, see, e.g., Ref. [154].

such that after a Wick rotation $\omega \to ip_\tau$ the effective action becomes

$$\Gamma^{(1)} = \frac{i}{2}\int_{\frac{1}{\Lambda^2}}^{\infty}\frac{\mathrm{d}T}{T}\mathrm{e}^{-m^2T}\int_{-\infty}^{\infty}\frac{i\mathrm{d}p_\tau}{\left(\frac{2\pi}{L}\right)}\int_{-\infty}^{\infty}\frac{\mathrm{d}p_\mathrm{z}}{\left(\frac{2\pi}{L}\right)}\sum_{n=0}^{\infty}L^2\frac{e\mathcal{B}}{2\pi}\mathrm{e}^{-\left(p_\tau^2+p_\mathrm{z}^2+e\mathcal{B}(2n+1)\right)T}\,\mathrm{tr}_\gamma\mathrm{e}^{\frac{e}{2}\sigma_{\mu\nu}F^{\mu\nu}T}. \tag{F.4}$$

Here, L is the length scale associated with the integration volume, and the factor $L^2\frac{e\mathcal{B}}{2\pi}$ takes into account the degeneracy of the Landau levels. The last trace is over the Dirac indices and becomes $\mathrm{tr}_\gamma\mathrm{e}^{\frac{e}{2}\sigma_{\mu\nu}F^{\mu\nu}T} = 4\cosh(e\mathcal{B}T)$. Additionally, both the summation over the Landau levels as well as the momentum integrals can be evaluated explicitly. The result is given by $\Gamma^{(1)} = \int_x \mathcal{L}^{(1)} = L^4\mathcal{L}^{(1)}$, where

$$\mathcal{L}^{(1)} = -\frac{1}{8\pi^2}\int_{\frac{1}{\Lambda^2}}^{\infty}\frac{\mathrm{d}T}{T^3}\mathrm{e}^{-m^2T}e\mathcal{B}T\coth(e\mathcal{B}T) \tag{F.5}$$

is the unregularized Heisenberg-Euler Lagrangian for a constant magnetic field. To make it finite we need to subtract the zero-field contribution at $\mathcal{B} \to 0$. Furthermore, a logarithmic divergence requires a renormalization of the field strength $\mathcal{B}$ and the coupling constant e, after which we obtain

$$\mathcal{L}^{(1)} = -\frac{1}{8\pi^2}\int_0^{\infty}\frac{\mathrm{d}T}{T^3}\mathrm{e}^{-m^2T}\left(e\mathcal{B}T\coth(e\mathcal{B}T) - \frac{1}{3}(e\mathcal{B}T)^2 - 1\right). \tag{F.6}$$

The Heisenberg-Euler Lagrangian for purely electric fields can be obtained from the result (F.6) by means of a duality transformation $\mathcal{B} \to i\mathcal{E}$. As a consequence, the Lagrangian generates an imaginary part at the poles $T = n\pi$. As the Lagrangian is connected to the vacuum-to-vacuum persistence amplitude via $\langle 0|0\rangle = \exp\left[i\int_x\mathcal{L}\right]$, the imaginary part of the Lagrangian corresponds to the local decay rate of the vacuum caused by the creation of real pairs of electrons and positrons.

Finally, the Heisenberg-Euler Lagrangian $\mathcal{L}_\mathrm{HE}$ for arbitrary constant electric and magnetic fields can be conveniently expressed in terms of the secular invariants $a = \left(\sqrt{\mathcal{F}^2+\mathcal{G}^2}-\mathcal{F}\right)^{\frac{1}{2}}$ and $b = \left(\sqrt{\mathcal{F}^2+\mathcal{G}^2}+\mathcal{F}\right)^{\frac{1}{2}}$. It is given by [8, 10, 28]

$$\mathcal{L}_\mathrm{HE} = \frac{\alpha}{2\pi}\int_0^{\infty}\frac{\mathrm{d}s}{s}\,\mathrm{e}^{-i\frac{m^2s}{e}}\left[a\,b\coth(as)\cot(bs) - \frac{a^2-b^2}{3} - \frac{1}{s^2}\right], \tag{F.7}$$

where the integration contour is prescribed implicitly through the substitution $m^2 \to m^2 - i0^+$.

For many practical applications it is sufficient to look at the regime of "weak" field strengths $\mathcal{E} \ll \mathcal{E}_\mathrm{cr}$, as has been done in Chap. 4. Expanding the Heisenberg-Euler

Lagrangian in terms of the field invariants $\mathcal{F}$ and $\mathcal{G}$, the proper time integrations can be performed and all the prefactors determined explicitly to arbitrary order. Due to CP-symmetry such an expansion is in even powers of $\mathcal{G}$. It reads

$$\mathcal{L}(\mathcal{F},\mathcal{G}) = \frac{\alpha}{90\pi}\left(\frac{e}{m^2}\right)^2\left(7\mathcal{G}^2+4\mathcal{F}^2\right) - \frac{2\alpha}{315\pi}\left(\frac{e}{m^2}\right)^4\left(13\mathcal{F}\mathcal{G}^2+8\mathcal{F}^3\right) + \mathcal{O}\left(\{\mathcal{F},\mathcal{G}\}^4\right). \tag{F.8}$$

The various derivatives of the Lagrangian with respect to $\mathcal{F}$ and $\mathcal{G}$, which are required for the representations of the two- and three-photon polarization tensors (4.4) and (4.5) in the weak-field limit, are then given by

$$\begin{aligned}
\frac{\partial\mathcal{L}}{\partial\mathcal{F}} &= \frac{4\alpha}{45\pi}\left(\frac{e}{m^2}\right)^2\mathcal{F} - \frac{2\alpha}{315\pi}\left(\frac{e}{m^2}\right)^4\left(13\mathcal{G}^2+24\mathcal{F}^2\right) + \mathcal{O}\big(\{\mathcal{F},\mathcal{G}\}^3\big)\,,\\
\frac{\partial\mathcal{L}}{\partial\mathcal{G}} &= \frac{7\alpha}{45\pi}\left(\frac{e}{m^2}\right)^2\mathcal{G} - \frac{52\alpha}{315\pi}\left(\frac{e}{m^2}\right)^4\mathcal{F}\mathcal{G} + \mathcal{O}\big(\{\mathcal{F},\mathcal{G}\}^3\big)\,,\\
\left\{\frac{\partial^2\mathcal{L}}{\partial\mathcal{F}^2},\frac{\partial^2\mathcal{L}}{\partial\mathcal{G}^2},\frac{\partial^2\mathcal{L}}{\partial\mathcal{F}\partial\mathcal{G}}\right\} &= \{4,7,0\}\frac{\alpha}{45\pi}\left(\frac{e}{m^2}\right)^2 - \{48\mathcal{F},13\mathcal{F},13\mathcal{G}\}\frac{2\alpha}{315\pi}\left(\frac{e}{m^2}\right)^4\\
&\qquad + \mathcal{O}\big(\{\mathcal{F},\mathcal{G}\}^2\big)\,,\\
\left\{\frac{\partial^3\mathcal{L}}{\partial\mathcal{F}^3},\frac{\partial^3\mathcal{L}}{\partial\mathcal{G}^3},\frac{\partial^3\mathcal{L}}{\partial\mathcal{F}\partial\mathcal{G}^2},\frac{\partial^3\mathcal{L}}{\partial\mathcal{F}^2\partial\mathcal{G}}\right\} &= -\{24,0,13,0\}\frac{4\alpha}{315\pi}\left(\frac{e}{m^2}\right)^4 + \mathcal{O}\big(\{\mathcal{F},\mathcal{G}\}\big)\,.
\end{aligned} \tag{F.9}$$

F.1. Strong-field limit

To obtain insights into the strong-field limit, the derivatives have to be computed straight from the nonperturbative Lagrangian (F.7). The expressions for the first and second derivatives of the Lagrangian in terms of the field invariants $\mathcal{F}$ and $\mathcal{G}$ have already been computed in Ref. [121]. For completeness we list them here. The first derivatives read

$$\begin{aligned}
\frac{\partial\mathcal{L}}{\partial\mathcal{F}} &= \frac{\alpha}{2\pi}\int_0^\infty\frac{\mathrm{d}s}{s}\,\mathrm{e}^{-i\frac{m^2s}{e}}\left\{\frac{ab}{a^2+b^2}\frac{as\cot(bs)}{\sinh^2(as)} + (a\leftrightarrow ib) + \frac{2}{3}\right\},\\
\frac{\partial\mathcal{L}}{\partial\mathcal{G}} &= \frac{\alpha}{2\pi}\int_0^\infty\frac{\mathrm{d}s}{s}\,\mathrm{e}^{-i\frac{m^2s}{e}}\mathcal{G}\left\{\frac{\coth(as)\cot(bs)}{2ab} - \frac{1}{a^2+b^2}\frac{bs\cot(bs)}{\sinh^2(as)} + (a\leftrightarrow ib)\right\}.
\end{aligned} \tag{F.10}$$

The second derivatives are given by

$$\begin{aligned}
\frac{\partial^2\mathcal{L}}{\partial\mathcal{F}^2} &= \frac{\alpha}{2\pi}\int_0^\infty \frac{\mathrm{d}s}{s}\,\mathrm{e}^{-i\frac{m^2 s}{e}}\frac{ab}{(a^2+b^2)^2}\Bigg\{-\frac{abs^2}{\sinh^2(as)\sin^2(bs)} \\
&\qquad -\left[1-2as\coth(as)-2\frac{a^2-b^2}{a^2+b^2}\right]\frac{as\cot(bs)}{\sinh^2(as)}+(a\leftrightarrow ib)\Bigg\}, \\
\frac{\partial^2\mathcal{L}}{\partial\mathcal{G}^2} &= \frac{\alpha}{2\pi}\int_0^\infty \frac{\mathrm{d}s}{s}\,\mathrm{e}^{-i\frac{m^2 s}{e}}\frac{ab}{(a^2+b^2)^2}\Bigg\{\frac{abs^2}{\sinh^2(as)\sin^2(bs)} \\
&\qquad -\left[1-2\frac{b^2}{a}s\coth(as)+\frac{2}{a^2}\frac{a^4+b^4}{a^2+b^2}\right]\frac{as\cot(bs)}{\sinh^2(as)}+(a\leftrightarrow ib)\Bigg\}, \\
\frac{\partial^2\mathcal{L}}{\partial\mathcal{F}\partial\mathcal{G}} &= \frac{\alpha}{2\pi}\int_0^\infty \frac{\mathrm{d}s}{s}\,\mathrm{e}^{-i\frac{m^2 s}{e}}\frac{\mathcal{G}}{(a^2+b^2)^2}\Bigg\{-\frac{1}{2}\frac{(a^2-b^2)s^2}{\sinh^2(as)\sin^2(bs)} \\
&\qquad +\left[1-2as\coth(as)+\frac{1}{b^2}\frac{(a^2-b^2)^2}{a^2+b^2}\right]\frac{bs\cot(bs)}{\sinh^2(as)}+(a\leftrightarrow ib)\Bigg\}.
\end{aligned} \tag{F.11}$$

Furthermore, the third derivatives read

$$\begin{aligned}
\frac{\partial^3\mathcal{L}}{\partial\mathcal{F}^3} &= \frac{\alpha}{2\pi}\int_0^\infty \mathrm{d}s\,\mathrm{e}^{-i\frac{m^2 s}{e}}\frac{ab}{(a^2+b^2)^5}\Bigg\{\frac{3a(a^4-10a^2b^2+5b^4)\cot(bs)}{\sinh^2(as)} \\
&\quad +\frac{6a^2(a^2+b^2)(a^2-3b^2)\coth(as)\sin(bs)\cos(bs)+6ab(b^4-a^4)}{\sinh^2(as)\sin^2(bs)}\,s \\
&\quad +\frac{2a(a^2+b^2)^2\cot(bs)}{\sinh^2(as)}\left[2a^2\coth^2(as)+\frac{a^2}{\sinh^2(as)}+\frac{3b^2}{\sin^2(bs)}\right]s^2\Bigg\} \\
&\quad +(a\leftrightarrow ib)\,, \\
\frac{\partial^3\mathcal{L}}{\partial\mathcal{G}^3} &= \frac{\alpha}{2\pi}\int_0^\infty \mathrm{d}s\,\mathrm{e}^{-i\frac{m^2 s}{e}}\frac{1}{(a^2+b^2)^5}\Bigg\{\frac{3a(a^6-6a^4b^2+5a^2b^4-4b^6)\cot(bs)}{\sinh^2(as)} \\
&\quad -\frac{6b^2(2a^4-a^2b^2+b^4)(a^2+b^2)\coth(as)\sin(bs)\cos(bs)}{\sinh^2(as)\sin^2(bs)}\,s \\
&\quad -\frac{\frac{3}{2}ab(a^2+b^2)(3a^4-2a^2b^2+3b^4)}{\sinh^2(as)\sin^2(bs)}\,s \\
&\quad +\frac{2ab^2(a^2+b^2)^2\cot(bs)}{\sinh^2(as)}\left[2b^2\coth^2(as)+\frac{b^2}{\sinh^2(as)}+\frac{3a^2}{\sin^2(bs)}\right]s^2\Bigg\} \\
&\quad +(a\leftrightarrow ib)\,,
\end{aligned} \tag{F.12}$$

and

$$
\begin{aligned}
\frac{\partial^3\mathcal{L}}{\partial\mathcal{F}\partial\mathcal{G}\partial\mathcal{G}} &= \frac{\alpha}{2\pi}\int_0^\infty \mathrm{d}s\,\mathrm{e}^{-i\frac{m^2 s}{e}}\frac{1}{(a^2+b^2)^5}\Bigg\{\frac{b(2b^6-17a^2b^4+20a^4b^2-9a^6)\cot(bs)}{\sinh^2(as)} \\
&\quad - \frac{2ab(3a^4-5a^2b^2+4b^4)(a^2+b^2)\coth(as)\sin(bs)\cos(bs)}{\sinh^2(as)\sin^2(bs)}\,s \\
&\quad - \frac{(a^2+b^2)(a^6-5a^4b^2+5a^2b^4-b^6)}{\sinh^2(as)\sin^2(bs)}\,s \\
&\quad + \frac{2a^2b(a^2+b^2)^2\cot(bs)}{\sinh^2(as)}\left[2b^2\coth^2(as)+\frac{b^2}{\sinh^2(as)}+\frac{a^2-2b^2}{\sin^2(bs)}\right]s^2\Bigg\} \\
&\quad + (a\leftrightarrow ib)\,, \\
\frac{\partial^3\mathcal{L}}{\partial\mathcal{F}\partial\mathcal{F}\partial\mathcal{G}} &= \frac{\alpha}{2\pi}\int_0^\infty \mathrm{d}s\,\mathrm{e}^{-i\frac{m^2 s}{e}}\frac{1}{(a^2+b^2)^5}\Bigg\{\frac{a(6b^6-25a^2b^4+16a^4b^2-a^6)\cot(bs)}{\sinh^2(as)} \\
&\quad - \frac{2a^2(a^4-5a^2b^2+6b^4)(a^2+b^2)\coth(as)\sin(bs)\cos(bs)}{\sinh^2(as)\sin^2(bs)}\,s \\
&\quad + \frac{\frac{1}{2}ab(a^2+b^2)(5a^4-14a^2b^2+5b^4)}{\sinh^2(as)\sin^2(bs)}\,s \\
&\quad + \frac{2ab^2(a^2+b^2)^2\cot(bs)}{\sinh^2(as)}\left[2a^2\coth^2(as)+\frac{a^2}{\sinh^2(as)}+\frac{b^2-2a^2}{\sin^2(bs)}\right]s^2\Bigg\} \\
&\quad + (a\leftrightarrow ib)\,.
\end{aligned}
\tag{F.13}
$$

In the limit of vanishing magnetic (electric) field, the invariant $\mathcal{G}$ vanishes and we have $\mathcal{F}<0$ ($\mathcal{F}>0$). Likewise, the secular invariants become $b=0, a=\sqrt{2|\mathcal{F}|}$ ($a=0, b=\sqrt{2\mathcal{F}}$). The same holds true for orthogonal electric and magnetic fields, for which we find $\mathcal{G}=0$ as well. Remarkably, in this limit the parameter integration can be carried out analytically. The strategy is similar to the one outlined in Sect. 3.2.5, employed to obtain the strong-field limit of Eq. (3.89). The results for the first- and

second-order derivative read [121]

$$\begin{aligned}
\left.\frac{\partial\mathcal{L}}{\partial\mathcal{F}}\right|_{\mathcal{G}=0} &= \frac{\alpha}{\pi}\left\{4\zeta'(-1,\chi) - \chi\left[2\zeta'(0,\chi) - \ln(\chi) + \chi\right] - \frac{1}{3}\ln(\chi) - \frac{1}{6}\right\},\\
\left.\frac{\partial^2\mathcal{L}}{\partial\mathcal{F}^2}\right|_{\mathcal{G}=0} &= \frac{1}{2\mathcal{F}}\frac{\alpha}{\pi}\left\{\frac{1}{3} - \chi\left[2\zeta'(0,\chi) + \ln(\chi) + 2\chi(1-\psi(\chi)) - 1\right]\right\},\\
\left.\frac{\partial^2\mathcal{L}}{\partial\mathcal{G}^2}\right|_{\mathcal{G}=0} &= \frac{1}{2\mathcal{F}}\frac{\alpha}{\pi}\left\{4\zeta'(-1,\chi) - \chi\left[2\zeta'(0,\chi) - \ln(\chi) + \chi\right] - \frac{1}{6}\left[2\psi(\chi) + \chi^{-1} + 1\right]\right\},
\end{aligned} \tag{F.14}$$

where we have defined

$$\chi = \frac{1}{2}\frac{m^2}{e\sqrt{2|\mathcal{F}|}} \times \begin{cases} 1 & \mathcal{F} > 0 \\ i & \mathcal{F} < 0 \end{cases}. \tag{F.15}$$

As a consequence of CP-invariance, the remaining derivatives of the Lagrangian vanish: $\frac{\partial\mathcal{L}}{\partial\mathcal{G}}\big|_{\mathcal{G}=0} = \frac{\partial^2\mathcal{L}}{\partial\mathcal{F}\partial\mathcal{G}}\big|_{\mathcal{G}=0} = 0$. As before, $\zeta(s,\chi)$ denotes the Hurwitz zeta-function, and $\zeta'(s,\chi) = \partial_s\zeta(s,\chi)$ its derivative with respect to the first argument. The Digamma-function is the logarithmic derivative of the Gamma-function, i.e. $\psi(\chi) = \partial_\chi \ln[\Gamma(\chi)]$. Lastly, $\gamma_\mathrm{E} \approx 0.57721$ denotes the Euler-Mascheroni constant. The result for the third derivatives reads

$$\begin{aligned}
\left.\frac{\partial^3\mathcal{L}}{\partial\mathcal{F}^3}\right|_{\mathcal{G}=0} &= -\frac{\alpha}{4\pi\mathcal{F}^2}\left\{-8\zeta(-1,\chi) + 2\chi^3\zeta(2,\chi) + 6\chi^2\Big[-1 + \gamma_\mathrm{E} + \ln(2) + \psi(\chi)\Big]\right.\\
&\qquad \left. + 6\chi\left[\frac{1}{2}\Big(1 - \gamma_\mathrm{E} - \ln(2\chi)\Big) + \zeta(0,\chi)\Big(1 + \gamma_\mathrm{E} + \ln(2)\Big) - \zeta'(0,\chi)\right]\right\},\\
\left.\frac{\partial^3\mathcal{L}}{\partial\mathcal{F}\partial\mathcal{G}^2}\right|_{\mathcal{G}=0} &= \frac{\alpha}{24\pi\mathcal{F}^2\chi}\left\{1 + 12\chi^3\Big(\gamma_\mathrm{E} + \ln(2) + \psi(\chi)\Big)\right.\\
&\qquad + \chi^2\Big[12\zeta'(0,\chi) + 2\zeta(2,\chi) + 12\Big(2 - \gamma_\mathrm{E} - \ln(2)\Big)\zeta(0,\chi)\\
&\qquad + 18\Big(1 - \gamma_\mathrm{E} - \ln(2\chi)\Big)\Big]\\
&\qquad + \chi\Big[-48\zeta'(-1,\chi) + 48\Big(-1 + \gamma_\mathrm{E} + \ln(2)\Big)\zeta(-1,\chi)\\
&\qquad \left. + 4\gamma_\mathrm{E} - 2 + \ln(16) + 4\psi(\chi)\Big]\right\},
\end{aligned} \tag{F.16}$$

where the remaining derivatives again vanish: $\frac{\partial^3\mathcal{L}}{\partial\mathcal{G}^3}\big|_{\mathcal{G}=0} = \frac{\partial^3\mathcal{L}}{\partial\mathcal{F}^2\partial\mathcal{G}}\big|_{\mathcal{G}=0} = 0$.

Figure F.1 shows plots of the real part of the derivatives (F.14) and (F.16) as a function of the constant field strength ratio $e^2\mathcal{F}/m^4$. Note that the derivatives have

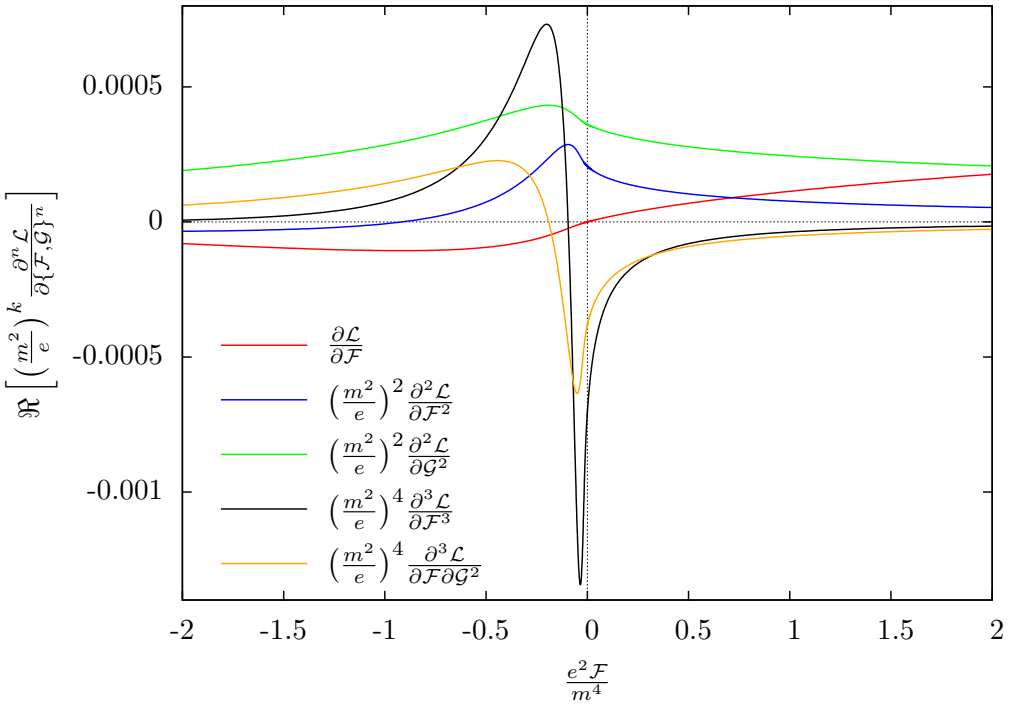

Figure F.1.: Plot of the real part of the normalized derivatives of the Heisenberg-Euler Lagrangian (F.7) for $\mathcal{G} = 0$, as a function of $e^2\mathcal{F}/m^4$. Positive (negative) values of $e^2\mathcal{F}/m^4$ correspond to purely magnetic (electric) pump fields. For $|e^2\mathcal{F}/m^4| \to 0$ the derivatives agree with the corresponding weak-field expressions (F.9).

been normalized by appropriate factors of $(m^2/e)^k = \mathcal{E}_{\mathrm{cr}}^k$. Positive values of $e^2\mathcal{F}/m^4$ correspond to purely magnetic fields, and negative values to purely electric fields. As can be seen in Fig. F.1, for $\mathcal{F} \to 0$ the real part $\Re[\partial\mathcal{L}/\partial\mathcal{F}]$ of the first derivative of the Lagrangian tends to zero, while higher derivatives are finite. The explicit values of these higher derivatives at $\mathcal{F} = 0$ can be read off from the expansion for weak fields (F.9), setting $\mathcal{G} = 0$. Analytical insights into the leading-order behavior in the strong-field limit can be straightforwardly obtained from Eqs. (F.14) and (F.16) by

expanding in orders of χ,

$$\begin{aligned}
\left.\frac{\partial\mathcal{L}}{\partial\mathcal{F}}\right|_{\mathcal{G}=0} &= \frac{\alpha}{\pi}\left\{-\frac{1}{3}\ln(\chi)+\frac{1}{6}\Big(1-24\ln(G)\Big)+\mathcal{O}\Big(\chi\ln(\chi)\Big)\right\}, \\
\left.\frac{\partial^2\mathcal{L}}{\partial\mathcal{F}^2}\right|_{\mathcal{G}=0} &= \frac{1}{\mathcal{F}}\frac{\alpha}{\pi}\left\{\frac{1}{6}+\mathcal{O}\Big(\chi\ln(\chi)\Big)\right\}, \\
\left.\frac{\partial^2\mathcal{L}}{\partial\mathcal{G}^2}\right|_{\mathcal{G}=0} &= \frac{1}{\mathcal{F}}\frac{\alpha}{\pi}\left\{\frac{1}{12\chi}+\frac{1}{12}\Big(1+2\gamma_{\mathrm{E}}-24\ln(G)\Big)+\mathcal{O}\Big(\chi\ln(\chi)\Big)\right\}, \\
\left.\frac{\partial^3\mathcal{L}}{\partial\mathcal{F}^3}\right|_{\mathcal{G}=0} &= -\frac{1}{\mathcal{F}^2}\frac{\alpha}{\pi}\left\{\frac{1}{6}+\mathcal{O}\Big(\chi\ln(\chi)\Big)\right\}, \\
\left.\frac{\partial^3\mathcal{L}}{\partial\mathcal{F}\partial\mathcal{G}^2}\right|_{\mathcal{G}=0} &= -\frac{1}{\mathcal{F}^2}\frac{\alpha}{\pi}\left\{\frac{1}{24\chi}+\frac{1}{12}\Big(1+2\gamma_{\mathrm{E}}-24\ln(G)\Big)+\mathcal{O}\Big(\chi\ln(\chi)\Big)\right\},
\end{aligned} \tag{F.17}$$

valid for $\mathcal{F}\gtrless 0$. Here, $G=\exp\left[\frac{1}{12}-\zeta'(-1)\right]\approx 1.28242712$ denotes the Glaisher-Kinkelin constant [155,156]. We find that in the limit of strong fields the first derivative of the Lagrangian diverges logarithmically, while the remaining derivatives tend to zero. With the help of $\frac{\partial^2\mathcal{L}}{\partial\mathcal{F}^2}\big|_{\mathcal{G}=0}$ and $\frac{\partial^2\mathcal{L}}{\partial\mathcal{G}^2}\big|_{\mathcal{G}=0}$ given in Eq. (F.17), it can be straightforwardly checked that the strong-field limit of the two-photon polarization tensor (4.4) in the low-energy limit agrees with the results obtained in Ref. [28]; cf. also Sect. 3.2.5.

The imaginary part of the derivatives (F.14) and (F.16) is depicted in Fig. F.2. By virtue of the optical theorem, for a photon propagating in a constant electromagnetic pump field the absorption rate due electron-positron pair production is given by $-\frac{1}{\omega}\Im\Pi_{\parallel,\perp}$, where the $\Pi_{\parallel,\perp}$ are the mode coefficients of the two-photon polarization tensor, cf. Eq. (B.6). From Fig. F.2, it can be seen that the polarization tensor in the low-energy regime develops an imaginary part only for $\mathcal{F}<0$, i.e. for either purely electric fields or alternatively for orthogonal electric and magnetic fields with $\mathcal{E}>\mathcal{B}$. The reason is given by the fact that in this regime by construction the energy of the photons is below the pair creation threshold $\omega=2m$. Hence, pair creation is only possible if additional energy is provided by the electric component of the pump field.

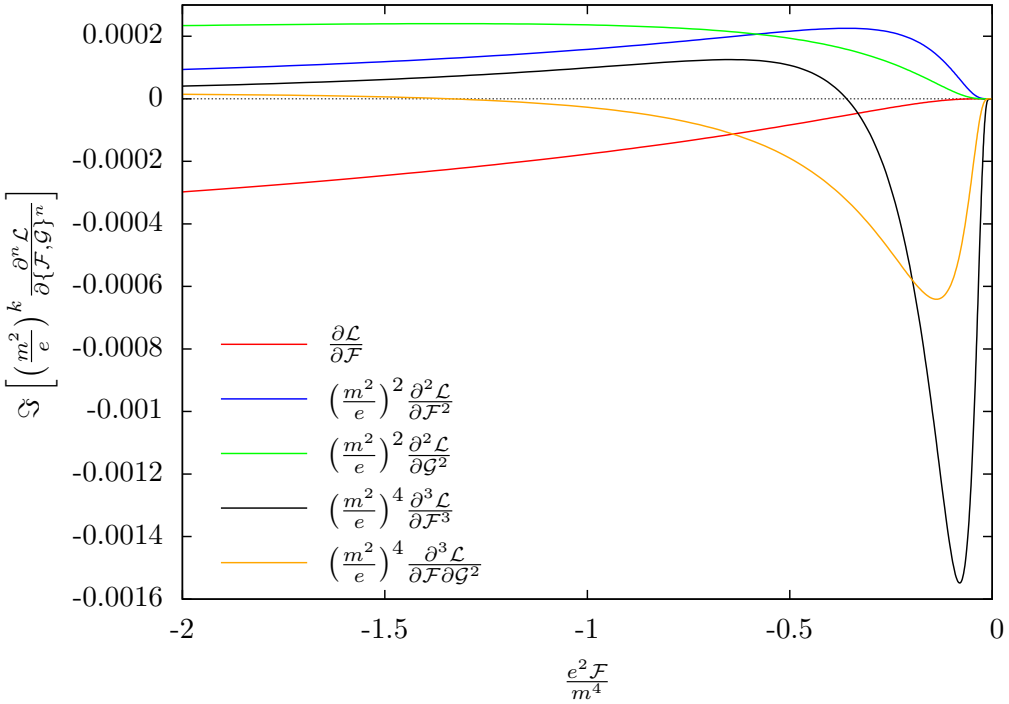

Figure F.2.: Plot of the imaginary parts of the normalized derivatives of the Heisenberg-Euler Lagrangian (F.7) for $\mathcal{G} = 0$, as a function of $e^2\mathcal{F}/m^4$. Only negative values of $e^2\mathcal{F}/m^4$, i.e. corresponding to either purely electric pump fields or crossed fields with $\mathcal{E} > \mathcal{B}$, have been plotted. For positive values the derivatives of the Euler-Heisenberg Lagrangian are purely real, signaling the absence of vacuum pair production for purely magnetic fields and in the limit of low-energy photons. Correspondingly, for $|e^2\mathcal{F}/m^4| \to 0^-$ the imaginary parts of the derivatives vanish, and the corresponding weak-field expressions (F.9) are purely real.

F.2. Parametric momentum analysis

In this section of the appendix we discuss in a little more detail the scaling of the low-energy approximation employed in Chap. 4 to examine photon merging and splitting in inhomogeneous crossed pump fields. Let us denote by $\left(\frac{e\mathcal{E}}{m^2}\right)$ the pump field scale, and by v the momentum scale of the photons.

Following [25], the QED Lagrangian in momentum space is a Lorentz-invariant scalar function composed of contractions of the components $F^{\mu\nu}$, ${}^\star F^{\mu\nu}$ and k^μ. For arbitrary $\mathcal{F}$ and $\mathcal{G}$, the basic contractions which compose the Lagrangian are of the kind k^2, FF, ${}^\star FF$, $kFFk$, $k{}^\star FFk$, $kFFFFk$, etc.[4] Elements with an odd number of contracted field strength tensors, i.e. $kFk = kFFFk = 0$, ..., vanish identically, which is a

[4]The shorthand notation employed here implies the contraction of all Lorentz indices, i.e. $FF \equiv F_{\mu\nu}F^{\mu\nu}$.

manifestation of Furry's theorem. The action $\mathcal{S} = \int_x \mathcal{L}$ is a dimensionless quantity and therefore, the individual contributions to the true Lagrangian in position space for inhomogeneous fields scale as

$$\mathcal{L}_{\text{QED}} = m^4\, \mathcal{O}\left(\left(\tfrac{e\mathcal{E}}{m^2}\right)^2\right)^{n+2} \mathcal{O}\left(\left(\tfrac{v}{m}\right)^2\right)^{l}, \qquad \text{with} \quad n, l \geq 0\,. \tag{F.18}$$

Consequentially, the procedure of employing the Heisenberg-Euler Lagrangian (F.7) and implementing a LCFA neglects contributions of $\mathcal{O}\left(\frac{v^2}{m^2}\right)$, i.e. terms with $l \geq 1$.

The crossed-field configuration is characterized by the vanishing of the invariants $\mathcal{F} = \mathcal{G} = 0$. Consequentially, this leads to the additional vanishing of all elements containing contractions of the field strength tensors except for $kFFk$, and the true Lagrangian for this configuration is thus given by Eq. (F.18) with the additional constraint $l \geq n + 2$.

The polarization tensors are obtained from Eq. (4.3). The derivatives with respect to the gauge field A^μ scale as $k\frac{\partial}{\partial F} \sim v\frac{1}{e\mathcal{E}}$, and hence the various contributions to the exact, unknown two and three-photon polarization tensors for arbitrary $\mathcal{F}$ and $\mathcal{G}$ in position space scale as

$$\begin{aligned} \Pi^{\mu\nu} &\sim m^2 \left(\frac{e\mathcal{E}}{m^2}\right)^2 \left(\frac{v}{m}\right)^2 \mathcal{O}\left(\left(\tfrac{e\mathcal{E}}{m^2}\right)^2\right)^n \mathcal{O}\left(\left(\tfrac{v}{m}\right)^2\right)^l, \\ \Pi^{\mu\nu\rho} &\sim m \left(\frac{e\mathcal{E}}{m^2}\right) \left(\frac{v}{m}\right)^3 \mathcal{O}\left(\left(\tfrac{e\mathcal{E}}{m^2}\right)^2\right)^n \mathcal{O}\left(\left(\tfrac{v}{m}\right)^2\right)^l, \end{aligned} \tag{F.19}$$

with $n, l \geq 0$. To obtain the proper scaling behavior for the crossed-field configuration, it is important to first calculate the derivatives of the Lagrangian with respect to the field strengths before taking the limit $\mathcal{F}, \mathcal{G} \to 0$. Consequentially, the scaling of the contributions to the two-photon polarization tensor in the crossed-field configuration can be written as

$$\Pi^{\mu\nu}_{\text{crossed}} \sim m^2 \left[\left(\frac{e\mathcal{E}}{m^2}\right)^2 \mathcal{O}\left(\left(\tfrac{v}{m}\right)^2\right)\right]^{n+1}, \qquad \text{with} \quad n \geq 0\,, \tag{F.20}$$

while the contributions to the three-photon polarization tensor scale as

$$\Pi^{\mu\nu\rho}_{\text{crossed}} \sim m \left(\frac{v}{m}\right)^3 \left(\frac{e\mathcal{E}}{m^2}\right) \left[1 + \mathcal{O}\left(\left(\tfrac{v}{m}\right)^2\right)\right] \tag{F.21}$$

for the lowest order in the field strength ratio, and as

$$\Pi^{\mu\nu\rho}_{\text{crossed}} \sim m \left(\frac{v}{m}\right) \left(\frac{e\mathcal{E}}{m^2}\right) \left[\left(\frac{e\mathcal{E}}{m^2}\right)^2 \mathcal{O}\left(\left(\tfrac{v}{m}\right)^2\right)\right]^{n+1}, \qquad \text{with} \quad n \geq 0, \tag{F.22}$$

for higher orders in the field strength ratio.

The scaling behavior given in Eq. (F.20) for the two-photon polarization tensor for crossed fields can be readily observed in Sect. 3.2.5, Eq. (3.81). There, the weak-field expansion is automatically tied to the expansion in terms of the energy ω_{in} of the probe photon, such that the order of $\frac{\omega_{\text{in}}}{m}$ coincides with the order of the field strength ratio $\left(\frac{e\mathcal{E}}{m^2}\right)$. Due to fact that the polarization tensor is evaluated on the light cone, only the lowest possible order in $\frac{\omega_{\text{in}}}{m}$ corresponding to a given order in the field strength appears in Eq. (3.81).

Let us briefly discuss the scaling of the induced numbers $\mathcal{N}$ of photons in the locally-constant field approximation, which neglects terms with $l \geq 1$. The scaling of the crossed-field polarization tensors in momentum space to the lowest order in the pump field strength follows from Eq. (4.3), and reads

$$\Pi^{\mu\nu}_{\text{crossed,LCFA}} \sim \frac{v^2_{\text{probe}}}{v^4_{\text{pump}}} \left(\frac{e\mathcal{E}}{m^2}\right)^2 \qquad \text{and} \qquad \Pi^{\mu\nu\rho}_{\text{crossed,LCFA}} \sim \frac{v^3_{\text{probe}}}{m^2\, v^4_{\text{pump}}} \left(\frac{e\mathcal{E}}{m^2}\right). \tag{F.23}$$

Here, we have introduced the momentum scales v_{probe} and v_{pump} of the probe and the pump photons respectively. With the help of Eqs. (4.17) and (4.16) we obtain for the scaling of the splitting and merging numbers

$$\begin{aligned} \mathcal{N}^{\text{Split}} &\sim \left(\frac{v_{\text{probe}}}{m}\right)^8 \left(\frac{m}{v_{\text{pump}}}\right)^8 \left(\frac{e\mathcal{E}}{m^2}\right)^2 \left(\frac{e\mathfrak{E}}{m^2}\right)^2, \qquad \text{and} \\ \mathcal{N}^{\text{Merg}} &\sim \left(\frac{v_{\text{probe}}}{m}\right)^4 \left(\frac{m}{v_{\text{pump}}}\right)^8 \left(\frac{e\mathcal{E}}{m^2}\right)^2 \left(\frac{e\mathfrak{E}}{m^2}\right)^4, \end{aligned} \tag{F.24}$$

where we assumed an identical peak field strength $\mathfrak{E}$ for all probe photon beams. Accordingly, the field strength $\mathcal{E}$ denotes the field strength of the pump beam. This scaling of the merging and splitting numbers can be straightforwardly observed at Eq. (4.23).[5] As has been discussed in the main text, for set-ups employing high-intensity lasers in the optical frequency range, photon splitting is greatly suppressed with respect to merging.

[5] Constant pump fields correspond to the limit $v_{\text{pump}} \to 0$. Consequentially, the number of induced photons diverges as the interaction region becomes infinitely extended.

For completeness, the scaling of the number of quantum reflected photons within the LCFA to lowest order in the pump field strength is given by

$$\mathcal{N}^{\mathrm{Qref}} \sim \left(\frac{v_{\mathrm{probe}}}{m}\right)^4 \left(\frac{m}{v_{\mathrm{pump}}}\right)^8 \left(\frac{e\mathcal{E}}{m^2}\right)^4 \left(\frac{e\mathfrak{E}}{m^2}\right)^2 . \tag{F.25}$$

G. Gaussian beams

Gaussian beams are a class of solutions of the paraxial Helmholtz equation in free space. The fundamental Gaussian mode, also denoted as the TEM_{00} mode, is most commonly employed to approximately describe the electric and magnetic field profile of focussed laser beams of wavelength λ as generated by finite-diameter mirrors [103]. It reads

$$\mathcal{E}(\mathrm{x},\mathrm{y},\mathrm{z}) = \mathcal{E}\frac{w_0}{w(\mathrm{z})}\mathrm{e}^{-\left(\frac{r_\perp}{w(z)}\right)^2}\mathrm{e}^{-i\left(\frac{2\pi \mathrm{z}}{\lambda}+\frac{\pi r_\perp^2}{\lambda R(\mathrm{z})}-\arctan\frac{\mathrm{z}}{\mathrm{z}_R}\right)}, \tag{G.1}$$

where $r_\perp^2 = \mathrm{x}^2+\mathrm{y}^2$ is the radial coordinate transverse to the propagation direction z of the Gaussian beam. In transverse direction, the laser beam features a Gaussian field profile with width $w(\mathrm{z}) = w_0\sqrt{1+\frac{\mathrm{z}^2}{\mathrm{z}_R^2}}$, where w_0 denotes the focal radius and $\mathrm{z}_R = \frac{\pi w_0^2}{\lambda}$ the Rayleigh length. The transversal beam profile therefore widens as one moves away from the focal spot at $\mathrm{z}=0$. The angle of divergence Θ of the beam is given by $\tan\Theta = \lim_{\mathrm{z}\to\infty}\frac{w(\mathrm{z})}{\mathrm{z}}$. A beam which is focussed down to the diffraction limit, i.e. $w_0=\lambda$, has therefore a divergence of $\Theta = \frac{1}{\pi} \approx 18°$. The radius of curvature $R(\mathrm{z}) = \mathrm{z}\left(1+\left(\frac{\mathrm{z}_R}{\mathrm{z}}\right)\right)$ of the wave fronts has a minimum for $\mathrm{z}=\mathrm{z}_R$, while increasing linearly for $\mathrm{z}\to\infty$ (as is the case for the wave fronts of a spherical wave). Near the focus, the radius of curvature diverges and the wave fronts become plane. The Gaussian beam therefore resembles a plane wave near the focus, and a spherical wave in the far-field region.

In this work we employ the Gaussian beam description to calculate the photon background generated by the probe and pump photon beams in Sect. 4.4. The intensity profile of a Gaussian beam propagating along the z direction, after averaging over one laser cycle, reads

$$\langle I\rangle(\mathrm{x},\mathrm{y},\mathrm{z}) = I_0\frac{w_0^2}{w^2(\mathrm{z})}\mathrm{e}^{-\frac{2r_\perp^2}{w^2(\mathrm{z})}}. \tag{G.2}$$

Here, I_0 denotes the peak intensity of the laser pulse. Integrating over the transverse coordinates of the cycle-averaged intensity profile relates it to the number $\mathcal{N}$ of photons

of frequency $\omega = \frac{2\pi}{\lambda}$ which are contained in the laser pulse of duration τ,

$$\mathcal{N} \approx \frac{\tau}{\omega} \int \mathrm{dx}\,\mathrm{dy}\ \langle I \rangle(\mathrm{x},\mathrm{y}) = \frac{2\pi\tau}{\omega} \int \mathrm{d}r_\perp\, r_\perp \langle I \rangle(r_\perp)\,. \tag{G.3}$$

The last equality is due to the Gaussian beam profile being symmetric about z.

To calculate the background generated by the probe and pump beams requires the transversal profile in the far-field region. For $r \to \infty$ we can substitute $r_\perp = r\sin\theta$ and $\mathrm{d}r_\perp = r\cos\theta \mathrm{d}\theta$, such that we find

$$\frac{\mathrm{d}\mathcal{N}(\theta)}{\mathrm{d}\cos\theta} \approx \frac{2\pi\tau}{\omega} \cos\theta \lim_{r\to\infty} r^2 \langle I \rangle(\theta, r)\,. \tag{G.4}$$

The peak intensity I_0 is related to the total energy W contained in the laser pulse by $I_0 = 2\frac{0.86W}{\sigma\tau}$. Taking the limit $r \to \infty$ yields

$$\frac{\mathrm{d}\mathcal{N}(\theta)}{\mathrm{d}\cos\theta} \approx \frac{0.86W\, 4\pi \mathrm{z}_R^2}{\sigma\omega} \cos\theta\ \mathrm{e}^{-2\tan^2\theta \frac{\mathrm{z}_R^2}{w_0^2}}\,. \tag{G.5}$$

A beam focussed down to ρ times the refraction limit, i.e. $w_0 = \rho\lambda$, has a Rayleigh length $\mathrm{z}_R = \rho^2\pi\lambda$ and occupies a focal area $\sigma = \rho^2\pi\lambda^2$. Hence, we obtain

$$\frac{\mathrm{d}\mathcal{N}(\theta)}{\mathrm{d}\cos\theta} \approx 0.86W\, 2\pi\lambda\, \cos\theta\ \mathrm{e}^{-2\pi^2\rho^2\tan^2\theta}\,. \tag{G.6}$$

Equation (G.6) estimates the differential number of photons for a Gaussian beam propagating along z. For a Gaussian beam propagating under an angle θ' with respect to the z axis, we slightly modify Eq. (G.6) to read

$$\frac{\mathrm{d}\mathcal{N}(\theta)}{\mathrm{d}\cos\theta} \approx 0.86W\, 2\pi\lambda\, \cos(\theta-\theta')\ \mathrm{e}^{-2\pi^2\rho^2\tan^2(\theta-\theta')}\,. \tag{G.7}$$

Equation (G.7) has been employed in Sect. 4.4 to compare the photon background noise as generated by the probe beams with the differential number of merged photons $\frac{\mathrm{d}\mathcal{N}_{\mathrm{Merg}}(\theta)}{\mathrm{d}\cos\theta}$, constituting the signal.

List of Figures

List of Tables

Danksagung (Acknowledgements)

An dieser Stelle möchte ich mich recht herzlich bei Prof. Dr. Holger Gies für seine Betreuung und Unterstützung während der Promotionsphase bedanken. Seine umfangreichen Fachkenntnisse, Originalität und positive Sichtweise sind Inspiration für jeden angehenden Wissenschaftler. Desweiteren danke ich Dr. Felix Karbstein für die sehr enge Zusammenarbeit und die stets gute Laune mit der er sich meiner Fragen annahm. Vielen Dank auch an meine Kollegen im Helmholtzweg 4, insbesondere Alexander Blinne, Dr. Christian Kohlfürst und Julia Borchardt, für die angenehme Atmosphäre und gute Zusammenarbeit.

Die Forschungsarbeit wurde am Helmholtz-Institut Jena im Rahmen der Research School of Advanced Photon Science durchgeführt. Die finanzielle Unterstützung ermöglichte die Teilnahme an interessanten Konferenzen, weiterhin stellten die angebotenen Seminare, Lecture Weeks und Softskill-Kurse eine große Bereicherung der Promotion dar.

Zu guter Letzt danke ich natürlich meiner Familie, welche mich stets vorbehaltlos in all meinen Vorhaben unterstützte. Diese Arbeit widme ich meinen beiden Großeltern Ruth und Werner Seegert.

Ehrenwörtliche Erklärung

Ich erkläre hiermit ehrenwörtlich, dass ich die vorliegende Arbeit selbständig, ohne unzulässige Hilfe Dritter und ohne Benutzung anderer als der angegebenen Hilfsmittel und Literatur angefertigt habe. Die aus anderen Quellen direkt oder indirekt übernommenen Daten und Konzepte sind unter Angabe der Quelle gekennzeichnet. Die in dieser Arbeit beschriebene Forschungsarbeit und Auswahl der Schwerpunkte fand in enger Zusammenarbeit mit Dr. Felix Karbstein und meinem betreuenden Hochschullehrer Prof. Dr. Holger Gies statt. Desweiteren gaben Dr. Felix Karbstein und Dr. Christian Kohlfürst inhaltliche und formelle Verbesserungsvorschläge im Rahmen des Korrekturlesens dieser Arbeit.

Weitere Personen waren an der inhaltlich-materiellen Erstellung der vorliegenden Arbeit nicht beteiligt. Insbesondere habe ich hierfür nicht die entgeltliche Hilfe von Vermittlungs- bzw. Beratungsdiensten (Promotionsberater oder andere Personen) in Anspruch genommen. Niemand hat von mir unmittelbar oder mittelbar geldwerte Leistungen für Arbeiten erhalten, die im Zusammenhang mit dem Inhalt der vorgelegten Dissertation stehen.

Die Arbeit wurde bisher weder im In- noch im Ausland in gleicher oder ähnlicher Form einer anderen Prüfungsbehörde vorgelegt.

Die geltende Promotionsordnung der Physikalisch-Astronomischen Fakultät ist mir bekannt.

Ich versichere ehrenwörtlich, dass ich nach bestem Wissen und Gewissen die reine Wahrheit gesagt und nichts verschwiegen habe.

Ort, Datum Unterschrift des Verfassers